Doctoral theses at NTNU, 2022:254

Andreas T. G. Janssønn

Cavity-mediated impact of superconductors on ferromagnetic insulators

Doctoral thesis

NTNU
Norwegian University of Science and Technology
Thesis for the Degree of
Philosophiae Doctor
Faculty of Natural Sciences
Department of Physics

NTNU
Norwegian University of
Science and Technology

Andreas T. G. Janssønn

Cavity-mediated impact of superconductors on ferromagnetic insulators

Thesis for the Degree of Philosophiae Doctor

Trondheim, September 2022

Norwegian University of Science and Technology
Faculty of Natural Sciences
Department of Physics

NTNU
Norwegian University of
Science and Technology

NTNU
Norwegian University of Science and Technology

Thesis for the Degree of Philosophiae Doctor

Faculty of Natural Sciences
Department of Physics

ISBN 978-82-326-6434-4 (printed ver.)
ISBN 978-82-326-6369-9 (electronic ver.)
ISSN 1503-8181 (printed ver.)
ISSN 2703-8084 (online ver.)

Doctoral theses at NTNU, 2022:254

Printed by NTNU Grafisk senter

Abstract

This dissertation is a presentation of the research conducted during three years at the QuSpin Center for Quantum Spintronics, on the cavity-mediation of interactions between ferromagnetic insulators (FI) and superconductors (SC). We begin with a semiclassical and intuitive demonstration, followed by a comprehensive derivation of an effective, microscopic theory based on the Matsubara path integral formalism. Then, we extract the leading-order effects of the SC on the FI, namely the induction of an effective anisotropy field leading to local reorientation of the FI spins, and corrections to the FI quasiparticle spectrum. We demonstrate that the respective effects imprint the FI with information about broken inversion symmetry in the SC, and momentum anisotropy in its gap. The set-up is applicable to spintronic and superconducting circuitry, both of which are energy-efficient technologies that challenge established electronic technology.

The use of cavity-mediation distinguishes this model from proximity systems, the conventional stage for FI–SC interactions. It presents an environment in which the FI and SC can interact without the mutual disruption of their orders associated with proximity effects. Furthermore, by the application of path integrals, the cavity is integrated out exactly, leaving an exact effective FI–SC theory. Integrating out the SC, we are readily able to extract influences on the FI an order beyond mean field theory. The theory moreover takes into account the differing finite dimensions of the FI, cavity and SC, and also the separation between the FI and the SC, leaving it versatile for realistic configurations. The path integral formalism distinguished this approach from conventional theoretical frameworks for analyzing cavity-coupled systems, including classical modelling, Jaynes–Cummings-like modelling, and in particular approaches involving the Schrieffer–Wolff transformation. Unlike the latter, we are not limited analytically to off-resonant regimes.

The research has resulted in one published paper in which we present the semiclassical proof of concept that motivates the microscopic inquiry. It has also resulted in one paper ready for submission, in which the microscopic model is presented, and the anisotropy field is extracted and estimated numerically. Additionally, we present here novel, analytical expressions for the corrections to the FI quasiparticle spectrum, along with promising numerical estimates within an experimentally detectable range.

Sammendrag

Denne avhandlingen er en sammenfatning av tre års forskning utført ved QuSpin Center for Quantum Spintronics, og omhandler kavitetsmedierte vekselvirkninger mellom ferromagnetiske isolatorer (FI) og superledere (SC). Vi begynner med en semiklassisk og intuitiv demonstrasjon, etterfulgt av en fullstendig utledning av en effektiv, mikroskopisk teori basert på Matsubaras stiintegralformalisme. Deretter trekker vi ut ledende ordens virkning av SC-en på FI-en, nemlig forårsakningen av et effektivt anisotropifelt som lokalt vender hvert av FI-ens spinn, samt av korreksjoner i spekteret til FI-ens kvasipartikler. Vi demonstrerer at de respektive virkningene etterlater avtrykk i FI-en av brutt inversjonssymmetri i SC-en, og momentumanisotropi i gapet. Oppsettet er anvendbart i spintroniske og superledende kretser, to energibesparende teknologier som utfordrer etablert elektronikk.

Bruken av kavitetsmediering skjelner vår modell fra proksimitetssystem, den konvensjonelle scenen for FI–SC-vekselvirkninger. Det legger til rette for vekselvirkninger mellom FI-en og SC-en uten den gjensidige forstyrrelsen av deres ordener tilknyttet proksimitetsvirkninger. Videre muliggjør stiintegralmetoden det å integrere ut kaviteten eksakt, som etterlater en eksakt effektiv FI–SC-teori. Etter følgelig å integrere ut SC-en, er vi lett i stand til å trekke ut virkninger på FI-en til en orden over middelfeltteori. Teorien tar dessuten høyde for de ulike, endelige størrelsene til FI-en, kaviteten og SC-en, samt separasjonen mellom FI-en og SC-en, som allsidiggjør teorien for realistiske konfigurasjoner. Stiintegralformalismen særpreger vår framgangsmåte over andre, konvensjonelle rammeverk for kavitetskoplede system, blant annet klassisk modellering, Jaynes–Cummings-lik modellering, og framgangsmåter som involverer Schrieffer–Wolff-transformasjonen. I motsetning til sistnevnte er vi ikke begrenset til ikke-resonante regimer.

Forskningen har resultert i én publisert artikkel der vi legger fram det semiklassiske konseptbeviset som motiverer videre mikroskopisk oppfølging. Den har også resultert i en artikkel klar til vurdering, der den mikroskopiske teorien legges fram, sammen med et uttrykk for anisotropifeltet og et numerisk anslag av dette. I tillegg presenterer vi her nye, analytiske uttrykk for korreksjonene i spekteret til FI-ens kvasipartikler, i lag med lovende numeriske anslag i målbar orden.

Preface

This dissertation is a result of a three-year doctoral program at the Center for Quantum Spintronics (QuSpin) at the Norwegian University of Science and Technology (NTNU), including coursing amounting to 30.5 ECTS. The research was supervised by Sol H. Jacobsen and Arne Brataas, and funded via the "Outstanding Academic Fellows" programme at NTNU, the Research Council of Norway Grant number 302315, as well as through its Centres of Excellence funding scheme, project number 262633, "QuSpin". The layout of the dissertation is based on the `ntnuthesis` template designed by CoPCSE@NTNU.

The title page painting is by my mother Anita Glaser Bjørnsen.

Acknowledgements

I would like to thank my supervisor Sol H. Jacobsen for being incredibly engaged and available throughout the entire period of our research. Daring to pursue uncharted territory, she was the one to propose the idea behind the project, of using a cavity to mediate interactions between a ferromagnet and a superconductor over unconventionally long distances. She has provided a great amount of support, both academically and extra-academically.

Moreover, I want to thank my incredibly talented colleague and long-time friend Haakon Krogstad, for all his academic and extra-academic support through the beginning of my doctoral program, until he defended in 2021. I want to thank my colleague Henning G. Hugdal, also incredulously competent, engaged and available, whose involvement has been pivotal to the later course of the research. Along with Sol, he has also given valuable feedback on this dissertation. I want to thank my supervisor Arne Brataas, with whom I have had regular meetings throughout the entire period of research, who has given much valuable feedback and guidance, and has a unique talent of extracting the physical picture from complicated theory. I want to thank Akashdeep Kamra, with whom I also had regular meetings during the first half of my research period, and who provided me with much valuable feedback. And, I want to thank Øyvind Johansen for his mentorship during the beginning of my doctoral program.

In no particular order, I also want to thank all the colleagues at QuSpin with whom I have had the pleasure to speak. I never met anyone not willing to offer time to help me understand material I was reading, or simply strike a chat.

Last but not least, I thank my mother Anita, father Jan, sister Jenny, brother Leif, partner Deepika, aunt Vibeke, grandmother Berit, grandaunt Liv, cousins and other family, as well as my good friends Mustafa, Steinar, Nikolai, Tomáž, Weizhi, Thomas, Sandra, Simone, Amin, Abdullah, Salah, Abdulrahman, Mohamad and many others, for all their support and care.

Contents

Chapter 1

Introduction

Chapter summary: We contextualize, present, and motivate the topic of research: the derivation of a microscopic theory of cavity-mediated interactions between a ferromagnetic insulator (FI) and a superconductor (SC), with a particular focus on the impact on the FI. In contrast to conventional proximity systems, this set-up facilitates relatively long-distance interactions between the FI and the SC without the proximity-induced mutual disruption of their orders. Our theoretical approach distinguishes itself from similar works by our application of the Matsubara path integral formalism, allowing for an exact integrating-out of the cavity, and perturbative treatment of the SC an order beyond mean field theory. We present relevant literature on similar proposals along with summaries of selected works. Finally, we provide an overview of the chapters and supplemental material of the dissertation.

Electronics is foundational to modern technology. Like the flow of water through canals, it relies on an oftentimes crude transport of electric charges to transmit and store information [1]. This carries with it energetic losses, of which scattering events collectively giving rise to *Joule heating* constitute a significant source. These manifest as the heating of electronic circuitry conducting electricity. Aside from ovens and other electrical appliances where this is in fact the purpose, it constitutes a wasteful aspect, especially in relation to electronic communication. In a world ever more connected by wires, the exploration of low-dissipation alternatives becomes ever more remuneratory.

Quantum physics is the sharp pair of goggles through which many fundamental phenomena of nature are examined and understood. While the field of electronics bears the weight and limitations of the macroscopic conduction of electric currents, quantum physics enables the stone-by-stone assembly of new fields. In particular, the field of spintronics, built on interactions involving particle spins; and the field of superconductivity, built on various microscopic phenomena, notably including the pairing of electrons by many-body interactions. From these

fields emerge energy-efficient means of transmitting and storing information, as compared to conventional electronics. These include the transmission of spin information between stationary particles (thus limiting transport-related losses) [2], and the transport of electron pairs energetically protected from scattering [3].

Spintronics and superconductivity are both extensively researched fields. Also their conjunction has amassed a rich literature: in particular, on the topic of magnets and superconductors interacting via the proximity effect and its inverse across an interface [4]. These are, respectively, the diffusion of superconducting correlations into the magnet, and the diffusion of magnetic order into the superconductor. These effects are limited to very small length scales, notably the length scale over which the electron pairs of the superconductor cohere, the *superconducting coherence length* [4–7]. This typically limits the proximity effect to nanometer scales [4–6], or in exceptional cases, upwards of a micrometer [7–9]. The magnet and the superconductor therefore need to be very closely situated for there to be a meaningful interfacial coupling;[1] hence these systems are known as *proximity systems*. These constitute the conventional frame for coupling spintronic and superconducting circuitry.

1.1 Cavity-mediated FI–SC interactions

The research behind this dissertation is a break from this convention, dedicated entirely to the development of a theoretical model for the cavity-mediated coupling of a ferromagnetic insulator (FI) and a superconductor (SC). The original idea behind this project was suggested by my supervisor Sol H. Jacobsen. The literature is rich in applications of cavities to mediate, manipulate and enhance interactions between magnetic and electric systems. Our project distinguishes itself from these by considering the mediated coupling of, specifically, an FI and an SC. It also distinguishes itself in technical aspects, including:

- The application of path integrals to exactly integrate out the cavity from the interactions, as well as perturbatively integrating out the SC without limiting ourselves to off-resonant regimes. The latter is a shortcoming of common approaches involving the Schrieffer–Wolff transformation. This perturbative treatment of the SC also readily enables us to go one order beyond mean field theory (Appendix A), which is necessary to resolve corrections to the FI quasiparticle spectrum (Ch. 7).
- Taking into account the non-conservation of (crystal) momenta, along with
- the interactions of a large range of modes, not only a handful. Both of these aspects follow from treating the FI, cavity and SC as finite-sized systems of differing dimensions. By contrast, a common theme in the literature is treating the cavity as two infinitely extending planes [2, 10, 11]. Furthermore, conservation of momentum may be assumed a priori [11], and the analysis may be limited to the effects of only one mediating mode [2, 10,

[1] An interface barrier or interstitial layer may be included.

12–14]. These aspects can serve to simplify the analysis, or follow from limiting its scope. For instance, in the context of spectroscopy, corrections to energy spectra may be limited to narrow resonance regimes involving only a few interacting modes, and only one or a few cavity modes are furthermore probed for, making it natural to limit analysis to a small subset of modes [14–17]. On the other hand, Refs. [13, 14] make use of dispersive coupling to a second cavity mode not meaningfully involved in a mediated interaction between an FI and a qubit, in order to probe for subsequent spectral renormalizations, demonstrating an interesting application of accounting for coupling to several cavity modes (see next section for more details). Furthermore, in Paper II, we demonstrate that a wide range of cavity modes can contribute to a single mediated effect, viz., the SC inducing an effective anisotropy field across the FI.

- The extraction of said effective anisotropy field across the FI, as the literature mostly focuses on renormalizations of energy spectra (specifically, anticrossings). We demonstrate that this enables the FI to resolve broken inversion symmetry in the SC. Nonetheless, we also extract and analyze corrections to the magnon spectra, and argue for their use as a means to resolve momentum anisotropy of the superconducting gap. The overall set-up can be useful in spintronic applications, as a device for remotely[2] resolving said properties of the SC in a spintronic circuit.

1.1.1 Semiclassical motivation

Before embarking on the involved microscopic theory to be presented in the main body of the dissertation, let us zoom out and explore semiclassically how an electromagnetic cavity can be harnessed to mediate an interaction between a ferromagnet (FM[3]) and a superconductor. In the following, we outline the proof of concept of a cavity-mediated remote FM–SC interaction that is covered in greater detail in Paper I, which is published as a Rapid Communication in Phys. Rev. B [12]. This proof of concept motivates the development of a microscopic theory, and demonstrates several important mechanisms in an accessible manner. This includes how the placement of the FM and the SC enable coupling purely to the magnetic and electric components of a cavity mode respectively, as well as how placement serves to select what mode mediates the interaction. It also broadly demonstrates the use of an FM to remotely probe features of an SC.

Consider the set-up illustrated in Fig. 1.1. A small ferromagnetic sphere (FM)

[2]Throughout this dissertation, we will use the qualifiers “remote” and “long-distance” to distinguish from proximity phenomena.

[3]In the microscopic theory, we limit ourselves to the more narrow category of ferromagnetic *insulators*. In this section and in Ref. [12] (Paper I), we only consider the magnetic aspect of the FM, neglecting the movement of electrons, electron–magnon scattering and so on. In effect, we are treating it on par with a ferromagnetic insulator.

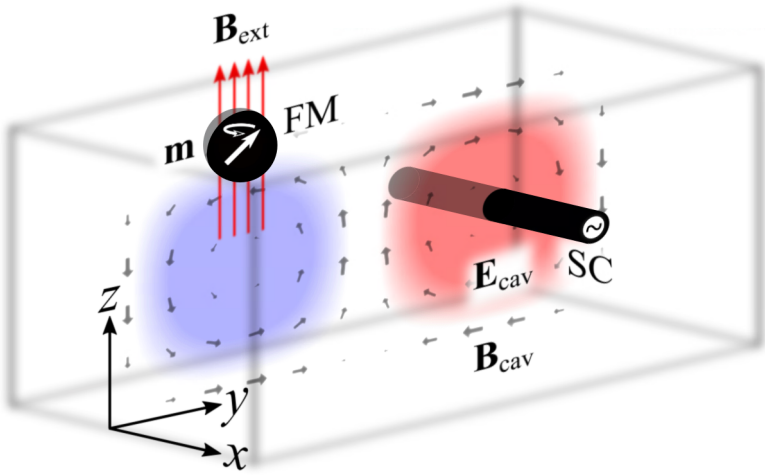

Figure 1.1: Set-up modified from Paper I. A small ferromagnetic sphere (FM) and a thin superconducting wire (SC) are placed inside a rectangular cavity. They are respectively placed at a magnetic and electric antinode of a selected cavity mode. The magnetic ($\mathbf{B}_{\text{cav}}$) and electric ($\mathbf{E}_{\text{cav}}$) field directions are respectively indicated by arrows and color (direction along x indicated by red ($+x$) and blue ($-x$)). The FM carries a magnetization $\mathbf{m}$, which precesses about the axis of a uniform, external aligning magnetostatic field $\mathbf{B}_{\text{ext}} \parallel \hat{e}_z$. The SC is connected to an external source of alternating current, and held at some temperature T.

and a thin superconducting wire (SC) is placed inside a rectangular[4] cavity. They are respectively placed at a magnetic ($\mathbf{B}_{\text{cav}}$) and electric ($\mathbf{E}_{\text{cav}}$) antinode of a selected cavity mode[5]. The FM carries a magnetization $\mathbf{m}$, which precesses about the axis of a strong, external magnetostatic field $\mathbf{B}_{\text{ext}} \parallel \hat{e}_z$. The precession frequency is determined by the magnitude of $\mathbf{B}_{\text{ext}}$. The SC is connected to an external source of alternating current (AC), and held at some temperature T around its critical temperature T_c (cf. Ch. 3). Note that in the microscopic theory, we will instead subject the SC to a direct current (giving rise to equilibrium phenomena compatible with the path integral approach), so the physical pictures are not directly comparable.

Owing to their small dimensions and suitable placement, the FM and SC are seen to couple well to the selected cavity mode (covered more rigorously through Chs. 2–5), and they do so purely to the magnetic and electric component of the mode, respectively. We subject the SC to an AC at a single frequency ω, which matches the resonance frequency of the cavity mode. Now, as the SC is cooled through T_c, the relative population of superconducting (N_s) to normal (N_n) electrons increases (cf. Sec. 3.1). The currents $\mathbf{J}_s$ and $\mathbf{J}_n$ of the populations relate locally to electric field in the SC by Ohm's law ($\mathbf{J}_n \propto \mathbf{E}_{\text{SC}}$) for normal electrons, and the London equation ($\partial_t \mathbf{J}_s \propto \mathbf{E}_{\text{SC}}$, Eq. (3.1)) for superconducting electrons.

[4] A rectangle is technically a two-dimensional shape; rectanguloid or rectangular cuboid would be more accurate terms, but these are semantics.

[5] More precisely the TE_{201} mode, as illustrated in Fig. 1.1.

These relations lead the local electric field to oscillate at a phase between 0 and $\pi/2$ radians relative to the AC drive, depending on the relative populations of electrons.

Because these fields oscillate at the frequency of the selected mode, and do so at its electric antinode, they excite it. The nearby $\mathbf{E}_{\text{cav}}$ oscillates at the same phase as the net electric field in the SC wire, relative to the AC drive, owing to the continuity of the tangential electric field across an interface ($\mathbf{E}_{\text{cav}} = \mathbf{E}_{\text{SC}}$, since the electric field is tangential to the wire). This consequently instantiates oscillation in $\mathbf{B}_{\text{cav}}$ near the FM and far away from the SC, perpendicularly to the aligning field $\mathbf{B}_{\text{ext}}$.

By suitable adjustment of $|\mathbf{B}_{\text{ext}}|$, the precession frequency of $\mathbf{m}$ is also matched to the resonance frequency of the cavity mode. Solving the dynamical equations for the $\mathbf{m}$, it is then shown in Paper I that its precession acquires the phase of $\mathbf{B}_{\text{cav}}$. Information about the superconducting transition has thus been imprinted on the precessing motion of the magnetization. This demonstrates in simple terms how a cavity mode can be harnessed to facilitate long-distance interactions between an FM and an SC, and how the FM can subsequently be used to probe properties of the SC.

1.1.2 Related works

There is a rich literature on cavity systems. Below, we present a limited overview of recent theoretical and experimental approaches close to our proposal. We start with a brief preliminary on anticrossings (or avoided crossings), which are often probed for in cavity-coupled systems, including the ones presented below. These are deflection-like features in the energy spectrum of a particle caused by interactions with other particles. Such features present unambiguous indications of hybridization (i.e., that the interacting particles behave as mixed states) if detectable. For anticrossings to be resolved experimentally, the coupling strength between the interacting particles must exceed losses. The amplitudes of cavity modes scale inversely with cavity volume (see Ch. 4); hence cavities are routinely utilized experimentally to access such strong coupling[6] regimes [18, 20–23].

The combined use of a cavity and the collective interactions in a magnetic lattice to enhance their mutual coupling above losses, has been explored theoretically [18, 25–31] and demonstrated experimentally [14–18, 24, 25, 30–36]. As an illustrative example, Y. Tabuchi *et al.* demonstrated an anticrossing experimentally in the spectrum of a cavity photon (quantum of light) interacting with a magnon (FI quasiparticle) [14, 17, 24, 25]. They probed this spectrum by way of transmission spectroscopy, and found that as they let the magnon energy ap-

[6]Here "strong coupling" is used in the sense that the coupling strength exceeds losses, not in the sense that some expansion parameter of an interaction Hamiltonian exceeds 1. In cavity-coupled systems, the latter sense is closely captured by the terms ultrastrong ($g/\omega \lesssim 1$) and deep strong ($g/\omega \geq 1$) coupling, with g some light–matter coupling strength, and ω the cavity frequency [18, 19]. These are regimes in which higher-order interactions with the cavity become either significant or dominant, respectively.

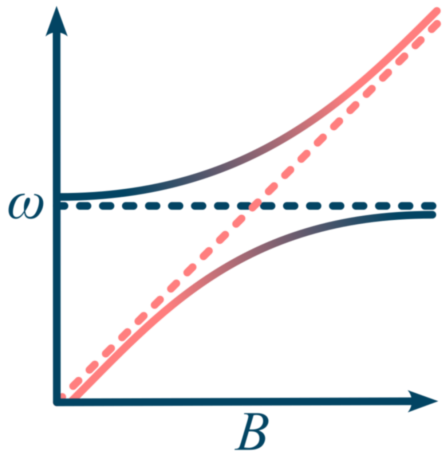

Figure 1.2: Illustration of a typical anticrossing. In the absence of interactions (dashed lines), the spectra (ω) of two particles (red and dark blue) simply cross as functions of some variable B. In the presence of interactions (solid lines), the eigenmodes of the system are two mixed states (indicated by the gradients). The particles mix considerably, or hybridize, near the crossing point of the bare spectra, leading to a significant renormalization of the spectra here. The degree of repulsion is determined by the strength of the interaction. This particular example is analogous to the anticrossing found spectroscopically by Y. Tabuchi *et al.* [14, 17, 24, 25] and others (see text) in the spectrum of a cavity mode (dark blue), near its crossing point with the spectrum of the uniform magnon mode (red) as a function of the strength B of an applied magnetostatic field.

proach the photon energy by the adjustment of an applied magnetic field, the energy by which they excited the photon increasingly also excited the magnon *via* the photon, leaving a visual discontinuity in the photon spectrum. By a careful choice of magnet, cavity, probe and placement of the magnet inside the cavity, the authors achieved a coupling strength an order of magnitude greater than losses, enabling the probe to unambiguously resolve the anticrossing.

Others have explored the use of photonic vacuum fluctuations in the cavity as mediators of interactions, through a variety of theoretical approaches. Ø. Johansen *et al.* theoretically demonstrated a mediated coupling between a ferro- and antiferromagnetic magnon mode by a perturbative diagonalization, using the Schrieffer–Wolff transformation [2, 10, 31]. This results in an anticrossing in the magnon spectra near their intersection, despite there being no direct coupling between the magnons. For a selection of material choices, the magnitude of the effective coupling was determined numerically, as the theoretical approach was limited to an off-resonant regime; by contrast, the path-integral approach presented in this dissertation allows for the effective coupling to be determined analytically, and is not limited to off-resonant regimes.

Analogously to Johansen *et al.*, F. Schlawin *et al.* employed a perturbative Schrieffer–Wolff approach to extract an effective electron pairing potential due to

mediated interactions of a normal[7] metal with itself [11, 18]. This was shown to give rise to unconventional (Amperean) superconductivity. Their pairing term can also be extracted from the path-integral approach presented in this dissertation, without limitations to an off-resonant regime. The pairing term appears explicitly in Paper II after integrating out the cavity, but we do not explore it in detail in this dissertation.

Similarly, cavity-mediated interactions have been utilized to induce exotic pairing in a fermionic gas trapped in an optical lattice [37]. Besides direct cavity mediation, others have furthermore considered superconductivity mediated by cavity polaritons, i.e. cavity photons hybridized with electromagnetic dipoles such as phonons (lattice vibrations) [38] or excitons (intraband electron–hole states in semiconductors) [39–42]. Interactions with cavity photons have also been considered as a means of enhancing superconductivity by manipulating the distribution of SC quasiparticles [43, 44].

Y. Tabuchi *et al.* [13, 14] and D. Lachance-Quirion *et al.* [24, 45] furthermore presented a Jaynes–Cummings-like model for the mediated coupling of a magnon and a qubit[8], and demonstrated this experimentally [25, 31]. Again, the mediated coupling induces an anticrossing in the qubit spectrum at its intersection with the magnon energy. In order to measure this, they construct a set-up in which the coupling is predominantly mediated by one specific cavity mode (TE_{102}), whose frequency is slightly detuned from the crossing point of the magnon and qubit energies. They then send microwaves into the cavity which are suppressed by the system, except in the narrow vicinity of the qubit resonance frequency. They then spectroscopically probe another mode (TE_{103}), which is detuned further away from the crossing. The great detuning means it does not significantly contribute to the mediated coupling, so probing it leaves the anticrossing unaffected; however, the spectrum of the TE_{103} mode is still renormalized by the qubit. Without the magnon mode, this renormalization is a constant shift, rendering the anticrossing in the qubit spectrum a discernible non-constant feature in the renormalized TE_{103} mode spectrum when exceeding losses. Note furthermore that interactions between only cavity photons and qubits have also been explored extensively in other works [19, 46–50].

Other cavity-coupled systems considered theoretically include that of two coupled ferromagnets, modelled classically [51] and with Jaynes–Cummings-like models [52]; and perturbative evolution of the density matrix, as well as perturbative diagonalization by the non-equilibrium Keldysh path integral formalism, for coupling a mesoscopic circuit to a cavity [53]. Cavities have furthermore been explored theoretically as means to introduce frustration (conflicting neighboring alignment) to ordered spin lattices, to engineer stable quantum spin liquids [54].

Addendum: During revisions of the dissertation August 2022, a recent pub-

[7] In the context of superconductivity, "normal" means not superconducting.

[8] They specify that the qubit is superconducting; however, they are using it as a controllable two-level system, not as a superconductor per se, beyond broad properties such as keeping losses low. They therefore do not couple an FI and an SC in the sense we are.

lication [55] has come to our attention in which the Matsubara path integral formalism is also made use of to construct effective interaction theories for cavity-coupled identical particles. Note that the work presented in this dissertation concerns cavity-mediated interactions between two *non-identical* classes of particles (FI and SC quasiparticles), so it does not fall under their broad category of systems. They highlight one of the same core advantages of this approach as we do in Chs. 6 and 7, namely that the formalism allows for an exact integrating-out of photonic degrees of freedom in actions (Hamiltonians) that are at most bilinear in photon variables (operators); the resulting effective theory is therefore not limited to perturbative cavity influence.

1.2 Papers, and structure of the thesis

Our research has resulted in two papers: In Paper I (published [12]), we present a semiclassical proof of concept showing the cavity-mediated impact of the ratio of resistive current to supercurrent in an SC, on the precession of the magnetization of a ferromagnet (FM).[9] This shows that the phase of the precession can be used to monitor the superconducting transition, and serves as a conceptual precursor to the quantum theory developed in the next papers. Next, in Paper II (ready for submission), we present a microscopic theory of cavity-mediated interactions between an FI and an SC. In particular, we extract the leading-order effect of the SC on the FI: the induction of an effective anisotropy field. This field is shown to resolve broken inversion symmetry in the SC. Additionally, our research has led to a number of results on corrections to the FI quasiparticle spectra due to the cavity-mediated interactions with the SC quasiparticles. We present analytical expressions for these along with a promising numerical analysis in Ch. 7. We argue for their application to resolving momentum anisotropy of the superconducting gap in an extended model in Ch. 8.

The microscopic modelling comprises by far been the most involved share of this research, and its elaboration will therefore also make up the brunt of this dissertation. On the other hand, the semiclassical proof of concept presented in Paper I is a useful and accessible preliminary to the microscopic theory: It outlines the application of cavities to mediate interactions between an FM and an SC, and more specifically how a driven[10] SC reorients the FI magnetization via a cavity mode; it furthermore illustrates how the placement of the FM and the SC inside the cavity, as well as their finite sizes, is utilized to limit contributing interactions.

[9] Ferromagnets is a broader category than ferromagnetic insulators. For instance, in the context of magnonics, metallic ferromagnets may give rise to significant damping due to magnon–electron scattering [14]. We do not consider this in detail in Paper I; in Paper II and throughout this thesis, we limit ourselves to ferromagnetic insulators, which does away with this complication.

[10] Note that in Paper I, we apply an alternating current (AC) is to the SC, while in the microscopic theory, we instead apply a direct current (DC) drive. Unlike an AC, a DC gives rise to an equilibrium supercurrent that can be analyzed within the framework of the Matsubara path integral formalism (Ch. 6). The results are therefore not comparable as such, although Paper I is still a useful conceptual preliminary for the reasons listed above.

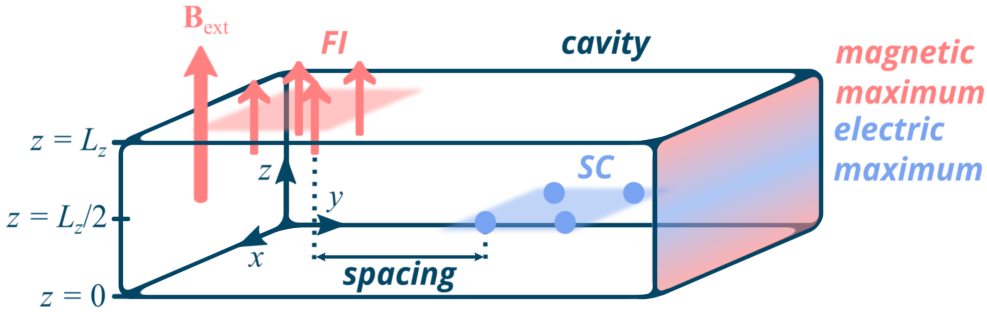

Figure 1.3: Set-up reproduced from Paper II. The origin is indicated by the coordinate axes. A thin ferromagnetic insulator and thin superconductor are placed spaced apart inside a rectangular, electromagnetic cavity. The FI is subjected to an aligning external magnetic field $\mathbf{B}_{\text{ext}}$ that vanishes across the SC; otherwise the superconductivity would be compromised.[11] The cavity is short along the z direction, and long along the perpendicular xy directions, causing cavity modes to separate into a band-like structure. The FI and the SC are respectively placed in regions of maximum magnetic ($z = L_z$) and electric ($z = L_z/2$) cavity field of the $\ell_z = 1$ modes, as defined in Sec. 4.2 and illustrated above by the colored field cross-section on the right wall.

For reference throughout Chs. 1–6, consider as a starting point the set-up illustrated in Fig. 1.3, which facilitates discussion on how the differing dimensions of the FI, cavity and SC influence the interactions. In Ch. 7, we will consider a modified set-up where the FI, cavity and SC share dimensions in the xy plane, enabling simplifications due to conservation of in-plane momentum.[12]

In the next three chapters, we give more in-depth introductions to the buildings blocks of our system: spin waves (magnons) (Ch. 2), superconductivity (Ch. 3), and electromagnetism in cavities (Ch. 4). In Ch. 2, we also provide a detailed recapitulation of the Fourier transform, as it plays an important role in our model. Through this review we elaborate on details relating to phases and momentum non-conservation in finite systems, that are often glossed over in the literature. Furthermore, in Ch. 5, we derive expressions for the Zeeman and paramagnetic coupling in the respective (quasi)particle bases. In Ch. 6, we introduce the Matsubara path integral formalism, and use it to derive an effective magnon theory that aggregates the influences of the cavity and the SC. We furthermore derive expressions that quantify the reorientation of FI spins due to the leading-order cavity-mediated influence of the SC, namely the induction of an effective anisotropy field. In Ch. 7, we direct our attention to its next-leading-order influence on the FI, namely to give rise to corrections in the magnon spectrum. Analytical expressions are derived, and we present numerical results along with an in-depth

[11] We question the importance of this assumption in Ch. 8 and in the concluding remarks in Paper II. This was anyhow assumed throughout the work behind this thesis, so we keep it here.

[12] Technically, the in-plane momentum is only conserved within the smallest of the two first Brillouin zones: one of the FI, the other of the SC. The analysis will anyhow be limited to this zone.

analysis of these. Finally, in Ch. 8, we discuss the results of this research, suggest applications and continuations, and provide a final summary. All chapters begin with a chapter summary, except Ch. 8, which itself constitutes a comprehensive summary of the dissertation. The technical chapters Ch. 2–7 conclude with a list of key takeaways.

Additionally, in Appendix A, we derive the result on the reorientation of FI spins by way of mean field theory; this serves to validate the results, and we also highlight advantages of the path integral approach. In Appendix B, we provide some analysis of the set-up in Fig. 1.3 based on the Schrieffer–Wolff transformation for contrast to the path integral approach. In Appendix C, we have attached a draft for a manuscript on corrections to the magnon spectrum. The results presented there were based on another approach than the one to be presented in Ch. 7, and led to overestimates of the magnitude of the corrections. This makes for an interesting discussion in light of our more resent results, which is presented along with the draft. Finally, in Appendix D, we provide a supplemental proof to the calculations in Sec. (6.1.4), as a step in showing that a shift in the magnon operators reflects reorientations of the individual spin quantization axes.

Chapter 2

Magnetism

Chapter summary: Spin waves result from the collective motion of individual spins in magnetically ordered systems. Here we outline their quantum-mechanical description, introducing in particular the Holstein–Primakoff transformation, which maps the spin basis onto a bosonic quasiparticle basis (magnons). As it is of particular relevance to our FI, cavity and SC, we also recapitulate the discrete Fourier transform in order to elaborate on momentum non-conservation, positional phase factors and Brillouin zones in lattices of finite dimensions and lattice spacing.

Emerging from the physical phenomenon of *spontaneous magnetism*, we begin this introduction to spin waves by turning the wheels back to its familiar origins, and give a brief review of the quantum-mechanical description of ferromagnetic order.

Colloquially and historically, the term "*ferromagnet*" has referred to materials exhibiting a spontaneous magnetic moment. This in distinction to *para-* and *diamagnets*, which exhibit parallel and antiparallel magnetic moments only in response to applied magnetic fields, but not in their absence. Many naturally occurring spontaneous magnets contain iron (Latin *ferrum*), including metallic iron and a range of iron oxides [56], whence "ferro-". The historical record on spontaneously magnetic materials date far back, with e.g. *magnetite* (Fe_3O_4 and $FeO{\cdot}Fe_2O_3$) mentioned in ancient Greek texts dating back as far as 800 BCE [57]. In fact, the term "magnet" originates from the name of this very ore, itself meaning the "stone of Μαγνησία[1]", a region of Greece rich in deposits [58].

Microscopically, the magnetic moment of such materials result from the constructive addition of many small, ordered magnetic moments carried by the constituent particles of the material, often arranged in a lattice. In this technical context, "ferromagnet" refers to materials exhibiting *ferromagnetic ordering*: the parallel ordering of equal, neighboring moments. Originally proposed by L. Néel

[1] For the physicist, the ability to read Greek is often a work-related accident.

during his research through the mid 1900s [59–61], other spontaneous orderings are possible: *ferrimagnetic* order (antiparallel ordering of unequal, neighboring moments), and *antiferromagnetic* order (antiparallel ordering of equal, neighboring spins). In particular, like ferromagnets, ferrimagnets also exhibit a net spontaneous magnetic moment, though the antiparallel moments add destructively. As it turned out, the historically archetypal "ferromagnet" magnetite was, technically, a ferrimagnet [56]. Of importance to our set-up, another ferrimagnet is *yttrium iron garnet* or *YIG* ($Y_3Fe_5O_{12}$), a ferrimagnetic insulator with exceptionally low losses in ferromagnetic resonance experiments [62–65]. This is due to the spherical charge distribution of its ions, leading to only weak coupling to lattice vibrations (phonons) [56]. The qualifier "insulator" means the material is a poor conductor of electricity; in the context of our model, it means we can treat the constituent particles of the lattice as stationary in response to electromagnetic fields. While technically a ferrimagnet, we will approximate YIG as a conceptually simpler ferromagnet in our work.

2.1 Ferromagnetic order

In the following, we give a review of the quantum-mechanical description of ferromagnetism, the variety of magnetic ordering to be considered in our model. We begin with its building block: Originally inferred from experimental evidence [66], *spin* $\mathbf{S}$ is an intrinsic property of elementary particles in quantum mechanics, along with mass m and charge q. Importantly, when zon-zero, spin gives rise to a magnetic moment μ, rendering the particle a minute magnet:

$$\mu = g\frac{q}{2m}\mathbf{S} = \frac{g\mu_B}{\hbar}\mathbf{S}, \tag{2.1}$$

with g the g-factor, a constant of proportionality; and $\mu_B \equiv \hbar q/2m$ the Bohr magneton.

As alluded to by its name, spin shares its mathematical description with angular momentum operators [66], though it is an inherent property of particles, not a result from rotational mechanics. In particular, spin is *quantized*, and its Cartesian components,

$$\mathbf{S} \equiv S_x\hat{e}_x + S_y\hat{e}_y + S_z\hat{e}_z, \tag{2.2}$$

are subject to the angular momentum algebra. Above, $\hat{e}_i$ are the Cartesian unit vectors. Letting z be the axis along which the spin is quantized, and $|S,s\rangle$ be the spin eigenstates, the mathematical description reads

$$\mathbf{S}^2|S,s\rangle = \hbar^2 S(S+1)|S,s\rangle, \quad S_z|S,s\rangle = \hbar s|S,s\rangle, \tag{2.3}$$

$$S = 0, \frac{1}{2}, 1, \frac{3}{2}, \ldots, \quad s = -S, -S+1, \ldots, S-1, S, \tag{2.4}$$

$$[S_i, S_j] = i\hbar\epsilon_{ijk}S_k. \tag{2.5}$$

Above, ϵ_{ijk} is the Levi–Civita symbol, the indices $i, j, k = x, y, z$, and S and s are the quantum numbers respectively associated with the absolute value and the z component of the spin. S is also referred to as simply "spin", distinguished from $\mathbf{S}$ by context. Whether S is integer of half-integer has profound consequences for identical particles, with the respective categories labeled *bosons* and *fermions*. Whereas identical bosons can share all quantum numbers, fermions cannot.

Elementary particles can be grouped together to form composite systems with a net spin [66]. In a lattice, the unit cell constitutes such a composite [56]. When a lattice is subjected to an applied field, the magnetic moment of the unit cells tend to align with or against the field direction. However, *ferromagnets* exhibit a spontaneous parallel alignment of spins even in the absence of applied fields [56]. This ferromagnetic order results from the *exchange interaction*, a spin–spin interaction favoring parallel alignment. This is captured by the Heisenberg Hamiltonian for a simple ferromagnetic insulator (FI),

$$\mathcal{H}_{\text{ex}} \equiv -J \sum_{\langle i,j \rangle} \mathbf{S}_i \cdot \mathbf{S}_j. \tag{2.6}$$

Above, $J > 0$ is the exchange interaction strength, and $\mathbf{S}_i$ is the spin vector at lattice site i. In this simple model, only nearest-neighbor interactions are taken into account, as indicated by the angle brackets around i, j. Since $J > 0$, the energy is minimal for parallel[2] neighboring spins $\mathbf{S}_i \parallel \mathbf{S}_j$.

Each lattice site in this simple system has the same spin S (i.e. magnitude $\hbar\sqrt{S(S+1)}$, cf. Eq. (2.3)), but the orientation of each $\mathbf{S}_i$ may differ. We therefore include a site index i also on s,

$$s \to s_i. \tag{2.7}$$

Hence the eigenstates read $|S, s_i\rangle$ for each spin.

2.2 Spin waves

Observe now that the exchange interaction (2.6) renders the motion of one spin dependent on that of its neighbor. Like beads on a string, this enables an ensemble of spins to transmit signals in waves of collective motion. Along with physical and mediated spin transport, spin waves is one of several magnetic phenomena harnessed in *spintronic technology*, as distinguished from *electronics*, technology that instead relies on charges and charge transport phenomena. Spintronic technology constitutes a part of the background for the theoretical work presented in this thesis, presenting low-energy alternatives to memory and processing applications of conventional electronics [67].

[2] On the other hand, $J < 0$ would favor antiferromagnetic order (antiparallel neighboring spins).

2.2.1 The Holstein–Primakoff transformation

While the quantum number s is either integer or half-integer, its values (2.4) always differ by integer increments for a given spin S. One may therefore conjecture that there exists a representation of spins comprised of bosonic excitations, with $s = \pm S$ a baseline from which they are excited. This is indeed affirmed by the *Holstein–Primakoff transformation* [2, 68, 69], which maps spin operators onto a space of bosonic operators known as *magnons*. This transformation was first used in 1940 by T. Holstein and H. Primakoff to analyse the variation of the magnetization of a ferromagnet, with an external magnetic field. Enabling analysis of the magnetic system in terms of oscillators, we seek to rewrite the Hamiltonian in terms of these.

Consider again the FI described by Eq. (2.6). Instead of leaving the alignment of spins to spontaneous ordering, we direct it by applying a uniform, magnetostatic field $\mathbf{B}_{\text{ext}} = B_{\text{ext}}\hat{e}_z$ along the positive z direction ($B_{\text{ext}} > 0$). This field interacts with the spins via the Zeeman interaction

$$\mathcal{H}_{\text{ext}} \equiv -\frac{g\mu_0}{\hbar} B_{\text{ext}} \sum_i S_{iz}. \tag{2.8}$$

Hence the Hamiltonian for the FI reads

$$\mathcal{H}_{\text{FI}} \equiv \mathcal{H}_{\text{ex}} + \mathcal{H}_{\text{ext}} = -J \sum_{\langle i,j \rangle} \mathbf{S}_i \cdot \mathbf{S}_j - \frac{g\mu_0}{\hbar} B_{\text{ext}} \sum_i S_{iz}. \tag{2.9}$$

With the spins aligned along z, our point of departure is the helical[3] spin operators $S_{i\pm}$, defined as

$$S_{i\pm} \equiv S_{ix} \pm i S_{iy}, \quad S_{i+} = S_{i-}^{\dagger}. \tag{2.10}$$

By defining a helical basis of unit vectors

$$\hat{e}_{\pm} \equiv \frac{1}{\sqrt{2}} (\hat{e}_x \mp i\hat{e}_y), \tag{2.11}$$

one finds that

$$\mathbf{S}_i = \frac{1}{\sqrt{2}} (S_{i+}\hat{e}_+ + S_{i-}\hat{e}_-) + S_{iy}\hat{e}_y. \tag{2.12}$$

Working out their algebra based on the spin algebra (2.5), and assessing the actions of $\mathbf{S}_i^2 S_{i\pm}$ and $S_{iz}S_{i\pm}$ on $|S,s\rangle$, one finds they act to raise and lower the spin states over a limited range [66, 69]:

$$S_{i+}|S,s_i\rangle = \hbar\sqrt{2S}\sqrt{1 - \frac{S-(s_i+1)}{2S}}\sqrt{S-s_i}\,|S,s_i+1\rangle, \tag{2.13}$$

$$S_{i-}|S,s_i\rangle = \hbar\sqrt{2S}\sqrt{S-(s_i-1)}\sqrt{1 - \frac{S-s_i}{2S}}\,|S,s_i-1\rangle. \tag{2.14}$$

[3] They are also known as "ladder" or "creation and annihilation" operators.

Note that $S_{i\pm}|S,\pm S\rangle = 0$.

This raising and lowering of states is similar, but not identical to the action of bosonic ladder operators, as their range of eigenstates is bounded only in one direction. For instance, there may be anywhere between zero and an infinite number of photons in the same quantum state. The *Holstein–Primakoff transformation* [2, 68, 69] captures both the similar actions and the dissimilar ranges.

The prefactors of Eqs. (2.13) and (2.14) invites us to introduce new ladder operators $\{\eta_i, \eta_i^\dagger\}$, that relate to $S_{i\pm}$ by

$$S_{i+} \equiv \hbar\sqrt{2S}\sqrt{1-\frac{\eta_i^\dagger\eta_i}{2S}}\,\eta_i, \tag{2.15}$$

$$S_{i-} \equiv \eta_i^\dagger\hbar\sqrt{2S}\sqrt{1-\frac{\eta_i^\dagger\eta_i}{2S}}. \tag{2.16}$$

They act on $|S,s_i\rangle$ as follows:

$$\eta_i|S,s_i\rangle = \sqrt{S-s_i}\,|S,s_i+1\rangle, \tag{2.17}$$

$$\eta_i^\dagger|S,s_i\rangle = \sqrt{S-(s_i-1)}\,|S,s_i-1\rangle. \tag{2.18}$$

In effect, $\eta_i^\dagger$ creates a new particle for each decrement in s_i relative to $s_i = +S$, and vice versa for η_i. Note the unphysical range: although $\eta_i|S,S\rangle = 0$, we find $\eta_i^\dagger|S,-S\rangle = \sqrt{2S+1}\,|S,-S-1\rangle$, implying the magnitude of S_{iz} can exceed that of $\mathbf{S}$. The range is truncated by the factor $\sqrt{1-\eta_i^\dagger\eta_i/2S}$ in Eqs. (2.15) and (2.16) in an exact analysis of spin systems.

By furthermore assuming bosonic statistics,

$$[\eta_i, \eta_j^\dagger] = \delta_{ij}, \tag{2.19}$$

and using

$$S_i^2 = \hbar^2 S(S+1) = S_{iz}^2 + \frac{1}{2}(S_{i+}S_{i-} + S_{i-}S_{i+}), \tag{2.20}$$

we find

$$\begin{aligned} S_{iz}^2 &= \hbar^2 S(S+1) - \frac{1}{2}(S_{i+}S_{i-} + S_{i-}S_{i+}) \\ &= \hbar^2 S(S+1) - \hbar^2\left(-(\eta_i^\dagger\eta_i)^2 + 2S\eta_i^\dagger\eta_i + S\right) \\ &= \hbar^2(S-\eta_i^\dagger\eta_i)^2. \end{aligned} \tag{2.21}$$

This equation has two solutions for S_{iz}. The one consistent with the actions (2.17)–(2.18) of $\eta_i, \eta_i^\dagger$ is

$$S_{iz} = \hbar(S-\eta_i^\dagger\eta_i). \tag{2.22}$$

This solution affirms the interpretation of $\eta_i, \eta_i^\dagger$ as ladder operators for bosonic quasiparticles, with a new particle created for every decrement in s_i.[4]

[4]The other solution $S_{iz} = -\hbar(S-\eta_i^\dagger\eta_i)$ would be consistent with quasiparticles created with each increment in s_i starting from $s_i = -S$, a natural choice if the aligning field $\mathbf{B}_{\text{ext}}$ instead had pointed in the negative z direction.

2.2.2 Magnons

The factors $\sqrt{1-\eta_i^\dagger\eta_i/2S}$ contained in the transformation (2.15)–(2.16) yields a Hamiltonian that is challenging to proceed with analytically. We therefore look for simplifications.

Under the influence of a sufficiently strong magnetostatic field $\mathbf{B}_{\text{ext}}$, all the spins of the lattice align strongly in the positive z direction. Nearly all $s_i = S$, and thus the number of quasiparticles averaged across the lattice is very small,

$$\langle \eta_i^\dagger \eta_i \rangle \ll 2S, \tag{2.23}$$

with $\langle\cdot\rangle$ the expectation value. This invites a series expansion of $\sqrt{1-\eta_i^\dagger\eta_i/2S}$ in orders of $\eta_i^\dagger\eta_i/2S$ [2, 68, 69]. For the rest of the calculations, we will hence only work to second order in magnon operators, as higher order terms (representing particle–particle scatterings) are challenging to deal with analytically. Accordingly, to lowest order,

$$\sqrt{1-\frac{\eta_i^\dagger\eta_i}{2S}} \approx 1. \tag{2.24}$$

Thus, by Eqs. (2.15)–(2.16),

$$S_{i+} \approx \hbar\sqrt{2S}\eta_i, \tag{2.25}$$

$$S_{i-} \approx \hbar\sqrt{2S}\eta_i^\dagger. \tag{2.26}$$

Since we intend to rewrite the Hamiltonian (2.9) in terms of the new quasiparticle basis, we recast the above expressions in a Cartesian basis. By Eq. (2.10),

$$S_{id} \approx \frac{\hbar\sqrt{2S}}{2}(\nu_d\eta_i + \nu_d^*\eta_i^\dagger), \tag{2.27}$$

where $d = x, y$ and $\{\nu_x, \nu_y\} = \{1, -i\}$.

Fourier transform

We now transition from the lattice site basis $\eta_i, \eta_i^\dagger$ to a wave vector (momentum) basis $\eta_{\mathbf{k}}, \eta_{\mathbf{k}}^\dagger$ by a Fourier transformation. This is conventional and becomes advantageous later, as we will look into the interaction between the FI and electromagnetic fields, which are also expressed in a momentum basis. $\eta_{\mathbf{k}}, \eta_{\mathbf{k}}^\dagger$ are termed *magnons* [68].

At this point, most texts would simply state the Fourier transform. However, the models covered in Paper I and II involve multiple subsystems (FI, SC and cavity, cf. Fig. 1.3) of differing dimensions and placements, giving rise to effects that are often glossed over, yet are consequential for our model. This includes momentum non-conservation, Brillouin zones, and phase factors. Covering the Fourier transform in detail is therefore instructional, here in the context of a square FI lattice.

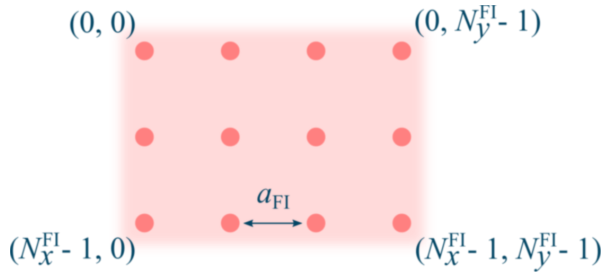

Figure 2.1: A top-down view of the square FI lattice with a rectangular boundary, from Fig. 1.3. N_d^{FI} is the number of points in direction $d = x, y$, and a_{FI} is the lattice constant. The points are labeled (n_x, n_y) with $n_d = 0, \ldots, N_d^{\mathrm{FI}} - 1$. Some selected points are labeled in the figure.

Fig. 2.1 shows a sketch of the square FI lattice. The number of lattice points are N_x^{FI} and N_y^{FI} in the respective directions, and the lattice constant is a_{FI}. The lattice points are labeled by (n_x, n_y) as shown in Fig. 2.1, with $n_d = 0, \ldots, N_d^{\mathrm{FI}} - 1$; this label is equivalent to the lattice index i used so far. Each lattice point is associated with an operator $\eta_i = \eta_{n_x n_y}$

The discrete Fourier transform (dFT[5]) projects the lattice of operators $\eta_{n_x n_y}$ onto a discrete orthonormal basis of Fourier harmonics [70]. This transformation is in general non-trivial for 2D lattices, as the decomposition into harmonics depends on the geometry and boundaries of the lattice.[6] We are only interested in the qualitative impact of the discrete nature of a lattice on our system, so by considering a square lattice with a rectangular boundary, we avoid a number of complications. In this case, the directions of periodicity are orthogonal and Cartesian.

The dFT can be expressed in terms of real sine or cosine harmonics, or in terms of complex exponentials [70]. We will return to the real dFT in Sec. 4.2 in the context of quantizing the electromagnetic field inside a cavity, with reflecting boundary conditions in the z direction. However, here we will proceed with the complex dFT, since it is mathematically advantageous that products of exponentials readily combine into a single exponential ($e^{ia} e^{ib} = e^{i(a+b)}$).

By definition, the Fourier components of $\eta_{n_x n_y}$ are

$$\begin{aligned}\eta_{m_x m_y} &\equiv \sum_{n_x=0}^{N_x^{\mathrm{FI}}-1} \sum_{n_y=0}^{N_y^{\mathrm{FI}}-1} \left(\frac{1}{\sqrt{N_x^{\mathrm{FI}}}} e^{-i \frac{2\pi m_x n_x}{N_x^{\mathrm{FI}}}} \right) \left(\frac{1}{\sqrt{N_y^{\mathrm{FI}}}} e^{-i \frac{2\pi m_y n_y}{N_y^{\mathrm{FI}}}} \right) \eta_{n_x n_y} \\ &= \frac{1}{\sqrt{N_{\mathrm{FI}}}} \sum_{n_x=0}^{N_x^{\mathrm{FI}}-1} \sum_{n_y=0}^{N_y^{\mathrm{FI}}-1} e^{-2\pi i \left(\frac{m_x n_x}{N_x^{\mathrm{FI}}} + \frac{m_y n_y}{N_y^{\mathrm{FI}}} \right)} \eta_{n_x n_y}, \end{aligned} \tag{2.28}$$

[5] Not to be confused with density functional theory (also abbreviated DFT), which is anyhow never mentioned in this dissertation.

[6] There are parallels between this discussion and the topic of reciprocal lattices in solid state physics; however, reciprocal lattices are Fourier transforms of real-space lattices of identical points, whereas we are concerned with lattices of magnon operators which can assume non-identical (expectation) values.

with $m_d = 0, \ldots, N_d^{\mathrm{FI}} - 1$. Above, we introduced the number of lattice points $N_{\mathrm{FI}} \equiv N_x^{\mathrm{FI}} N_y^{\mathrm{FI}}$. The normalization constant $1/\sqrt{N_d^{\mathrm{FI}}}$ follows convention in physics, as it renders the dFT unitary: defining the single-direction transformation matrix

$$U_{m_d n_d} \equiv \frac{1}{\sqrt{N_d^{\mathrm{FI}}}} e^{-i\frac{2\pi m_d n_d}{N_d^{\mathrm{FI}}}}, \tag{2.29}$$

we have

$$\begin{aligned}
(U^\dagger U)_{n_d' n_d} &= \sum_{m_d=0}^{N_d^{\mathrm{FI}}-1} U^*_{m_d n_d'} U_{m_d n_d} = \sum_{m_d=0}^{N_d^{\mathrm{FI}}-1} \frac{1}{\sqrt{N_d^{\mathrm{FI}}}} e^{i\frac{2\pi m_d n_d'}{N_d^{\mathrm{FI}}}} \frac{1}{\sqrt{N_d^{\mathrm{FI}}}} e^{-i\frac{2\pi m_d n_d}{N_d^{\mathrm{FI}}}} \\
&= \frac{1}{N_d^{\mathrm{FI}}} \sum_{m_d=0}^{N_d^{\mathrm{FI}}-1} e^{-i\frac{2\pi m_d (n_d - n_d')}{N_d^{\mathrm{FI}}}} = \frac{1}{N_d^{\mathrm{FI}}} \sum_{m_d=0}^{N_d^{\mathrm{FI}}-1} \left(e^{-i\frac{2\pi (n_d - n_d')}{N_d^{\mathrm{FI}}}} \right)^{m_d} \\
&= \frac{1}{N_d^{\mathrm{FI}}} \frac{1 - e^{-2\pi i (n_d - n_d')}}{1 - e^{-2\pi i \frac{n_d - n_d'}{N_d^{\mathrm{FI}}}}} = \mathbb{1}_{n_d' n_d}.
\end{aligned} \tag{2.30}$$

Above, we recognize the sum as a geometric series, and write it in closed form. In the last equality, we use $n_d - n_d' \in \{-N_d^{\mathrm{FI}} + 1, -N_d^{\mathrm{FI}} + 2, \ldots, N_d^{\mathrm{FI}} - 2, N_d^{\mathrm{FI}} - 1\}$ to find that the closed form evaluates to zero for all $n_d - n_d'$ except $n_d - n_d' = 0$. In this case, the sum is a sum over ones, and evaluates to N_d^{FI}, which is divided by the squared normalization constant $1/N_d^{\mathrm{FI}}$ to yield the unit matrix $\mathbb{1}$.[7]

Unitarity implies the inverse transformation $U^{-1} = U^\dagger$. The inverse dFT is therefore

$$\eta_{n_x n_y} = \frac{1}{\sqrt{N_{\mathrm{FI}}}} \sum_{m_x=0}^{N_x^{\mathrm{FI}}-1} \sum_{m_y=0}^{N_y^{\mathrm{FI}}-1} e^{2\pi i \left(\frac{m_x n_x}{N_x^{\mathrm{FI}}} + \frac{m_y n_y}{N_y^{\mathrm{FI}}} \right)} \eta_{m_x m_y}. \tag{2.31}$$

Note that the choice of normalization constant ensures unitarity; other common conventions include normalizing the dFT by a factor $1/N_d^{\mathrm{FI}}$ or 1, which would result in $U^\dagger U \neq \mathbb{1}$.

Ranges and the first Brillouin zone

The Fourier transforms are currently expressed in terms of the rather abstract integer parameters m_d and n_d, so we recast them in terms of familiar momentum and positions variables. Before doing so, we note that the summation ranges of the inverse transform (2.31) do not correspond to the conventional ranges in theoretical physics. In momentum terms (cf. Sec. 2.2.2), these ranges correspond to $[0, 2\pi/a_{\mathrm{FI}})$, but conventionally the interval is taken to be $(-\pi/a_{\mathrm{FI}}, \pi/a_{\mathrm{FI}}]$, i.e. the *first Brillouin zone* (1BZ).

[7] The closed form is then technically undefined, but can alternatively be evaluated using L'Hôpital's rule with $n_d - n_d' \to 0^+$.

To this end, observe that the harmonics of the dFT are all 2π periodic. We therefore have, e.g.,

$$\exp\left(-2\pi i\frac{N_d^{\mathrm{FI}}}{N_d^{\mathrm{FI}}}n_d\right)=\exp\left(-2\pi i\left(1+\frac{0}{N_d^{\mathrm{FI}}}\right)n_d\right)=\exp\left(-2\pi i\frac{0}{N_d^{\mathrm{FI}}}n_d\right). \quad (2.32)$$

That is, the Fourier mode corresponding to $m_d = N_d^{\mathrm{FI}}$ gives rise to the same spatial oscillation on the lattice, as a mode corresponding to $m_d = 0$, cf. Fig. 2.2. This expresses the equivalence of Fourier modes across intervals of the Fourier parameters; these intervals are the Brillouin zones [56]. We can use this periodicity to shift the limits of the sums in Eq. (2.31): the ranges for m_d can be any set of N_d consecutive integers, or in momentum terms, any interval of length $2\pi/a_{\mathrm{FI}}$.

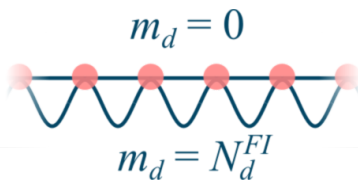

Figure 2.2: The physical equivalence of the $m_d = N_d^{\mathrm{FI}}$ and $m_d = 0$ modes. The rapidly oscillating wave touches the lattice points at the same height, making it physically equivalent to the uniform mode.

The conventional momentum interval $(-\pi/a_{\mathrm{FI}}, \pi/a_{\mathrm{FI}}]$ is achieved by shifting the ranges for m_d to

$$m_d = \begin{cases} -\frac{N_d-1}{2},\ldots,\frac{N_d-1}{2}, & N_d \text{ odd},\\ -\frac{N_d}{2}+1,\ldots,\frac{N_d}{2}-1, & N_d \text{ even}. \end{cases} \quad (2.33)$$

The periodicity also holds for the dFT. While not necessary in order to meet some convention, it will prove convenient later to shift the summation intervals also for n_d, to the same intervals:

$$n_d = \begin{cases} -\frac{N_d-1}{2},\ldots,\frac{N_d-1}{2}, & N_d \text{ odd},\\ -\frac{N_d}{2}+1,\ldots,\frac{N_d}{2}-1, & N_d \text{ even}. \end{cases} \quad (2.34)$$

In Ch. 5.1, this enables us to readily separate the quantity $N_{\mathrm{FI}}D^{\mathrm{FI}}_{\mathbf{kq}}$ (Eq. (5.11)) into a magnitude and a phase. Phases are important for the discussion in Ch. 8, as they will prove to be limiting factors for a strong result as a function of the separation of the FI and the SC inside the cavity.

Recasting in terms of physical quantities

We now recast the Fourier transform in terms of position $\mathbf{r}_i$ and momentum $\mathbf{k}$ by identifying

$$\mathbf{r}_i \equiv \mathbf{r}_{n_x n_y} \equiv (x_0 + a_{\mathrm{FI}}n_x, y_0 + a_{\mathrm{FI}}n_y, L_z) \equiv (x, y, L_z), \quad (2.35)$$

$$\mathbf{k} \equiv (2\pi m_x/l_x, 2\pi m_y/l_y, 0) \equiv (k_x, k_y, 0), \quad (2.36)$$

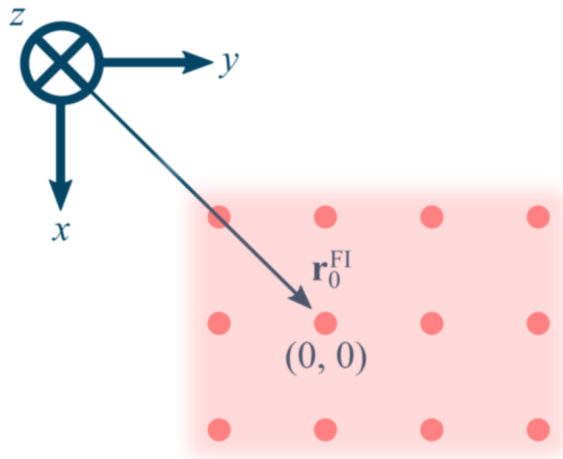

Figure 2.3: The same square FI lattice as was illustrated in Fig. 2.1. Here we have included the position vector $\mathbf{r}_0^{\mathrm{FI}}$ of the $(0,0)$ point defined by the new ranges (2.34), relative to the origin.

where $(x_0, y_0, L_z) \equiv \mathbf{r}_0^{\mathrm{FI}}$ is the distance between the $(n_x, n_y) = (0,0)$ center point and the origin of the coordinate system (see Figs. 1.3 and 2.3), and we introduced the dimensions of the FI

$$l_d^{\mathrm{FI}} \equiv a_{\mathrm{FI}}(N_d^{\mathrm{FI}} - 1) \approx a_{\mathrm{FI}} N_d^{\mathrm{FI}}. \tag{2.37}$$

The approximation holds for $N_d^{\mathrm{FI}} \gg 1$. We thus have

$$\begin{aligned}
\eta_{\mathbf{k}} &\equiv \frac{1}{\sqrt{N_{\mathrm{FI}}}} \sum_{x=x_0-l_x/2}^{x_0+l_x/2} \sum_{y=y_0-l_y/2}^{y_0+l_y/2} e^{-i\left(k_x(a_{\mathrm{FI}} n_x + x_0 - x_0) + k_y(a_{\mathrm{FI}} n_y + y_0 - y_0)\right)} \eta_{\mathbf{r}_i} \\
&= \frac{e^{i\left(k_x x_0 + k_y y_0\right)}}{\sqrt{N_{\mathrm{FI}}}} \sum_{x=x_0-l_x/2}^{x_0+l_x/2} \sum_{y=y_0-l_y/2}^{y_0+l_y/2} e^{-i\left(k_x x + k_y y\right)} \eta_{\mathbf{r}_i} \\
&\equiv \frac{e^{i\mathbf{k}\cdot\mathbf{r}_0^{\mathrm{FI}}}}{\sqrt{N_{\mathrm{FI}}}} \sum_i \eta_{\mathbf{r}_i} e^{-i\mathbf{k}\cdot\mathbf{r}_i},
\end{aligned} \tag{2.38}$$

where we introduced the sum $\sum_i$ as short-hand for $\sum_{x=x_0-l_x/2}^{x_0+l_x/2} \sum_{y=y_0-l_y/2}^{y_0+l_y/2}$. It is these operators, $\eta_{\mathbf{k}}$, that are termed *magnons* [68]. Similarly, the inverse relation becomes

$$\eta_{\mathbf{r}_i} = \frac{1}{\sqrt{N_{\mathrm{FI}}}} \sum_{\mathbf{k}} \eta_{\mathbf{k}} e^{i\mathbf{k}\cdot(\mathbf{r}_i - \mathbf{r}_0^{\mathrm{FI}})}, \tag{2.39}$$

with the sum $\sum_{\mathbf{k}}$ taken over the 1BZ of the FI. The factor $e^{\pm i\mathbf{k}\cdot\mathbf{r}_0^{\mathrm{FI}}}$ expresses the dependency of the Fourier modes on the position of the FI inside the cavity. Note

that we can technically simplify the expression for $\eta_{\mathbf{k}}$ by absorbing $e^{i\mathbf{k}\cdot\mathbf{r}_0^{\mathrm{FI}}}$ into its definition, which is equivalent to moving the origin of the coordinate system to the center $(n_x, n_y) = (0,0)$ of the FI; however, we will also perform Fourier transforms on other subsystems (cavity and SC) later, and moving the origin will simply spawn similar positional dependencies elsewhere. This dependency is more complicated for the real dFT, which will be applied to the cavity electromagnetic field; we eliminate the latter dependency by leaving the origin in the corner of the cavity, as illustrated in Fig. 1.3.

2.2.3 Magnon Hamiltonian

We conclude this introductory section on ferromagnetism by recasting the Hamiltonian (2.9) in the magnon basis. A similar derivation is found in Ref. [68, Ch. 4].

First, we insert Eqs. (2.22), (2.27) and (2.39) into $\mathcal{H}_{\mathrm{ex}}$ (Eq. (2.6)). We introduce the nearest-neighbor lattice vectors $\boldsymbol{\delta} = \pm a_{\mathrm{FI}}\hat{e}_x, \pm a_{\mathrm{FI}}\hat{e}_y$, substitute the sum $\sum_{\langle i,j\rangle}$ for $\sum_i \sum_{\boldsymbol{\delta}}$, and recast indices accordingly. This substitution is only approximate, since edges and corners of the lattice do not have neighboring points in certain directions; this only affects length scales on the order of the lattice constant, i.e. momenta at the border of the 1BZ, which are irrelevant to our model. Then

$$
\begin{aligned}
&-J\sum_{\langle i,j\rangle}\mathbf{S}_i\cdot\mathbf{S}_j \approx -J\sum_i\sum_{\boldsymbol{\delta}}\mathbf{S}_{\mathbf{r}_i}\cdot\mathbf{S}_{\mathbf{r}_i+\boldsymbol{\delta}} = -J\sum_i\sum_{\boldsymbol{\delta}}(S_{\mathbf{r}_i z}S_{\mathbf{r}_i+\boldsymbol{\delta},z} + \sum_d S_{\mathbf{r}_i d}S_{\mathbf{r}_i+\boldsymbol{\delta},d}) \\
&\approx -\frac{J}{N_{\mathrm{FM}}}\sum_{\mathbf{k}\mathbf{k}'}\sum_{\boldsymbol{\delta}}\sum_i\Bigg[-\hbar^2\frac{S^2}{S}\eta_{\mathbf{k}}^\dagger\eta_{\mathbf{k}'}\left(1+e^{-i(\mathbf{k}-\mathbf{k}')\cdot\boldsymbol{\delta}}\right)e^{-i(\mathbf{k}-\mathbf{k}')\cdot(\mathbf{r}_i-\mathbf{r}_0^{\mathrm{FI}})} \\
&\quad+\sum_d\left(\frac{\hbar\sqrt{2S}}{2}\right)^2\Bigg(\nu_d^2\eta_{\mathbf{k}}\eta_{\mathbf{k}'}e^{i(\mathbf{k}+\mathbf{k}')\cdot(\mathbf{r}_i-\mathbf{r}_0^{\mathrm{FI}})}e^{i\mathbf{k}'\cdot\boldsymbol{\delta}} + (\nu_d^*)^2\eta_{\mathbf{k}}^\dagger\eta_{\mathbf{k}'}^\dagger e^{-i(\mathbf{k}+\mathbf{k}')\cdot(\mathbf{r}_i-\mathbf{r}_0^{\mathrm{FI}})}e^{-i\mathbf{k}'\cdot\boldsymbol{\delta}} \\
&\quad+\eta_{\mathbf{k}}\eta_{\mathbf{k}'}^\dagger e^{i(\mathbf{k}-\mathbf{k}')\cdot(\mathbf{r}_i-\mathbf{r}_0^{\mathrm{FI}})}e^{-i\mathbf{k}'\cdot\boldsymbol{\delta}} + \eta_{\mathbf{k}}^\dagger\eta_{\mathbf{k}'}e^{-i(\mathbf{k}-\mathbf{k}')\cdot(\mathbf{r}_i-\mathbf{r}_0^{\mathrm{FI}})}e^{i\mathbf{k}'\cdot\boldsymbol{\delta}}\Bigg) - J\sum_i\sum_{\boldsymbol{\delta}}\hbar^2S^2.
\end{aligned}
\tag{2.40}
$$

In the last equality, we neglected a quadrilinear magnon term, since we only consider terms to second order.

The terms in Eq. (2.40) with products of two annihilation or two creation operators cancel upon summing over d. Note now that

$$
\sum_i e^{i\mathbf{k}\cdot\mathbf{r}_i} = N_{\mathrm{FM}}\delta(\mathbf{k}), \tag{2.41}
$$

which can be verified by identifying the sum as a geometric series, as was done in Eq. (2.30). Gathering the terms, we then find that

$$
\begin{aligned}
-J\sum_{\langle i,j\rangle}\mathbf{S}_i\cdot\mathbf{S}_j \approx &\sum_{\mathbf{k}}2\hbar^2JSN_d\left(1-\frac{1}{2}(\gamma_{-\mathbf{k}}+\gamma_{\mathbf{k}})\right)\eta_{\mathbf{k}}^\dagger\eta_{\mathbf{k}} \\
&-J\sum_{\mathbf{k}}\sum_{\boldsymbol{\delta}}\hbar^2Se^{-i\mathbf{k}\cdot\boldsymbol{\delta}} - J\sum_i\sum_{\boldsymbol{\delta}}\hbar^2S^2.
\end{aligned}
\tag{2.42}
$$

Above, $N_d = 4$ is the number of nearest neighbors on a square lattice, and we introduced

$$\gamma_{\mathbf{k}} \equiv \frac{1}{N_d} \sum_{\boldsymbol{\delta}} e^{i\mathbf{k}\cdot\boldsymbol{\delta}} = \frac{1}{N_d} \sum_{\boldsymbol{\delta}} \cos \mathbf{k} \cdot \boldsymbol{\delta}. \tag{2.43}$$

The second equality follows from inversion symmetry in the FI lattice. The inversion symmetry also implies $\gamma_{-\mathbf{k}} = \gamma_{\mathbf{k}}$. Furthermore, the factor $\sum_{\mathbf{k}} e^{-i\mathbf{k}\cdot\boldsymbol{\delta}} = N_{\mathrm{FI}}\delta(\boldsymbol{\delta}) = 0$ because $\boldsymbol{\delta} \neq \mathbf{0}$,[8] hence one term vanishes. Finally, the last term on the right-hand side of Eq. (2.42) is a constant, and is not important for our analysis, so it is neglected. The exchange interaction is thus recast in the magnon basis as

$$-J \sum_{\langle i,j \rangle} \mathbf{S}_i \cdot \mathbf{S}_j \quad \longrightarrow \quad \sum_{\mathbf{k}} 2\hbar^2 JSN_d \left(1 - \gamma_{\mathbf{k}}\right) \eta_{\mathbf{k}}^{\dagger} \eta_{\mathbf{k}}. \tag{2.44}$$

Analogously, recasting $\mathcal{H}_{\mathrm{ext}}$ in the magnon basis yields

$$\begin{aligned} -\frac{g\mu_B}{\hbar} B_{\mathrm{ext}} \sum_i S_{iz} &= \sum_{\mathbf{k}} g\mu_B B_{\mathrm{ext}} \eta_{\mathbf{k}}^{\dagger} \eta_{\mathbf{k}} - g\mu_B B_{\mathrm{ext}} S N_{\mathrm{FM}} \\ &\longrightarrow \quad \sum_{\mathbf{k}} g\mu_B B_{\mathrm{ext}} \eta_{\mathbf{k}}^{\dagger} \eta_{\mathbf{k}}. \end{aligned} \tag{2.45}$$

In the last step, we again neglected an inconsequential constant term. Thus, the Hamiltonian (2.9) becomes

$$\mathcal{H}_{\mathrm{FI}} \quad \longrightarrow \quad \sum_{\mathbf{k}} \hbar\lambda_{\mathbf{k}} \eta_{\mathbf{k}}^{\dagger} \eta_{\mathbf{k}}, \tag{2.46}$$

where we have introduced the magnon dispersion relation

$$\lambda_{\mathbf{k}} \equiv 2\hbar J N_{\delta} S(1 - \gamma_{\mathbf{k}}) + \frac{g\mu_B}{\hbar} B_{\mathrm{ext}}. \tag{2.47}$$

This concludes the introductory part on ferromagnetism, and we move onto superconductivity.

[8] Bold $\mathbf{0}$ is the zero-vector.

Key takeaways:

- Magnets are systems (usually crystals) of constituent spin-carrying particles. Ferromagnets exhibit spontaneous parallel ordering of neighboring spins $\mathbf{S}_i$.
- Spin waves are collective spin phenomena in spontaneously ordered magnets.
- Magnons ($\eta_{\mathbf{k}}$, $\eta_{\mathbf{k}}^{\dagger}$) are bosonic quasiparticles and quanta of spin waves. These relate to the spin basis by the Holstein–Primakoff transformation, which maps the spin basis onto a bosonic quasiparticle basis, followed by a Fourier transform. We consider systems with few magnons, allowing for linearization of the Holstein–Primakoff transformation.
- The discrete Fourier transformation resolves a finite-dimensional system onto a discrete, orthonormal basis of monochromatic waves. Expressed in terms of position $\mathbf{r}_i$ and momenta $\mathbf{k}$, the transformation carries a position-dependent phase factor $e^{-i\mathbf{k}\cdot\mathbf{r}_0^{\mathrm{FI}}}$ that is usually glossed over in the literature. For lattices with finite lattice spacing, Fourier space is additionally divided into Brillouin zones, across which exist physically equivalent modes.

Chapter 3

Superconductivity

Chapter summary: Below a critical temperature, superconductors exhibit a vanishing electrical resistivity, and a partial to complete expulsion of applied magnetic fields. We provide an instructional overview of the London, BCS and quasiclassical theories of superconductivity, and elaborate on the quantum-mechanical implementation of BCS superconductivity in our microscopic model.

Superconductors are extraordinary materials characterized by their ability to conduct currents with no electrical resistance, and the partial to complete expulsion of applied magnetic fields underneath a thin surface layer (the Meissner effect), below a material critical temperature T_c and applied field strength H_c [71]. The first observations of the respective effects were made by H. Kamerlingh Onnes in 1911 [72], and W. Meissner and R. Ochsenfeld in 1933 [73]. Since then, a number of theoretical models of superconductivity have been proposed, with several breakthroughs taking place during the mid 1900s. However, many varieties of superconductivity are still inadequately understood theoretically, and have remained highly active fields of research to date. Its profundity and intricacy is reflected in the number of Nobel laureates that have been involved in the field [74–76], including H. Kamerlingh Onnes [77]. In the following, we provide a chronological outline of the three theories of superconductivity relevant to our research: the classical London theory (used in Paper I), the microscopic Bardeen–Cooper–Schrieffer theory (used in Paper II and throughout this dissertation), and the Eilenberger and Usadel quasiclassical theories (commonly used to analyze proximity systems, which we include for contrast to our approach)

3.1 London and BCS theory

One of the earliest and simplest attempts at constructing a theory of superconductivity, was made by F. London and H. London in 1935. They supposed a portion of

the electrons moved freely through the superconductor, and were therefore only *accelerated* by an applied electric field [78].[1] This was predicated on the experimental evidence of a persistent current in superconductors even in the absence of electromagnetic fields. This forms the theoretical background for the *two-fluid model*, which we used in the analytics[2] of Paper I. Here, the superconductor is modelled as two parallel channels: one which conducts "normal" electrons (subject to Ohm's law), and one which conducts "superconducting" electrons [71].

Specifically, the London brothers assumed the relationship

$$\frac{\partial \mathbf{J}_s}{\partial t} = \frac{1}{\Lambda}\mathbf{E} \tag{3.1}$$

between the persistent (superconducting) current density $\mathbf{J}_s$ and the electric field $\mathbf{E}$, for some constant Λ (compare this to Ohm's law for the "normal" current density $\mathbf{J}_n = \sigma\mathbf{E}$, with σ the conductivity). Combining this with Maxwell's equations for classical electromagnetism, they furthermore found that

$$\nabla \times \frac{\partial \mathbf{J}_s}{\partial t} = -\frac{1}{c\Lambda}\frac{\partial \mathbf{H}}{\partial t}, \tag{3.2}$$

with c the speed of light, which leads to an exponential suppression of magnetic field near the surface of the superconductor; the theory thus also accounted for the Meissner effect. In the absence of electric potentials, Eqs. (3.1) and (3.2) can be stated succinctly in terms of the vector potential $\mathbf{A}$ as [3]

$$\mathbf{J}_s = -\frac{1}{c\Lambda}\mathbf{A}. \tag{3.3}$$

Λ is usually given as $\Lambda = c^2/4\pi\lambda^2$, with λ the *London penetration depth*, the length scale of the exponential suppression.

In light of experimental evidence conflicting with London theory upon adding adding impurities to superconducting Sn, A. B. Pippard developed an extended

[1] Reading their original paper, they were clearly not particularly fond of this assumption as it gave rise to mathematical issues and unphysical predictions, but remained pragmatic about it.

[2] Note that for the numerics, we instead opted for Mattis–Bardeen theory [79]. This is a microscopic theory of conductivity that accounts for anomalies in the conductivity of superconductors in regimes where the penetration depth is exceeded by the mean free path or the superconducting coherence length. It is derived from the microscopic BCS theory, an motivated by the phenomenological Pippard theory of anomalous conductivity in superconductors (the jargon and these theories are covered later in this section). We made this choice for the sake of accuracy, as Mattis–Bardeen theory resolves, in particular, optical excitations across the gap near T_c [80], which modifies the results relative to the two-fluid prediction. However, the two-fluid model captures the overall change in the conductivity as the superconductor transitions between its normal and superconducting state, and is considerably simpler to proceed with analytically. We therefore proceeded with the two-fluid model for the analytics, since it did not influence the conceptual outline of remote monitoring of the superconducting transition.

[3] This equation can also be derived from the minimal coupling scheme, requiring that the canonical momentum $\mathbf{p} = m\mathbf{v} + e\mathbf{A}/c = 0$ [71, 81]. This is motivated by arguing that the ground state in the absence of applied fields has zero net momentum, and that for a superconductor, this ground state criterion persists also upon applying a field.

theory: while local London theory took $\mathbf{J}_s$ at position $\mathbf{r}$ to scale with $\mathbf{A}$ also at $\mathbf{r}$, he suggested $\mathbf{J}_s$ at $\mathbf{r}$ instead non-locally scaled with $\mathbf{A}$ integrated over a volume around $\mathbf{r}$ [71, 82]. The observed phenomenon was analogous to the anomalous skin effect in normal conductors, in which the conductivity becomes modified as the skin depth drops below the mean free path ℓ of the electrons [83], and the non-local dependency of the response would extend over a volume of radius ℓ. A. B. Pippard similarly introduced a non-local length scale ξ', which was taken to scale as $(\xi')^{-1} = (\xi)^{-1} + (\ell)^{-1}$ with impurities (ℓ) and a new length specific to superconductors (ξ). This foreshadowed the first microscopic theory of superconductivity, to be presented below, in which ξ found its interpretation as the *superconducting coherence length*, the length over which pairs of electrons cohere in the superconducting state [71, 80]. This is the theory we will elaborate on and proceed with in this dissertation, entering the model presented in Paper II.

In their landmark paper of 1957 [84], J. Bardeen, L. N. Cooper and J. R. Schrieffer (BCS) proposed the first microscopic mechanism by which superconductivity may arise: the pairing of electrons near the Fermi surface by, in general, some weak attractive interaction; in their original work, they specifically considered interactions by the exchange of virtual phonons [68, 84, 85].[4] This gives rise to states (*Cooper pairs*) that are energetically protected from scattering by the appearance of a gap $\Delta \neq 0$ in the quasiparticle dispersion, the mechanism behind Joule heating [3]. That is, in a manner similar to how insulators resist the conduction of electrons due to a gap between the valence and conduction band, the superconducting gap suppresses low-energy ($< 2\Delta$) excitations of electrons across the Fermi surface. This and extended theories have proven to be successful descriptions for a wide range of superconducting materials, usually with a critical temperature T_c within a few Kelvin above absolute zero. For this theory, J. Bardeen, L. N. Cooper and J. R. Schrieffer were awarded the 1972 Nobel Prize in physics [74].

3.2 Quasiclassical theory

Lastly in this outline, for contrast to our set-up aimed at *long-distance* coupling of an FI and an SC, we mention the quasiclassical theory of superconductivity. This theory is applicable in a wide range of set-ups, in particular including *proximity systems* [3, 7, 86, 87], and distinguishes itself from the aformentioned approaches in its application of Green's function methods. It results from a succession of approximations, starting from a very general theory of superconductivity formulated by L. P. Gor'kov in 1958, and subsequently built upon by G. M. Eliashberg in 1960. L. P. Gor'kov took as his point of departure a Hamiltonian with a diagonal electron term of the form $a^\dagger a$, and a postulated quadrilinear interaction term of the form $a^\dagger a'^\dagger a'' a'''$, with a ($a^\dagger$) the electron annihilation (creation) operator [88]; G. M. Eliashberg instead considered a phonon-mediated interaction term of the

[4] Phonons are quanta of lattice vibrations.

form $a^\dagger a'(b + b^\dagger)$, with $b, b^\dagger$ the phonon field operators [89]. The physics of the system was then extracted by considering two-point Green's functions (electron–electron correlation functions, i.e. expectation values of two electron operators), a very powerful approach that allows for strong pairing potentials and systems out of equilibrium.

However, for many applications, the general Green's functions carry more information than necessary, and the general equations of motions can be challenging to solve. Thus, in a 1968 paper, G. Eilenberger performed a series of approximations to the equations of L. P. Gor'kov based on the following, often applicable assumptions: the interesting physics of superconductivity is concentrated in a low-energy regime near the much greater Fermi energy, and material impurities (giving rise to scattering) are weak and randomly distributed [3, 86, 90, 91]. This allows for averaging across microscopic details appearing as rapid oscillations in the Gor'kov Green's functions, leaving a slowly varying envelope accounting for the interesting physics, hence it is known as the *quasiclassical approximation* [92]. K. D. Usadel furthermore showed that for superconductors with particularly high concentrations of impurities (diffusive limit), the Eilenberger equations could still be substantially simplified owing to the suppression of anisotropy in the Green's functions due to scattering [93].

The theories of G. Eilenberger and K. D. Usadel, as well as generalizations, find broad applications in proximity systems. In these systems, superconducting order diffuses into a neighboring material across an interface (the *proximity effect*), and the (e.g. magnetic) order of the neighboring material likewise diffuses into the superconductor (the *inverse proximity effect*). This diffusion is often disruptive of the respective orders; for instance, ferromagnetic ordering favors parallel alignment of neighboring spins ($\uparrow\uparrow$), but the spins of the electrons in a singlet Cooper pair are aligned oppositely ($\uparrow\downarrow - \downarrow\uparrow$), so the orders interact disruptively. These effects are limited to very small length scales near the interface, typically on the order of nm [4–6], and in anomalous cases upwards of a μm [7–9]. By contrast, our approach of using a cavity to mediate interactions between an FI and an SC across comparatively greater length scales, precludes proximity effects from disrupting their orders.

This concludes the outline of relevant theories of superconductivity, we proceed to cover superconductivity in our system.

3.3 Superconductivity in our model

As the historical outline suggests, superconductivity is an incredibly diverse and intricate phenomenon, still with outstanding theoretical questions despite a century of inquiry and many breakthroughs. This is reflected in a broad number of features distinguishing different varieties of superconductivity. However, we are only interested in the qualitative impact of involving *a* superconducting gap in our model. In the model to be presented, we therefore limit ourselves to one of the simplest varieties: BCS superconductivity with Cooper pairs in the antisymmetric

spin state $\uparrow\downarrow - \downarrow\uparrow$, and a gap in the energy spectrum that does not change with direction in momentum space (i.e., the gap is isotropic); in short, we consider a singlet s-wave gap.[5] In the outlook to be presented in Ch. 8, we furthermore provide reflections on the anticipated impact of anisotropic gaps on our results, arguing that such anisotropies could be resolved remotely in the magnon spectrum.

We begin by briefly commenting on the geometry of the SC, in analogy with the detailed treatment of the FI in Sec. 2.2.2. Then, we move onto the description of the superconductivity itself, or more precisely the BCS pairing Hamiltonian. Finally, we bring the SC Hamiltonian onto a diagonal form by recasting it in terms of its eigenmodes (quasiparticle basis).

3.3.1 Geometry and momenta

First, some preliminaries on the geometry of our SC, and the discretization of particle momenta. With the set-up in Fig. 1.3 in mind, the SC is treated as a square lattice with a lattice constant a_{SC}, a center position vector $\mathbf{r}_0^{\mathrm{SC}}$, and sites labeled by $j = (n_x^{\mathrm{SC}}, n_y^{\mathrm{SC}})$; cf. Fig. 3.1. Each lattice site is associated with an electron creation and annihilation operator, $c_{j\sigma}^\dagger$ and $c_{j\sigma}$ respectively, with $\sigma = \uparrow, \downarrow$ the spin index.

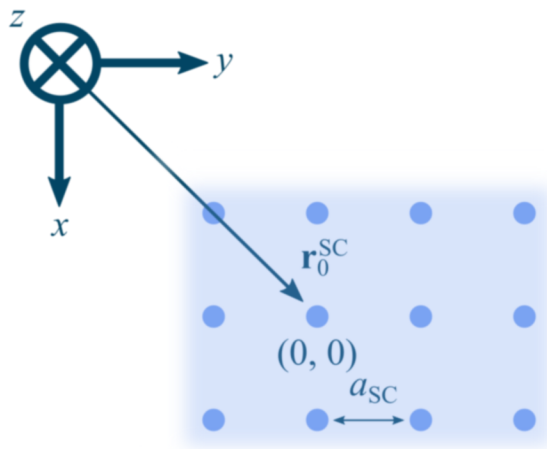

Figure 3.1: A top-down view of the square SC lattice. The illustration is analogous to Fig. 2.3. The points are labeled $(n_x^{\mathrm{SC}}, n_y^{\mathrm{SC}})$ with the ranges (3.6) for n_d^{SC}. a_{FI} is the lattice constant, and $\mathbf{r}_0^{\mathrm{FI}}$ is the position vector of the $(0,0)$ point relative to the origin.

Thus, in analogy with the magnon operators (cf. Sec. 2.2.2, in particular Eq. (2.39)),

[5] Technically, there are more qualifiers to this gap: it is even-frequency (even in the time coordinate), and single-orbital (electrons are paired within the same orbital) [94]. These details are not important for us.

the Fourier transform of the electron operators read

$$\begin{aligned} c_{j\sigma} =& \frac{1}{\sqrt{N_{\mathrm{SC}}}} \sum_{p_x \in (-\pi/a_{\mathrm{SC}}, \pi/a_{\mathrm{SC}}]} \sum_{p_y \in (-\pi/a_{\mathrm{SC}}, \pi/a_{\mathrm{SC}}]} c_{\mathbf{p}\sigma} e^{i\mathbf{p}\cdot(\mathbf{r}_j - \mathbf{r}_0^{\mathrm{SC}})} \\ \equiv& \frac{1}{\sqrt{N_{\mathrm{SC}}}} \sum_{\mathbf{p}} c_{\mathbf{p}\sigma} e^{i\mathbf{p}\cdot(\mathbf{r}_j - \mathbf{r}_0^{\mathrm{SC}})}, \end{aligned} \tag{3.4}$$

where $\mathbf{p} \equiv (p_x, p_y, 0)$, and N_{SC} is the number of lattice sites in the SC. $\mathbf{r}_j$ is the position of SC lattice site j, given by

$$\mathbf{r}_j \equiv \mathbf{r}_{n_x^{\mathrm{SC}} n_y^{\mathrm{SC}}} \equiv (x_0^{\mathrm{SC}} + a_{\mathrm{SC}} n_x^{\mathrm{SC}}, y_0^{\mathrm{SC}} + a_{\mathrm{SC}} n_y^{\mathrm{SC}}, L_z/2), \tag{3.5}$$

$$n_d^{\mathrm{SC}} = \begin{cases} -\frac{N_d^{\mathrm{SC}}-1}{2}, \ldots, \frac{N_d^{\mathrm{SC}}-1}{2}, & N_d^{\mathrm{SC}} \text{ odd}, \\ -\frac{N_d^{\mathrm{SC}}}{2}+1, \ldots, \frac{N_d^{\mathrm{SC}}}{2}-1, & N_d^{\mathrm{SC}} \text{ even}, \end{cases} \tag{3.6}$$

where $(x_0^{\mathrm{SC}}, y_0^{\mathrm{SC}}, L_z/2) \equiv \mathbf{r}_0^{\mathrm{SC}}$. The sum $\sum_{\mathbf{p}}$ was introduced as short-hand notation for the sum over electron momenta inside the 1BZ of the SC. Note that the SC 1BZ is *not the same* as the FI 1BZ; both their extensions in momentum space, and the discretization of momenta of the respective systems, are generally *different*. The electron momenta are discretized as

$$\mathbf{p} = (p_x, p_y, 0) = (2\pi m_x^{\mathrm{SC}}/l_x^{\mathrm{SC}}, 2\pi m_y^{\mathrm{SC}}/l_y^{\mathrm{SC}}, 0), \tag{3.7}$$

$$m_d^{\mathrm{SC}} = \begin{cases} -\frac{N_d^{\mathrm{SC}}-1}{2}, \ldots, \frac{N_d^{\mathrm{SC}}-1}{2}, & N_d^{\mathrm{SC}} \text{ odd}, \\ -\frac{N_d^{\mathrm{SC}}}{2}+1, \ldots, \frac{N_d^{\mathrm{SC}}}{2}-1, & N_d^{\mathrm{SC}} \text{ even}, \end{cases} \tag{3.8}$$

where $d = x, y$ labels directions on the lattice, m_d^{SC} are integers labeling modes within the SC 1BZ, N_d^{SC} are the numbers of lattice points in the respective directions, and

$$l_d^{\mathrm{SC}} \equiv a_{\mathrm{SC}}(N_d^{\mathrm{SC}} - 1) \approx a_{\mathrm{SC}} N_d^{\mathrm{SC}} \tag{3.9}$$

are the lengths of the sides of the SC lattice. The total number of SC lattice points is then

$$N_{\mathrm{SC}} = N_x^{\mathrm{SC}} N_y^{\mathrm{SC}}. \tag{3.10}$$

The z component of $\mathbf{p}$ is zero because the electrons are confined to a 2D lattice in the xy plane. Note that the discretization of electron momenta generally differs from that of magnon momenta $\mathbf{k}$ (see Eq. (2.36)). Lastly, the orthogonality relation is

$$\sum_j e^{i\mathbf{p}\cdot\mathbf{r}_j} = N_{\mathrm{SC}} \delta(\mathbf{p}), \tag{3.11}$$

corresponding to Eq. (2.41) for the magnons.

3.3.2 Pairing Hamiltonian

Moving onto the superconductivity itself, we consider one of the simplest pairing terms, the BCS singlet *s*-wave:

$$\mathcal{H}_{\mathrm{BCS}} = -\sum_{\mathbf{p}} \left(\Delta_{\mathbf{p}} c^{\dagger}_{\mathbf{p}\uparrow} c^{\dagger}_{-\mathbf{p}\downarrow} + \Delta^{*}_{\mathbf{p}} c_{-\mathbf{p}\downarrow} c_{\mathbf{p}\uparrow} \right). \tag{3.12}$$

The term can be derived as follows, cf. Ch. 3.5 of Ref. [71]: Consider the effective Cooper pair interaction Hamiltonian

$$\mathcal{H}'_{\mathrm{BCS}} \equiv \sum_{\mathbf{p}\mathbf{p}'} V_{\mathbf{p}\mathbf{p}'} c^{\dagger}_{\mathbf{p}\uparrow} c^{\dagger}_{-\mathbf{p}\downarrow} c_{-\mathbf{p}'\downarrow} c_{\mathbf{p}'\uparrow}. \tag{3.13}$$

Such a term was derived in a precursory article to the original BCS paper by considering electron–phonon interactions and performing a partial diagonalization (Schrieffer–Wolff transformation, cf. Appendix B) [68, 84, 85]; similar terms have been derived by considering other mediators than phonons, such as photons [11] and magnons [95]. As it stands, this quadrilinear interaction is difficult to proceed with analytically. We therefore seek to simplify the calculations by way of mean-field theory. The pair operators trivially satisfy the relation

$$c_{-\mathbf{p}\downarrow} c_{\mathbf{p}\uparrow} = \langle c_{-\mathbf{p}\downarrow} c_{\mathbf{p}\uparrow} \rangle + \left(c_{-\mathbf{p}\downarrow} c_{\mathbf{p}\uparrow} - \langle c_{-\mathbf{p}\downarrow} c_{\mathbf{p}\uparrow} \rangle \right), \tag{3.14}$$

where the angle brackets denote the expectation value, and the parentheses denote fluctuations. Assuming a considerable amount of electrons have condensed into the superconducting state, the fluctuations about the expected number of pairs is comparatively small (see also the discussion on mean field theory in Appendix A). Thus, inserting Eq. (3.14) into Eq. (3.13) and neglecting the resulting bilinear term in the fluctuations, one finds that

$$\begin{aligned} &\sum_{\mathbf{p}\mathbf{p}'} V_{\mathbf{p}\mathbf{p}'} \left[\langle c_{-\mathbf{p}\downarrow} c_{\mathbf{p}\uparrow} \rangle + \left(c_{-\mathbf{p}\downarrow} c_{\mathbf{p}\uparrow} - \langle c_{-\mathbf{p}\downarrow} c_{\mathbf{p}\uparrow} \rangle \right) \right]^{\dagger} \left[\langle c_{-\mathbf{p}'\downarrow} c_{\mathbf{p}'\uparrow} \rangle + \left(c_{-\mathbf{p}'\downarrow} c_{\mathbf{p}'\uparrow} - \langle c_{-\mathbf{p}'\downarrow} c_{\mathbf{p}'\uparrow} \rangle \right) \right] \\ &\approx \sum_{\mathbf{p}\mathbf{p}'} V_{\mathbf{p}\mathbf{p}'} \left(\langle c_{-\mathbf{p}'\downarrow} c_{\mathbf{p}'\uparrow} \rangle c^{\dagger}_{\mathbf{p}\uparrow} c^{\dagger}_{-\mathbf{p}\downarrow} + \langle c_{-\mathbf{p}\downarrow} c_{\mathbf{p}\uparrow} \rangle^{*} c_{-\mathbf{p}'\downarrow} c_{\mathbf{p}'\uparrow} - \langle c_{-\mathbf{p}\downarrow} c_{\mathbf{p}\uparrow} \rangle^{*} \langle c_{-\mathbf{p}'\downarrow} c'_{\mathbf{p}\uparrow} \rangle \right). \end{aligned} \tag{3.15}$$

The last term in the summand is constant, and can be neglected for our purposes. Swapping $\mathbf{p}$ and $\mathbf{p}'$ in the second term in the summand, and defining the gap parameter

$$\Delta_{\mathbf{p}} = -\sum_{\mathbf{p}'} V_{\mathbf{p}\mathbf{p}'} \langle c_{-\mathbf{p}'\downarrow} c_{\mathbf{p}'\uparrow} \rangle, \tag{3.16}$$

the BCS Hamiltonian (3.12) follows. The equation Eq. (3.16) is the self-consistency equation for the gap, so-called because $\Delta_{\mathbf{p}}$ appears on both sides of the equation; explicitly on the left-hand side, and implicitly on the right-hand side, through the gap-dependent expectation value $\langle c_{-\mathbf{p}'\downarrow} c_{\mathbf{p}'\uparrow} \rangle$. Note that we assume *s*-wave symmetry in our model, i.e. $\Delta_{\mathbf{p}} = \Delta$.

In our model, we will need to break **p**-space inversion symmetry, as the leading-order effect of the SC on the FI (namely, the reorientation of FI spins) otherwise vanishes. We show this at the end of Sec. 6.1.4, after having derived an expression for this effect. To this end, we opt to break inversion symmetry here by inducing an equilibrium supercurrent, which can be achieved by passing a direct current (DC) through the SC [71], as is done in Ref. [96]. A supercurrent distributed evenly throughout a cross section of the SC in its direction, is the leading effect of the DC only provided the sample width does not exceed the Pearl length $\Lambda = \lambda^2/d$ [71, 96, 97], with λ the effective magnetic penetration depth, and d the sample depth. This length expresses the cross-sectional area $(2\Lambda) \times d$ of the SC film over which a screening current (giving rise to the Meissner effect) distributes, around a normal-metal filament passing the DC. This leading-order effect is expressed mathematically as the Cooper pairs attaining a finite center-of-mass momentum $2\mathbf{P}$,

$$\mathcal{H}_{\mathrm{BCS}} = -\sum_{\mathbf{p}} \left(\Delta_{\mathbf{p}} c^{\dagger}_{\mathbf{p}+\mathbf{P},\uparrow} c^{\dagger}_{-\mathbf{p}+\mathbf{P},\downarrow} + \Delta^{*}_{\mathbf{p}} c_{-\mathbf{p}+\mathbf{P},\downarrow} c_{\mathbf{p}+\mathbf{P},\uparrow} \right). \tag{3.17}$$

To accommodate for this, we pass a thin electric wire carrying the DC through a small hole in the cavity wall. The dimensions of the wire and hole are assumed too small to interfere with the cavity modes.

3.3.3 Eigenmodes: Bogoliubov quasiparticles

The BCS Hamiltonian (3.17) is non-diagonal in the electron basis. It is convenient to absorb this term into a diagonal basis, to reduce the number of terms involved in the calculations.

For the diagonal electron term, we use the tight-binding expression for a square lattice, [56]

$$\mathcal{H}_{\mathrm{diag}} \equiv \sum_{\mathbf{p}\sigma} \xi_{\mathbf{p}} c^{\dagger}_{\mathbf{p}\sigma} c_{\mathbf{p}\sigma}. \tag{3.18}$$

Above, $\xi_{\mathbf{p}}$ is the tight-binding dispersion

$$\xi_{\mathbf{p}} = -2t(\cos p_x a_{\mathrm{SC}} + \cos p_y a_{\mathrm{SC}}) - \mu, \tag{3.19}$$

where t is the hopping parameter, and μ is the chemical potential. t is given by

$$t = \frac{\hbar^2}{2m^* a_{\mathrm{SC}}^2}, \tag{3.20}$$

where m^* is the effective mass of the electrons. This expression is found by series-expanding $\xi_{\mathbf{p}}$ in $p_x a_{\mathrm{SC}}$ and $p_y a_{\mathrm{SC}}$, and equating the $p_x^2 + p_y^2$ term with a would-be free-electron expression $\hbar^2 \mathbf{p}^2/2m^*$ [56].

The simple SC Hamiltonian then reads

$$\mathcal{H}_{\mathrm{SC}} \equiv \mathcal{H}_{\mathrm{diag}} + \mathcal{H}_{\mathrm{BCS}}. \tag{3.21}$$

Diagonalizing $\mathcal{H}_{\mathrm{SC}}$ is straight-forward:

$$\begin{aligned}
\mathcal{H}_{\mathrm{SC}} &= \sum_{\mathbf{p}\sigma} \xi_{\mathbf{p}} c^{\dagger}_{\mathbf{p}\sigma} c_{\mathbf{p}\sigma} - \sum_{\mathbf{p}} \left(\Delta_{\mathbf{p}} c^{\dagger}_{\mathbf{p}+\mathbf{P},\uparrow} c^{\dagger}_{-\mathbf{p}+\mathbf{P},\downarrow} + \Delta^{*}_{\mathbf{p}} c_{-\mathbf{p}+\mathbf{P},\downarrow} c_{\mathbf{p}+\mathbf{P},\uparrow} \right) \\
&= \sum_{\mathbf{p}} \begin{pmatrix} c_{\mathbf{p}+\mathbf{P},\uparrow} \\ c^{\dagger}_{-\mathbf{p}+\mathbf{P},\downarrow} \end{pmatrix}^{\dagger} \begin{pmatrix} \xi_{\mathbf{p}+\mathbf{P}} & -\Delta_{\mathbf{p}} \\ -\Delta^{*}_{\mathbf{p}} & -\xi_{-\mathbf{p}+\mathbf{P}} \end{pmatrix} \begin{pmatrix} c_{\mathbf{p}+\mathbf{P},\uparrow} \\ c^{\dagger}_{-\mathbf{p}+\mathbf{P},\downarrow} \end{pmatrix} \\
&= \sum_{\mathbf{p}} \begin{pmatrix} \gamma_{\mathbf{p}0} \\ \gamma_{\mathbf{p}1} \end{pmatrix}^{\dagger} \begin{pmatrix} E_{\mathbf{p}0} & 0 \\ 0 & E_{\mathbf{p}1} \end{pmatrix} \begin{pmatrix} \gamma_{\mathbf{p}0} \\ \gamma_{\mathbf{p}1} \end{pmatrix} \\
&= \sum_{\mathbf{p}m} E_{\mathbf{p}m} \gamma^{\dagger}_{\mathbf{p}m} \gamma_{\mathbf{p}m},
\end{aligned} \tag{3.22}$$

where $m = 0, 1$. The eigenmodes are called *Bogoliubov quasiparticles*,[6] and their dispersion relations read

$$E_{\mathbf{p}m} = \frac{1}{2} \left(\xi_{\mathbf{p}+\mathbf{P}} - \xi_{-\mathbf{p}+\mathbf{P}} + (-1)^{m} \sqrt{\left(\xi_{\mathbf{p}+\mathbf{P}} + \xi_{-\mathbf{p}+\mathbf{P}} \right)^{2} + 4|\Delta_{\mathbf{p}}|^{2}} \right), \tag{3.23}$$

They relate to the electron basis by the transformation elements $u_{\mathbf{p}}$ and $v_{\mathbf{p}}$, defined via

$$c_{\mathbf{p}+\mathbf{P},\uparrow} \equiv u^{*}_{\mathbf{p}} \gamma_{\mathbf{p}0} + v_{\mathbf{p}} \gamma_{\mathbf{p}1}, \quad c^{\dagger}_{-\mathbf{p}+\mathbf{P},\downarrow} \equiv -v^{*}_{\mathbf{p}} \gamma_{\mathbf{p}0} + u_{\mathbf{p}} \gamma_{\mathbf{p}1}. \tag{3.24}$$

Inserting these expressions for $c_{\mathbf{p}+\mathbf{P},\uparrow}$ and $c_{-\mathbf{p}+\mathbf{P},\downarrow}$ into Eq. (3.22), and equating coefficients in the Bogoliubov quasiparticle basis, we find

$$\frac{\Delta^{*}_{\mathbf{p}} v_{\mathbf{p}}}{u_{\mathbf{p}}} = \frac{1}{2} \left[\left(E_{\mathbf{p}0} - E_{\mathbf{p}1} \right) - \left(\xi_{\mathbf{p}+\mathbf{P}} + \xi_{-\mathbf{p}+\mathbf{P}} \right) \right], \tag{3.25}$$

$$|v_{\mathbf{p}}|^{2} = 1 - |u_{\mathbf{p}}|^{2} = \frac{1}{2} \left(1 - \frac{\xi_{\mathbf{p}+\mathbf{P}} + \xi_{-\mathbf{p}+\mathbf{P}}}{E_{\mathbf{p}0} - E_{\mathbf{p}1}} \right). \tag{3.26}$$

The latter ensures normalized fermionic statistics for the new quasiparticles:

$$\{\gamma_{\mathbf{p}0}, \gamma^{\dagger}_{\mathbf{p}'0}\} = (u_{\mathbf{p}} u^{*}_{\mathbf{p}'} + v_{\mathbf{p}} v^{*}_{\mathbf{p}'}) \delta_{\mathbf{p}\mathbf{p}'} = (|u_{\mathbf{p}}|^{2} + |v_{\mathbf{p}}|^{2}) \delta_{\mathbf{p}\mathbf{p}'} = \delta_{\mathbf{p}\mathbf{p}'}, \tag{3.27}$$

$$\{\gamma^{\dagger}_{\mathbf{p}0}, \gamma^{\dagger}_{\mathbf{p}'0}\} = (u^{*}_{\mathbf{p}} v^{*}_{\mathbf{p}'} - v^{*}_{\mathbf{p}} u^{*}_{\mathbf{p}'}) \delta_{\mathbf{p}\mathbf{p}'} = (u^{*}_{\mathbf{p}} v^{*}_{\mathbf{p}} - v^{*}_{\mathbf{p}} u^{*}_{\mathbf{p}}) \delta_{\mathbf{p}\mathbf{p}'} = 0, \tag{3.28}$$

$$\{\gamma_{\mathbf{p}1}, \gamma^{\dagger}_{\mathbf{p}'1}\} = \delta_{\mathbf{p}\mathbf{p}'}, \tag{3.29}$$

$$\{\gamma^{\dagger}_{\mathbf{p}1}, \gamma^{\dagger}_{\mathbf{p}'1}\} = 0, \tag{3.30}$$

$$\{\gamma_{\mathbf{p}0}, \gamma^{\dagger}_{\mathbf{p}'1}\} = 0, \tag{3.31}$$

and so on.

This concludes the introductory part on superconductivity. Next, we give an introduction to the final subsystem of our set-up: the electromagnetic cavity.

[6] We will also refer to them as SC quasiparticles.

Key takeaways:

- Superconducting materials are characterized by a vanishing electrical resistance, and the partial to complete expulsion of applied magnetic fields inside their bulk, below a material critical temperature T_c and critical field strength H_c.
- London theory is a classical, phenomenological model of superconductivity. A persistent current (the supercurrent) is taken to be accelerated by an applied electric field: $\partial_t \mathbf{J}_s \propto \mathbf{E}$. This is in contrast to Ohm's law for resistive current: $\mathbf{J}_n \propto \mathbf{E}$. In Paper I, we apply the two-fluid model to the superconductor, by which it is modelled as two parallel channels passing superconducting and normal electrons according to the respective laws.
- BCS theory is a microscopic theory of superconductivity. Superconductivity results from the pairing of electrons (Cooper pairs) by some weak attractive interaction (e.g. the exchange of phonons), giving rise to a gap in the particle spectrum $\Delta_{\mathbf{p}} = -\sum_{\mathbf{p}'} V_{\mathbf{p}\mathbf{p}'} \langle c_{-\mathbf{p}'\downarrow} c_{\mathbf{p}'\uparrow} \rangle$. This protects electrons (Cooper pairs) energetically from scattering. The corresponding quasiparticle excitations $\gamma_{\mathbf{p}}$, $\gamma_{\mathbf{p}}^\dagger$ are linear combinations of electrons and holes. This is the theory with which we proceed in this dissertation.
- Quasiclassical theory of superconductivity is often used to analyze proximity systems, which stand in contrast to our cavity-based set-up. This is a Green's functions formalism involving an electron pairing term, in which the Fermi wave length is taken to be the dominant length scale (Eilenberger theory), and impurity scattering is furthermore taken to be considerable (Usadel theory).

Chapter 4

Electromagnetic cavities

Chapter summary: Electromagnetic cavities organize currents and charge accumulations inside its walls in such a manner that all but a discrete subset of electromagnetic oscillations are suppressed within the enclosed volume. In contrast to free-space waves, this subset of modes distribute electric and magnetic oscillations unevenly in space and remain strong over considerable distances for sufficiently small cavity volumes. In our set-up, we utilize these modes to mediate interactions between the FI and the SC. Here, we outline the classical theory of electromagnetism, and derive expressions for the quantized cavity gauge field in our system.

Like the history of magnetism—outlined in Sec. 2—the history of electric phenoma dates far back. Greek philosopher Thales of Miletus observed in 600 BCE the ability of rubbed amber (Ancient Greek ἤλεκτρον) to attract light objects [98], a phenomenon now known as static electricity. The nascence of the modern systematic inquiry into magnetic and electric phenomena is usually attested to the middle of the last millennium. During the centuries that followed, they were believed to be separate phenomena, until a series of experimental observations indicating their interdependency were made by H. C. Ørsted and M. Faraday in the early 1800s, leading J. C. Maxwell to formulate a unified theory of electric and magnetic forces [57]. This is expressed in the set of equations now known as the Maxwell equations, the foundation of *classical electromagnetism*.

In short, these equations tell us that oscillating electric fields $\mathbf{E}$ beget oscillating magnetic fields $\mathbf{B}$, and vice versa. In the absence of losses, it is then easy to conceive of a scenario in which an initial disturbance in one of the fields, can occasion an indefinite chain of oscillations. Furthermore, charge densities ρ occasion electric fields, and their movement (current densities $\mathbf{J}$) magnetic fields, and vice versa. Electromagnetic cavities are systems of conducting walls enclosing a non-conducting volume that organize these interdependencies in a rhythmic harmony. Upon some initial disturbance of the fields inside the cavity, the fields

will propagate until they reach the vicinity of the walls, instantiating charge accumulations and currents that give rise to reflected fields. This happens in every direction of the enclosed volume, mixing waves and suppressing a range of oscillations, eventually leaving a set of standing waves known as the *normal* or *resonant modes* of the cavity. The smaller the losses in the cavity, the more sharply defined are these modes with respect to frequencies and spatial distributions, as well as their longevity and the relative phases of the fields. These modes carry a number of peculiar features:

- Magnetic and electric oscillations can concentrate in separate parts of the cavity (cf. Fig. 1.1). This is unlike waves propagating in free space, where every point along the trajectory of the wave has both a magnetic *and* electric oscillation.
- Oscillations instantiated in one part of the cavity can give rise to substantial oscillations in another. This again in contrast to free-space waves, where the intensity of a signal diminishes with distance from the source.
- Related to the last point, the amplitude of the field oscillations depend inversely on the cavity volume. Therefore, two points inside the cavity can be far apart, yet oscillations instantiated at one point can occasion substantial oscillations at the other, if the cavity is sufficiently narrow in the orthogonal directions. Volume is determined by the lengths of the cavity in all directions, and for the same volume, one length can be increased provided the other lengths are decreased proportionally.

These are the properties harnessed in cavitronic systems, i.e. systems that have electromagnetic circuitry interact with the normal modes of cavities. In our systems, we make use of all three in order to have magnetic (FI) and electric (SC) subsystems interact substantially across relatively large distances ($\gtrsim \mu$m) as compared to proximity systems (nm–μm). By suitable choices of placement inside the cavity, they are also made to interact with the magnetic and electric fields separately owing to the inhomogeneous spatial distribution of the normal modes. This carries advantages such as simplifying interactions with the resonant modes; making these interactions particularly strong; and for the SC in particular, keeping magnetic fields from destructively interfering with the superconducting order.

In the following, we give a technical introduction to electromagnetism in cavities. We begin with classical preliminaries, before we derive the quantized cavity fields for our specific set-up.

4.1 Classical electromagnetism

The Maxwell equations can be formulated in a number of ways; in particular, they can be expressed locally in terms of derivatives, meaning the fields and sources can be considered on a point-by-point basis in spacetime, and solutions determined uniquely by boundary conditions [99]. Consider therefore a scenario in which charges and currents only exist at the boundaries of a spacetime volume. The

eight[1] Maxwell equations for the enclosed volume can then be expressed as

$$\nabla \cdot \mathbf{B} = \nabla \cdot \mathbf{E} = 0, \tag{4.1}$$

$$\partial_t \mathbf{B} = -\nabla \times \mathbf{E}, \tag{4.2}$$

$$\partial_t \mathbf{E} = c^2 \nabla \times \mathbf{B}. \tag{4.3}$$

We now make some observations. First, we can express the Maxwell equations in terms of a scalar potential ϕ and a vector potential (gauge field) $\mathbf{A}$ by identifying $\mathbf{E} = -\nabla\phi - \partial_t \mathbf{A}$ and $\mathbf{B} = \nabla \times \mathbf{A}$. This formulation immediately has four of the Maxwell equations satisfied, leaving

$$\left(-\nabla^2 + \partial_t^2/c^2\right)\mathbf{A} + \nabla(\nabla \cdot \mathbf{A} + \partial_t \phi/c^2) = \mathbf{0}, \tag{4.4}$$

$$\nabla \cdot (\nabla\phi + \partial_t \mathbf{A}) = 0. \tag{4.5}$$

Second, these potentials are not unique: For some function Λ, the combined transformations $\phi \to \phi - \partial_t \Lambda$ and $\mathbf{A} \to \mathbf{A} + \nabla\Lambda$ yield the same physical fields $\mathbf{E}$ and $\mathbf{B}$ as before. This expresses redundancy in the formulation in terms of potentials, or *gauge invariance*. We can use this to our advantage, simplifying Eqs. (4.4) and (4.5) by an appropriate choice of Λ (known as *fixing the gauge*); this is achieved by imposing another condition of our choice on the potentials. In systems without charges or currents, the transversal (Coulomb) gauge

$$\nabla \cdot \mathbf{A} = 0 \tag{4.6}$$

is particularly useful. Eq. (4.5) then reduces to the Laplace equation $\nabla^2\phi = 0$, with the well-known solution $\phi = 0$ [99]. We are then left with simply

$$\left(-\nabla^2 + \partial_t^2/c^2\right)\mathbf{A} = \mathbf{0}. \tag{4.7}$$

Each component of $\mathbf{A}$ thus has solutions on the form $f_+(\mathbf{Q}\cdot\mathbf{r} + \omega_\mathbf{Q} t) + f_-(\mathbf{Q}\cdot\mathbf{r} - \omega_\mathbf{Q} t)$. These functions are waves of arbitrary shapes and initial locations, propagating with $(-)$ or against $(+)$ the direction of the wave vector $\mathbf{Q}$, at the speed of light. The relationship between the angular[2] frequency $\omega_\mathbf{Q}$ and $\mathbf{Q}$ is readily found by inserting $f_\pm$ into the equation:

$$\omega_\mathbf{Q} = c\sqrt{\mathbf{Q}^2}. \tag{4.8}$$

[1] Keep in mind that one vectorial equation constitutes three scalar equations.

[2] Why angular frequency, and not simply frequency? This is because we are implicitly employing the conventional definition of the wave vector. For a sinusoidal wave, it relates to the wave length λ by the familiar relation $|\mathbf{Q}| = 2\pi/\lambda$. It is this conventional factor 2π that leads us to consider angular frequencies (radians per second), differing from frequencies (revolutions per second) by precisely this factor.

It is important to not confuse these, as the factor 2π can scale a numerical value by nearly order of magnitude. In the context of cavity systems, the size of a cavity can determine the energies involved, which are often expressed in Hz. For a cm-scale cavity, the frequencies involved will be at least on the order $c/(10\,\text{cm}) \approx 3\,\text{GHz}$. This not to be confused with an angular frequency of $3 \cdot 10^9$ rad/s, which would correspond to a frequency of $\approx 477\,\text{MHz}$!

Thirdly, because derivatives are linear operators (e.g. $\nabla(a+b) = \nabla a + \nabla b$), it is clear that if $\mathbf{A}_1$ and $\mathbf{A}_2$ are two solutions to the Maxwell equations for the vector potential, then so is $\mathbf{A}_1 + \mathbf{A}_2$. This is the *superposition principle*, which was alluded to when we touched on standing waves in the introduction to this chapter. This renders the Fourier transform particularly well suited to analyze the Maxwell equations: Every physically reasonable solution to these equations can be decomposed into a linear combination of Fourier modes (see Sec. 2.2.2), each of which is a separate solution to the Maxwell equations.

4.2 The cavity gauge field and its quantization

With the classical theory in mind, we proceed in this chapter to derive an expression for the gauge field inside the rectangular electromagnetic cavity in our model (Fig. 1.3). The electromagnetic cavity translates mathematically to a set of boundary conditions that limits the set of waves that can be supported within its volume. We derive unique solutions for this case. We subsequently quantize the cavity gauge field by identifying (canonically quantizing) Fourier expansion coefficients with bosonic quanta (photons), which enter our model as mediators of the indirect coupling between the FI and the SC.

Our cavity has spatial extensions $L_x, L_y \gg L_z$ in the respective directions, cf. Fig. 1.3. We employ perfectly reflective boundary conditions for the upper and lower cavity walls, and periodic boundary conditions for the remaining walls, as is done in Ref. [11]. The reflective boundary conditions in the z direction resolve the spatial dependence of the cavity field strength in this direction, while we ignore this dependence in the x and y directions (see Ch. 8 for discussion on this). There are multiple ways of implementing these boundary conditions. One common method is to simply directly derive solutions to the Maxwell equations given the boundary conditions on the volume [100]. We will present another derivation, in which we implement the boundary conditions by imposing symmetries on the classical expansion coefficients and Fourier mode functions. This serves to clarify the mathematical origin of some prefactors and momentum ranges.

Consider a rectangular cavity that is twice the size of the cavity we wish to study. The larger cavity has dimensions $L_x \times L_y \times 2L_z$, enclosing a volume $2V$, where $V = L_x L_y L_z$. The cavity represents a bounded region of continuous space. Because it is bounded, the Fourier spectrum is discrete; because the region is spatially continuous, the Fourier spectrum is unbounded. As will be shown, upon imposing symmetries on the Fourier coefficients of the electromagnetic fields, the complex Fourier transform of the $2V$ volume with symmetrical coefficients, can also serve as a description of the actual cavity volume V subject to the desired boundary conditions.

Consider the classical electromagnetic gauge field $\mathbf{A}_{\text{cav}}$ inside the cavity volume. Because there is by assumption no charge imbalance imposed on the cavity (i.e., there is no scalar potential), the electric and magnetic fields are entirely described by $\mathbf{A}_{\text{cav}}$ (cf. Sec. 4.1). Expressed in terms of its Fourier expansion, by the definition

of the complex Fourier transform,

$$\mathbf{A}_{\text{cav}}(\mathbf{r}) \equiv \sum_{\mathbf{Q}S} \sqrt{\frac{\hbar}{2\epsilon\omega_{\mathbf{Q}}(2V)}}\hat{e}_S(a_{\mathbf{Q}S}e^{i\mathbf{Q}\cdot\mathbf{r}} + a^*_{\mathbf{Q}S}e^{-i\mathbf{Q}\cdot\mathbf{r}}). \tag{4.9}$$

Above,

$$\begin{aligned}\mathbf{Q} &\equiv (Q_x, Q_y, Q_z)\\ &\equiv (2\pi\ell_x/L_x, 2\pi\ell_y/L_y, 2\pi\ell_z/2L_z)\\ &= (2\pi\ell_x/L_x, 2\pi\ell_y/L_y, \pi\ell_z/L_z)\end{aligned} \tag{4.10}$$

are the momenta (Fourier parameters) of each Fourier mode $e^{\pm i\mathbf{Q}\cdot\mathbf{r}}$ labeled by $\ell \equiv \{\ell_x, \ell_y, \ell_z\}$, with $\ell_x, \ell_y, \ell_z = 0, \pm1, \pm2, \ldots$. Furthermore, $S = x, y, z$ labels directions and polarizations, ϵ is the permittivity of the material filling the cavity, $\omega_{\mathbf{Q}} = c\sqrt{\mathbf{Q}^2}$ is the cavity dispersion relation (Eq. (4.8)), $\hat{e}_S$ is the unit vector in the S direction, and $a_{\mathbf{Q}S}$ are classical Fourier expansion coefficients for modes with linear polarization S and carrying momentum $\mathbf{Q}$. We have extracted the prefactor $\sqrt{\hbar/2\epsilon\omega_{\mathbf{Q}}}$ from the expansion coefficients for later convenience, since it renders one-to-one the correspondence between the expansion coefficients and photon operators of the quantized field, to be introduced later. Furthermore, the remaining prefactor $\sqrt{1/(2V)}$ is a normalization factor, which we have chosen such that the Fourier transform (and by extension its inverse) is unitary, cf. Eq. (2.30).

Now, we implement boundary conditions by imposing symmetries. Consider first the x and y directions, in which opposing walls are separated by lengths L_x and L_y, respectively. We only seek to resolve the effects of a finite separation of the walls on the Fourier modes; to this end, periodic boundary conditions are appropriate. These conditions amount to imposing the following periodicities on the Fourier modes:

$$e^{\pm i\mathbf{Q}\cdot(\mathbf{r}+L_x\hat{e}_x)} = e^{\pm i\mathbf{Q}\cdot(\mathbf{r}+L_y\hat{e}_y)} = e^{\pm i\mathbf{Q}\cdot\mathbf{r}}. \tag{4.11}$$

This symmetry implies that Q_x and Q_y are discretized as $2\pi\ell_x/L_x$ and $2\pi\ell_y/L_y$, and is in fact already a symmetry of the complex Fourier transform. Periodic boundary conditions can be visualized as connecting the edges of a domain, which in our case would amount to treating the rectangular cavity as a torus.

Consider now the z direction, for which we assume reflective boundary conditions. To this end, we seek to reduce the complex Fourier transforms in this direction to real sine or cosine transforms. In principle, both transforms project functions onto a complete basis on the open interval $z \in (0, L_z)$ between the walls, but the behavior we seek at the boundary will determine the appropriate choice of transform. Sine transforms are appropriate for clamped end points, like those of vibrating strings attached to walls; cosine transforms are appropriate for unclamped end points, like those of pressure oscillations of sound waves at the inner

walls of closed resonators. Below, we determine the appropriate behavior by physical considerations.[3]

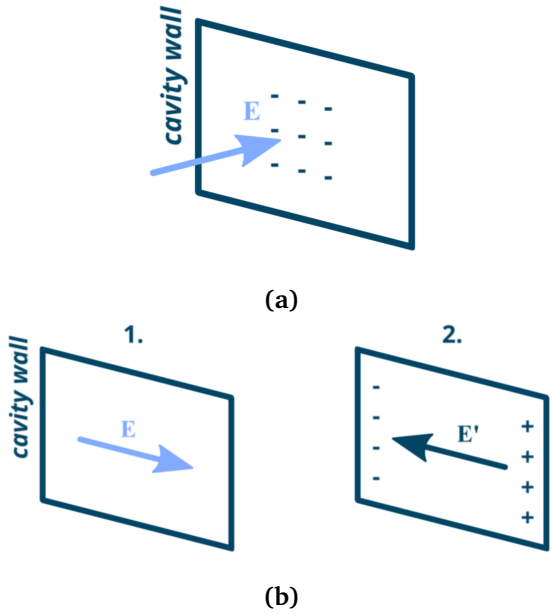

Figure 4.1: Illustration of the reflective boundary conditions at a cavity wall, for the dynamic electric field (**E**). In (a), the perpendicular electric field is complemented by local charge accumulation of at the inner face of wall. This is in turn complemented by a local charge accumulation of opposite polarity at the outer face (not illustrated), which leads to extinguishing of the internal electric field, while leaving the external field unaffected. In (b), the initial tangential electric field causes charges to migrate to each end of the wall and accumulate, spawning an opposite electric field $\mathbf{E}'$. The net tangential electric field at the wall is then zero. In a perfect conductor, the sequence in (b) happens instantaneously in response to initial fields, so there is never a tangential electric field at the wall, leaving no accumulation of charges at the ends.

In the last section, we established that in the transversal gauge, the spatial oscillations of the electric and magnetic fields are proportional to those of the vector potential. We can therefore deduce the behavior of the vector potential on the upper and lower boundaries by instead considering the electric and magnetic fields [102]:

- For the electric field, at the perfectly reflective inner walls of the cavity, tangential components of the field are extinguished by the free movement of charges at the walls (Fig. 4.1b). The tangential components of the field

[3]The technical, textbook approach to boundary conditions is to integrate the Maxwell equations over a volume (area) Ω crossing the boundary, followed by the application of Gauss' (Stokes') theorem to re-express some integrals as going over the surface (line) $\partial\Omega$. Then one shrinks Ω near the boundary in such a way that the volume (area) goes to zero, while the surface (line) $\partial\Omega$ remains finite, from which conditions on normal (tangential) field components are extracted [99, 101].

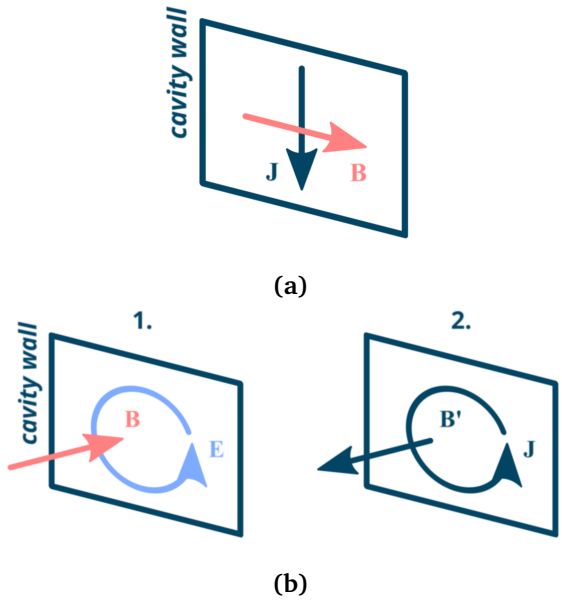

Figure 4.2: Illustration of the reflective boundary conditions at a cavity wall, for the dynamic magnetic field (**B**). In (a), the tangential magnetic field is complemented by sheet current density **J** at the inner face of the wall (this continues into adjacent walls (not illustrated), so there is no accumulation of charges on this face). The subsequent magnetic field of **J** spawns an oppositely directed sheet current at the outer face of the wall (not illustrated), whose field in turn leads to the cancellation of internal magnetic fields in the cavity wall, leaving the external tangential field untouched. In (b), the initial perpendicular magnetic field spawns a circulating electric field (**E**), which at the wall gives rise to a sheet current vortex. This vortex spawns an opposite magnetic field $\mathbf{B}'$, which cancels the net perpendicular magnetic field at the wall. In a perfect conductor, the sequence in (b) happens instantaneously in response to initial fields, so there is never a perpendicular magnetic field at the wall.

therefore have clamped end points, i.e. they cannot oscillate spatially. By contrast, the normal component of the field is complemented by charge accumulation of opposite polarity at the inner face of the wall (Fig. 4.1a), which in turn is complemented by an accumulation of positive charges at the opposite face of the wall. This extinguishes the net electric field *inside* the conducting wall, while leaving the outside unaffected, and furthermore preserves charge neutrality. The normal component therefore has unclamped end points.

- While the above considerations suffice to deduce the proper transformation of the vector potential, we repeat the exercise by considering the magnetic field. At the reflective boundaries, the normal component of the magnetic field will induce sheet current vortices that spawn an equal and oppositely directed magnetic field (Fig. 4.2b). The net result is that the normal component of the magnetic field is extinguished at the boundary. This corres-

ponds to clamped end points. By contrast, the tangential components of the magnetic field are complemented by perpendicular sheet currents at the inner face of the wall (Fig. 4.2a). These currents spawn their own magnetic fields that give rise to oppositely directed sheet currents at the outer face, spawning yet more magnetic fields of opposite polarity. The net effect is that internal magnetic fields are extinguished, while the tangential fields at the boundary are unaffected. This corresponds to unclamped end points.

Note that the behavior at the cavity walls outlined above is only approximate, as perfectly reflective boundary conditions are only ideal. We have neglected the influence of e.g. cavity losses, which give rise to some transmission.

Now, write $a_{\mathbf{Q}S}$ as $a_{\ell_x\ell_y\ell_z S}$. The appropriate sine and cosine transforms are implemented by imposing the following odd and even symmetries on the expansion coefficients:

$$a_{\ell_x\ell_y-\ell_z x} = -a_{\ell_x\ell_y\ell_z x}, \tag{4.12}$$

$$a_{\ell_x\ell_y-\ell_z y} = -a_{\ell_x\ell_y\ell_z y}, \tag{4.13}$$

$$a_{\ell_x\ell_y-\ell_z z} = a_{\ell_x\ell_y\ell_z z}. \tag{4.14}$$

Since $\omega_{\mathbf{Q}} = \omega_{|\mathbf{Q}|}$, the prefactor of the summand of Eq. (4.9) is unaffected by flipping the sign of ℓ_z. With the symmetries presented above, we find that we can order the terms of the sum in Eq. (4.9) with respect to $\ell_z \neq 0$ such that

$$\begin{aligned}
&a_{\ell_x\ell_y\ell_z x} e^{i\mathbf{Q}(\ell_x\ell_y\ell_z)\cdot\mathbf{r}} + a_{\ell_x\ell_y-\ell_z x} e^{i\mathbf{Q}(\ell_x\ell_y-\ell_z)\cdot\mathbf{r}} \\
&= a_{\ell_x\ell_y\ell_z x}\left(e^{i\mathbf{Q}(\ell_x\ell_y\ell_z)\cdot\mathbf{r}} - e^{i\mathbf{Q}(\ell_x\ell_y-\ell_z)\cdot\mathbf{r}}\right) \\
&= 2ia_{\ell_x\ell_y\ell_z x} e^{i(Q_x x+Q_y y)} \sin Q_z z,
\end{aligned} \tag{4.15}$$

$$\begin{aligned}
&a_{\ell_x\ell_y\ell_z y} e^{i\mathbf{Q}(\ell_x\ell_y\ell_z)\cdot\mathbf{r}} + a_{\ell_x\ell_y-\ell_z y} e^{i\mathbf{Q}(\ell_x\ell_y-\ell_z)\cdot\mathbf{r}} \\
&= a_{\ell_x\ell_y\ell_z y}\left(e^{i\mathbf{Q}(\ell_x\ell_y\ell_z)\cdot\mathbf{r}} - e^{i\mathbf{Q}(\ell_x\ell_y-\ell_z)\cdot\mathbf{r}}\right) \\
&= 2ia_{\ell_x\ell_y\ell_z y} e^{i(Q_x x+Q_y y)} \sin Q_z z,
\end{aligned} \tag{4.16}$$

$$\begin{aligned}
&a_{\ell_x\ell_y\ell_z z} e^{i\mathbf{Q}(\ell_x\ell_y\ell_z)\cdot\mathbf{r}} + a_{\ell_x\ell_y-\ell_z z} e^{i\mathbf{Q}(\ell_x\ell_y-\ell_z)\cdot\mathbf{r}} \\
&= a_{\ell_x\ell_y\ell_z z}\left(e^{i\mathbf{Q}(\ell_x\ell_y\ell_z)\cdot\mathbf{r}} + e^{i\mathbf{Q}(\ell_x\ell_y-\ell_z)\cdot\mathbf{r}}\right) \\
&= 2a_{\ell_x\ell_y\ell_z z} e^{i(Q_x x+Q_y y)} \cos Q_z z.
\end{aligned} \tag{4.17}$$

We have here gathered one term per opposite half momentum space, and subsequently reduced the range for our sum over $\mathbf{Q}$ to the $Q_z \geq 0$ half-space. In real space this corresponds to reducing the supposed volume $2V = L_x L_y 2L_z$ to the actual volume $V = L_x L_y L_z$; in other words, mathematically, only the volume V needs to enter the inverse Fourier transform in order to recover the original vector potential from its Fourier transform. Note that the Fourier transform can now serve as a description of *either* the supposed $2V$ volume subject to the above

even and odd symmetries, *or* the actual volume V subject to reflective boundary conditions in the z direction.

The terms for which $\ell_z = 0$ (corresponding to the $Q_x Q_y$ plane in momentum space) must be handled separately in order to avoid double counting: with $\ell_z = 0$, we find $e^{i\mathbf{Q}(\ell_x \ell_y \ell_z)\cdot\mathbf{r}} = e^{i\mathbf{Q}(\ell_x \ell_y - \ell_z)\cdot\mathbf{r}} = e^{i\mathbf{Q}(\ell_x \ell_y 0)\cdot\mathbf{r}}$, because 0 is its own negative. In other words, there is no complementary term in the sum in Eq. (4.9) with which the $a_{\ell_x \ell_y 0 S}$ terms can be paired in the same manner as in Eqs. (4.15)–(4.17). We take this into account by introducing the following prefactor to the expressions (4.15)–(4.17):

$$w_{\ell_z} = \begin{cases} \frac{1}{2}, & \ell_z = 0, \\ 1 & \text{otherwise.} \end{cases} \tag{4.18}$$

This prefactor only affects Eq. (4.17), since the other Fourier terms are modulated as sine functions with respect to Q_z, and are thus anyhow zero for $\ell_z = 0$. Now, naively, it is tempting to add this prefactor alone to the expressions (4.15)–(4.17); however, this would render the Fourier transform non-unitary. Collapsing the supposed volume $2V$ to V introduces an analogous prefactor to the inverse transform,

$$w_z = \begin{cases} \frac{1}{2}, & z = 0, \\ 1 & \text{otherwise.} \end{cases} \tag{4.19}$$

Requiring that the Fourier transform be unitary amounts to dividing the net prefactor $w_{\ell_z} w_z = \sqrt{w_{\ell_z} w_z}\sqrt{w_{\ell_z} w_z}$ equally between the Fourier transform and its inverse, as was done previously with the volume factor $1/V$ (Eq. (4.9)), and with the number factor $1/N_{\mathrm{FI}}$ for the magnons (Eq. (2.30)).

Implementing the symmetries above, we can thus write

$$\begin{aligned} \mathbf{A}_{\mathrm{cav}} &= \sum_{\ell_x=-\infty}^{\infty} \sum_{\ell_y=-\infty}^{\infty} \sum_{\ell_z=0}^{\infty} \sum_{S=x,y,z} \sqrt{\frac{\hbar}{2\epsilon\omega_\ell}} \hat{e}_S (a_{\ell S} u_{\ell S} + a^*_{\ell S} u^*_{\ell S}) \\ &= \sum_{\ell S} \sqrt{\frac{\hbar}{2\epsilon\omega_\ell}} \hat{e}_S (a_{\ell S} u_{\ell S} + a^*_{\ell S} u^*_{\ell S}) \\ &= \sum_{\mathbf{Q}S} \sqrt{\frac{\hbar}{2\epsilon\omega_{\mathbf{Q}}}} \hat{e}_S (a_{\mathbf{Q}S} u_{\mathbf{Q}S} + a^*_{\mathbf{Q}S} u^*_{\mathbf{Q}S}), \end{aligned} \tag{4.20}$$

where now $\ell_x, \ell_y = 0, \pm 1, \pm 2, \ldots$ and $\ell_z = 0, 1, 2, \ldots$ (note that by contrast, in Eq. (4.9), the range for ℓ_z was $-\infty, \ldots, \infty$). Furthermore, we have defined the normalized mode functions

$$u_{\mathbf{Q}x} = u_{\mathbf{Q}y} = \sqrt{\frac{2}{V}} e^{iQ_x x + iQ_y y} i \sin Q_z z, \quad u_{\mathbf{Q}z} = \sqrt{w_{\ell_z} w_z}\sqrt{\frac{2}{V}} e^{iQ_x x + iQ_y y} \cos Q_z z. \tag{4.21}$$

Note that our derivation of the quantized vector potential with reflective boundary conditions highlights why the prefactor of the mode functions Eq. (4.21) involves the factor $\sqrt{2/V} = 2\sqrt{1/(2V)}$ instead of the prefactor $\sqrt{1/V}$ which one

normally expects from the unitary complex Fourier transform. I.e., it originates from assuming certain reflective symmetries on the Fourier transform of a doubled volume. It also highlights why the range of the momentum sum in Eq. (4.20) is restricted to the $Q_z \geq 0$ half-space, and why there is a special prefactor $\sqrt{w_{\ell_z} w_z}$ in the mode functions (4.21) which divides $\ell_z = 0$ terms by $\sqrt{2}$ and $z = 0$ terms by another $\sqrt{2}$.

4.3 Transversal (Coulomb) gauge

Before we perform the canonical quantization, we must fix the gauge. We seek to implement transversality

$$\mathbf{Q} \cdot \mathbf{A}_{\text{cav}} = 0 \tag{4.22}$$

directly into our expression for $\mathbf{A}_{\text{cav}}$, in order to avoid linear dependence between photon operators which follow from Gauss' law in the absence of charges,

$$\nabla \cdot \partial_t \mathbf{A}_{\text{cav}} = 0 \quad \Rightarrow \quad \mathbf{Q} \cdot \sum_S a_{\mathbf{Q}S} \hat{e}_S = \mathbf{Q} \cdot \sum_S a^*_{\mathbf{Q}S} \hat{e}_S = 0, \tag{4.23}$$

cf. Ref. [100, Eq. (2.13)]. The linear dependencies would otherwise lead to non-conventional commutator relations after canonical quantization. Our strategy for achieving this will be to first rotate the original xyz basis to a new Cartesian basis labeled by $1, 2, 3$; the original z axis is now aligned with the photon momentum $\mathbf{Q}$ and becomes the 3 axis (cf. Fig. 4.3). Then Eq. (4.22) is immediately satisfied by neglecting the classical expansion coefficient $a_{\mathbf{Q}3}$, found by an identical rotation of the original coefficients.

In terms of spherical parameters $\{Q, \theta, \varphi\}$, where $Q \equiv |\mathbf{Q}|$, $\theta \equiv \theta_{\mathbf{Q}}$ is the polar angle and $\varphi \equiv \varphi_{\mathbf{Q}}$ is the azimuthal angle (cf. Fig. 4.3), $\mathbf{Q}$ becomes

$$\mathbf{Q} = Q \begin{pmatrix} \sin\theta \cos\varphi \\ \sin\theta \sin\varphi \\ \cos\theta \end{pmatrix} \tag{4.24}$$

in the original xyz basis. Note that the angles carry a dependency on $\mathbf{Q}$, because they are defined with respect to this vector. Following Ref. [100], we introduce the rotated basis

$$\begin{pmatrix} \hat{e}^{\mathbf{Q}}_1 \\ \hat{e}^{\mathbf{Q}}_2 \\ \hat{e}^{\mathbf{Q}}_3 \end{pmatrix} = O^{\mathbf{Q}} \begin{pmatrix} \hat{e}_x \\ \hat{e}_y \\ \hat{e}_z \end{pmatrix}, \quad O^{\mathbf{Q}} \equiv \begin{pmatrix} \cos\theta\cos\varphi & \cos\theta\sin\varphi & -\sin\theta \\ -\sin\varphi & \cos\varphi & 0 \\ \sin\theta\cos\varphi & \sin\theta\sin\varphi & \cos\theta \end{pmatrix}. \tag{4.25}$$

Thus $\hat{e}^{\mathbf{Q}}_3 = \mathbf{Q}/Q$ by comparison with Eq. (4.24). Equivalently,

$$\hat{e}^{\mathbf{Q}}_\Sigma = \sum_S O^{\mathbf{Q}}_{\Sigma S} \hat{e}_S, \tag{4.26}$$

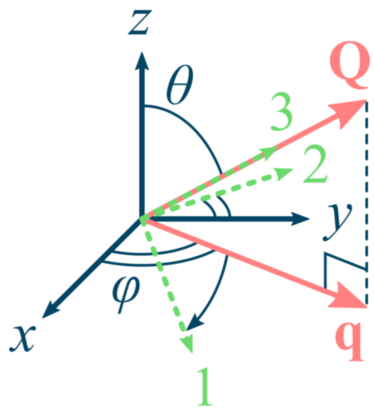

Figure 4.3: Illustration of the 123 coordinate system, reproduced from Paper II. **Q** is a specific photon momentum vector, and **q** is its component in the xy plane. θ (single arch) is the polar, and φ (double arch) the azimuthal angle associated with **Q** in relation to the xyz basis. The 123 axes follows from rotating the xyz axes by an angle θ about the y axis, followed by rotating by an angle φ about the original z axis. In the drawing, the 1 axis points somewhat outwards, the 2 axis points somewhat inwards and is confined to the original xy plane, and the 3 axis aligns with **Q**.

where $\Sigma = 1, 2, 3$. Furthermore, the rotation matrix is orthogonal (i.e., it preserves vector dot products),

$$O^{\mathbf{Q}T} O^{\mathbf{Q}} = I, \tag{4.27}$$

where T denotes the matrix transpose, and $I \equiv I_3$ is the 3×3 identity matrix. Since the original set of basis vectors is orthonormal, the orthogonality of $O^{\mathbf{Q}}$ implies that the new basis is also orthonormal. Furthermore, along with Eq. (4.26), Eq. (4.27) implies the inverted relationship

$$\begin{aligned}
\hat{e}_S &= \sum_\Sigma O^{\mathbf{Q}}_{\Sigma S} \hat{e}^{\mathbf{Q}}_\Sigma = \sum_\Sigma O^{\mathbf{Q}}_{\Sigma S} \sum_{S'} O^{\mathbf{Q}}_{\Sigma S'} \hat{e}_{S'} \\
&= \sum_{S'} \hat{e}_{S'} \left(\sum_\Sigma (O^{\mathbf{Q}T})_{S\Sigma} O^{\mathbf{Q}}_{\Sigma S'} \right) = \sum_{S'} \hat{e}_{S'} \left(O^{\mathbf{Q}T} O^{\mathbf{Q}} \right)_{SS'} \\
&= \sum_{S'} \hat{e}_{S'} \delta_{SS'} = \hat{e}_S,
\end{aligned} \tag{4.28}$$

where $\delta_{SS'}$ is the Kronecker delta function.

Returning to the linear dependency (4.23), we find, using Eq. (4.28), that

$$\begin{aligned}\mathbf{Q}\cdot\sum_S a_{\mathbf{Q}S}\hat{e}_S &= \mathbf{Q}\cdot\sum_S a_{\mathbf{Q}S}\sum_\Sigma O^{\mathbf{Q}}_{\Sigma S}\hat{e}^{\mathbf{Q}}_\Sigma \\ &= \mathbf{Q}\cdot\sum_\Sigma\left(\sum_S O^{\mathbf{Q}}_{\Sigma S}a_{\mathbf{Q}S}\right)\hat{e}^{\mathbf{Q}}_\Sigma \\ &= \mathbf{Q}\cdot\sum_\Sigma a_{\mathbf{Q}\Sigma}\hat{e}^{\mathbf{Q}}_\Sigma \\ &= 0,\end{aligned} \tag{4.29}$$

and likewise for the complex conjugate equation. In the last line, we defined the expansion coefficients in the rotated basis

$$a_{\mathbf{Q}\Sigma} \equiv \sum_S O^{\mathbf{Q}}_{\Sigma S}a_{\mathbf{Q}S}. \tag{4.30}$$

Since $\hat{e}^{\mathbf{Q}}_3$ by definition is parallel to $\mathbf{Q}$, the transversality condition (4.29) reduces to

$$a_{\mathbf{Q}3} = a^*_{\mathbf{Q}3} = 0. \tag{4.31}$$

The relationship of $a_{\mathbf{Q}S}$ to $a_{\mathbf{Q}\Sigma}$ is analogous to the inverse relation in Eq. (4.28), i.e.

$$a_{\mathbf{Q}S} = \sum_\Sigma O^{\mathbf{Q}}_{\Sigma S}a_{\mathbf{Q}\Sigma}. \tag{4.32}$$

Implementing transversality by neglecting $a_{\mathbf{Q}3}$, this reduces to

$$a_{\mathbf{Q}S} = \sum_\varsigma O^{\mathbf{Q}}_{\varsigma S}a_{\mathbf{Q}\varsigma}, \tag{4.33}$$

with $\varsigma = 1,2$. Inserting this into the gauge field (4.20), one finds the gauged expression for $\mathbf{A}_{\text{cav}}$

$$\begin{aligned}\mathbf{A}_{\text{cav}} &= \sum_{\mathbf{Q}S}\sqrt{\frac{\hbar}{2\epsilon\omega_{\mathbf{Q}}}}\hat{e}_S\sum_\varsigma(O^{\mathbf{Q}}_{\varsigma S}a_{\mathbf{Q}\varsigma}u_{\mathbf{Q}S} + O^{\mathbf{Q}}_{\varsigma S}a^*_{\mathbf{Q}\varsigma}u^*_{\mathbf{Q}S}) \\ &= \sum_{\mathbf{Q}\varsigma}\sqrt{\frac{\hbar}{2\epsilon\omega_{\mathbf{Q}}}}(a_{\mathbf{Q}\varsigma}\overline{\mathbf{u}}_{\mathbf{Q}\varsigma} + a^*_{\mathbf{Q}\varsigma}\overline{\mathbf{u}}^*_{\mathbf{Q}\varsigma}),\end{aligned} \tag{4.34}$$

where we defined the new mode functions

$$\overline{\mathbf{u}}_{\mathbf{Q}\varsigma} \equiv \sum_S \hat{e}_S O^{\mathbf{Q}}_{\varsigma S}u_{\mathbf{Q}S}, \tag{4.35}$$

in accordance with Ref. [100]. Thus we have obtained a gauged expression for $\mathbf{A}_{\text{cav}}$, and may safely proceed to canonically quantize the field (hence $*$ becomes †

for the Fourier coefficients) with bosonic commutation relations for $a_{\mathbf{Q}1}$, $a_{\mathbf{Q}2}$ and their Hermitian conjugates:

$$\mathbf{A}_{\text{cav}} = \sum_{\mathbf{Q}\varsigma} \sqrt{\frac{\hbar}{2\epsilon\omega_{\mathbf{Q}}}} (a_{\mathbf{Q}\varsigma}\overline{\mathbf{u}}_{\mathbf{Q}\varsigma} + a^{\dagger}_{\mathbf{Q}\varsigma}\overline{\mathbf{u}}^{*}_{\mathbf{Q}\varsigma}), \tag{4.36}$$

$$[a_{\mathbf{Q}\varsigma}, a_{\mathbf{Q}'\varsigma'}] = 0, \quad [a_{\mathbf{Q}\varsigma}, a^{\dagger}_{\mathbf{Q}'\varsigma'}] = \delta_{\mathbf{Q}\mathbf{Q}'}\delta_{\varsigma\varsigma'}. \tag{4.37}$$

This concludes the introductory part on electromagnetic cavities. In the next chapter, we specialize the general expression (4.36) for the vector potential to suit our set-up.

Key takeaways:

- By the ideally free movement of charges on its walls, electromagnetic cavities suppress all but a discrete subset of standing electromagnetic waves (normal modes) within its enclosed volume. Losses lead to some transmission and broadening of spectra.
- In contrast to free-space waves, these modes have an amplitude that persists over relatively long distances, and scale inversely with the enclosed volume. Electric and magnetic oscillations are furthermore spatially separated. These features are used in our model to couple the FI and the SC over unconventionally large distances, respectively via the magnetic and electric components of the cavity modes.
- The classical cavity gauge field (vector potential) $\mathbf{A}_{\text{cav}}$ is quantized by identifying Fourier expansion coefficients ($a_{\mathbf{q}\varsigma}$, $a^{*}_{\mathbf{q}\varsigma}$) with photon operators ($a_{\mathbf{q}\varsigma}$, $a^{\dagger}_{\mathbf{q}\varsigma}$), known as canonical quantization.

Chapter 5

Cavity couplings

Chapter summary: We derive expressions for the cavity interactions under consideration, in the various particle bases. Between the FI and the cavity, we consider the Zeeman coupling; between the cavity and the SC, the paramagnetic coupling. We subsequently write down the complete FI and SC Hamiltonians for our system.

So far, we have analysed the FI, cavity and SC without regards to any interactions between these. In this chapter, we provide detailed derivations of the couplings of choice, in the respective particle bases (magnons, photons and Bogoliubov quasiparticles) introduced in the last chapter.

For the FI placed at a maximum of magnetic field strength of the cavity modes, the natural coupling to consider is the Zeeman coupling. The Zeeman coupling was outlined already in the last chapter (Eq. (2.8)), but then with the spins subjected to a classical uniform field. In this chapter, we consider their subjection to the quantized cavity modes. Because the xy dimensions of the FI and the cavity generally differ in the set-up in Fig. 1.3, with the FI the smallest, a single magnon mode with momentum $\mathbf{k}$ can couple to photons with a range of in-plane momenta $\mathbf{q}$, as will be shown in Sec. 5.1.

For the SC placed at the electric field strength maximum, we consider the paramagnetic coupling, the $-e\hbar\mathbf{p}\cdot\mathbf{A}$ term originating from the minimal coupling Hamiltonian $(\hbar\mathbf{p}-e\mathbf{A})^2/2m$, with e and m the electron charge and mass. This coupling was also considered in Ref. [11] for a normal metal coupling to itself via a cavity. We neglect the diamagnetic term $(e\mathbf{A})^2/2m$ as it was found to be negligible in Ref. [11] (cf. their Supplemental Material).

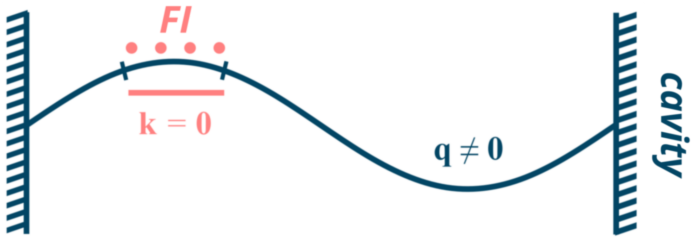

Figure 5.1: Illustration of modes interacting without conservation of (in-plane) momentum. The cavity is represented by the left and right walls, and the FI by the red dots. The FI is much smaller than the cavity. The spatial oscillation of the $\mathbf{q} \neq \mathbf{0}$ cavity mode (solid black line) appears almost uniform locally across the FI, nearly corresponding to the (non)oscillation of the $\mathbf{k} = \mathbf{0}$ magnon mode (solid red line). If the FI and cavity couple, the local near-correspondence of these particular modes cause them to interact, despite the unequal momenta $\mathbf{q} \neq \mathbf{k}$. Note that owing to the periodic boundary conditions, the waves are modulated in-plane as complex exponentials in our model, not sinusoidals as illustrated.

5.1 FI–cavity Zeeman coupling

We start with the interaction coupling the FI to the cavity, recasting it in the bases of magnons and photons. This Zeeman coupling is given by

$$\mathcal{H}_{\text{FI}-\text{cav}} \equiv -\frac{g\mu_B}{\hbar} \sum_i \mathbf{S}_i \cdot \mathbf{B}_{\text{cav}}(\mathbf{r}_i). \tag{5.1}$$

As before, g is the g-factor, which we take to be 2; and μ_B is the Bohr magneton. The FI lattice sites are indexed by i with the corresponding position $\mathbf{r}_i$, and $\mathbf{S}_i$ and $\mathbf{B}_{\text{cav}}(\mathbf{r}_i)$ are the spin and cavity magnetic field at these sites.

We begin by deriving the expression for $\mathbf{B}_{\text{cav}}(\mathbf{r}_i)$ based on the general expression for the vector potential from the last chapter. Specializing to the set-up in Fig. 1.3, we set $\ell_z = 1$. The FI is positioned at $z \approx L_z$, where $u_{\mathbf{Q}x} = u_{\mathbf{Q}y} = 0$ by Eq. (4.21). We introduce the momenta $\mathbf{q}$ restricted to the xy plane, which relate to $\mathbf{Q}$ as

$$\mathbf{Q} \equiv \mathbf{q} + \pi \hat{e}_z / L_z, \tag{5.2}$$

cf. Eq. (4.10) and Fig. 4.3. Then

$$\overline{\mathbf{u}}_{\mathbf{Q}\varsigma} \equiv \hat{e}_z O^{\mathbf{Q}}_{\varsigma z} u_{\mathbf{Q}z}, \quad u_{\mathbf{q}z}(\mathbf{r}) \equiv -\sqrt{\frac{2}{V}} e^{i\mathbf{q}\cdot\mathbf{r}}, \tag{5.3}$$

where $\mathbf{r} = (x, y, z)^T$. Then the expression (4.36) for $\mathbf{A}_{\text{cav}}$ across the FI can be

written as

$$\begin{aligned}\mathbf{A}_{\text{cav}}\big|_{\text{FM}} &= -\sum_{\mathbf{q}\varsigma}\sqrt{\frac{\hbar}{\epsilon\omega_{\mathbf{q}}V}}\hat{e}_z(a_{\mathbf{q}\varsigma}O^{\mathbf{q}}_{\varsigma z}e^{i\mathbf{q}\cdot\mathbf{r}} + a^{\dagger}_{\mathbf{q}\varsigma}O^{\mathbf{q}}_{\varsigma z}e^{-i\mathbf{q}\cdot\mathbf{r}}) \\ &= -\sum_{\mathbf{q}\varsigma}\sqrt{\frac{\hbar}{\epsilon\omega_{\mathbf{q}}V}}\hat{e}_z O^{\mathbf{q}}_{\varsigma z}e^{i\mathbf{q}\cdot\mathbf{r}}(a_{\mathbf{q}\varsigma} + a^{\dagger}_{-\mathbf{q}\varsigma}) \\ &= \sum_{\mathbf{q}}\sqrt{\frac{\hbar}{\epsilon\omega_{\mathbf{q}}V}}\hat{e}_z\sin\theta_{\mathbf{q}}e^{i\mathbf{q}\cdot\mathbf{r}}(a_{\mathbf{q}1} + a^{\dagger}_{-\mathbf{q}1}),\end{aligned} \tag{5.4}$$

where

$$\omega_{\mathbf{q}} \equiv \omega_{\mathbf{Q}}\big|_{\mathbf{Q}=\mathbf{q}+\pi\hat{e}_z/L_z} = \omega_0\sqrt{1+\left(\frac{c\mathbf{q}}{\omega_0}\right)^2}, \quad \omega_0 \equiv \frac{c\pi}{L_z}, \tag{5.5}$$

$$a_{\mathbf{q}\varsigma} \equiv a_{\mathbf{Q}\varsigma}\big|_{\mathbf{Q}=\mathbf{q}+\pi\hat{e}_z/L_z}, \tag{5.6}$$

$$O^{\mathbf{q}}_{\varsigma S} \equiv O^{\mathbf{Q}}_{\varsigma S}\big|_{\mathbf{Q}=\mathbf{q}+\pi\hat{e}_z/L_z}. \tag{5.7}$$

In writing down the expression Eq. (5.4), we performed the substitution $\mathbf{q}\to-\mathbf{q}$ (i.e. $\varphi\to\varphi+\pi$, $\theta\to\theta$ in spherical coordinates) in the terms involving photon creation operators, and used

$$O^{-\mathbf{q}}_{\varsigma z} = O^{\mathbf{q}}_{\varsigma z}, \tag{5.8}$$

which holds for the relevant $1z$ and $2z$ entries of $O^{\mathbf{Q}}$, as defined in Eq. (4.25). In the final equality of Eq. (5.4), we used that the $2z$ entry of $O^{\mathbf{Q}}$ (cf. Eq. (4.25)) is 0 to reduce the sum over ς. This 0 entry results from the confinement of the 2 axis to the xy plane by its definition, cf. Fig. 4.3. Therefore only 1 components generally carry a finite z component and thus contribute to the sum, since $\mathbf{A}_{\text{cav}}$ points purely in the z direction for $z\approx L_z$.

In order to prevent clutter, we have introduced the following notation: Wherever $\mathbf{q}$ enters expressions as an *index* (i.e., not explicitly, as in $e^{i\mathbf{q}\cdot\mathbf{r}}$), it is to be understood as $\mathbf{q}+\pi\hat{e}_z/L_z$. For instance, $a_{\mathbf{q}\varsigma}$ has been defined as the annihilation operator for a photon of polarization ς and momentum $\mathbf{q}+\pi\hat{e}_z/L_z$, *not* $\mathbf{q}$.

Thus, $\mathbf{B}_{\text{cav}}(\mathbf{r})\big|_{\text{FI}}$ across the FM becomes

$$\begin{aligned}\mathbf{B}_{\text{cav}}(\mathbf{r})\big|_{\text{FI}} &= \nabla\times\mathbf{A}_{\text{cav}}(\mathbf{r})\big|_{\text{FI}} \\ &= \sum_{\mathbf{q}}\sqrt{\frac{\hbar}{\epsilon\omega_{\mathbf{q}}V}}i\left(q_y\hat{e}_x - q_x\hat{e}_y\right)\sin\theta_{\mathbf{q}}e^{i\mathbf{q}\cdot\mathbf{r}}(a_{\mathbf{q}1} + a^{\dagger}_{-\mathbf{q}1}).\end{aligned} \tag{5.9a}$$

For the calculations based on the set-up in Fig. 1.3, we will use the compacted expression

$$\mathbf{B}_{\text{cav}}(\mathbf{r}_i)\big|_{\text{FI}} = \sum_{\mathbf{q}d} i\nu_d^2 q_{\bar{d}}\hat{e}_d\sin\theta_{\mathbf{q}}\sqrt{\frac{\hbar}{\epsilon\omega_{\mathbf{q}}V}}e^{i\mathbf{q}\cdot\mathbf{r}_i}(a_{\mathbf{q}1} + a^{\dagger}_{-\mathbf{q}1}). \tag{5.9b}$$

Above, $\bar{d}$ "inverts" d such that $\bar{x} = y$ and $\bar{y} = x$, and $\{\nu_x, \nu_y\} = \{1, -i\}$ as before. Note that $q_{\bar{d}}$ enters the sum with an inverted lower index.

We can now derive an expression $\mathcal{H}_{\text{FI}-\text{cav}}$ in terms of the magnon and photon bases. Inserting Eqs. (2.27), (2.28) and (5.9b) into Eq. (5.1), one finds

$$\begin{aligned}
\mathcal{H}_{\text{FI}-\text{cav}} \approx & -\frac{g\mu_B}{\hbar}\sum_i\Bigg[\frac{1}{\sqrt{N_{\text{FI}}}}\sum_{\mathbf{k}}\sum_{d=x,y}\frac{\hbar\sqrt{2S}}{2}(\nu_d\eta_{\mathbf{k}}e^{i\mathbf{k}\cdot(\mathbf{r}_i-\mathbf{r}_0^{\text{FI}})}+\nu_d^*\eta_{\mathbf{k}}^\dagger e^{-i\mathbf{k}\cdot(\mathbf{r}_i-\mathbf{r}_0^{\text{FI}})})\hat{\boldsymbol{e}}_d \\
& +\hbar S\Bigg(1-\frac{1}{N_{\text{FI}}}\sum_{\mathbf{k}\mathbf{k}'}\frac{\eta_{\mathbf{k}}^\dagger\eta_{\mathbf{k}'}}{S}e^{i(\mathbf{k}'-\mathbf{k})\cdot(\mathbf{r}_i-\mathbf{r}_0^{\text{FI}})}\Bigg)\hat{\boldsymbol{e}}_z\Bigg] \\
& \cdot\Bigg[\sum_{\mathbf{q}}\sum_{d'=x,y}i\nu_{d'}^2 q_{\bar{d}'}\hat{\boldsymbol{e}}_{d'}\sin\theta_{\mathbf{q}}\sqrt{\frac{\hbar}{\epsilon\omega_{\mathbf{q}}V}}e^{i\mathbf{q}\cdot\mathbf{r}_i}(a_{\mathbf{q}1}+a_{-\mathbf{q}1}^\dagger)\Bigg]. \\
= & -\frac{g\mu_B}{\hbar}\sum_{\mathbf{k}\mathbf{q}d}\frac{\hbar\sqrt{2S}}{2}\nu_d^2 i\sqrt{\frac{\hbar}{\epsilon\omega_{\mathbf{q}}V}}\sin\theta_{\mathbf{q}}q_{\bar{d}}\frac{1}{\sqrt{N_{\text{FI}}}} \\
& \cdot e^{i\mathbf{k}\cdot\mathbf{r}_0^{\text{FI}}}\Bigg(\sum_i e^{-i(\mathbf{k}-\mathbf{q})\cdot\mathbf{r}_i}\Bigg)\Big(\nu_d\eta_{-\mathbf{k}}+\nu_d^*\eta_{\mathbf{k}}^\dagger\Big)\Big(a_{\mathbf{q}1}+a_{-\mathbf{q}1}^\dagger\Big),
\end{aligned} \tag{5.10}$$

where the approximate relation in the first line is due to the linearization of the Holstein–Primakoff transformation (Sec. 2.2.2).

As was alluded to in Sec. 2.2.2, we must treat the sum over i carefully. In systems of infinite extent, it normally reduces to a Kronecker (discrete case) or Dirac (continuous case) delta function like Eq. (2.41), implying conservation of momentum; however, in the present set-up (Fig. 1.3), we have assumed the FI and the cavity are finite, and generally do not share dimensions. This gives rise to coupling between modes carrying different momenta, cf. Fig. 5.1. We introduce a new quantity $D_{\mathbf{kq}}^{\text{FI}}$ that captures this: using Eqs. (4.10), (5.2), (2.35) and (2.36), we define it via

$$\begin{aligned}
N_{\text{FI}}D_{\mathbf{kq}}^{\text{FI}} \equiv & e^{i(\mathbf{k}-\mathbf{q})\cdot\mathbf{r}_0^{\text{FI}}}\sum_i e^{-i(\mathbf{k}-\mathbf{q})\cdot\mathbf{r}_i} \\
\approx & \prod_d\sum_{n_d=-N_d/2}^{N_d/2}\exp\Bigg[-i\Bigg(\frac{2\pi m_d n_d}{N_d}-\frac{2\pi\ell_d a_{\text{FI}}n_d}{L_d}\Bigg)\Bigg] \\
\approx & \prod_d\sum_{n_d=1}^{N_d/2}2\cos\Bigg[2\pi\Bigg(\frac{m_d}{N_d}-\frac{\ell_d a_{\text{FI}}}{L_d}\Bigg)n_d\Bigg] \\
= & \prod_d 2\frac{\sin\Big[\frac{\pi N_d}{2}\Big(\frac{m_d}{N_d}-\frac{\ell_d a_{\text{FI}}}{L_d}\Big)\Big]\cos\Big[\frac{\pi N_d}{2}\Big(\frac{m_d}{N_d}-\frac{\ell_d a_{\text{FI}}}{L_d}\Big)\Big]}{\sin\Big[\pi\Big(\frac{m_d}{N_d}-\frac{\ell_d a_{\text{FI}}}{L_d}\Big)\Big]} \\
\approx & N_{\text{FI}}\prod_d\text{sinc}\Bigg[\pi N_d\Bigg(\frac{m_d}{N_d}-\frac{\ell_d a_{\text{FI}}}{L_d}\Bigg)\Bigg] \\
\neq & N_{\text{FI}}\delta_{\mathbf{kq}}.
\end{aligned} \tag{5.11}$$

Above we used that $N_d \gg 1$ to simplify calculations; otherwise we would have had to deal with four separate cases depending on whether N_d are odd or even. Furthermore, the closed form of the sums is a tabulated result [103].

Upon inspection, one finds with the help of L'Hôpital's rule that $D_{\mathbf{kq}}$ reduces to a Kronecker delta function when $L_d = l_d = a_{\mathrm{FI}} N_d$, i.e. when the FI and the cavity share dimensions, but not in general.[1] On the other hand, when the FI becomes infinitely small, $D^{\mathrm{FI}}_{\mathbf{kq}}$ reduces to $\delta_{\mathbf{k0}}$, implying all cavity modes couple exclusively to the uniform magnon mode, which is often assumed in cavity implementations, cf. Paper I and Refs. [10, 14, 15]. Hence

$$\mathcal{H}_{\mathrm{FI-cav}} \approx \sum_{\mathbf{k}d} \sum_{\mathbf{q}\varsigma} g_d^{\mathbf{kq}} (\nu_d \eta_{-\mathbf{k}} + \nu_d^* \eta_{\mathbf{k}}^\dagger)(a_{\mathbf{q}1} + a_{-\mathbf{q}1}^\dagger). \tag{5.12}$$

Above, we defined the coupling strength

$$g_d^{\mathbf{kq}} \equiv -g\mu_B q_{\bar{d}}\, i\nu_d^2 \sin\theta_{\mathbf{q}} \sqrt{\frac{S\hbar N_{\mathrm{FI}}}{2\epsilon\omega_{\mathbf{q}} V}}\, D^{\mathrm{FI}}_{\mathbf{kq}} e^{i\mathbf{q}\cdot\mathbf{r}_0^{\mathrm{FI}}}. \tag{5.13}$$

Combining Eqs. (2.46) and (5.12), the complete FI Hamiltonian for the set-up in Fig. 1.3 is then

$$\mathcal{H}_{\mathrm{FI}} \approx \sum_{\mathbf{k}} \hbar\lambda_{\mathbf{k}} \eta_{\mathbf{k}}^\dagger \eta_{\mathbf{k}} + \sum_{\mathbf{k}d} \sum_{\mathbf{q}} g_d^{\mathbf{kq}} (\nu_d \eta_{-\mathbf{k}} + \nu_d^* \eta_{\mathbf{k}}^\dagger)(a_{\mathbf{q}1} + a_{-\mathbf{q}1}^\dagger). \tag{5.14}$$

5.2 Cavity–SC paramagnetic coupling

We now move on to the paramagnetic coupling $-q\hbar\mathbf{p}\cdot\mathbf{A}$. We will derive its expression in the Fourier transformed electron and photon bases, before recasting the expression upon introducing the Bogoliubov quasiparticle basis.

Our starting point is the discretized expression also found in the Supplemental Material of Ref. [11], viz.,

$$\mathcal{H}_{\mathrm{cav-SC}} = \sum_d \sum_j j_d(\mathbf{r}_j) A_d \left(\frac{\mathbf{r}_{j+I_d} + \mathbf{r}_j}{2} \right). \tag{5.15}$$

Here, $j \equiv (n_x^{\mathrm{SC}}, n_y^{\mathrm{SC}})$ labels lattice sites in analogy with the labeling in Fig. 2.1, with $(0,0)$ the upper left corner, and $(N_x^{\mathrm{SC}}-1, N_y^{\mathrm{SC}}-1)$ the lower right corner. The number of lattice sites in the respective directions are N_d^{SC}. $j_d(\mathbf{r}_j)$ are the Cartesian components of the discretized electric current operator, at lattice site j with the position vector $\mathbf{r}_j$. They are defined as [11]

$$j_d(\mathbf{r}_j) \equiv \frac{i a_{\mathrm{SC}} e t}{\hbar} \sum_\sigma (c^\dagger_{j+I_d,\sigma} c_{j\sigma} - c^\dagger_{j\sigma} c_{j+I_d,\sigma}), \tag{5.16}$$

[1] More precisely, when the FI and the cavity share dimensions, $D_{\mathbf{kq}}$ equals an infinite sum of Kronecker delta functions: one for each $\mathbf{q}$ that is equivalent to $\mathbf{k}$ up to an FI Brillouin zone. We are anyhow only concerned with the first Brillouin zone, since the interaction strengths decrease rapidly with increasing $|\mathbf{q}|$ due to factors $\omega_{\mathbf{q}}^{-1/2}$ entering the coupling constants.

where a_{SC} is the lattice constant, e is the electric charge, t is the lattice hopping parameter, and $c_{j\sigma}$ are the electron operators introduced in Sec. 3.3.1. Furthermore, I_d represents a step to the next lattice site in the d direction. For instance, if $j = (1,1)$, then $j + I_x = (1+1,1) = (2,1)$. [2]

We now proceed to compute the right-hand side of Eq. (5.15). First, the expression for $\mathbf{A}_{\mathrm{cav}}$ across the SC. The SC is positioned at $z = L_z/2$, and we let $\ell_z = 1$. Then the mode functions (4.21) and (4.35) become

$$u_{\mathbf{q}x} = u_{\mathbf{q}y} = i\sqrt{\frac{2}{V}}e^{i\mathbf{q}\cdot\mathbf{r}}, \quad u_{\mathbf{q}z} = 0 \quad \Rightarrow \quad \overline{\mathbf{u}}_{\mathbf{q}\varsigma} = i\sqrt{\frac{2}{V}}e^{i\mathbf{q}\cdot\mathbf{r}}\sum_d \hat{e}_d O^{\mathbf{q}}_{\varsigma d} \tag{5.17}$$

where $\mathbf{q}$ was defined in Eq. (5.2), and when appearing as an index, must be understood as $\mathbf{q} + \pi\hat{e}_z/L_z$, like before. Then the gauged expression (4.36) for $\mathbf{A}_{\mathrm{cav}}$ across the SC becomes

$$\begin{aligned}
\mathbf{A}_{\mathrm{cav}}(\mathbf{r})\big|_{\mathrm{SC}} &= \sum_{\mathbf{q}\varsigma d}\sqrt{\frac{\hbar}{\epsilon\omega_{\mathbf{q}}V}}\hat{e}_d(a_{\mathbf{q}\varsigma}ie^{i\mathbf{q}\cdot\mathbf{r}}O^{\mathbf{q}}_{\varsigma d} + a^\dagger_{\mathbf{q}\varsigma}(-ie^{-i\mathbf{q}\cdot\mathbf{r}})O^{\mathbf{q}}_{\varsigma d}) \\
&= \sum_{\mathbf{q}\varsigma d} i\sqrt{\frac{\hbar}{\epsilon\omega_{\mathbf{q}}V}}O^{\mathbf{q}}_{\varsigma d}\hat{e}_d e^{i\mathbf{q}\cdot\mathbf{r}}(a_{\mathbf{q}\varsigma} + a^\dagger_{-\mathbf{q}\varsigma}) \\
&= \sum_{\mathbf{q}d}\left(\sum_\varsigma i\sqrt{\frac{\hbar}{\epsilon\omega_{\mathbf{q}}V}}O^{\mathbf{q}}_{\varsigma d}(a_{\mathbf{q}\varsigma} + a^\dagger_{-\mathbf{q}\varsigma})\right)\hat{e}_d e^{i\mathbf{q}\cdot\mathbf{r}}.
\end{aligned} \tag{5.18}$$

The last equality is just a reordering of sums which explicitly shows the components of the gauged field. As before, $d = x, y$, and $\varsigma = 1, 2$. We also used that

$$O^{-\mathbf{q}}_{\varsigma d} = -O^{\mathbf{q}}_{\varsigma d}, \tag{5.19}$$

which holds for the upper left 2×2 block of $O^{\mathbf{q}}$, as defined in Eq. (4.25).

We are now equipped to recast $\mathcal{H}_{\mathrm{cav-SC}}$ in the Fourier bases. Inserting the

[2] As with the split of $\sum_{\langle i,j\rangle}$ into $\sum_i\sum_\delta$ for spin operators on the FI (Sec. 2.2.3), we ignore the inaccuracy at the boundary, where taking a step can bring us out of the lattice. This overextension spans a length scale of a single lattice constant, hence only affecting irrelevant high-momenta regimes.

gauge field (5.18) and Fourier-basis electron operators (3.4) into Eq. (5.15):

$$\begin{aligned}
\mathcal{H}_{\text{cav–SC}} &= \sum_d \sum_j j_d(\mathbf{r}_j) A_d\left(\frac{\mathbf{r}_{j+I_d}+\mathbf{r}_j}{2}\right) \\
&= \sum_j \frac{i a_{\text{SC}} e t}{\hbar} \sum_{d\sigma\mathbf{q}\varsigma} (c^\dagger_{j+I_d,\sigma} c_{j\sigma} - c^\dagger_{j\sigma} c_{j+I_d,\sigma}) i \sqrt{\frac{\hbar}{\epsilon\omega_{\mathbf{q}} V}} O^{\mathbf{Q}}_{\varsigma d}(a_{\mathbf{q}\varsigma} + a^\dagger_{-\mathbf{q}\varsigma}) e^{i\mathbf{q}\cdot(\mathbf{r}_j+\delta_d/2)} \\
&= \frac{i a_{\text{SC}} e t}{\hbar} \sum_{d\sigma\mathbf{q}\varsigma\mathbf{p}\mathbf{p}'} c^\dagger_{\mathbf{p}\sigma} c_{\mathbf{p}'\sigma} e^{i\mathbf{q}\cdot\mathbf{r}_0^{\text{SC}}} D^{\text{SC}}_{\mathbf{p}\mathbf{p}'\mathbf{q}} \left(e^{-i(\mathbf{p}-\mathbf{q}/2)\cdot\delta_d} - e^{i(\mathbf{p}'+\mathbf{q}/2)\cdot\delta_d}\right) \\
&\quad \cdot i \sqrt{\frac{\hbar}{\epsilon\omega_{\mathbf{q}} V}} O^{\mathbf{q}}_{\varsigma d}(a_{\mathbf{q}\varsigma} + a^\dagger_{-\mathbf{q}\varsigma}) \\
&= \sum_{\mathbf{p}\mathbf{p}'\sigma} \sum_{\mathbf{q}\varsigma} g^{\mathbf{q}\mathbf{p}\mathbf{p}'}_\varsigma (a_{\mathbf{q}\varsigma} + a^\dagger_{-\mathbf{q}\varsigma}) c^\dagger_{\mathbf{p}\sigma} c_{\mathbf{p}'\sigma}.
\end{aligned} \tag{5.20}$$

Above, we introduced the quantity $D^{\text{SC}}_{\mathbf{p}-\mathbf{p}',\mathbf{q}}$, defined analogously to $D^{\text{FI}}_{\mathbf{k}\mathbf{q}}$ (cf. Eq. (5.11)):

$$\begin{aligned}
N_{\text{SC}} D^{\text{SC}}_{\mathbf{p}-\mathbf{p}',\mathbf{q}} &\equiv e^{i(\mathbf{p}-\mathbf{p}'-\mathbf{q})\cdot\mathbf{r}_0^{\text{FI}}} \sum_i e^{-i(\mathbf{p}-\mathbf{p}'-\mathbf{q})\cdot\mathbf{r}_i} \\
&\approx N_{\text{SC}} \prod_d \text{sinc}\left[\pi N_d^{\text{SC}} \left(\frac{m_d^{\text{SC}} - m_d^{\text{SC}\prime}}{N_d^{\text{SC}}} - \frac{\ell_d a_{\text{FI}}}{L_d}\right)\right] \\
&\neq N_{\text{SC}} \delta_{\mathbf{p}-\mathbf{p}',\mathbf{q}}.
\end{aligned} \tag{5.21}$$

where $m_d^{\text{SC}\prime}$ has the same range as m_d'. The last line stresses that in general, momentum is not conserved, with $D^{\text{SC}}_{\mathbf{p}-\mathbf{p}',\mathbf{q}}$ reducing to a Kronecker delta function only when $L_d = l_d^{\text{SC}} = a_{\text{SC}} N_d^{\text{SC}}$. $D^{\text{SC}}_{\mathbf{p}-\mathbf{p}',\mathbf{q}}$ differs from $D^{\text{FI}}_{\mathbf{k}\mathbf{q}}$ only in the input $\mathbf{p}-\mathbf{p}'$ in place of $\mathbf{k}$, and the sum over SC lattice points $\sum_j$ in place of FI lattice points $\sum_i$.

Furthermore, we introduced the coupling constant

$$g^{\mathbf{q}\mathbf{p}\mathbf{p}'}_\varsigma \equiv -\frac{a_{\text{SC}} e t}{\hbar} \sqrt{\frac{\hbar}{\epsilon\omega_{\mathbf{q}} V}} D^{\text{SC}}_{\mathbf{p}-\mathbf{p}',\mathbf{q}} e^{i\mathbf{q}\cdot\mathbf{r}_0^{\text{SC}}} \sum_d \left(e^{-i(\mathbf{p}-\mathbf{q}/2)\cdot\delta_d} - e^{i(\mathbf{p}'+\mathbf{q}/2)\cdot\delta_d}\right) O^{\mathbf{q}}_{\varsigma d}. \tag{5.22}$$

The Hermiticity of Eq. (5.20) is not trivial, so we briefly present a proof to validate the recast expression. First, note that

$$(D^{\text{SC}}_{\mathbf{p}'-\mathbf{p},-\mathbf{q}})^* = D^{\text{SC}}_{\mathbf{p}-\mathbf{p}',\mathbf{q}}, \quad \omega_{-\mathbf{q}} = \omega_{\mathbf{q}}, \quad O^{-\mathbf{q}}_{\varsigma d} = -O^{\mathbf{q}}_{\varsigma d}, \quad \Rightarrow \quad (g^{-\mathbf{q},\mathbf{p}'\mathbf{p}}_\varsigma)^* = g^{\mathbf{q}\mathbf{p}\mathbf{p}'}_\varsigma. \tag{5.23}$$

The first equality is readily verified by inspection of Eq. (5.21).[3] The second equality follows from $\omega_{\mathbf{q}} = \omega_{|\mathbf{q}|}$. The third equality is valid for the relevant entries of $O^{\mathbf{q}}$, viz., the upper left 2×2 block (recall that $\varsigma = 1, 2$ and $s = x, y$); cf. Eq. (4.25).

[3] Note that the complex conjugation is technically redundant as $D^{\text{SC}}_{\mathbf{p}-\mathbf{p}',\mathbf{q}}$ is real-valued.

Furthermore, note that $\mathbf{q} \to -\mathbf{q}$ does not alter the range of the sum $\sum_{\mathbf{q}}$, since the ranges of the components $q_x = Q_x$ and $q_y = Q_y$ are symmetric with respect to inversion about 0 (cf. Eq. (4.10)).

Thus,

$$\begin{aligned}\left(\sum_{\mathbf{p}\mathbf{p}'\sigma}\sum_{\mathbf{q}\varsigma} g_{\varsigma}^{\mathbf{q}\mathbf{p}\mathbf{p}'}(a_{\mathbf{q}\varsigma} + a_{-\mathbf{q}\varsigma}^{\dagger})c_{\mathbf{p}\sigma}^{\dagger}c_{\mathbf{p}'\sigma}\right)^{\dagger} &= \sum_{\mathbf{p}\mathbf{p}'\sigma}\sum_{\mathbf{q}\varsigma}(g_{\varsigma}^{\mathbf{q}\mathbf{p}\mathbf{p}'})^{*}(a_{\mathbf{q}\varsigma}^{\dagger} + a_{-\mathbf{q}\varsigma})c_{\mathbf{p}'\sigma}^{\dagger}c_{\mathbf{p}\sigma} \\ &= \sum_{\mathbf{p}\mathbf{p}'\sigma}\sum_{\mathbf{q}\varsigma}(g_{\varsigma}^{-\mathbf{q},\mathbf{p}'\mathbf{p}})^{*}(a_{-\mathbf{q}\varsigma}^{\dagger} + a_{\mathbf{q}\varsigma})c_{\mathbf{p}\sigma}^{\dagger}c_{\mathbf{p}'\sigma} \\ &= \sum_{\mathbf{p}\mathbf{p}'\sigma}\sum_{\mathbf{q}\varsigma} g_{\varsigma}^{\mathbf{q}\mathbf{p}\mathbf{p}'}(a_{\mathbf{q}\varsigma} + a_{-\mathbf{q}\varsigma}^{\dagger})c_{\mathbf{p}\sigma}^{\dagger}c_{\mathbf{p}'\sigma}.\end{aligned} \tag{5.24}$$

That is, the expression is Hermitian. From the first to the second line, we let $\mathbf{p} \longleftrightarrow \mathbf{p}'$ and $\mathbf{q} \to -\mathbf{q}$, and used that the summation ranges remain invariant under these actions. From the second to the last line, we used Eq. (5.23) to rewrite the coupling constant.

5.2.1 Bogoliubov quasiparticle basis

In Sec. 3.3.3, we diagonalized the SC Hamiltonian by introducing the Bogoliubov quasiparticle basis (Eq. (3.22)). We now seek to recast also $\mathcal{H}_{\text{cav}-\text{SC}}$ in terms of this basis. Shifting the electron momenta $\pm\mathbf{p} \to \pm\mathbf{p} + \mathbf{P}$ and inserting the Bogolibuov quasiparticle basis (3.24), we find

$$\begin{aligned}\mathcal{H}_{\text{cav}-\text{SC}} &= \sum_{\mathbf{p}\mathbf{p}'}\sum_{\mathbf{q}\varsigma}(a_{\mathbf{q}\varsigma} + a_{-\mathbf{q}\varsigma}^{\dagger})\Big[g_{\varsigma}^{\mathbf{q},\mathbf{p}+\mathbf{P},\mathbf{p}'+\mathbf{P}} c_{\mathbf{p}+\mathbf{P},\uparrow}^{\dagger} c_{\mathbf{p}'+\mathbf{P},\uparrow} \\ &\quad + g_{\varsigma}^{\mathbf{q},-\mathbf{p}+\mathbf{P},-\mathbf{p}'+\mathbf{P}} c_{-\mathbf{p}+\mathbf{P},\downarrow}^{\dagger} c_{-\mathbf{p}'+\mathbf{P},\downarrow}\Big] \\ &= \sum_{\mathbf{p}\mathbf{p}'}\sum_{\mathbf{q}\varsigma}(a_{\mathbf{q}\varsigma} + a_{-\mathbf{q}\varsigma}^{\dagger})\Big[g_{\varsigma}^{\mathbf{q},\mathbf{p}+\mathbf{P},\mathbf{p}'+\mathbf{P}}(u_{\mathbf{p}}\gamma_{\mathbf{p}0}^{\dagger} + v_{\mathbf{p}}^{*}\gamma_{\mathbf{p}1}^{\dagger})(u_{\mathbf{p}'}^{*}\gamma_{\mathbf{p}'0} + v_{\mathbf{p}'}\gamma_{\mathbf{p}'1}) \\ &\quad + g_{\varsigma}^{\mathbf{q},-\mathbf{p}+\mathbf{P},-\mathbf{p}'+\mathbf{P}}(-v_{\mathbf{p}}^{*}\gamma_{\mathbf{p}0} + u_{\mathbf{p}}\gamma_{\mathbf{p}1})(-v_{\mathbf{p}'}\gamma_{\mathbf{p}'0}^{\dagger} + u_{\mathbf{p}'}^{*}\gamma_{\mathbf{p}'1}^{\dagger})\Big] \\ &= \sum_{\mathbf{p}\mathbf{p}'}\sum_{\mathbf{q}\varsigma}(a_{\mathbf{q}\varsigma} + a_{-\mathbf{q}\varsigma}^{\dagger})\Big[g_{\varsigma}^{\mathbf{q},\mathbf{p}+\mathbf{P},\mathbf{p}'+\mathbf{P}}(u_{\mathbf{p}}\gamma_{\mathbf{p}0}^{\dagger} + v_{\mathbf{p}}^{*}\gamma_{\mathbf{p}1}^{\dagger})(u_{\mathbf{p}'}^{*}\gamma_{\mathbf{p}'0} + v_{\mathbf{p}'}\gamma_{\mathbf{p}'1}) \\ &\quad - g_{\varsigma}^{\mathbf{q},-\mathbf{p}'+\mathbf{P},-\mathbf{p}+\mathbf{P}}(-v_{\mathbf{p}'}^{*}\gamma_{\mathbf{p}'0} + u_{\mathbf{p}'}\gamma_{\mathbf{p}'1})(-v_{\mathbf{p}}\gamma_{\mathbf{p}0}^{\dagger} + u_{\mathbf{p}}^{*}\gamma_{\mathbf{p}1}^{\dagger})\Big].\end{aligned} \tag{5.25}$$

For the last line, we swapped $\mathbf{p} \leftrightarrow \mathbf{p}'$. This expression can be compacted as follows. Using the anticommutator relations (3.27)–(3.31), one finds that

$$\begin{aligned}
&(-v^*_{\mathbf{p}'}\gamma_{\mathbf{p}'0} + u_{\mathbf{p}'}\gamma_{\mathbf{p}'1})(-v_{\mathbf{p}}\gamma^\dagger_{\mathbf{p}0} + u^*_{\mathbf{p}}\gamma^\dagger_{\mathbf{p}1}) \\
&= -(-v_{\mathbf{p}}\gamma^\dagger_{\mathbf{p}0} + u^*_{\mathbf{p}}\gamma^\dagger_{\mathbf{p}1})(-v^*_{\mathbf{p}'}\gamma_{\mathbf{p}'0} + u_{\mathbf{p}'}\gamma_{\mathbf{p}'1}) + (v^*_{\mathbf{p}'}v_{\mathbf{p}} + u_{\mathbf{p}'}u^*_{\mathbf{p}})\delta_{\mathbf{p}'\mathbf{p}} \\
&= -(-v_{\mathbf{p}}\gamma^\dagger_{\mathbf{p}0} + u^*_{\mathbf{p}}\gamma^\dagger_{\mathbf{p}1})(-v^*_{\mathbf{p}'}\gamma_{\mathbf{p}'0} + u_{\mathbf{p}'}\gamma_{\mathbf{p}'1}) + \delta_{\mathbf{p}'\mathbf{p}}. \qquad (5.26)
\end{aligned}$$

The last term drops out because

$$\sum_{\mathbf{p}\mathbf{p}'} g^{\mathbf{q},-\mathbf{p}'+\mathbf{P},-\mathbf{p}+\mathbf{P}}_{\varsigma}\delta_{\mathbf{p}'\mathbf{p}} = \sum_{\mathbf{p}} g^{\mathbf{q},-\mathbf{p}+\mathbf{P},-\mathbf{p}+\mathbf{P}}_{\varsigma} = \sum_{\mathbf{p}} g^{\mathbf{q}\mathbf{p}\mathbf{p}}_{\varsigma}, \qquad (5.27)$$

and $g^{\mathbf{q}\mathbf{p}\mathbf{p}}_{\varsigma}$ is odd in $\mathbf{p}$ (see Eq. (5.22)), hence the sum is 0. Now, inserting Eq. (5.26) into Eq. (5.25), $\mathcal{H}_{\text{cav–SC}}$ can be recast succinctly as

$$\mathcal{H}_{\text{cav–SC}} = \sum_{\mathbf{q}\varsigma}\sum_{\mathbf{p}m}\sum_{\mathbf{p}'m'} g^{\mathbf{q}\mathbf{p}\mathbf{p}'}_{\varsigma mm'}(a_{\mathbf{q}\varsigma} + a^\dagger_{-\mathbf{q}\varsigma})\gamma^\dagger_{\mathbf{p}m}\gamma_{\mathbf{p}'m'}, \qquad (5.28)$$

where the coupling constant is now

$$g^{\mathbf{q}\mathbf{p}\mathbf{p}'}_{\varsigma mm'} \equiv \begin{pmatrix} g^{\mathbf{q},\mathbf{p}+\mathbf{P},\mathbf{p}'+\mathbf{P}}_{\varsigma} u_{\mathbf{p}}u^*_{\mathbf{p}'} - g^{\mathbf{q},-\mathbf{p}+\mathbf{P},-\mathbf{p}'+\mathbf{P}}_{\varsigma} v_{\mathbf{p}}v^*_{\mathbf{p}'} & g^{\mathbf{q},\mathbf{p}+\mathbf{P},\mathbf{p}'+\mathbf{P}}_{\varsigma} u_{\mathbf{p}}v_{\mathbf{p}'} + g^{\mathbf{q},-\mathbf{p}+\mathbf{P},-\mathbf{p}'+\mathbf{P}}_{\varsigma} v_{\mathbf{p}}u_{\mathbf{p}'} \\ g^{\mathbf{q},-\mathbf{p}+\mathbf{P},-\mathbf{p}'+\mathbf{P}}_{\varsigma} u^*_{\mathbf{p}}v^*_{\mathbf{p}'} + g^{\mathbf{q},\mathbf{p}+\mathbf{P},\mathbf{p}'+\mathbf{P}}_{\varsigma} v^*_{\mathbf{p}}u^*_{\mathbf{p}'} & -g^{\mathbf{q},-\mathbf{p}+\mathbf{P},-\mathbf{p}'+\mathbf{P}}_{\varsigma} u^*_{\mathbf{p}}u_{\mathbf{p}'} + g^{\mathbf{q},\mathbf{p}+\mathbf{P},\mathbf{p}'+\mathbf{P}}_{\varsigma} v^*_{\mathbf{p}}v_{\mathbf{p}'} \end{pmatrix}_{mm'}. \qquad (5.29)$$

Gathering all terms, the complete SC Hamiltonian for the set-up in Fig. 1.3 thus reads

$$\mathcal{H}_{\text{SC}} = \sum_{\mathbf{p}m} E_{\mathbf{p}m}\gamma^\dagger_{\mathbf{p}m}\gamma_{\mathbf{p}m} + \sum_{\mathbf{q}\varsigma}\sum_{\mathbf{p}m}\sum_{\mathbf{p}'m'} g^{\mathbf{q}\mathbf{p}\mathbf{p}'}_{\varsigma mm'}(a_{\mathbf{q}\varsigma} + a^\dagger_{-\mathbf{q}\varsigma})\gamma^\dagger_{\mathbf{p}m}\gamma_{\mathbf{p}'m'}. \qquad (5.30)$$

In the next chapter, we gather all terms of the system Hamiltonian, from which we construct an effective magnon theory.

Key takeaways:

- With the FI film placed at the upper magnetic antinode of the $\ell_z = 1$ cavity modes, we consider the Zeeman coupling $\mathcal{H}_{\text{FI-cav}} = -\frac{g\mu_B}{\hbar}\sum_i \mathbf{S}_i \cdot \mathbf{B}_{\text{cav}}(\mathbf{r}_i)$ between the FI and the cavity. In the magnon and photon bases, it reads

$$\mathcal{H}_{\text{FI-cav}} \approx \sum_{\mathbf{k}d}\sum_{\mathbf{q}\varsigma} g_d^{\mathbf{kq}}(v_d\eta_{-\mathbf{k}} + v_d^*\eta_{\mathbf{k}}^\dagger)(a_{\mathbf{q}1} + a_{-\mathbf{q}1}^\dagger).$$

  The approximate equality is due to the linearization of the Holstein–Primakoff transformation.
- Likewise, with the SC film placed at the corresponding electric antinode, we consider the paramagnetic coupling $\mathcal{H}_{\text{cav-SC}} = \sum_d \sum_j j_d(\mathbf{r}_j)A_d\left([\mathbf{r}_{j+l_d} + \mathbf{r}_j]/2\right)$. In the photon and SC quasiparticle bases, it reads

$$\mathcal{H}_{\text{cav-SC}} = \sum_{\mathbf{q}\varsigma}\sum_{\mathbf{p}m}\sum_{\mathbf{p}'m'} g_{\varsigma mm'}^{\mathbf{qpp}'}(a_{\mathbf{q}\varsigma} + a_{-\mathbf{q}\varsigma}^\dagger)\gamma_{\mathbf{p}m}^\dagger\gamma_{\mathbf{p}'m'}.$$

- Notably, because the FI, cavity and SC in-plane dimensions generally differ, (crystal) momenta are not conserved in the interactions. In other words, magnons couple to, and SC quasiparticles are scattered by, a range of photonic modes, not only the modes that conserve momenta. This effect is expressed in the respective coupling constants through the factors $D_{\mathbf{kq}}^{\text{FI}}$ and $D_{\mathbf{p}-\mathbf{p}',\mathbf{q}}^{\text{SC}}$: sinc functions that reduce to the familiar Kronecker delta functions only when the interacting subsystems share in-plane dimensions.

Chapter 6

Effective magnon theory, and reorientation of spins

Chapter summary: We introduce the Matsubara path integral formalism, and use it to collect the interactions between the FI, cavity and SC into an effective magnon theory. From this theory, we extract the effective anisotropy field induced across the FI, and the subsequent local reorientation of the FI spins; this is shown to express broken inversion symmetry in the SC.

Gathering all terms from Eqs. (5.14) and (5.30), the complete system Hamiltonian for the set-up in Fig. 1.3 reads

$$\begin{aligned}\mathcal{H} = &\sum_{\mathbf{k}} \hbar\lambda_{\mathbf{k}} \eta^\dagger_{\mathbf{k}} \eta_{\mathbf{k}} + \sum_{\mathbf{p}m} E_{\mathbf{p}m} \gamma^\dagger_{\mathbf{p}m} \gamma_{\mathbf{p}m} + \sum_{\mathbf{q}\varsigma} \hbar\omega_{\mathbf{q}} a^\dagger_{\mathbf{q}\varsigma} a_{\mathbf{q}\varsigma} \\ &+ \sum_{\mathbf{k}d} \sum_{\mathbf{q}} g_d^{\mathbf{kq}} (\nu_d \eta_{-\mathbf{k}} + \nu_d^* \eta^\dagger_{\mathbf{k}})(a_{\mathbf{q}1} + a^\dagger_{-\mathbf{q}1}) \\ &+ \sum_{\mathbf{q}\varsigma} \sum_{\mathbf{p}m} \sum_{\mathbf{p}'m'} g^{\mathbf{qpp}'}_{\varsigma mm'} (a_{\mathbf{q}\varsigma} + a^\dagger_{-\mathbf{q}\varsigma}) \gamma^\dagger_{\mathbf{p}m} \gamma_{\mathbf{p}'m'},\end{aligned} \tag{6.1}$$

where we have also included the well-known photon field energy term $\sum_{\mathbf{q}\varsigma} \hbar\omega_{\mathbf{q}} a^\dagger_{\mathbf{q}\varsigma} a_{\mathbf{q}\varsigma}$. The challenge is now to extract the cavity-mediated influence of the FI and the SC on each other. Our project has been dedicated in particular to the effects that the SC has on the FI, viz., inducing a reorientation of spins across the FI, as well as anticrossings in the magnon dispersion. We cover the latter in Ch. 7, and focus on the former here. In Paper II, we present promising numerical estimates of the anisotropy field in an arbitrary practical example, with the effect mediated across 130 µm, 2–5 orders above the scale of proximity effects (cf. Sec. 3.2) [5–9].

To this end, we seek to aggregate the influences of the photons and SC quasiparticles on the magnons; i.e., to construct an effective magnon theory. Plain matrix diagonalization does not cut it analytically: First, incorporating the triniliear

term $((a+a^\dagger)\gamma^\dagger\gamma)$ into a vector–matrix–vector product is not trivial. Second, even when ignoring the SC terms, the finite and different dimensions of the FI and the cavity cause an enormous number of modes to couple: in general, a magnon mode of momentum $\mathbf{k}$ couples to photon modes of all momenta $\mathbf{q}$, which in turn couples back to every single magnon mode. Even ignoring that the number of photon modes is infinite, $\mathcal{H}$ written as a vector–matrix–vector product would then look like

$$\mathcal{H} \approx \sum_d \begin{pmatrix} \eta_{\mathbf{k}_1} \\ \eta_{\mathbf{k}_2} \\ \vdots \\ a_{\mathbf{q}_1} \\ a_{\mathbf{q}_2} \\ \vdots \\ \eta^\dagger_{\mathbf{k}_1} \\ \eta^\dagger_{\mathbf{k}_2} \\ \vdots \\ a^\dagger_{\mathbf{q}_1} \\ a^\dagger_{\mathbf{q}_2} \\ \vdots \end{pmatrix}^\dagger \begin{pmatrix} \hbar\lambda_{\mathbf{k}_1}/2 & 0 & \dots & \nu_d^* g_d^{\mathbf{k}_1\mathbf{q}_1} & \nu_d^* g_d^{\mathbf{k}_1\mathbf{q}_2} & \dots \\ 0 & \hbar\lambda_{\mathbf{k}_2}/2 & & \nu_d^* g_d^{\mathbf{k}_2\mathbf{q}_1} & \nu_d^* g_d^{\mathbf{k}_2\mathbf{q}_2} & \\ \vdots & & \ddots & \vdots & & \ddots \\ \nu_d g_d^{-\mathbf{k}_1,-\mathbf{q}_1} & \nu_d g_d^{-\mathbf{k}_2,-\mathbf{q}_1} & \dots & \hbar\omega_{\mathbf{q}_1}/2 & 0 & \dots \\ \nu_d g_d^{-\mathbf{k}_1,-\mathbf{q}_2} & \nu_d g_d^{-\mathbf{k}_2,-\mathbf{q}_2} & & 0 & \hbar\omega_{\mathbf{q}_2}/2 & \\ \vdots & & \ddots & \vdots & & \ddots \end{pmatrix} \begin{pmatrix} \eta_{\mathbf{k}_1} \\ \eta_{\mathbf{k}_2} \\ \vdots \\ a_{\mathbf{q}_1} \\ a_{\mathbf{q}_2} \\ \vdots \\ \eta^\dagger_{\mathbf{k}_1} \\ \eta^\dagger_{\mathbf{k}_2} \\ \vdots \\ a^\dagger_{\mathbf{q}_1} \\ a^\dagger_{\mathbf{q}_2} \\ \vdots \end{pmatrix}. \tag{6.2}$$

The inclusion of both the operator (e.g. $\eta_{\mathbf{k}_1}$) and its conjugate ($\eta^\dagger_{\mathbf{k}_1}$) in the vectors accounts for the annihilation–annihilation (ηa) and creation–creation ($\eta^\dagger a^\dagger$) products in $\mathcal{H}$; cf. Refs. [104, 105]. The energies of the eigenmodes of the system are the eigenvalues of this enormous $2\mathcal{N} \times 2\mathcal{N}$ matrix. These are the roots of its characteristic polynomial, which is of order $2\mathcal{N}$. Polynomials of order $2\mathcal{N} > 4$ are analytically solvable only under particular circumstances, meaning this diagonalization procedure generally falls short for our system.

Another, perturbative approach is to apply mean field theory to decouple the SC from the remaining system. From this it is possible to extract the leading-order effect (with respect to the cavity–SC coupling) of the SC on the FI, namely a leading-order reorientation of its spins. We demonstrate this in Appendix A.

Yet another perturbative approach is to apply the Schrieffer–Wolff transformation in an off-resonant regime; i.e., the frequencies of coupled modes are not matched, and their difference is much greater than the coupling constant. This is a unitary transformation that decouples systems up to a desired order in interaction vertices, in favor of an effective theory, which in off-resonant regimes becomes precise [2, 106]. This was performed in Refs. [2, 10] in conjunction with the rotating wave approximation, in order to recast the cavity-mediated coupling of two magnon modes as an effective direct coupling, ultimately to extract renormalized dispersions. This off-resonant Schrieffer–Wolff approach was also used in Ref. [11] in conjunction with mean field theory to extract a cavity-mediated

electron–electron pairing. All of the aforementioned references demonstrated indirect couplings due to vacuum fluctuations in the cavity field. We also attempted this approach; however, it was eventually discarded in favor of the path integral approach presented below, which is more versatile for our system. The results and details on this approach can be found in Appendix B.

Instead, we will favor a Matsubara path integral approach to constructing an effective theory. As we will see, this approach renders diagonalization a non-issue to us, as Gaussian integrals do not have to be diagonal in integration variables in order to be performed. Unlike the Schrieffer–Wolff approach, this approach allows for an *exact* integrating-out of the cavity, leaving an exact effective FI–SC theory, as shown in Paper II. The SC can furthermore be integrated out perturbatively, leaving us with an effective magnon theory. The order of integration is inconsequential; in Paper II, we integrate out the cavity first, while below we do the SC first.

6.1 Matsubara path integral formalism

The Matsubara path integral formalism reformulates expectation values as path integrals in *thermal equilibrium*; i.e., we consider a system held uniformly at a single temperature T, without any time dependency.[1] In this case, the density matrix $\hat{\rho}$ takes the well-known form [107]

$$\hat{\rho} \equiv e^{-\beta \mathcal{H}/\hbar}, \tag{6.3}$$

where $\beta \equiv \hbar/k_B T$ is the inverse temperature in units of time. The thermal (i.e. finite temperature) expectation value of any operator $\hat{O}$ is then

$$\langle \hat{O} \rangle \equiv \frac{\mathrm{Tr}(\hat{\rho}\hat{O})}{\mathrm{Tr}\hat{\rho}}. \tag{6.4}$$

Here the trace

$$\mathrm{Tr}\hat{X} = \sum_n \langle n|\hat{X}|n\rangle \tag{6.5}$$

must be understood as a sum over diagonal matrix elements, with $|n\rangle$ all the eigenstates of the system. We now observe that $\hat{\rho}$ looks suggestively similar to the time evolution operator $e^{-i\mathcal{H}t/\hbar}$, the operator which by the Schrödinger equation evolves an initial state $\psi(0)$ to a state $\psi(t) = e^{-i\mathcal{H}t/\hbar}\psi(0)$ at time t assuming a time-independent $\mathcal{H}$ [108]. This time evolution operator serves as the starting point to a path integrals formulation of zero-temperature expectation values, as explained in detail in Refs. [108–110]. Indeed, by introducing an imaginary

[1] We expect the main results of our analysis to hold also when the FI, cavity and SC are held at different temperatures, so long as there are no temperature gradients inside the respective subsystems. This because there is no exchange of heat between the subsystems. Implementing this analytically would require deriving an appropriate expression for $\hat{\rho}$, which would presumably look similar to Eq. (6.3), and result in a similar path integral formulation.

time parameter $i\tau$, the temperature-dependency of the system is absorbed into a complex time parameter, and we can rewrite the traces in Eq. (6.4) as path integrals [108, 110]. The partition function (ground state persistence amplitude) Z then becomes

$$\begin{aligned} Z \equiv & \mathrm{Tr}\hat{\rho} \\ = & \langle \mathrm{vac}, t=\infty | \mathrm{vac}, t=-\infty \rangle \\ = & \int \mathcal{D}[\eta,\eta^\dagger] \int \mathcal{D}[a,a^\dagger] \int \mathcal{D}[\gamma,\gamma^\dagger] e^{-S/\hbar}, \end{aligned} \tag{6.6}$$

where e.g.

$$\int \mathcal{D}[\gamma,\gamma^\dagger] \equiv \prod_{pm} \int \mathcal{D}[\gamma_{pm},\gamma_{pm}^\dagger] \tag{6.7}$$

is shorthand for the path integrals over every SC quasiparticle mode, and the Matsubara action

$$\begin{aligned} S \equiv \frac{1}{\beta} \int_0^\beta \mathrm{d}\tau \Bigg(& \sum_{\mathbf{k}} \eta_{\mathbf{k}}^\dagger(\tau) \hbar \partial_\tau \eta_{\mathbf{k}}(\tau) + \sum_{\mathbf{q}\varsigma} a_{\mathbf{q}\varsigma}^\dagger(\tau) \hbar \partial_\tau a_{\mathbf{q}\varsigma}(\tau) \\ & + \sum_{\mathbf{p}m} \gamma_{\mathbf{p}m}^\dagger(\tau) \hbar \partial_\tau \gamma_{\mathbf{p}m}(\tau) + \mathcal{H} \Bigg). \end{aligned} \tag{6.8}$$

Note that in reformulating Z as a path integral, the particle operators are replaced by numbers, more precisely the eigenvalues of coherent states; see Ref. [108] for details. In the Matsubara action, the bosonic magnon and photon operators are therefore replaced by complex numbers, and the fermionic SC quasiparticle operators by Graßmann numbers. Notably, this means that in the context of the Matsubara action,

$$[\eta_{\mathbf{k}}, \eta_{\mathbf{k}'}^\dagger] = 0, \tag{6.9}$$

$$[a_{\mathbf{q}\varsigma}, a_{\mathbf{q}'\varsigma'}^\dagger] = 0, \tag{6.10}$$

$$\{\gamma_{\mathbf{p}m}, \gamma_{\mathbf{p}'m'}^\dagger\} = 0; \tag{6.11}$$

i.e. the numbers always commute (bosons) or anticommute (fermions).

Next, we recast the integral in the action (6.8) as a sum over frequencies, *Matsubara frequencies*, by resolving the particles into thermal Fourier modes:

$$\eta_{\mathbf{k}}(\tau) = \frac{1}{\sqrt{\beta}} \sum_{\Omega_m} \eta_k e^{-i\Omega_m \tau}, \tag{6.12}$$

$$a_{\mathbf{q}\varsigma}(\tau) = \frac{1}{\sqrt{\beta}} \sum_{\Omega_n} a_{q\varsigma} e^{-i\Omega_n \tau}, \tag{6.13}$$

$$\gamma_{\mathbf{p}m}(\tau) = \frac{1}{\sqrt{\beta}} \sum_{\omega_n} \gamma_{pm} e^{-i\omega_n \tau}. \tag{6.14}$$

Above, we introduced the 4-vectors

$$k \equiv (-\Omega_m, \mathbf{k}), \tag{6.15}$$
$$q \equiv (-\Omega_n, \mathbf{q}), \tag{6.16}$$
$$p \equiv (-\omega_n, \mathbf{p}), \tag{6.17}$$

and the Matsubara frequencies read

$$\Omega_n = \frac{2n\pi}{\beta} \tag{6.18}$$

for bosons, and

$$\omega_n = \frac{(2n+1)\pi}{\beta} \tag{6.19}$$

for fermions, with $n \in \mathbb{Z}$. Note that since $\eta_{\mathbf{k}}$, $a_{\mathbf{q}\varsigma}$ and $\gamma_{\mathbf{p}m}$ are dimensionless, the new variables η_k etc. must have units $[\sqrt{\beta}]$.

Inserting the resolved particles (6.12)–(6.14) into the action (6.8) yields the terms

$$S_0^{\mathrm{FI}} \equiv \sum_k \hbar\lambda_k \eta_k^\dagger \eta_k, \tag{6.20}$$
$$S_0^{\mathrm{cav}} \equiv \sum_{q\varsigma} \hbar\omega_q a_{q\varsigma}^\dagger a_{q\varsigma}, \tag{6.21}$$
$$S_0^{\mathrm{SC}} \equiv \sum_{pm} E_{pm} \gamma_{pm}^\dagger \gamma_{pm}, \tag{6.22}$$

$$S_{\mathrm{int}}^{\mathrm{FI-cav}} \equiv \sum_{kd}\sum_{q\varsigma} g_{d\varsigma}^{kq} (\nu_d \eta_{-k} + \nu_d^* \eta_k^\dagger)(a_{q\varsigma} + a_{-q\varsigma}^\dagger), \tag{6.23}$$
$$S_{\mathrm{int}}^{\mathrm{cav-SC}} \equiv \frac{1}{\sqrt{\beta}} \sum_{q\varsigma}\sum_{pm}\sum_{p'm'} g_{\varsigma mm'}^{qpp'} (a_{q\varsigma} + a_{-q\varsigma}^\dagger)\gamma_{pm}^\dagger \gamma_{p'm'}. \tag{6.24}$$

In the FI–cavity coupling, we wrote $a_{\mathbf{q}1} + a_{-\mathbf{q}1}^\dagger = \delta_{\varsigma,1}(a_{\mathbf{q}\varsigma} + a_{-\mathbf{q}\varsigma}^\dagger)$ for later convenience. We furthermore used the orthogonality relation $\int_0^\beta \mathrm{d}\tau e^{-i\Omega\tau} = \beta\delta_{\Omega,0}$. The energies and coupling strengths are now

$$\hbar\lambda_k \equiv -i\hbar\Omega_m + \hbar\lambda_{\mathbf{k}}, \tag{6.25}$$
$$\hbar\omega_q \equiv -i\hbar\Omega_n + \hbar\omega_{\mathbf{q}}, \tag{6.26}$$
$$E_{pm} \equiv -i\hbar\omega_n + E_{\mathbf{p}m}, \tag{6.27}$$

$$g_{d\varsigma}^{kq} \equiv g_d^{\mathbf{kq}} \delta_{\varsigma 1} \delta_{\Omega_m \Omega_n}, \tag{6.28}$$
$$g_{\varsigma mm'}^{qpp'} \equiv g_{\varsigma mm'}^{\mathbf{qpp'}} \delta_{\omega_{n'}, \omega_n - \Omega_n}. \tag{6.29}$$

Note that extracting the factor $1/\sqrt{\beta}$ in Eq. (6.24) has left all of the quantities above in units of energy.

We are now equipped to construct an effective action by integrating out the photonic and fermionic degrees of freedom.

6.1.1 Integrating out the SC

We begin by integrating the SC out of the problem, leaving us with an effective FI–cavity action. To this end, we introduce the interaction matrix Σ with elements

$$\Sigma^{pp'}_{mm'} \equiv \frac{1}{\sqrt{\beta}} \sum_{q\varsigma} g^{qpp'}_{\varsigma mm'} (a_{q\varsigma} + a^{\dagger}_{-q\varsigma}), \tag{6.30}$$

and furthermore the diagonal matrix E with elements

$$E^{pp'}_{mm'} \equiv E_{pm} \delta_{pp'} \delta_{mm'}. \tag{6.31}$$

Hence, the action involving the SC can be written as

$$S^{\mathrm{SC}} \equiv S^{\mathrm{SC}}_0 + S^{\mathrm{cav-SC}}_{\mathrm{int}} = \sum_{pm} \sum_{p'm'} (E + \Sigma)^{pp'}_{mm'} \gamma^{\dagger}_{pm} \gamma_{p'm'}. \tag{6.32}$$

The SC sector of the partition function (6.6) is thus a Gaussian integral, which is readily evaluated [108, 110]:

$$\begin{aligned} Z^{\mathrm{SC}} &\equiv \int \mathcal{D}[\gamma, \gamma^{\dagger}] e^{-S^{\mathrm{SC}}/\hbar} \\ &= \int \mathcal{D}[\gamma, \gamma^{\dagger}] \exp\left[-\frac{1}{\hbar} \sum_{pm} \sum_{p'm'} (E + \Sigma)^{pp'}_{mm'} \gamma^{\dagger}_{pm} \gamma_{p'm'} \right] \\ &= \det(\beta(E + \Sigma)/\hbar) \\ &= \exp[\mathrm{tr}[\ln(\beta(E + \Sigma)/\hbar)]] \\ &= \exp\left[\mathrm{tr}\left[\ln(\beta E/\hbar) + \ln\left(1 + E^{-1}\Sigma\right) \right] \right]. \end{aligned} \tag{6.33}$$

Note that the factor β appearing in the determinant results from the definitions (6.12)–(6.14) of the transformed variables, which are *not* dimensionless [108]. This factor ensures that the quantity inside the determinant *is* dimensionless, which it should be, since Z^{SC} is dimensionless. Above, the functions exp and ln of some matrix X must be understood in terms of their series expansion, e.g.

$$\ln(1 + X) = X - \frac{X^2}{2} + \ldots \tag{6.34}$$

The determinant (det) and trace (tr) of a matrix X are understood as usual. If the elements of X are $X^{pp'}_{mm'}$, the trace is

$$\mathrm{tr} X = \sum_{pm} X^{pp}_{mm}. \tag{6.35}$$

The general expression for the determinant is not relevant here, although we note it can be expressed as the product of its eigenvalues (used in Sec. 7.1.2). Furthermore, since E is diagonal, E^{-1} is simply

$$(E^{-1})^{pp'}_{mm'} = \frac{\delta_{pp'} \delta_{mm'}}{E_{pm}}. \tag{6.36}$$

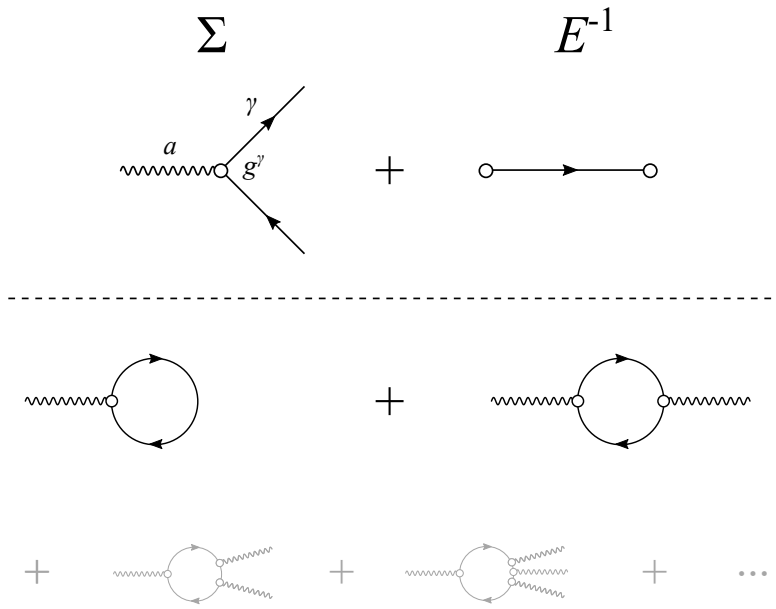

Figure 6.1: Interactions resulting from integrating out the SC. Diagrammatically, they are obtained by joining the ends of the cavity–SC interaction vertex (Σ) and the Bogolibov quasiparticle propagator (E^{-1}) (above dashed line), such that SC quasiparticles only appear in internal lines. Of these interactions (below dashed line), the first two (black) are kept, and the rest (grey) are neglected. Here a are photons, γ are SC quasiparticles, and g^γ is the cavity–SC coupling strength. Inspired by the corresponding figure in Paper II, courtesy of H. G. Hugdal.

The factor $\ln(\beta E/\hbar)$ in the last line of Eq. (6.33) does not depend on any variables of integration (photons), so we neglect this. Meanwhile, by Eq. (6.34), the other factor $\ln\left(1+E^{-1}\Sigma\right)$ represents an infinite series involving products of $E^{-1}\Sigma$ to arbitrary order, and Σ is linear in photons. This means the cavity sector of Z is Gaussian only to second order in this series, beyond which point the evaluation of the cavity sector becomes complicated. We therefore truncate the series by assuming weak coupling between the cavity and the SC, or

$$1 \gg |E^{-1}\Sigma|. \tag{6.37}$$

Thus

$$
\begin{aligned}
Z^{\mathrm{SC}} &\approx \exp\left[\mathrm{Tr}\left[E^{-1}\Sigma - E^{-1}\Sigma E^{-1}\Sigma/2\right]\right] \\
&= \exp\Bigg[-\Bigg(-\sum_{pm}\sum_{p'm'}\hbar(E^{-1})^{pp'}_{mm'}\Sigma^{p'p}_{m'm} \\
&\qquad + \sum_{pm}\sum_{p'm'}\sum_{\tilde{p}\tilde{m}}\sum_{\tilde{p}'\tilde{m}'}\hbar(E^{-1})^{pp'}_{mm'}\Sigma^{p'\tilde{p}}_{m'\tilde{m}}(E^{-1})^{\tilde{p}\tilde{p}'}_{\tilde{m}\tilde{m}'}\Sigma^{\tilde{p}'p}_{\tilde{m}'m}/2\Bigg)\Big/\hbar\Bigg] \\
&= \exp\left[-\left(-\sum_{pm}\hbar\frac{\Sigma^{pp}_{mm}}{E_{pm}} + \sum_{pm}\sum_{p'm'}\hbar\frac{\Sigma^{pp'}_{mm'}\Sigma^{p'p}_{m'm}}{2E_{pm}E_{p'm'}}\right)\Big/\hbar\right] \\
&= \exp\Bigg[-\Bigg(-\sum_{q\varsigma}\sum_{pm}\frac{\hbar}{\sqrt{\beta}}\frac{g^{qpp}_{\varsigma mm}}{E_{pm}}(a_{q\varsigma} + a^{\dagger}_{-q\varsigma}) \\
&\qquad + \sum_{q\varsigma}\sum_{q'\varsigma'}\Gamma^{qq'}_{\varsigma\varsigma'}(a_{q\varsigma} + a^{\dagger}_{-q\varsigma})(a_{q'\varsigma'} + a^{\dagger}_{-q'\varsigma'})\Bigg)\Big/\hbar\Bigg],
\end{aligned}
\tag{6.38}
$$

where we introduced the coefficient

$$
\Gamma^{qq'}_{\varsigma\varsigma'} \equiv \sum_{pm}\sum_{p'm'}\frac{\hbar}{\beta}\frac{g^{qpp'}_{\varsigma mm'}g^{q'p'p}_{\varsigma'm'm}}{2E_{pm}E_{p'm'}} \tag{6.39}
$$

for later convenience. Hence, integrating out the SC to second order in the cavity–SC coupling yields an effective action S_1^{cav}, given by

$$
S_1^{\mathrm{cav}} \equiv -\sum_{q\varsigma}\sum_{pm}\frac{\hbar}{\sqrt{\beta}}\frac{g^{qpp}_{\varsigma mm}}{E_{pm}}(a_{q\varsigma} + a^{\dagger}_{-q\varsigma}) + \sum_{q\varsigma}\sum_{q'\varsigma'}\Gamma^{qq'}_{\varsigma\varsigma'}(a_{q\varsigma} + a^{\dagger}_{-q\varsigma})(a_{q'\varsigma'} + a^{\dagger}_{-q'\varsigma'}). \tag{6.40}
$$

The interactions contained in Z^{SC} and S_1^{cav} are illustrated in Fig. 6.1.

6.1.2 Integrating out the cavity

The partition function of the system (6.6) now reads

$$
Z = \int \mathcal{D}[\eta,\eta^{\dagger}]\int \mathcal{D}[a,a^{\dagger}]\exp\left[-(S_0^{\mathrm{FI}} + S_0^{\mathrm{cav}} + S_1^{\mathrm{cav}} + S_{\mathrm{int}}^{\mathrm{FI-cav}})/\hbar\right]. \tag{6.41}
$$

We now proceed to integrate out the cavity sector, i.e.

$$
Z^{\mathrm{cav}} \equiv \int \mathcal{D}[a,a^{\dagger}]e^{-S^{\mathrm{cav}}/\hbar}, \tag{6.42}
$$

where the effective cavity action is

$$
S^{\mathrm{cav}} \equiv S_0^{\mathrm{cav}} + S_1^{\mathrm{cav}} + S_{\mathrm{int}}^{\mathrm{FI-cav}}. \tag{6.43}
$$

This action contains both linear and bilinear photon terms.[2] The cavity interacts with the FI only through the FI–cavity coupling, a linear photon term. This means we can decouple the cavity and FI sectors by two equivalent methods: a shift of integration variables followed by cancelling linear terms, which is done in Paper II; or completing the square followed by a shift of integration variables, which we do here.

Outlined, the method entails writing a^2+2Aa as $(a+A)^2-A^2$ for a variable and A constant, then substituting $a' = a+A$ and using that the integration measure is unaffected: $\mathrm{d}a' = \mathrm{d}a$. With a the photons and A the magnons, the coupling term $2Aa$ is thus absorbed into the decoupled photons a', leaving a remainder $-A^2$ that contains all effective magnon terms.[3]

Specifically, in our case, absorbing the linear terms leads to a bilinear theory in the new photon basis

$$a'_{q\varsigma} \equiv a_{q\varsigma} + J_{-q\varsigma}/\hbar\omega_q, \tag{6.44}$$

$$a'^{\dagger}_{q\varsigma} \equiv a^{\dagger}_{q\varsigma} + J_{q\varsigma}/\hbar\omega_q. \tag{6.45}$$

Above, we introduced the source term

$$J_{q\varsigma} \equiv \sum_{kd} G^{kq}_{d\varsigma}(\nu_d \eta_{-k} + \nu^*_d \eta^{\dagger}_k) - s_{q\varsigma}, \tag{6.46}$$

where the quantities $G^{kq}_{d\varsigma}$ and $s_{q\varsigma}$ are coefficients to be determined by requiring that the original linear terms be absorbed. Then by postulation, the cavity action (6.43) can be written as

$$S^{\mathrm{cav}} = S^{\mathrm{cav}}_{\mathrm{bil}} + S^{\mathrm{cav}}_{\mathrm{con}}, \tag{6.47}$$

where

$$\begin{aligned} S^{\mathrm{cav}}_{\mathrm{bil}} \equiv & \sum_{q\varsigma} (a^{\dagger}_{q\varsigma} + J_{q\varsigma}/\hbar\omega_q)\hbar\omega_q (a_{q\varsigma} + J_{-q\varsigma}/\hbar\omega_q) \\ & + \sum_{q\varsigma}\sum_{q'\varsigma'} \Gamma^{qq'}_{\varsigma\varsigma'} \left((a_{q\varsigma} + J_{-q\varsigma}/\hbar\omega_q) + (a^{\dagger}_{-q\varsigma} + J_{-q\varsigma}/\hbar\omega_{-q}) \right) \\ & \cdot \left((a_{q'\varsigma'} + J_{-q'\varsigma'}/\hbar\omega_{q'}) + (a^{\dagger}_{-q'\varsigma'} + J_{-q'\varsigma'}/\hbar\omega_{-q'}) \right), \end{aligned} \tag{6.48}$$

$$\begin{aligned} S^{\mathrm{cav}}_{\mathrm{con}} \equiv & -\sum_{q\varsigma} \frac{J_{q\varsigma} J_{-q\varsigma}}{\hbar\omega_q} \\ & - \sum_{q\varsigma}\sum_{q'\varsigma'} \Gamma^{qq'}_{\varsigma\varsigma'} J_{-q\varsigma} J_{-q'\varsigma'} \left[\frac{1}{\hbar\omega_q} + \frac{1}{\hbar\omega_{-q}} \right] \left[\frac{1}{\hbar\omega_{q'}} + \frac{1}{\hbar\omega_{-q'}} \right]. \end{aligned} \tag{6.49}$$

[2] I.e., the terms contain a product of one or two photon variables.

[3] By comparison, the method in Paper II entails substituting a for $a'-A$ and requiring that linear terms are cancelled. $a = a'-A$ implies $a' = a+A$, hence the methods are equivalent.

$S^{\text{cav}}_{\text{bil}}$ contains all bilinear terms with respect to the shifted variables, and $S^{\text{cav}}_{\text{con}}$ the constant remainder. Expanding the parentheses in $S^{\text{cav}}_{\text{bil}}$ yields linear terms

$$\begin{aligned} S^{\text{cav}}_{\text{lin}} \equiv & \sum_{q\varsigma} (J_{q\varsigma} a_{q\varsigma} + J_{-q\varsigma} a^\dagger_{q\varsigma}) \\ & + \sum_{q\varsigma} \sum_{q'\varsigma'} \Gamma^{qq'}_{\varsigma\varsigma'} \Big[\left(J_{-q\varsigma}/\hbar\omega_q + J_{-q\varsigma}/\hbar\omega_{-q} \right) \left(a_{q'\varsigma'} + a^\dagger_{-q'\varsigma'} \right) \\ & \qquad + \left(a_{q\varsigma} + a^\dagger_{-q\varsigma} \right) \left(J_{-q'\varsigma'}/\hbar\omega_{q'} + J_{-q'\varsigma'}/\hbar\omega_{-q'} \right) \Big] \\ = & \sum_{q\varsigma} \left(J_{q\varsigma} + \sum_{q'\varsigma'} 2\Gamma^{qq'}_{\varsigma\varsigma'} \left[\frac{1}{\hbar\omega_{q'}} + \frac{1}{\hbar\omega_{-q'}} \right] J_{-q'\varsigma'} \right) \left(a_{q\varsigma} + a^\dagger_{-q\varsigma} \right). \end{aligned} \tag{6.50}$$

In the last line, we used $\Gamma^{qq'}_{\varsigma\varsigma'} + \Gamma^{q'q}_{\varsigma'\varsigma} = 2\Gamma^{qq'}_{\varsigma\varsigma'}$, which is seen by inspection of Eq. (6.39). Meanwhile, the original linear terms in the cavity action (6.43) read

$$S^{\text{cav}}_{\text{lin}} = \sum_{kd} \sum_{q\varsigma} g^{kq}_{d\varsigma} (\nu_d \eta_{-k} + \nu^*_d \eta^\dagger_k)(a_{q\varsigma} + a^\dagger_{-q\varsigma}) - \sum_{q\varsigma} \sum_{pm} \frac{\hbar}{\sqrt{\beta}} \frac{g^{qpp}_{\varsigma mm}}{E_{pm}} (a_{q\varsigma} + a^\dagger_{-q\varsigma}). \tag{6.51}$$

By the requirement that these be absorbed, the actions (6.50) and (6.51) are now equated. We can equate the magnonic and non-magnonic terms separately, yielding self-consistent equations for $G^{kq}_{d\varsigma}$ and $s_{q\varsigma}$:

$$G^{kq}_{d\varsigma} + \sum_{q'\varsigma'} 2\Gamma^{qq'}_{\varsigma\varsigma'} \left[\frac{1}{\hbar\omega_{q'}} + \frac{1}{\hbar\omega_{-q'}} \right] G^{k-q'}_{d\varsigma'} = g^{kq}_{d\varsigma}, \tag{6.52}$$

$$s_{q\varsigma} + \sum_{q'\varsigma'} 2\Gamma^{qq'}_{\varsigma\varsigma'} \left[\frac{1}{\hbar\omega_{q'}} + \frac{1}{\hbar\omega_{-q'}} \right] s_{-q'\varsigma'} = \sum_{pm} \frac{\hbar}{\sqrt{\beta}} \frac{g^{qpp}_{\varsigma mm}}{E_{pm}}. \tag{6.53}$$

Recall that these equations are valid only to second order in the cavity–SC coupling. We can therefore neglect the correction term in the equation for $s_{q\varsigma}$ since it is at most first order in this coupling. We can furthermore perform the sum over ω_n and isolate a Kronecker delta function. This leaves

$$s_{q\varsigma} \approx -\delta_{\Omega_n 0} \sqrt{\beta} \sum_{\mathbf{p}m} g^{\mathbf{qpp}}_{\varsigma mm} n_F(E_{\mathbf{p}m}). \tag{6.54}$$

Here we used the standard Matsubara result [108]

$$\frac{\hbar}{\beta} \sum_{\omega_n} \frac{1}{-i\hbar\omega_n + E_{\mathbf{p}m}} = -n_{\text{F}}(E_{\mathbf{p}m}), \tag{6.55}$$

with n_{F} the Fermi–Dirac distribution. We can furthermore simplify Eq. (6.52) for $G^{kq}_{d\varsigma}$, since corrections involving the cavity–SC coupling is at most second order

in this coupling. We can therefore swap $G^{kq}_{d\varsigma}$ for $g^{kq}_{d\varsigma}$ in the second term on the left-hand side, yielding

$$G^{kq}_{d\varsigma} \approx g^{kq}_{d\varsigma} - \sum_{q'\varsigma'} 2\Gamma^{qq'}_{\varsigma\varsigma'} \left[\frac{1}{\hbar\omega_{q'}} + \frac{1}{\hbar\omega_{-q'}} \right] g^{k-q'}_{d\varsigma'}. \tag{6.56}$$

Inserting the expression (6.39) for $\Gamma^{qq'}_{\varsigma\varsigma'}$, and summing over or factoring out Kronecker delta functions, this reads

$$\begin{aligned} G^{kq}_{d\varsigma} \approx \delta_{\Omega_m\Omega_n} \Bigg(& \delta_{\varsigma 1} g^{\mathbf{kq}}_{d} \\ & - \sum_{\mathbf{q}'} \sum_{pm} \sum_{\mathbf{p}'m'} \frac{\hbar}{\beta} \frac{g^{\mathbf{qpp}'}_{\varsigma mm'} g^{\mathbf{q}'\mathbf{p}'\mathbf{p}}_{1m'm}}{(E_{\mathbf{p}m} - i\hbar\omega_n)(E_{\mathbf{p}'m'} - i\hbar(\omega_n - \Omega_n))} \\ & \cdot \left[\frac{1}{\hbar\omega_{\mathbf{q}'} + i\hbar\Omega_m} + \frac{1}{\hbar\omega_{\mathbf{q}'} - i\hbar\Omega_m} \right] g^{\mathbf{k}-\mathbf{q}'}_{d} \Bigg). \end{aligned} \tag{6.57}$$

The sum over ω_n can be performed using the Matsubara result

$$\frac{\hbar}{\beta} \sum_{\omega_n} \frac{1}{(E_{\mathbf{p}m} - i\hbar\omega_n)(E_{\mathbf{p}'m'} - i\hbar(\omega_n - \Omega_n))} = \frac{n_F(E_{\mathbf{p}m}) - n_F(E_{\mathbf{p}'m'} + i\hbar\Omega_n)}{E_{\mathbf{p}m} - (E_{\mathbf{p}'m'} + i\hbar\Omega_n)}, \tag{6.58}$$

which holds provided $E_{\mathbf{p}m} \neq E_{\mathbf{p}'m'} + i\hbar\Omega_n$. We do not consider the special case where they are equal in this thesis (in which case the Matsubara sum evaluates a derivative of the Fermi–Dirac distribution). This is further simplified by use of the definition of the Matsubara frequency (6.18), leading to

$$\begin{aligned} n_F(E_{\mathbf{p}'m'} + i\hbar\Omega_n) &= \frac{1}{1 + \exp\left[\beta\left(E_{\mathbf{p}'m'} + i\hbar\Omega_n\right)/\hbar\right]} \\ &= \frac{1}{1 + \exp\left[\beta E_{\mathbf{p}'m'}/\hbar + i2\pi m\right]} \\ &= \frac{1}{1 + \exp\left[\beta E_{\mathbf{p}'m'}/\hbar\right]} \\ &= n_F(E_{\mathbf{p}'m'}). \end{aligned} \tag{6.59}$$

Inserting the above into Eq. (6.57) then ultimately yields

$$\begin{aligned} G^{kq}_{d\varsigma} \approx \delta_{\Omega_m\Omega_n} \Bigg(& \delta_{\varsigma 1} g^{\mathbf{kq}}_{d} \\ & - \sum_{\mathbf{q}'} \sum_{\mathbf{p}m} \sum_{\mathbf{p}'m'} 2 g^{\mathbf{qpp}'}_{\varsigma mm'} g^{\mathbf{q}'\mathbf{p}'\mathbf{p}}_{1m'm} \frac{n_F(E_{\mathbf{p}m}) - n_F(E_{\mathbf{p}'m'})}{(E_{\mathbf{p}m} - E_{\mathbf{p}'m'}) - i\hbar\Omega_n} \frac{\hbar\omega_{\mathbf{q}'}}{\hbar^2\omega^2_{\mathbf{q}'} + \hbar^2\Omega^2_n} g^{\mathbf{k}-\mathbf{q}'}_{d} \Bigg). \end{aligned} \tag{6.60}$$

Returning to the cavity partition function (6.42), by the shifts (6.44) and (6.45), and the recast action (6.47), we now have

$$Z^{\mathrm{cav}} = \int \mathcal{D}[a, a^\dagger] e^{-S^{\mathrm{cav}}/\hbar} = e^{-S^{\mathrm{cav}}_{\mathrm{con}}/\hbar} \int \mathcal{D}[a', a'^\dagger] e^{-S^{\mathrm{cav}}_{\mathrm{bil}}/\hbar}. \tag{6.61}$$

The integrand is independent of magnons, and therefore inconsequential to the physics of the FI. We therefore neglect this integral altogether, leaving only the exponential prefactor.

6.1.3 Effective magnon theory

We are thus left with an effective FI partition function

$$Z^{\mathrm{FI}} \equiv \int \mathcal{D}[\eta,\eta^\dagger] e^{-S^{\mathrm{FI}}/\hbar}, \tag{6.62}$$

where the effective FI action is

$$S^{\mathrm{FI}} \equiv S_0^{\mathrm{FI}} + S_{\mathrm{con}}^{\mathrm{cav}}. \tag{6.63}$$

We proceed to extract the magnon-dependent terms from $S_{\mathrm{con}}^{\mathrm{cav}}$, which contains the following products of source terms:

$$\begin{aligned} J_{-q\varsigma}J_{-q'\varsigma'} = &\sum_{kd}\sum_{k'd'} G_{d\varsigma}^{k-q}G_{d'\varsigma'}^{k'-q'}(\nu_d\eta_{-k}+\nu_d^*\eta_k^\dagger)(\nu_{d'}\eta_{-k'}+\nu_{d'}^*\eta_{k'}^\dagger) \\ &-\sum_{kd} G_{d\varsigma}^{k-q}s_{-q'\varsigma'}(\nu_d\eta_{-k}+\nu_d^*\eta_k^\dagger) - \sum_{kd} G_{d\varsigma'}^{k-q'}s_{-q\varsigma}(\nu_d\eta_{-k}+\nu_d^*\eta_k^\dagger) + \mathcal{O}(\eta^0), \end{aligned} \tag{6.64}$$

and $J_{q\varsigma}J_{-q\varsigma}$, which is readily found from the expression above. Here $\mathcal{O}(\eta^0)$ represent magnon-independent terms; neglecting these terms, S^{FI} reads, after some rewriting,

$$\begin{aligned} S^{\mathrm{FI}} = &\sum_k \hbar\lambda_k\eta_k^\dagger\eta_k - \sum_{kd}\sum_{k'd'}\sum_{q\varsigma}\frac{G_{d\varsigma}^{kq}G_{d'\varsigma}^{k'-q}}{\hbar\omega_q}(\nu_d\eta_{-k}+\nu_d^*\eta_k^\dagger)(\nu_{d'}\eta_{-k'}+\nu_{d'}^*\eta_{k'}^\dagger) \\ &+\sum_{kd}\sum_{q\varsigma} G_{d\varsigma}^{kq}s_{-q\varsigma}\left[\frac{1}{\hbar\omega_q}+\frac{1}{\hbar\omega_{-q}}\right](\nu_d\eta_{-k}+\nu_d^*\eta_k^\dagger) \\ &-\sum_{kd}\sum_{k'd'}\sum_{q\varsigma}\sum_{q'\varsigma'}\Gamma_{\varsigma\varsigma'}^{qq'}\left[\frac{1}{\hbar\omega_q}+\frac{1}{\hbar\omega_{-q}}\right]\left[\frac{1}{\hbar\omega_{q'}}+\frac{1}{\hbar\omega_{-q'}}\right] \\ &\quad\cdot G_{d\varsigma}^{k-q}G_{d'\varsigma'}^{k'-q'}(\nu_d\eta_{-k}+\nu_d^*\eta_k^\dagger)(\nu_{d'}\eta_{-k'}+\nu_{d'}^*\eta_{k'}^\dagger) \\ &+\sum_{kd}\sum_{q\varsigma}\sum_{q'\varsigma'}2\Gamma_{\varsigma\varsigma'}^{qq'}\left[\frac{1}{\hbar\omega_q}+\frac{1}{\hbar\omega_{-q}}\right]\left[\frac{1}{\hbar\omega_{q'}}+\frac{1}{\hbar\omega_{-q'}}\right]G_{d\varsigma'}^{k-q'}s_{-q\varsigma}(\nu_d\eta_{-k}+\nu_d^*\eta_k^\dagger). \end{aligned} \tag{6.65}$$

Finally, gathering terms, S^{FI} reads

$$S^{\mathrm{FI}} = \sum_k \hbar\lambda_k\eta_k^\dagger\eta_k + \sum_{kd}\sum_{k'd'} Q_{dd'}^{kk'}(\nu_d\eta_{-k}+\nu_d^*\eta_k^\dagger)(\nu_{d'}\eta_{-k'}+\nu_{d'}^*\eta_{k'}^\dagger) - \sum_{kd} P_d^k(\nu_d\eta_{-k}+\nu_d^*\eta_k^\dagger). \tag{6.66}$$

Above, we introduced the effective magnon–magnon coupling

$$Q_{dd'}^{kk'} \equiv -\sum_{q\varsigma}\left[\frac{G_{d\varsigma}^{kq}G_{d'\varsigma}^{k'-q}}{\hbar\omega_q} + \sum_{q'\varsigma'}\Gamma_{\varsigma\varsigma'}^{qq'}\left[\frac{1}{\hbar\omega_q}+\frac{1}{\hbar\omega_{-q}}\right]\left[\frac{1}{\hbar\omega_{q'}}+\frac{1}{\hbar\omega_{-q'}}\right]G_{d\varsigma}^{k-q}G_{d'\varsigma'}^{k'-q'}\right], \tag{6.67}$$

aggregating FI–cavity–FI interactions to all orders in the Zeeman coupling, and FI–cavity–SC–cavity–FI interactions to second order in the paramagnetic coupling (see Fig. 7.1). Furthermore, we introduced the coefficients of the linear magnon terms

$$\begin{aligned} P_d^k \equiv -\sum_{q\varsigma}\Bigg[& G_{d\varsigma}^{kq}s_{-q\varsigma}\left[\frac{1}{\hbar\omega_q}+\frac{1}{\hbar\omega_{-q}}\right] \\ & + \sum_{q'\varsigma'}2\Gamma_{\varsigma\varsigma'}^{qq'}\left[\frac{1}{\hbar\omega_q}+\frac{1}{\hbar\omega_{-q}}\right]\left[\frac{1}{\hbar\omega_{q'}}+\frac{1}{\hbar\omega_{-q'}}\right]G_{d\varsigma'}^{k-q'}s_{-q\varsigma}\Bigg]. \end{aligned} \tag{6.68}$$

Since our theory is only valid to second order in the cavity–SC coupling, and $\Gamma_{\varsigma\varsigma'}^{qq'}$ and $s_{-q\varsigma}$ are respectively second (Eq. (6.39)) and first (Eq. (6.54)) order, the second line in the summand drops out. Furthermore, $G_{d\varsigma}^{kq}$ contains a second-order term (see Eq. (6.60)) that also drops out when multiplied by $s_{-q\varsigma}$. Inserting for $G_{d\varsigma}^{kq}$ and $s_{-q\varsigma}$, we are then left with

$$\begin{aligned} P_d^k &\approx -\sum_{q\varsigma}G_{d\varsigma}^{kq}s_{-q\varsigma}\left[\frac{1}{\hbar\omega_q}+\frac{1}{\hbar\omega_{-q}}\right] \\ &\approx \delta_{\Omega_m 0}\sum_{\mathbf{q}}\sum_{\mathbf{p}m}\frac{2\sqrt{\beta}\,g_{1mm}^{-\mathbf{qpp}}\,g_d^{\mathbf{kq}}}{\hbar\omega_{\mathbf{q}}}n_F(E_{\mathbf{p}m}). \end{aligned} \tag{6.69}$$

Up to a multiplicative constant, this represents the components (d) of the effective anisotropy field induced across the FI due to the cavity-mediated interactions with the SC (see Paper II).

$Q_{dd'}^{kk'}$ can be simplified by the same arguments. Using Eqs. (6.58)–(6.60), we ultimately find

$$\begin{aligned} Q_{dd'}^{kk'} \equiv & -\delta_{\Omega_m,-\Omega_{m'}}g_d^{\mathbf{kq}}g_{d'}^{\mathbf{k}',-\mathbf{q}}\sum_{\mathbf{q}}\Bigg(\frac{1}{\hbar\omega_{\mathbf{q}}-i\hbar\Omega_m} \\ & -\frac{1}{2}\sum_{\mathbf{q}'}\sum_{\mathbf{p}m}\sum_{\mathbf{p}'m'}\frac{2\hbar\omega_{\mathbf{q}'}}{\hbar^2\omega_{\mathbf{q}'}^2+\hbar^2\Omega_m^2}\frac{2\hbar\omega_{\mathbf{q}}}{\hbar^2\omega_{\mathbf{q}}^2+\hbar^2\Omega_m^2}g_{1mm'}^{-\mathbf{q},\mathbf{pp}'}\,g_{1m'm}^{\mathbf{q}'\mathbf{p}'\mathbf{p}}\frac{n_F(E_{\mathbf{p}m})-n_F(E_{\mathbf{p}'m'})}{(E_{\mathbf{p}m}-E_{\mathbf{p}'m'})-i\hbar\Omega_m}\Bigg). \end{aligned} \tag{6.70}$$

We now have an effective FI action from which we can extract quantities of interest. The effective coupling $Q_{dd'}^{kk'}$ gives rise to corrections in the magnon spectrum due to interactions with the cavity and the SC. Deriving such corrections is

involved, so we return to this in more detail in Ch. 7, where we also present numerical results for the corrections. In the following section, we derive the reorientation of spins effectuated across the FI, due to the effective anisotropy field (6.69).

6.1.4 Reorientation of spins

Repeating the exercise from Sec. 6.1.2, we now seek to complete the square by absorbing the linear magnon terms in the effective FI action (6.66) into the bilinear terms.[4] This leads to a bilinear theory in a new magnon basis,

$$\eta'_k \equiv \eta_k - t_k, \tag{6.71}$$

$$\eta'_k \equiv \eta_k^\dagger - t_k^*, \tag{6.72}$$

where t_k is a constant. This implies the expectation value $\langle \eta'_k \rangle = 0$, and thus $\langle \eta_k \rangle = t_k$. For a proof, see Appendix D. A finite t_k can thus give rise to a finite expectation value of the in-plane spin components: By Eqs. (2.27), (2.39), (6.12), (6.71) and (6.72), we have

$$\begin{aligned}
\langle S_{id} \rangle =& \frac{\hbar\sqrt{2S}}{2}(\nu_d \langle \eta_i \rangle + \nu_d^* \langle \eta_i^\dagger \rangle) \\
=& \frac{\hbar\sqrt{2S}}{2} \frac{1}{\sqrt{\beta N_{\mathrm{FI}}}} \sum_k (\nu_d \langle \eta_k \rangle + \nu_d^* \langle \eta_{-k}^\dagger \rangle) e^{ik\cdot r_i} \\
=& \frac{\hbar\sqrt{2S}}{2} \frac{1}{\sqrt{\beta N_{\mathrm{FI}}}} \sum_k (\nu_d t_k + \nu_d^* t_{-k}^*) e^{ik\cdot r_i} \\
=& \hbar \sqrt{\frac{2S}{\beta N_{\mathrm{FI}}}} \sum_k \Re\left[\nu_d t_k e^{ik\cdot r_i} \right],
\end{aligned} \tag{6.73}$$

with $r_i \equiv (\tau, \mathbf{r}_i)$. A non-zero $\langle S_{id} \rangle$ indicates that the spin axis of quantization is tilted away from the z axis, which was assumed to be the axis of quantization when introducing the magnon basis in the introductory section 2.2. In other words, a finite t_k implies the FI is subjected to an (effective) anisotropy field.

Note that the initial assumption (2.23) on the low number of magnons limits the range for the magnitude of t_k, beyond which our calculations are no longer consistent. We therefore recast the inequality to highlight this. We opt for an intuitive recasting, expressing the inequality as a condition on the magnitude of the in-plane spin component. This is done as follows: The expectation value of the in-plane spin component is $\sum_d \langle S_{id} \rangle \hat{e}_d$, hence by Eq. (6.73) its squared magnitude is

$$\langle S_{ix} \rangle^2 + \langle S_{iy} \rangle^2 = \frac{\hbar^2 2S}{\beta N_{\mathrm{FI}}} \sum_{kk'} t_k^* t_{k'} e^{i(k'-k)\cdot r_i}. \tag{6.74}$$

[4] Again, in this context, “linear" and “bilinear" mean the terms contain a product of one or two magnon variables.

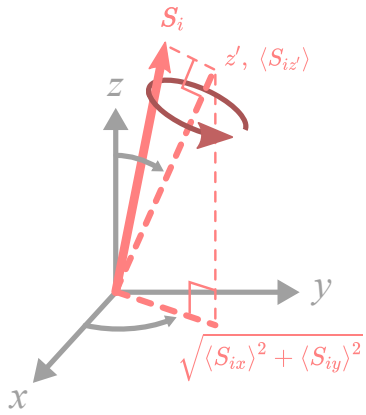

Figure 6.2: Illustration showing the projections of the single-site spin $\mathbf{S}_i$ onto the new axis z' of quantization ($\langle S_{iz'}\rangle$) and the xy plane ($\sqrt{\langle S_{ix}\rangle^2 + \langle S_{iy}\rangle^2}$).

Meanwhile, upon introducing the shifts (6.71) and (6.72), the inequality (2.23) can be written as

$$\begin{aligned}
&\left\langle \left(\eta_i'^{\dagger} + \frac{1}{\sqrt{\beta N_{\mathrm{FM}}}} \sum_k t_k^* e^{-ik\cdot r_i} \right) \left(\eta_i' + \frac{1}{\sqrt{\beta N_{\mathrm{FM}}}} \sum_k t_k e^{ik\cdot r_i} \right) \right\rangle \\
&= \langle \eta_i'^{\dagger} \eta_i' \rangle + \frac{1}{\beta N_{\mathrm{FI}}} \sum_{kk'} t_k^* t_{k'} e^{i(k'-k)\cdot r_i} \\
&= \langle \eta_i^{\dagger} \eta_i \rangle + \frac{1}{\hbar^2 2S} \left(\langle S_{ix}\rangle^2 + \langle S_{iy}\rangle^2 \right) \\
&\ll 2S. \qquad (6.75)
\end{aligned}$$

Using $2S \approx S$ and the now weaker inequality $\langle \eta_i'^{\dagger} \eta_i' \rangle \ll 2S$, this can be rewritten as

$$\langle S_{ix}\rangle^2 + \langle S_{iy}\rangle^2 \ll \hbar^2 (S - \langle \eta_i'^{\dagger} \eta_i' \rangle)^2 \equiv \langle S_{iz'}\rangle^2. \qquad (6.76)$$

Here z' is the new axis of quantization, and $\langle S_{iz'}\rangle$ the corresponding projection of $\mathbf{S}_i$, as illustrated in Fig. 6.2. For very low temperatures, $\langle \eta_i'^{\dagger} \eta_i' \rangle \approx 0$, and $\langle S_{iz'}\rangle \approx \hbar S$. Thus, the inequality reads

$$\langle S_{ix}\rangle^2 + \langle S_{iy}\rangle^2 \ll \hbar^2 S^2. \qquad (6.77)$$

Equation for t_k

Moving on, we now seek to derive an equation from which t_k can be determined. By postulation, the new bilinear theory in the $\{\eta'_k, \eta'^{\dagger}_k\}$ basis, reads

$$\begin{aligned} S^{\mathrm{FI}} = &\sum_k \hbar\lambda_k (\eta_k + t_k)^\dagger (\eta_k + t_k) \\ &+ \sum_{kd}\sum_{k'd'} Q^{kk'}_{dd'} (\nu_d(\eta_{-k} + t_{-k}) + \nu^*_d(\eta_k + t_k)^\dagger) \\ &\cdot (\nu_{d'}(\eta_{-k'} + t_{-k'}) + \nu^*_{d'}(\eta_{k'} + t_{k'})^\dagger) + \text{const.}, \end{aligned} \tag{6.78}$$

where the last term comprises magnon-independent terms. Expanding the parentheses, we get linear magnon terms that by assumption equal the linear terms in Eq. (6.66). This equality can be divided into one for η_k terms and one for $\eta^\dagger_k$ terms, which are equivalent up to a Hermitian conjugation. The equality of $\eta^\dagger_k$-dependent terms reads

$$\begin{aligned} &\sum_k \hbar\lambda_k t_k \eta^\dagger_k + \sum_{kd}\sum_{k'd'} Q^{kk'}_{dd'} \Big(\nu^*_d(\nu_{d'} t_{-k'} + \nu^*_{d'} t^*_{k'})\eta^\dagger_k + \nu^*_{d'}(\nu_d t_{-k} + \nu^*_d t^*_k)\eta^\dagger_{k'} \Big) \Big] \\ &= \sum_{kd} P^k_d \nu^*_d \eta^\dagger_k. \end{aligned} \tag{6.79}$$

With some rewriting, we can collect all the coefficients in front of $\eta^\dagger_k$ under the sum over k. Since $\eta^\dagger_k$ for all k are independent variables of integration, we can equate coefficients for each k, yielding the self-consistency equation for t_k

$$t_k = -\frac{1}{\hbar\lambda_k} \left(\sum_d \sum_{k'd'} \left(Q^{kk'}_{dd'} + Q^{k'k}_{d'd} \right) \nu^*_d (\nu_{d'} t_{-k'} + \nu^\dagger_{d'} t^*_{k'}) + \sum_d P^k_d \nu^*_d \right). \tag{6.80}$$

We have thus arrived at one of the main results of this thesis: The reorientation of FI spins due to the presence of the SC inside the cavity, or more precisely Eq. (6.80). Note the general dependence of t_k on $\mathbf{k}$, meaning the spins are reoriented locally (i.e. per lattice site).

An expression for the effective anisotropy field, along with a numerical example, is presented in Paper II. In Sec. 8.2, we provide reflections on the anisotropy result: we compare it to the response when the SC is in the normal state, address the issue of cavity modes spatially decohering over the separation distance of the FI and the SC, and suggest ways of easing constraints on the set-up, in particular the Pearl length criterion and that the SC be screened from the aligning field $\mathbf{B}_{\mathrm{ext}}$. Moreover, in Appendix A, we use mean field theory to derive the FI spin reorientation to leading order in the cavity–SC coupling, which validates the result (6.80) above.

In Paper II, we furthermore elaborate on why the contributions to the effective anisotropy field originate from interactions with states in a narrow vicinity of

the Fermi surface. The extent of this vicinity is determined by the supercurrent momentum $\mathbf{P}$. This is not a trivial observation based on the general expressions presented here (Eq. (6.68) for the anisotropy field), but is more readily seen in the simple example presented in the paper. This is sensible, since the interactions involve scattering of SC quasiparticles, and the low-energy events are concentrated near the Fermi energy.

The next quantity we seek to extract are the corrections to the magnon spectrum due to cavity-mediated interaction with the SC quasiparticles. For practical purposes, we consider a modified set-up in this case. We therefore address this in the next chapter.

Trivial result in absence of supercurrent

We conclude this chapter by showing that in the absence of a supercurrent ($\mathbf{P} = \mathbf{0}$), there is no reorientation of the FI spins. By inspection of Eq. (6.69) for P_d^k, one sees that for $\mathbf{P} = \mathbf{0}$, the summand is odd in $\mathbf{p}$, as $g_{1mm}^{-\mathbf{q},-\mathbf{p},-\mathbf{p}} = -g_{1mm}^{-\mathbf{qpp}}$, and $E_{-\mathbf{p}m} = E_{\mathbf{p}m}$. Thus $P_d^k = 0$. We are then left with the equation

$$t_k = -\frac{1}{\hbar\lambda_k} \sum_d \sum_{k'd'} \left(Q_{dd'}^{kk'} + Q_{d'd}^{k'k} \right) \nu_d^* (\nu_{d'} t_{-k'} + \nu_{d'}^\dagger t_{k'}^*) \tag{6.81}$$

for t_k (cf. Eq. (6.80)). Every term in this equation scales with t_k, meaning one solution is $t_k = 0$. This is indeed *the* solution: Expanding t_k in orders of the FI–cavity and cavity–SC coupling constant, it is clear that to lowest order, the right-hand side vanishes, and $t_k = 0$. To higher orders, t_k is a function of itself to lower orders; since $t_k = 0$ to lowest order, we therefore have $t_k = 0$ to all orders.

Thus, in the absence of supercurrent, there is no reorientation of FI spins, and there is also no anisotropy field. This is seen to originate from the odd inversion symmetry of the summand in the anisotropy field (6.69), which the supercurrent breaks. From this we can infer that the reorientation (anisotropy field) gauges the broken inversion symmetry of the SC.

Key takeaways:

- In the Matsubara path integral formalism, expectation values at thermal equilibrium are evaluated using imaginary-time path integrals.
- The formalism allows for an exact integrating-out of the cavity photons. In contrast to common perturbative approaches involving in particular the Schrieffer–Wolff transformation, the resulting effective theory is valid also in resonant regimes, i.e. when the magnon energy, or the SC quasiparticle energy differences, match the photon energy. The formalism furthermore readily enables us to integrate out the SC sector to second order in the cavity–SC coupling, an order beyond mean field theory.
- The resulting effective magnon theory (action) reads

$$S^{\mathrm{FI}} = \sum_{k} \hbar\lambda_k \eta_k^\dagger \eta_k + \sum_{kd}\sum_{k'd'} Q_{dd'}^{kk'} (\nu_d \eta_{-k} + \nu_d^* \eta_k^\dagger)(\nu_{d'} \eta_{-k'} + \nu_{d'}^* \eta_{k'}^\dagger) - \sum_{kd} P_d^k (\nu_d \eta_{-k} + \nu_d^* \eta_k^\dagger).$$

  In order, it contains bare diagonal magnon terms, bilinear magnon terms originating from FI–cavity–FI and FI–cavity–SC–cavity–FI interactions, and linear magnon terms originating from SC–cavity–FI interactions. The bilinear terms renormalize the magnon spectrum, the continued analysis of which is deferred to Ch. 7.
- The linear terms express broken inversion symmetry in the SC. In our set-up, we break this with a finite supercurrent. These terms represent an effective in-plane anisotropy field across the FI, resulting in a local reorientation of the FI spins. This is expressed as a shift t_k (t_k^*) in the magnon variables η_k ($\eta_k^\dagger$) found by absorbing the linear terms into the bilinear terms. The shift reads

$$t_k = -\frac{1}{\hbar\lambda_k}\left(\sum_{d}\sum_{k'd'}\left(Q_{dd'}^{kk'} + Q_{d'd}^{k'k}\right)\nu_d^*(\nu_{d'} t_{-k'} + \nu_{d'}^\dagger t_{k'}^*) + \sum_d P_d^k \nu_d^*\right).$$

  A numerical example for the effective anisotropy field is presented in Paper II.

Chapter 7

Anticrossings in the magnon dispersion

Chapter summary: Applying the effective magnon theory found in the previous chapter to a revised set-up, we extract an expression for the renormalized magnon spectrum. The spectrum is modified by a large number of anticrossings induced by scattering events in the SC. We provide a numerical analysis of the magnon self-energy for a specific material choice of the FI and SC, including results within a detectable range. The shape and magnitude of the self-energy depend in particular on directional derivatives near the SC Fermi surface, and is sensitive to the onset of superconductivity. This suggests the renormalized magnon spectrum can be used to resolve momentum anisotropy in generalized SC gaps.

The effective FI action (6.66) can in principle be diagonalized to yield new quasiparticle energies. The new dispersion relations are only affected by the bilinear magnon terms, since the linear terms can be absorbed into a new magnon basis (cf. Eq. (6.78)) without affecting the coefficients of the bilinear terms. Of particular interest is the effect of the SC on the new FI quasiparticle energies: We will show that by matching magnon energies with differences in SC quasiparticle energies, vacuum fluctations in the cavity field will induce anticrossings despite the FI and the SC not being coupled to each other directly.

The corrections to the magnon spectrum emerge from the effective magnon–magnon coupling $Q^{kk'}_{dd'}$ (Eq. (6.67)) in the effective action (6.66). The contributions involving the SC enter via the factor $\Gamma^{qq'}_{\varsigma\varsigma'}$ (Eq. (6.39)), and the corresponding interactions are illustrated in Fig. 7.1a. The remaining contributions to $Q^{kk'}_{dd'}$ are due to FI–cavity–FI interactions, and are illustrated in Fig. 7.1b. After presenting our results, we will elaborate in Ch. 8 on the application of these corrections to remotely resolve anisotropy of generalized SC gaps in the magnon spectrum, for future work.

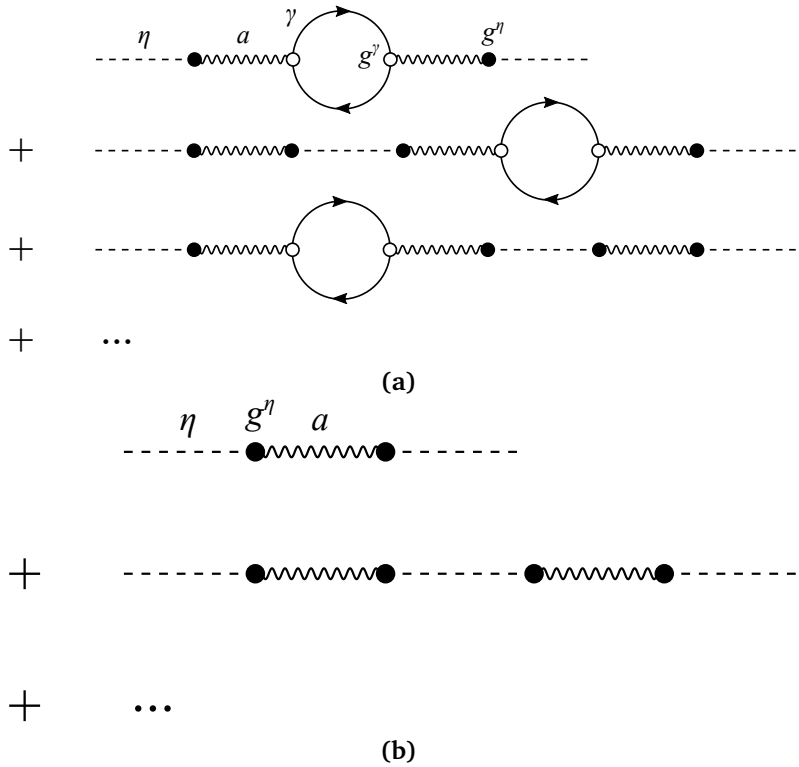

Figure 7.1: Feynman diagrams of the interactions that contribute to the effective magnon–magnon coupling (6.67), and give rise to corrections in the magnon spectrum. (a) shows the contributions involving the SC. Here, a magnon (η) is converted to a photon (a) and back again an arbitrary number of times, due to the FI–cavity coupling (g^η). At some point, the photon is absorbed by an SC quasiparticle (γ) via the cavity–SC coupling (g^γ), and another photon is subsequently re-emitted. It then oscillates between a photon and a magnon state an arbitrary number of times, eventually exiting as another magnon. (b) shows the contributions that only involve the cavity.

Anticrossings in particle spectra due to indirect, cavity-mediated interactions, have been demonstrated for a ferro- and antiferromagnetic magnon mode [10], and a magnon mode and a qubit [13, 14], in both case interacting via a single cavity mode. Our research distinguishes itself in that we consider an FI coupling to an SC, and that we consider the individual couplings of every magnon mode, to a broad range of SC quasiparticle modes, via a range of cavity modes. This many-particle aspect is inherent to the system as one photon can scatter any SC quasiparticle state.

7.1 Deriving quasiparticle energies

To determine corrections to the magnon spectrum, we must derive them. One common method by which quasiparticle (i.e. eigenmode) energies are derived, is by diagonalizing the system. The diagonalization of bosonic systems is highly non-trivial. Care must be taken in order to preserve bosonic commutation relations, as stressed in Refs. [104, 105], who present a general diagonalization procedure for many-particle, bilinear, Hermitian Hamiltonians. In the non-Hermitian case ($\mathcal{H}^\dagger \neq \mathcal{H}$)[1], which becomes relevant to us when we eventually assess losses, the diagonalization is even more involved as conjugate quasiparticle operators $(b, \bar{b})$ are no longer generally Hermitian conjugates ($\bar{b} \neq b^\dagger$). However, they still share a bosonic commutator relation ($[b, \bar{b}] = 1$), and relate to opposite complex eigenvalues ($\pm\Lambda \in \mathbb{C}$) [111–113].

The path integral formalism is a powerful tool in the context of diagonalizing many-particle systems, or more precisely in extracting quantities that normally require some level of diagonalization in operator mechanics. In particular, so long as the terms entering the action are no more than bilinear in the respective particle types (integration variables), the often convoluted process of diagonalizing a Hamiltonian can for many purposes be disregarded altogether in favor of making use of well-known properties of Gaussian integrals. This has already been demonstrated twice in integrating out both the SC and the cavity in Ch. 6. In this chapter, we will continue to make use of the properties of Gaussian integrals, this time in order to extract the quasiparticle energies via the two-point correlation functions (propagators) of the eigenmodes.

First, inspecting the effective action (6.66), note that a Matsubara basis magnon η_k or $\eta_k^\dagger$ couples to a finite set of other magnons, even though there are infinitely many Matsubara frequencies. $Q^{kk'}_{dd'}$ involves a product of delta functions that can be rewritten as

$$\delta_{\omega_n',\omega_n-\Omega_n}\delta_{\omega_n,\omega_n'-\Omega_n'}\delta_{\Omega_m\Omega_n}\delta_{\Omega_m'\Omega_n'} = \delta_{\omega_n',\omega_n-\Omega_m}\delta_{\Omega_n',-\Omega_n}\delta_{\Omega_m\Omega_n}\delta_{\Omega_m',-\Omega_m}, \tag{7.1}$$

where ω_n, ω_n' are Matsubara frequencies of the SC quasiparticles, Ω_n, Ω_n' those of the photons, and Ω_m, Ω_m' those of the magnons. The last delta function $\delta_{\Omega_m',-\Omega_m}$ implies only magnons with frequencies $\pm\Omega_m$ couple. In analogy to the treatment of non-Hermitian Hamiltonians [111–113], we can therefore write the non-Hermitian effective action (6.66) as an infinite sum of finite vector–matrix–vector products,

[1]This mathematical jargon means that the eigenvalues of $\mathcal{H}$ (i.e. the quasiparticle energies) are no longer guaranteed to be real valued. Hence the time evolution operator $e^{-iEt/\hbar}$ acquires an exponentially increasing or decreasing part $e^{\Im Et/\hbar}$, reflecting changes in the energy of the system due to e.g. external drives or losses.

one for each set of coupled modes:

$$S^{\mathrm{FI}} = \sum_{\Omega_m} \begin{pmatrix} \eta_{k_1} \\ \eta_{k_2} \\ \vdots \\ \eta^\dagger_{k_1} \\ \eta^\dagger_{k_2} \\ \vdots \end{pmatrix}^\dagger \begin{pmatrix} & \omega & & \nu & \\ & & & & \\ & & & & \\ & \nu^* & & \omega^T & \end{pmatrix} \begin{pmatrix} \eta_{k_1} \\ \eta_{k_2} \\ \vdots \\ \eta^\dagger_{k_1} \\ \eta^\dagger_{k_2} \\ \vdots \end{pmatrix} \equiv \sum_{\Omega_m} \eta^\dagger \mathcal{M} \eta. \tag{7.2}$$

Here, $\eta_{k_1}, \eta_{k_2}, \ldots$ are $\mathcal{N} = 2N_{\mathrm{FI}}$ coupled modes (one mode for each Matsubara frequency $\pm\Omega_m$ and every value of $\mathbf{k}$), and ω and ν are $\mathcal{N}$-by-$\mathcal{N}$ matrices. So long as the magnons couple to the photons (the alternative $Q^{kk'}_{dd'} = 0$ is not interesting to us), we have $Q^{kk'}_{dd'} \neq 0$, hence $\nu \neq 0$, hence the overall $2\mathcal{N}$-by-$2\mathcal{N}$ matrix cannot be reduced to an $\mathcal{N}$-by-$\mathcal{N}$ matrix.

Suppose now we diagonalized S^{FI}. The diagonal Matsubara basis is $\{\mu_k, \bar{\mu}_k\}$, and the effective action (7.2) can be written as

$$\begin{aligned} S^{\mathrm{FI}} &= \frac{1}{2} \sum_{\Omega_m} \begin{pmatrix} \bar{\mu}_1 & \bar{\mu}_2 & \ldots & \mu_1 & \mu_2 & \ldots \end{pmatrix} \begin{pmatrix} \mathcal{G}_1^{-1} & & & & & \\ & \mathcal{G}_2^{-1} & & & & \\ & & \ddots & & & \\ & & & \mathcal{G}_1^{-1} & & \\ & & & & \mathcal{G}_2^{-1} & \\ & & & & & \ddots \end{pmatrix} \begin{pmatrix} \mu_1 \\ \mu_2 \\ \vdots \\ \bar{\mu}_1 \\ \bar{\mu}_2 \\ \vdots \end{pmatrix} \\ &\equiv \frac{1}{2} \sum_{\Omega_m} \overline{\mu} \mathcal{G}^{-1} \mu, \end{aligned} \tag{7.3}$$

with $\mathcal{G}_\rho^{-1}$ the inverse propagators (which are complex numbers, not matrices like ω and ν), and $\mathcal{G}^{-1}$ is the diagonal matrix of these. The factor $\frac{1}{2}$ takes into account the double counting of modes. The quasiparticle energies are then given by the poles of $\mathcal{G}_\rho$ upon analytical continuation for complex values of

$$z = i\hbar\Omega_m. \tag{7.4}$$

In other words, we must find the solutions for z for which

$$\mathcal{G}_\rho^{-1}(z) = 0. \tag{7.5}$$

The interpretation of the propagator poles as quasiparticle energies is elegantly presented in Ref. [114], where it is demonstrated by resolving Green's functions in many-particle eigenstates.

With the aim of extracting the quasiparticle energies, the challenge we are faced with now is to arrive at an expression for the inverse propagators in Eq. (7.5). This would appear to involve diagonalizing the matrix (7.2) in order to determine the diagonal elements of Eq. (7.3). However, there are methods by which this is circumvented, of which we mention two below.

7.1.1 Self-energy approach

The self energy $\Sigma^{\mathbf{k}}$ expresses the collective corrections to the energy of a particle due to interactions with its surroundings, and is a standard object of study in many-particle physics [115]. It is also the quantity we will proceed to analyze in this chapter. The self energy is by definition the difference between the bare particle energy (here $\hbar\lambda_{\mathbf{k}}$) and the renormalized particle energy in the presence of interactions. In the particle propagator, this generally appears as a factor $(z-\hbar\lambda_{\mathbf{k}}-\Sigma^{\mathbf{k}}(z))^{-1}$ that diverges form some z [114], which is essentially the condition (7.5), hence this solution represents a quasiparticle energy.

Eq. (7.5) can be divided into a real and an imaginary part, from which the real and imaginary part of the quasiparticle energy can be extracted. These represent the renormalized spectrum and (essentially) the lifetime of the quasiparticle, respectively [114–116]; in this chapter we will only be concerned with the former, as corrections to the particle energies are only meaningful if they can first be shown to be detectable. The equation for the renormalized energies therefore reads

$$\Re[\hbar\lambda_{\mathbf{k}} + \Sigma^{\mathbf{k}}(z) - z] = 0. \tag{7.6}$$

It seems, then, that we have only supplanted the question of determining the unknown quantity $\mathcal{G}_{\rho}^{-1}(z)$ with another one, viz., $\Re\Sigma^{\mathbf{k}}(z)$. However, as it turns out, by a suitable configuration of the system and an assumption on weak coupling, the effective action (6.66) is immediately diagonalized, enabling us to read off $\Sigma^{\mathbf{k}}(z)$ (Sec. 7.3). The weak coupling assumption can then be invoked again to argue that corrections to the self energy, itself a correction, is negligible. We can thus replace the quasiparticle energy z entering the argument, by the bare energy $\hbar\lambda_{\mathbf{k}}$. We then straight-away obtain an expression for $\Re\Sigma^{\mathbf{k}}$ (Sec. 7.4), which we go on to compute numerically in an example. With material parameters for Bismuth-doped YIG (Bi:YIG) (FI) and Nb (SC), we achieve promising results measured against expected losses (Sec. 7.4.1). Finally, we analyze the correction, attempting to understand the intricacies that modulate its shape and magnitude (Sec. 7.4.2).

7.1.2 Determinant approach

We present here briefly another approach that was applied in the first attempt to extract quasiparticle energies from the effective action (6.66). In Appendix C, we have attached a draft for a manuscript that was written in parallel with these calculations, which later turned out to be overestimates when compared with the numerics. We nevertheless find it interesting to include the draft for contrast to the self-energy approach (Sec. 7.1.1) to be pursued in this chapter: Near the final step, we replace SC quasiparticle energy differences with a weighted average, which in effect collapses an enormous number of FI–SC interactions into one. As we will elaborate on in in Sec. 7.4.2, this step was the source of the overestimation. This was done in order to make analytical solutions for the quasiparticle energy equation tractable; in hindsight it is clear the solutions found via the determinant would have been the same as those found via the self-energy approach, if the

weak coupling assumption had been invoked in place of introducing the weighted average (see Appendix C).

The method is based on the following. Consider the determinant $\det \mathcal{G}^{-1}$ of the diagonal matrix in Eq. (7.3). Since this simply equates to the product of the propagators,

$$\det \mathcal{G}^{-1} = \prod_{\rho} \mathcal{G}_{\rho}^{-1}, \tag{7.7}$$

equating it to zero,

$$\det \mathcal{G}^{-1}(z) = 0, \tag{7.8}$$

amounts to aggregating all the equations (7.5) into one. We now use that $\mathcal{G}^{-1}$ and the non-diagonal matrix $\mathcal{M}$ (Eq. (7.2)) must relate by some transformation matrices

$$\eta^{\dagger}\mathcal{M}\eta = \eta^{\dagger}(\bar{\mathcal{T}}\bar{\mathcal{T}}^{-1})\mathcal{M}(\mathcal{T}^{-1}\mathcal{T})\eta = (\eta^{\dagger}\bar{\mathcal{T}})(\bar{\mathcal{T}}^{-1}\mathcal{M}\mathcal{T}^{-1})(\mathcal{T}\eta) = \overline{\mu}\mathcal{G}^{-1}\mu, \tag{7.9}$$

cf. Refs. [111–113].[2] The matrices $\mathcal{T}$ and $\bar{\mathcal{T}}$ must be invertible in order for their inverses to exist, hence $\det \mathcal{T}, \det \bar{\mathcal{T}} \neq 0$. Therefore

$$\det \mathcal{G}^{-1}(z) = \det \bar{\mathcal{T}}^{-1}(z)\mathcal{M}(z)\mathcal{T}^{-1}(z) = (\det \bar{\mathcal{T}}^{-1}(z))(\det \mathcal{M}(z))(\det \mathcal{T}^{-1}(z)) = 0 \tag{7.10}$$

implies

$$\det \mathcal{M}(z) = 0. \tag{7.11}$$

We thus circumvent the issue of having to determine expressions for $\mathcal{G}_{\rho}^{-1}(z)$; instead, we can look for solutions for z satisfying Eq. (7.11). Now we again use that the determinant of a matrix is the product of its eigenvalues, this time to reduce the order of calculations in z. With $\det \mathcal{M}(z) = \prod_{\rho} m_{\rho}(z)$, the equations for determining the renormalized spectra are

$$m_{\rho}(z) = 0. \tag{7.12}$$

This approach is a good starting point for numerical analysis, as deriving the eigenvalues (or simply the determinant) from the effective action (6.66) is straightforward. Plotting $\log \frac{1}{\sqrt{\det \mathcal{M}(z)}}$ for a range of z and (in our case) $\mathbf{k}$ immediately gives an idea of renormalized spectra.

As in the self-energy approach, a prerequisite to obtaining interesting analytical solutions is a suitable choice of system configuration. We address this in the next section.

[2] These references technically concern matrix diagonalization in *operator mechanics* (not in the context of path integrals), but our statements here are general and do not invoke operator mechanics.

7.2 Choosing a set-up

We seek system configurations that simplify the effective action (6.66). As it stands, generally all modes couple to each other. The number of quasiparticles being the same as the number of particles (including all the cavity and SC modes that were integrated out in Ch. 6), the number and order of equations (7.5) to be solved would generally be analytically insurmountable. However, there are system configurations for which modes couple mutually only in small subsets, while coupling to modes outside these sets are either vanishing or negligible. These subsets can consequently be considered separately, substantially simplifying our calculations.

Our first task is therefore to find a specific set-up for which the $2\mathcal{N}$-by-$2\mathcal{N}$ matrix (7.2) reduces to an uncoupled set of small matrices. By inspection of the action (6.66), we find two particular special cases of interest:

- If the FI is much smaller than the cavity, only $k = (\Omega_m, \mathbf{0})$ and $k = (-\Omega_m, \mathbf{0})$ modes couple.
- If the FI spans the cavity, only $+k$ and $-k$ modes couple.

For the set-up analyzed thus far (Fig. 1.3), we expect the following results:

- If the FI spans the cavity, the aligning external field $\mathbf{B}_{\text{ext}}$ will invariably pass through the SC as well, compromising its superconducting properties.[3] If the FI only approximately spans the cavity, there will be space for only a small SC, and its influence becomes vanishingly small.[4] So, we discard these configurations.
- If the FI is very small, the SC will only affect the $\mathbf{k} = \mathbf{0}$ mode. While this does give rise to an anticrossing, the anticrossing will not be able to resolve momentum information about the superconducting gap, aside from a net contribution by all SC quasiparticle modes. This is because in this case, the $\mathbf{k} = \mathbf{0}$ mode couples to all relevant photon modes, meaning it aggregates information about all the scattering events in the SC, regardless of the magnitude and direction of the momentum transfer in each event.

While an anticrossing in itself can be interesting, we instead opt to study a modified set-up, which not only leads to corrections to the magnon spectrum, but also leaves each magnon coupled to a minimal set of photons (instead of the entire range of photons), thus enabling the magnons to distinguish between scattering events in the SC. This opens the doors to remotely resolving momentum information about generalized gaps in the corrections to the magnon spectrum in future works (to be addressed in Ch. 8). Before addressing this prospect, it is first necessary to establish a measurable correction to the magnon spectra, so we consider the simpler case of an isotropic gap in this chapter.

The modified set-up is illustrated in Fig. 7.2. As in the previous set-up (Fig. 1.3),

[3] See Ch. 8 for discussion on this assumption.

[4] Some of the results to be presented in Sec. 7.4.1 for an SC that spans the *entire* cavity are promising, but do not far exceed expected losses. This validates the assertion that a considerably smaller SC would result in an insignificant response.

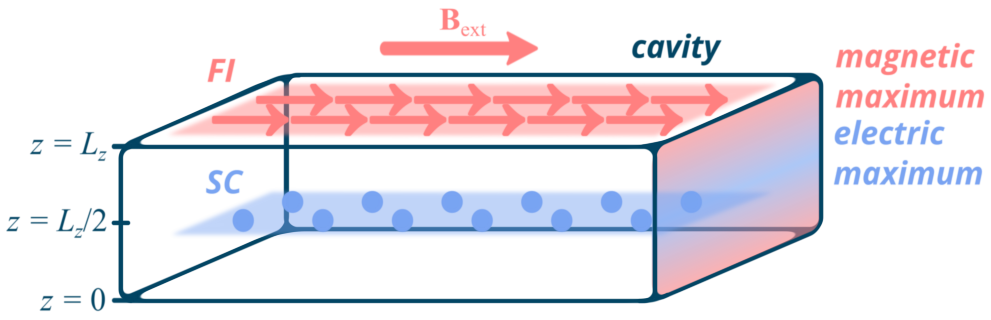

Figure 7.2: Set-up for analyzing corrections to the magnon spectrum due to cavity-mediated interactions with the SC quasiparticles. The set-up is the same as in Fig. 1.3, except the FI and the SC span the cavity, and the aligning field $\mathbf{B}_{\text{ext}}$ points along the y direction. Note that the axes and origin are the same as in Fig. 1.3, but omitted here to prevent clutter.

we respectively place an FI and an SC thin film at the top and in the middle of a cavity with dimensions $L_x, L_y \gg L_z$. However, we now direct the applied external field $\mathbf{B}_{\text{ext}}$ *in-plane* across the FI. We thus consider a configuration not permitted by the one in Fig. 1.3: the FI and the SC *both* spanning the cavity. In this case, only $+k$ and $-k$ modes couple in the FI, and each magnon mode ($\mathbf{k}$) couples to only two photon modes ($\mathbf{q} = \pm\mathbf{k}$)[5], in turn carrying information from only two scattering events on the SC ($\mathbf{p} \pm \mathbf{q}$ scattered to $\mathbf{p}$). This minimally aggregates momentum information from the SC in the FI, which is promising for the prospect of probing a generalized SC gap using the FI.

7.3 Effective action

The effective action (6.66) referred to so far was derived based on the set-up in Fig. 1.3, so we first need to derive the corresponding effective action based on the set-up in Fig. 7.2. This elicits modifications of the Hamiltonian.

The SC Hamiltonian (5.30) is the same as before, but can be simplified since the SC spans the cavity; then $D^{\text{SC}}_{\mathbf{p}-\mathbf{p}',\mathbf{q}} \approx \delta_{\mathbf{p}',\mathbf{p}-\mathbf{q}}$ (limiting ourselves to the SC 1BZ), so

$$\mathcal{H}_{\text{SC}} = \sum_{\mathbf{p}m} E_{\mathbf{p}m} \gamma^\dagger_{\mathbf{p}m} \gamma_{\mathbf{p}m} + \sum_{\mathbf{k}\varsigma} \sum_{\mathbf{p}m} \sum_{m'} g^{\mathbf{kp}}_{\varsigma m m'} (a_{\mathbf{k}\varsigma} + a^\dagger_{-\mathbf{k}\varsigma}) \gamma^\dagger_{\mathbf{p}m} \gamma_{\mathbf{p}-\mathbf{k},m'}, \tag{7.13}$$

where we have defined $g^{\mathbf{kp}}_{\varsigma m m'} \equiv g^{\mathbf{k},\mathbf{p},\mathbf{p}-\mathbf{k}}_{\varsigma m m'}$ (see Eq. (5.29)). For completeness, we

[5] A detail to note here is that this means the magnon $\mathbf{k}$ mode couples to the magnon $-\mathbf{k}$ mode via the photons. But, these are the only magnon modes to couple mutually for a given $\mathbf{k}$.

write this coupling constant out in full for this special case:

$$g^{\mathbf{kp}}_{\varsigma mm'} \equiv \begin{pmatrix} g^{\mathbf{k},\mathbf{p}+\mathbf{P}}_{\varsigma} u_{\mathbf{p}} u^*_{\mathbf{p}-\mathbf{k}} - g^{\mathbf{k},-\mathbf{p}+\mathbf{P}}_{\varsigma} v_{\mathbf{p}} v^*_{\mathbf{p}-\mathbf{k}} & g^{\mathbf{k},\mathbf{p}+\mathbf{P}}_{\varsigma} u_{\mathbf{p}} v_{\mathbf{p}-\mathbf{k}} + g^{\mathbf{k},-\mathbf{p}+\mathbf{P}}_{\varsigma} v_{\mathbf{p}} u_{\mathbf{p}-\mathbf{k}} \\ g^{\mathbf{k},-\mathbf{p}+\mathbf{P}}_{\varsigma} u^*_{\mathbf{p}} v^*_{\mathbf{p}-\mathbf{k}} + g^{\mathbf{k},\mathbf{p}+\mathbf{P}}_{\varsigma} v^*_{\mathbf{p}} u^*_{\mathbf{p}-\mathbf{k}} & -g^{\mathbf{k},-\mathbf{p}+\mathbf{P}}_{\varsigma} u^*_{\mathbf{p}} u_{\mathbf{p}-\mathbf{k}} + g^{\mathbf{k},\mathbf{p}+\mathbf{P}}_{\varsigma} v^*_{\mathbf{p}} v_{\mathbf{p}-\mathbf{k}} \end{pmatrix}_{mm'}, \tag{7.14}$$

where we have reduced the expression (5.22) for $g^{\mathbf{kpp}'}_{\varsigma}$ to

$$g^{\mathbf{k}}_{\mathbf{p}\varsigma} \equiv \sum_d O^{\mathbf{k}}_{\varsigma d} 2i \frac{eat}{\hbar} \sqrt{\frac{\hbar}{\epsilon \omega_{\mathbf{k}} V}} \sin[a_{\mathrm{SC}}(p_d + k_d/2)]. \tag{7.15}$$

Here we substituted $\mathbf{p} \to \mathbf{p} + \mathbf{k}$, which reproduces the coupling constant from Ref. [11].[6]

The FI Hamiltonian requires more extensive modifications, which we address in the section below.

7.3.1 Modifying the FI Hamiltonian

Because the aligning field $\mathbf{B}_{\mathrm{ext}}$ is in-plane, pointing along $\hat{e}_y$, we first need to redefine the magnons with respect to this new axis of quantization.

First, we define the helical spin operators

$$S_{i\pm} \equiv S_{iz} \pm i S_{ix}, \quad S_{i+} = S^{\dagger}_{i-}, \tag{7.16}$$

and perform the Holstein–Primakoff transformation

$$\begin{aligned} S_{i-} &\equiv \eta^{\dagger}_i \hbar \sqrt{2S} \sqrt{1 - \frac{\eta^{\dagger}_i \eta_i}{2S}}, \\ S_{i+} &\equiv \hbar \sqrt{2S} \sqrt{1 - \frac{\eta^{\dagger}_i \eta_i}{2S}} \eta_i. \end{aligned} \tag{7.17}$$

Hence, as before,

$$S_{iy} = \hbar(S - \eta^{\dagger}_i \eta_i), \tag{7.18}$$

and assuming a strong aligning field $\mathbf{B}_{\mathrm{ext}}$ (i.e. few magnons, $\langle \eta^{\dagger}_i \eta_i \rangle \ll 2S$),

$$S_{i-} \approx \hbar \sqrt{2S} \eta^{\dagger}_i, \quad S_{i+} \approx \hbar \sqrt{2S} \eta_i. \tag{7.19}$$

The Cartesian spin components are then

$$S_{id} = \frac{\hbar \sqrt{2S}}{2} (\nu_d \eta_i + \nu^*_d \eta^{\dagger}_i), \tag{7.20}$$

where now $d = z, x$ and $\{\nu_z, \nu_x\} = \{1, -i\}$.

[6] Observe then that in Ref. [11], equal transversal dimensions of the normal metal (corresponding to our SC) and the cavity is implicitly assumed upon invoking conservation of momentum.

The new magnon basis alters the expression for the Zeeman coupling with the FI: Inserting Eqs. (7.20), (5.9b) and (2.28) into Eq. (5.1), one finds

$$\begin{aligned}
\mathcal{H}_{\text{FI-cav}} =& -\frac{g\mu_B}{\hbar}\sum_i \mathbf{S}_i\cdot\mathbf{B}_{\text{cav}}(\mathbf{r}_i)\\
=& -\frac{g\mu_B}{\hbar}\sum_i\Bigg(\frac{1}{\sqrt{N_{\text{FI}}}}\sum_{\mathbf{k}}\sum_d \frac{\hbar\sqrt{2S}}{2}(\nu_d\eta_{\mathbf{k}}e^{i\mathbf{k}\cdot\mathbf{r}_i}+\nu_d^*\eta_{\mathbf{k}}^\dagger e^{-i\mathbf{k}\cdot\mathbf{r}_i})\hat{e}_d\\
&+\hbar S\left(1-\frac{1}{N_{\text{FI}}}\sum_{\mathbf{k}\mathbf{k}'}\frac{\eta_{\mathbf{k}}^\dagger\eta_{\mathbf{k}'}}{S}e^{i(\mathbf{k}'-\mathbf{k})\cdot\mathbf{r}_i}\right)\hat{e}_y\Bigg)\\
&\cdot\left(\sum_{\mathbf{q}}\left(q_y\hat{e}_x-q_x\hat{e}_y\right)i\sin\theta_{\mathbf{q}}\sqrt{\frac{\hbar}{\epsilon\omega_{\mathbf{q}}V}}e^{i\mathbf{q}\cdot\mathbf{r}_i}(a_{\mathbf{q}1}+a_{-\mathbf{q}1}^\dagger)\right).
\end{aligned}\tag{7.21}$$

Some terms vanish. First, the product of the z components vanishes as $\mathbf{B}_{\text{cav}}$ has no z component at $z=L_z$ (the location of the FI). Secondly, some linear photon terms vanish, as

$$\frac{g\mu_B}{\hbar}\sum_i\hbar S\sum_{\mathbf{q}}iq_x\sin\theta_{\mathbf{q}}\sqrt{\frac{\hbar}{\epsilon\omega_{\mathbf{q}}V}}e^{i\mathbf{q}\cdot\mathbf{r}_i}(a_{\mathbf{q}1}+a_{-\mathbf{q}1}^\dagger)\propto\sum_i e^{i\mathbf{q}\cdot\mathbf{r}_i}\propto\delta_{\mathbf{q}\mathbf{0}}.\tag{7.22}$$

Both q_x and $\sin\theta_{\mathbf{q}}$ in the summand are zero for $\mathbf{q}=\mathbf{0}$, so these linear terms vanish. More precisely, the sum $\sum_i e^{i\mathbf{q}\cdot\mathbf{r}_i}=N^{\text{FI}}\sum_{\tilde{\mathbf{0}}}\delta_{\mathbf{q}\tilde{\mathbf{0}}}$ (cf. Eq. (7.26)), with $\tilde{\mathbf{0}}$ any photon momentum $\mathbf{q}$ that is equivalent to $\mathbf{0}$ across FI Brilluoin zones. However, the coefficient of the linear photon terms scale as $q_x/\sqrt{|\mathbf{q}|}$ for large $\mathbf{q}$, while the coefficient of the diagonal photon terms scale as $\omega_{\mathbf{q}}\sim|\mathbf{q}|$. Hence the influence of the linear terms on the theory is expected to be vanishingly small for $\mathbf{q}$ outside the 1BZ, i.e. for large $\mathbf{q}$.

We therefore find

$$\begin{aligned}
\mathcal{H}_{\text{FI-cav}} =& -\frac{g\mu_B}{\hbar}\sum_i\Bigg(\frac{1}{\sqrt{N_{\text{FI}}}}\sum_{\mathbf{k}}\frac{\hbar\sqrt{2S}}{2i}(\eta_{\mathbf{k}}e^{i\mathbf{k}\cdot\mathbf{r}_i}-\eta_{\mathbf{k}}^\dagger e^{-i\mathbf{k}\cdot\mathbf{r}_i})\sum_{\mathbf{q}}iq_y\sin\theta_{\mathbf{q}}\sqrt{\frac{\hbar}{\epsilon\omega_{\mathbf{q}}V}}e^{i\mathbf{q}\cdot\mathbf{r}_i}(a_{\mathbf{q}1}+a_{-\mathbf{q}1}^\dagger)\\
&+\hbar S\frac{1}{N_{\text{FI}}}\sum_{\mathbf{k}\mathbf{k}'}\frac{\eta_{\mathbf{k}}^\dagger\eta_{\mathbf{k}'}}{S}e^{i(\mathbf{k}'-\mathbf{k})\cdot\mathbf{r}_i}\sum_{\mathbf{q}}iq_x\sin\theta_{\mathbf{q}}\sqrt{\frac{\hbar}{\epsilon\omega_{\mathbf{q}}V}}e^{i\mathbf{q}\cdot\mathbf{r}_i}(a_{\mathbf{q}1}+a_{-\mathbf{q}1}^\dagger)\Bigg)\\
=& -\sum_{\mathbf{k}}\sum_{\mathbf{q}}\hbar\frac{g\mu_B}{\hbar}q_y\sin\theta_{\mathbf{q}}\sqrt{\frac{\hbar S}{2\epsilon\omega_{\mathbf{q}}VN_{\text{FI}}}}(\eta_{\mathbf{k}}\sum_i e^{i(\mathbf{k}+\mathbf{q})\cdot\mathbf{r}_i}-\eta_{\mathbf{k}}^\dagger\sum_i e^{-i(\mathbf{k}-\mathbf{q})\cdot\mathbf{r}_i})(a_{\mathbf{q}1}+a_{-\mathbf{q}1}^\dagger)\\
&-\sum_{\mathbf{k}\mathbf{k}'}\sum_{\mathbf{q}}\hbar\frac{g\mu_B}{\hbar N_{\text{FI}}}iq_x\sin\theta_{\mathbf{q}}\sqrt{\frac{\hbar}{\epsilon\omega_{\mathbf{q}}V}}\sum_i e^{i(\mathbf{k}'-\mathbf{k}+\mathbf{q})\cdot\mathbf{r}_i}\eta_{\mathbf{k}}^\dagger\eta_{\mathbf{k}'}(a_{\mathbf{q}1}+a_{-\mathbf{q}1}^\dagger)\\
\approx& \sum_{\mathbf{k}}g_{\mathbf{k}}^{\eta}(\eta_{-\mathbf{k}}-\eta_{\mathbf{k}}^\dagger)(a_{\mathbf{k}1}+a_{-\mathbf{k}1}^\dagger)+\sum_{\mathbf{k}\mathbf{k}'}g_{\mathbf{k}'}^{\eta\eta}\eta_{\mathbf{k}}^\dagger\eta_{\mathbf{k}-\mathbf{k}'}(a_{\mathbf{k}'1}+a_{-\mathbf{k}'1}^\dagger),
\end{aligned}\tag{7.23}$$

where we introduced the FI–cavity coupling constants

$$g_{\mathbf{q}}^{\eta} \equiv -g\mu_B q_y \sin\theta_{\mathbf{q}} \sqrt{\frac{\hbar S N_{\mathrm{FI}}}{2\epsilon\omega_{\mathbf{q}} V}}, \tag{7.24}$$

$$g_{\mathbf{q}}^{\eta\eta} \equiv -ig\mu_B q_x \sin\theta_{\mathbf{q}} \sqrt{\frac{\hbar}{\epsilon\omega_{\mathbf{q}} V}}. \tag{7.25}$$

For the last line of Eq. (7.23), we used

$$\sum_i e^{-i(\mathbf{k}-\mathbf{q})\cdot\mathbf{r}_i} = N^{\mathrm{FI}} \sum_{\tilde{\mathbf{k}}} \delta_{\mathbf{q}\tilde{\mathbf{k}}}, \tag{7.26}$$

with $\tilde{\mathbf{k}}$ any photon momentum $\mathbf{q}$ that is equivalent to $\mathbf{k}$ across FI Brilluoin zones. We then limited the photon momentum range to the FI 1BZ (hence the approximation sign in Eq. (7.23)): as argued below Eq. (7.22) in regards to neglecting linear photon terms, the coefficients of the interaction terms in Eq. (7.23) also scale slower with $\mathbf{q}$ than the diagonal photon terms, so their influence become negligible for high photon momenta.

This concludes the modifications for the FI Hamiltonian, and we move onto deriving the effective action.

7.3.2 Deriving the effective action

The system Hamiltonian for the set-up in Fig. 7.2 is thus

$$\begin{aligned}\mathcal{H} = &\sum_{\mathbf{k}} \hbar\lambda_{\mathbf{k}} \eta_{\mathbf{k}}^{\dagger}\eta_{\mathbf{k}} + \sum_{\mathbf{p}m} E_{\mathbf{p}m}\gamma_{\mathbf{p}m}^{\dagger}\gamma_{\mathbf{p}m} + \sum_{\mathbf{k}\varsigma} \hbar\omega_{\mathbf{k}} a_{\mathbf{k}\varsigma}^{\dagger} a_{\mathbf{k}\varsigma} \\ &+ \sum_{\mathbf{k}} g_{\mathbf{k}}^{\eta}(\eta_{-\mathbf{k}} - \eta_{\mathbf{k}}^{\dagger})(a_{\mathbf{k}1} + a_{-\mathbf{k}1}^{\dagger}) + \sum_{\mathbf{k}\mathbf{k}'} g_{\mathbf{k}'}^{\eta\eta}\eta_{\mathbf{k}}^{\dagger}\eta_{\mathbf{k}-\mathbf{k}'}(a_{\mathbf{k}'1} + a_{-\mathbf{k}'1}^{\dagger}) \\ &+ \sum_{\mathbf{k}\varsigma}\sum_{\mathbf{p}m}\sum_{m'} g_{\varsigma m m'}^{\mathbf{k}\mathbf{p}}(a_{\mathbf{k}\varsigma} + a_{-\mathbf{k}\varsigma}^{\dagger})\gamma_{\mathbf{p}m}^{\dagger}\gamma_{\mathbf{p}-\mathbf{k},m'}. \end{aligned} \tag{7.27}$$

We do not need to derive the effective action in order to conclude that the contributions from the scattering terms $\sim \eta_{\mathbf{k}}^{\dagger}\eta_{\mathbf{k}-\mathbf{k}'}(a_{\mathbf{k}'1} + a_{-\mathbf{k}'1}^{\dagger})$ are negligible in the effective theory. It suffices to sketch the terms precipitating from integrating out the cavity and the SC from the theory:

- Sketched, the initial action contains interaction terms of the following forms: $(\eta + \eta^{\dagger})(a + a^{\dagger})$, $\eta^{\dagger}\eta(a + a^{\dagger})$ and $(a + a^{\dagger})\gamma^{\dagger}\gamma$.
- After integrating out the cavity, the effective interaction terms are of the forms $(\eta + \eta^{\dagger})(\eta + \eta^{\dagger})$, $(\eta + \eta^{\dagger})\gamma^{\dagger}\gamma$, $\gamma^{\dagger}\gamma\gamma^{\dagger}\gamma$, $(\eta + \eta^{\dagger})\eta^{\dagger}\eta$, $\eta^{\dagger}\eta\eta^{\dagger}\eta$ and $\eta^{\dagger}\eta\gamma^{\dagger}\gamma$. Only the last three forms are due to the interaction $\eta^{\dagger}\eta(a + a^{\dagger})$. All the terms involving products of more than two magnon operators are negligible, since we have assumed a small number of magnons (i.e. $\langle\eta_i^{\dagger}\eta_i\rangle \ll 2S$), leaving $\eta^{\dagger}\eta\gamma^{\dagger}\gamma$ the only form that traces back to $\eta^{\dagger}\eta(a + a^{\dagger})$.

- After integrating out the SC, the effective interactions due to $\eta^\dagger\eta\gamma^\dagger\gamma$ are of the forms $(\eta+\eta^\dagger)\eta^\dagger\eta$ and $\eta^\dagger\eta\eta^\dagger\eta$. These are also negligible due to the low number of magnons.

Furthermore, the coupling constant $g^\eta_{\mathbf{q}}$ scales as $\sqrt{N_{\mathrm{FI}}}$ with the number of FI lattice points, while $g^{\eta\eta}_{\mathbf{q}}$ does not, leaving the latter relatively diminished for any sizable lattice. Hence, we can neglect the terms $\sim \eta^\dagger_{\mathbf{k}}\eta_{\mathbf{k}-\mathbf{k}'}(a_{\mathbf{k}'1}+a^\dagger_{-\mathbf{k}'1})$ from our initial Hamiltonian altogether. This is convenient, since we may then recycle the effective action (6.66) with only a few modifications to the sums and coefficients. Neglecting the linear magnon terms for the reasons argued in the beginning of Ch. 7, the effective Matsubara action reads

$$S^{\mathrm{FI}} = \sum_k \hbar\lambda_k \eta^\dagger_k\eta_k + \sum_k Q^k(\eta_{-k}-\eta^\dagger_k)(\eta_k-\eta^\dagger_{-k}), \tag{7.28}$$

with

$$\begin{aligned}
Q^k \equiv& -\frac{g^\eta_{\mathbf{k}}g^\eta_{-\mathbf{k}}}{\hbar\omega_k} + \frac{\hbar}{2\beta}\sum_{pmm'}\frac{g^{\mathbf{kp}}_{1mm'}g^{-\mathbf{k},\mathbf{p}-\mathbf{k}}_{1m'm}}{(E_{\mathbf{p}m}-i\hbar\omega_n)(E_{\mathbf{p}-\mathbf{k},m'}-i\hbar(\omega_n-\Omega_m))} \\
&\cdot\left[\frac{1}{\hbar\omega_k}+\frac{1}{\hbar\omega_{-k}}\right]\left[\frac{1}{\hbar\omega_{-k}}+\frac{1}{\hbar\omega_k}\right]g^\eta_{\mathbf{k}}g^\eta_{-\mathbf{k}} \\
=&|g^\eta_{\mathbf{k}}|^2\left(\frac{1}{\hbar\omega_k}-\frac{1}{2}\sum_{\mathbf{p}mm'}|g^{\mathbf{kp}}_{1mm'}|^2\frac{n_F(E_{\mathbf{p}m})-n_F(E_{\mathbf{p}-\mathbf{k},m'}+i\hbar\Omega_m)}{E_{\mathbf{p}m}-(E_{\mathbf{p}-\mathbf{k},m'}+i\hbar\Omega_m)}\frac{4\hbar^2\omega^2_{\mathbf{k}}}{(\hbar^2\omega^2_{\mathbf{k}}+\hbar^2\Omega^2_m)^2}\right) \\
=&|g^\eta_{\mathbf{k}}|^2\left(\frac{1}{\hbar\omega_k}-\frac{2\hbar^2\omega^2_{\mathbf{k}}}{(\hbar^2\omega^2_{\mathbf{k}}+\hbar^2\Omega^2_m)^2}\sum_{\mathbf{p}mm'}|g^{\mathbf{kp}}_{1mm'}|^2\frac{n_F(E_{\mathbf{p}m})-n_F(E_{\mathbf{p}-\mathbf{k},m'})}{\Delta E^{\mathbf{kp}}_{mm'}-i\hbar\Omega_m}\right).
\end{aligned} \tag{7.29}$$

Above, we used that $g^\eta_{\mathbf{k}}g^\eta_{-\mathbf{k}} = -|g^\eta_{\mathbf{k}}|^2$ and $g^{\mathbf{kp}}_{1mm'}g^{-\mathbf{k},\mathbf{p}-\mathbf{k}}_{1m'm} = |g^{\mathbf{kp}}_{1mm'}|^2$, as can be verified by inspection of Eqs. (7.14) and (7.24). We furthermore used the Matsubara result (6.58) along with Eq. (6.59) (note that the special case $E_{\mathbf{p}m} = E_{\mathbf{p}-\mathbf{k},m'}+i\hbar\Omega_m$ is not interesting. It implies $\mathbf{k}=\mathbf{0}$, in which case $Q^k = 0$ because $g^\eta_{\mathbf{0}} = 0$, so we can discard this special case). Finally, we introduced the energy difference

$$\Delta E^{\mathbf{kp}}_{mm'} \equiv E_{\mathbf{p}m} - E_{\mathbf{p}-\mathbf{k},m'}. \tag{7.30}$$

Clearly, the terms inside the parenthesis in Eq. (7.29) respectively stem from FI–cavity–FI and FI–cavity–SC–cavity–FI interactions, cf. Fig. 7.1.

7.3.3 Simplifications

Several contribution to the effective coupling Q^k are small, and only serve to complicate further analysis. In the following, we therefore perform a series of simplifications.

Consider the analytical continuation $i\hbar\Omega_m \to z$. First, we find numerically that $\hbar\omega_{\mathbf{k}}$ tends to be much greater than $\Delta E^{\mathbf{kp}}_{mm'}$ in our set-up. Because we are interested in anticrossings between $\Delta E^{\mathbf{kp}}_{mm'}$ and $\hbar\lambda_{\mathbf{k}}$, we can assume z is on the order of $\Delta E^{\mathbf{kp}}_{mm'}$, and thus $z \ll \hbar\omega_{\mathbf{k}}$. We can therefore let

$$\frac{1}{\hbar\omega_{\mathbf{k}} \pm z} \approx \frac{1}{\hbar\omega_{\mathbf{k}}}. \tag{7.31}$$

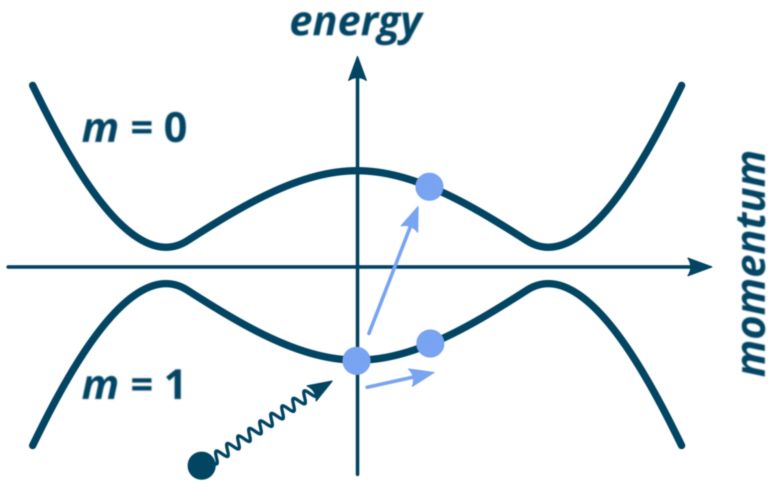

Figure 7.3: Illustration of an SC quasiparticle (light blue) being scattered by an incoming photon (dark blue). The quasiparticle type and corresponding band is labeled m. The scattering can result in the type either persisting or changing (light blue arrows), with the former generally requiring more energy.

Secondly, we find numerically that the off-diagonal $m \neq m'$ elements of the summand in Q^k are very small compared to the diagonal elements. Physically, these elements originate from scattering processes in which the photon not only imparts its momentum onto the scattered SC quasiparticle, but also changes its type, cf. Fig. 7.3. This requires more energy than scattering that preserves the quasiparticle type, which suppresses the interaction.

Mathematically, this is because the critical current is typically low (associated with momenta $\mathbf{P}$ near the origin of the SC 1BZ); and the coupling is suppressed at large $\mathbf{k}$ due to a factor $1/\sqrt{\omega_{\mathbf{k}}}$, and is furthermore modulated slowly as $\sim \sin(p_d a_{\mathrm{SC}})$. We can therefore rule out interactions beyond a regime where $\mathbf{P}, \mathbf{k} \ll \mathbf{p}$; in this regime, however, the terms in the $m \neq m'$ elements in Eq. (5.29) are seen to nearly cancel. By contrast, in the same regime, the terms in the $m = m'$ elements in Eq. (5.29) add constructively. We therefore neglect the $m \neq m'$ elements. The regime can be narrowed down further by observing that the factor $n_F(E_{\mathbf{p}m}) - n_F(E_{\mathbf{p}-\mathbf{k},m})$ in Eq. (7.29) is highly peaked near the Fermi surface, and zero everywhere else; we can therefore narrow the range of $\mathbf{p}$ down to Fermi momenta $\mathbf{p}_F$, which are usually very large, i.e. $\mathbf{P}, \mathbf{k} \ll \mathbf{p}_F$.

With the simplifications thus far, the expression for Q^k becomes

$$Q^k \approx |g_{\mathbf{k}}^{\eta}|^2 \left(\frac{1}{\hbar\omega_{\mathbf{k}}} - \frac{2}{\hbar^2\omega_{\mathbf{k}}^2} \sum_{\mathbf{p}\approx\mathbf{p}_F,m} |g_{1mm}^{\mathbf{kp}}|^2 \frac{n_F(E_{\mathbf{p}m}) - n_F(E_{\mathbf{p}-\mathbf{k},m})}{\Delta E_{mm}^{\mathbf{kp}} - z} \right). \tag{7.32}$$

Here "$\mathbf{p} \approx \mathbf{p}_F$" symbolically represents a summation interval around the Fermi momenta; the limits of the interval are left to be determined numerically by gauging the stability of the sum. Now, we can simplify Q^k further by performing the sum over m. Using $E_{-\mathbf{p}1} = -E_{\mathbf{p}0}$ (hence $\Delta E_{11}^{\mathbf{kp}} = -\Delta E_{00}^{-\mathbf{k},-\mathbf{p}}$), we find

$$Q^k \approx |g_{\mathbf{k}}^{\eta}|^2 \Bigg(\frac{1}{\hbar\omega_{\mathbf{k}}} - \frac{2}{\hbar^2\omega_{\mathbf{k}}^2} \sum_{\mathbf{p}\approx\mathbf{p}_F} \Bigg[|g_{100}^{\mathbf{kp}}|^2 \frac{n_F(E_{\mathbf{p}0}) - n_F(E_{\mathbf{p}-\mathbf{k},0})}{\Delta E_{00}^{\mathbf{kp}} - z} + |g_{111}^{\mathbf{kp}}|^2 \frac{n_F(-E_{-\mathbf{p}0}) - n_F(-E_{-\mathbf{p}+\mathbf{k},0})}{-\Delta E_{00}^{-\mathbf{k},-\mathbf{p}} - z} \Bigg] \Bigg). \tag{7.33}$$

We now substitute $\mathbf{p} \longrightarrow -(\mathbf{p}-\mathbf{k})$, and shift the range of $\sum_{\mathbf{p}\approx\mathbf{p}_F}$ back to the SC 1BZ as before. Using $-\Delta E_{00}^{-\mathbf{k},\mathbf{p}-\mathbf{k}} = \Delta E_{00}^{\mathbf{kp}}$, we then get

$$Q^k \approx |g_{\mathbf{k}}^{\eta}|^2 \Bigg(\frac{1}{\hbar\omega_{\mathbf{k}}} - \frac{2}{\hbar^2\omega_{\mathbf{k}}^2} \sum_{\mathbf{p}\approx\mathbf{p}_F} \frac{1}{\Delta E_{00}^{\mathbf{kp}} - z} \Bigg[|g_{100}^{\mathbf{kp}}|^2 \left(n_F(E_{\mathbf{p}0}) - n_F(E_{\mathbf{p}-\mathbf{k},0}) \right) + |g_{111}^{\mathbf{k},-(\mathbf{p}-\mathbf{k})}|^2 \left(n_F(-E_{\mathbf{p}-\mathbf{k},0}) - n_F(-E_{\mathbf{p}0}) \right) \Bigg] \Bigg). \tag{7.34}$$

By inspection of Eq. (5.29), we find that $g_{111}^{\mathbf{k},-(\mathbf{p}-\mathbf{k})} = -g_{100}^{\mathbf{kp}}$. Thus, using $n_F(x) - n_F(-x) = -\tanh(\beta x/2\hbar)$, we finally get

$$Q^k \approx |g_{\mathbf{k}}^{\eta}|^2 \left(\frac{1}{\hbar\omega_{\mathbf{k}}} - \frac{2}{\hbar^2\omega_{\mathbf{k}}^2} \sum_{\mathbf{p}\approx\mathbf{p}_F} |g_{100}^{\mathbf{kp}}|^2 \frac{\tanh\left(\frac{\beta E_{\mathbf{p}-\mathbf{k},0}}{2\hbar}\right) - \tanh\left(\frac{\beta E_{\mathbf{p},0}}{2\hbar}\right)}{\Delta E_{00}^{\mathbf{kp}} - z} \right). \tag{7.35}$$

Having performed the sum over m, we can easily implement the following, final simplification. Because the external field $\mathbf{B}_{\text{ext}}$ raises the magnon energy and is assumed strong, the magnon energy $\hbar\lambda_{\mathbf{k}}$ can be assumed non-negative for all $\mathbf{k}$. There will therefore be no anticrossings at negative energies, so we can neglect negative values of $\Delta E_{00}^{\mathbf{kp}}$. Hence

$$Q^k \approx |g_{\mathbf{k}}^{\eta}|^2 \left(\frac{1}{\hbar\omega_{\mathbf{k}}} - \frac{2}{\hbar^2\omega_{\mathbf{k}}^2} \sum_{\mathbf{k}\mathbf{p}\approx\mathbf{p}_F}{}' |g_{100}^{\mathbf{kp}}|^2 \frac{\tanh\left(\frac{\beta E_{\mathbf{p}-\mathbf{k},0}}{2\hbar}\right) - \tanh\left(\frac{\beta E_{\mathbf{p},0}}{2\hbar}\right)}{\Delta E_{00}^{\mathbf{kp}} - z} \right), \tag{7.36}$$

where $\sum'_{\mathbf{p}\approx\mathbf{p}_F}$ only sums over $\mathbf{p}$ for which $\Delta E_{00}^{\mathbf{kp}} \geq 0$. Note finally that $\Delta E_{00}^{\mathbf{kp}} \geq 0$ implies $E_{\mathbf{p}0} \geq E_{\mathbf{p}-\mathbf{k},0}$, meaning

$$\tanh\left(\frac{\beta E_{\mathbf{p}-\mathbf{k},0}}{2\hbar}\right) - \tanh\left(\frac{\beta E_{\mathbf{p},0}}{2\hbar}\right) \leq 0. \tag{7.37}$$

With increasing values of z along the real axis, the summand in Eq. (7.36) is therefore clearly negative for $z \ll \Delta E_{00}^{\mathbf{kp}}$ and positive for $z \gg \Delta E_{00}^{\mathbf{kp}}$. Near $z \approx \Delta E_{00}^{\mathbf{kp}}$, the summand becomes relatively large before switching its overall sign, only kept from diverging by an imaginary contribution $\Im z$ owing to losses. In other words, every term in the sum represents an anticrossing in the renormalized magnon dispersion, and their number is enormous for any SC larger than a few lattice points.

7.4 Self energy

With the number of interactions involved, and the high energies associated with small cavity systems, we anticipate that an assumption $|Q^k| \ll |\hbar\lambda_k|$ on weak coupling holds; to linear order in $|Q^k/\hbar\lambda_k|$, we can thus neglect the off-diagonal contributions to the eigenmodes in the effective action (7.28). This conveniently leaves us with a diagonal action from which we can immediately extract the eigenmode propagator.

The effective action (7.28) is thus

$$\begin{aligned} S^{\mathrm{FI}} &= \sum_k \hbar\lambda_k \eta_k^\dagger \eta_k - \sum_k Q^k (\eta_{-k}\eta_{-k}^\dagger + \eta_k^\dagger \eta_k) \\ &= \sum_k \left(\hbar\lambda_k - (Q^k + Q^{-k})\right) \eta_k^\dagger \eta_k. \end{aligned} \tag{7.38}$$

Since it is diagonal, the renormalized magnon propagator can simply be read off:

$$\mathcal{G} = \frac{1}{\hbar\lambda_k - (Q^k + Q^{-k})} = \frac{1}{\hbar\lambda_{\mathbf{k}} + \Sigma^{\mathbf{k}}(z) - z}, \tag{7.39}$$

where we have defined the self energy

$$\Sigma^{\mathbf{k}}(z) \equiv -(Q^k + Q^{-k}) = \Sigma_{\mathrm{cav}}^{\mathbf{k}} + \Sigma_{\mathrm{SC}}^{\mathbf{k}}(z), \tag{7.40}$$

which is divided into the FI–cavity–FI and FI–cavity–SC–cavity–FI contributions

$$\Sigma_{\mathrm{cav}}^{\mathbf{k}} = -2\frac{|g_{\mathbf{k}}^{\eta}|^2}{\hbar\omega_{\mathbf{k}}}, \tag{7.41}$$

$$\Sigma_{\mathrm{SC}}^{\mathbf{k}}(z) = \frac{2|g_{\mathbf{k}}^{\eta}|^2}{\hbar^2\omega_{\mathbf{k}}^2} \sum_{\mathbf{p}\approx\mathbf{p}_F}{}' \left(|g_{100}^{\mathbf{kp}}|^2 + |g_{111}^{\mathbf{kp}}|^2\right) \frac{\tanh\left(\frac{\beta E_{\mathbf{p}-\mathbf{k},0}}{2\hbar}\right) - \tanh\left(\frac{\beta E_{\mathbf{p},0}}{2\hbar}\right)}{\Delta E_{00}^{\mathbf{kp}} - z}, \tag{7.42}$$

where we used $|g_{100}^{-\mathbf{k},\mathbf{p}-\mathbf{k}}|^2 = |g_{111}^{\mathbf{kp}}|^2$.

We proceed to solve Eq. (7.6) in order to determine an expression for the renormalized energy. Observe first that the solution for z is generally

$$z = \hbar\lambda_{\mathbf{k}} + \Im z + \mathcal{O}\left(|Q^k/\hbar\lambda_k|\right), \tag{7.43}$$

with the imaginary term $\Im z$ representing losses inserted by hand, and $\mathcal{O}\left(|Q^k/\hbar\lambda_k|\right)$ representing corrections to the energy. Now, the self energy $\Sigma^{\mathbf{k}}_{\mathrm{SC}}(z)$ is already a correction; corrections to this correction will therefore be of higher order in $|Q^k/\hbar\lambda_k|$. We may therefore again invoke the weak coupling assumption $|Q^k| \ll |\hbar\lambda_k|$. To leading order, then,

$$\Re\Sigma^{\mathbf{k}}(z) = \Re\Sigma^{\mathbf{k}}(\hbar\lambda_{\mathbf{k}} + \Im z) + \mathcal{O}\left(|Q^k/\hbar\lambda_k|^2\right) \approx \Re\Sigma^{\mathbf{k}}(\hbar\lambda_{\mathbf{k}} + \Im z). \tag{7.44}$$

We have thus obtained a leading-order expression for $\Re\Sigma^{\mathbf{k}}(z)$, and the equation (7.6) is immediately solved for the renormalized energies.

In the next section, we investigate numerically whether or not this self energy is appreciable.

7.4.1 Expected losses, and numerical estimates of the self energy

In general, losses smear and blur features in particle spectra. For instance, in spectroscopic probing of cavity mode energies, losses give rise to a finite linewidth [14–16], which leaves smaller features increasingly indiscernible. We therefore look for realistic parameter choices that produce self energies in excess of expected losses (strong coupling[7]), which indicates that the results are measurable. Below, we first comment on the expected magnitude of losses, and then present numerical estimates of the self energy (7.42).

Losses are usually cited in units of Hz, meaning energies are divided by $2\pi\hbar = h$. For reference, Ref. [14] cites losses of 2.7 MHz for a copper cavity, 2.0 MHz for a superconducting qubit, and 1.1 MHz for the uniform mode in a YIG sphere, below 1 K (the latter increases to about 3.5 MHz at 10 K). They achieve a measurable anticrossing corresponding to a coupling of 47 MHz; in another similar set-up, they achieve discernible features in the spectra corresponding to single-digit MHz couplings (Ref. [13, Fig. 3]). Furthermore, Ref. [16] cites linewidths of 1.029–11.84 MHz for a range of low cavity modes, and 3.247 MHz for the uniform mode in a YIG sphere, in the mK temperature range. Their couplings are far greater, at 0.78–7.11 GHz, yielding clear features. Lastly, Ref. [15] cites losses of 3 MHz for a coplanar superconducting Nb cavity, and 50 MHz for the uniform mode in a Ga-doped YIG crystal. The last figure is exceptionally high because their YIG is doped with Ga; Ref. [15] stresses that losses are significantly lower in pure YIG. Their coupling is 450 MHz, again resulting in clear features.

With these numbers as guides, we expect our $\Re\Sigma^k_{\mathrm{SC}}$ to be appreciable if it exceeds $\gtrsim 1$ MHz for similar material choices.

As a specific example, consider Bi:YIG (FI) and Nb (SC) inside a 2 mm × 2 mm × 12 μm cavity. The cavity dimensions accommodate for a vertical separation of the FI and SC of 6 μm, an order above the scale of anomalous proximity effects. Bi:YIG is YIG doped with bismuth, which exhibits smaller linewidths than pure YIG [63].

[7] As mentioned in the introduction, "strong coupling" is used here in the sense that the coupling strength exceeds losses, not in the sense that some expansion parameter of an interaction Hamiltonian exceeds 1.

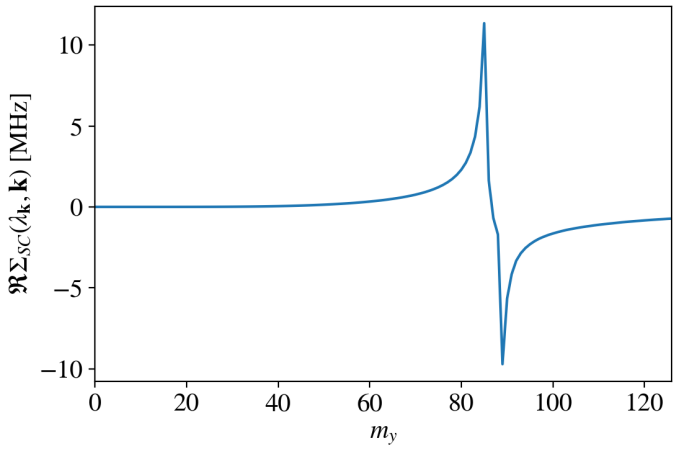

(a)

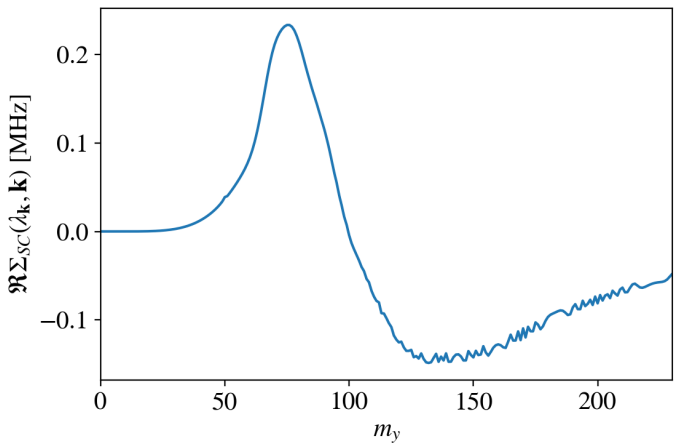

(b)

Figure 7.4: Real part of the leading-order magnon self energy $\Re\Sigma_{\mathrm{SC}}^{k_y}(\hbar\lambda_{k_y})$ originating from interactions with SC quasiparticles, for Bi:YIG (FI) and Nb (SC) films interacting via a $2\,\mathrm{mm} \times 2\,\mathrm{mm} \times 12\,\mu\mathrm{m}$ cavity at $T = 6.1\,\mathrm{K}$ ($T_c = 6.0\,\mathrm{K}$). This is a cross-section of $\mathbf{k}$ space along the positive $k_y = 2\pi m_y / l_y^{\mathrm{FM}}$ axis, along which the response is greater than the k_x axis, because the Zeeman coupling (7.24) is linear in $q_y = k_y$. (a) is plotted assuming a tight-binding electron dispersion, with $B_{\mathrm{ext}} = 0.357\,\mathrm{T}$; and (b) assuming a 2D electron gas (2DEG) dispersion, with $B_{\mathrm{ext}} = 1.231\,\mathrm{T}$. We overestimate losses at $\Im z/h = 30\,\mathrm{MHz}$ for good measure. The remaining parameter inputs are identical and summarized in Table 7.1.

Refs. [117, 118] furthermore reports low in-plane coercivities of only about 0.5–35 mT in nm-thin Bi:YIG films. Coercivity is a measure of how strong an applied field is needed to demagnetize a magnet. The low coercivity is beneficial here because we seek to align the spins with an external magnetostatic field (cf. Fig. 7.2) without compromising the superconductor. For comparison, Ref. [119] reports an

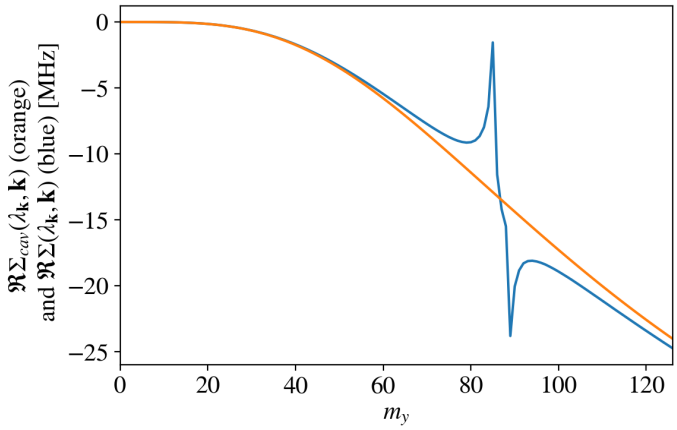

Figure 7.5: Real part of self energy, with (blue) and without (orange) the contribution from the SC, using a tight binding electron dispersion. The anticrossing-like feature is evidently somewhat accentuated by appearing on the slope of $\Re\Sigma^k_{\text{cav}}$. The variation in the bare magnon energy is less than 0.1 MHz across this range, so it does not affect the slope.

out-of-plane critical field of some 1–4 T for nm-thin Nb films, and Ref. [120] suggests the in-plane critical field is much greater. As for the material of the cavity, we leave it unspecified, only assuming losses are $\gtrsim 1$ MHz as in Refs. [14–16]. Lastly, because we consider films and not monolayers, we expect the finite depth of the film will benefit the coupling strength as it increases the number of FI spins participating in the interaction. Since the depth is still much smaller than the other dimensions in the film as well as L_z (such that the mediating cavity modes do not vary significantly across the depth), we anticipate the leading effect of the depth is to multiply the number of lattice sites N_{FI} by the number of layers (compare this to the macrospin approximation [15, 26, 27]). We consider 100 layers, corresponding to a typical film depth of about 124 nm for Bi:YIG.[8] Figs. 7.4 and 7.5 show numerical results for the magnon energy correction $\Re\Sigma^{\mathbf{k}}(\hbar\lambda_{\mathbf{k}} + \mathfrak{I}z)$ at $T = 6.1\,\text{K}$ ($T_c = 6.0\,\text{K}$), with the remaining parameters summarized in Tab. 7.1. Fig. 7.6 shows the self energy for a range of temperatures around T_c, showing a strong sensitivity to the onset of superconductivity.

The self energy in Fig. 7.4a is on the order of 1–5 MHz, a very promising result given expected losses. It appears even more pronounced when plotting the full self energy, cf. Fig. 7.5. On the other hand, the self energy in Fig. 7.4b is only on the order of 0.05–0.5 MHz. The difference is down to the choice of electron dispersion, which determines gradients near the Fermi surface. Supercurrent was not needed to produce a finite result here (in contrast to the results for the effective anisotropy field derived in Ch. 6, for which a symmetry-breaking supercurrent was required to yield a finite result), and was therefore not included in the numerics here. Note

[8] Note also that this is still much smaller than the dimension L_z of the cavity in the same direction, one of the initial assumptions in our model.

Table 7.1: Table of numerical parameter values.

YIG/Bi:YIG (FI)		Nb (SC)	
a_{FI}	12.4 Å [121]	a_{SC}	0.330 nm [122]
S	14 [123, 124]	T_{c0}	6.0 K [125]
$2\hbar^2 J N_\delta S$	6.09 meV [126][a]	t	0.35 eV[b]
Layers	100	E_F	5.32 eV [122]

[a]Based on the reported spin-wave stiffness. [b]Based on the tight-binding expression $t = \hbar^2/2ma_{\mathrm{SC}}^2$ [11, 56], with m the effective electron mass.

finally that while the self energy here is at most on the order 10 MHz (Fig. 7.5), the magnon energy is on the order of tens of GHz (Fig. 7.8), which validates the weak coupling assumption $|Q^k| \ll |\hbar\lambda_k|$ since $\Sigma^{\mathbf{k}}(z) = -(Q^k + Q^{-k})$ (Eq. (7.40)).

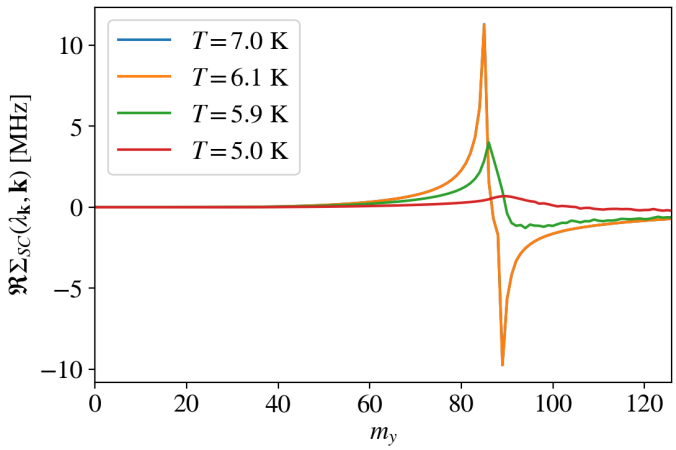

Figure 7.6: Temperature dependence of the tight-binding self energy $\Re\Sigma_{\mathrm{SC}}^{k_y}(\hbar\lambda_{k_y})$ around the critical temperature $T_c = 6$ K. Note that the $T = 7.0$ K and $T = 6.1$ K curves differ by less than 0.03 MHz, so they are indistinguishable here. Below T_c, the self energy is rapidly suppressed by the SC gap.

7.4.2 Analyzing the results

The shape, magnitude and peculiarities of the plots in Fig. 7.4 leave much to unravel. In this section, we reflect over technical aspects of the observed self energy in order to build an understanding of the results. In light of this analysis, we furthermore provide an instructional comparison in Appendix C between the self-energy approach and the results presented here, and a previous attempt at extracting renormalized magnon energies based on the determinant approach outlined in Sec. 7.1.2, which resulted in overestimated corrections.

Choice of B_{ext}

First, some comments directly to the plots in Fig. 7.4. The magnetic field strength B_{ext} was adjusted to achieve good coupling, as the interaction strength depends on $\mathbf{k}$ and by extension the crossing point of the magnon energy ($\approx g\mu_B B_{\text{ext}}$ at these energies) with the differences in SC quasiparticle energies.

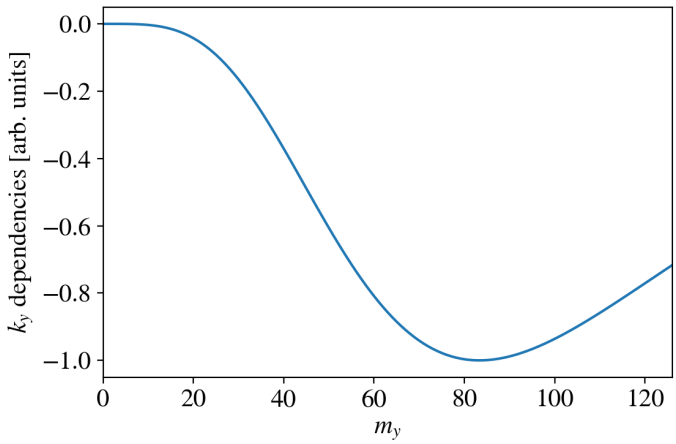

Figure 7.7: k_y dependent part of the coupling (7.29) (specified in Eq. (7.45)), normalized to unit strength at maximum. Here we neglect slowly-varying k_y dependencies because $k_y a_{\text{SC}} \ll 1$, and furthermore disregard the k_y-dependencies entering through the differences in Fermi–Dirac distributions, and the inverse energy differences $(\Delta E_{00}^{\mathbf{kp}} - z)^{-1}$. This gives an indication of which m_y the densest collection of intersections (see Fig. 7.8) should occur for, in order to achieve the strongest possible self energy. This is in turn achieved by adjusting the magnitude of B_{ext}.

A plot of the normalized k_y dependent part of the coupling is shown in Fig. 7.7. Here we neglect the slowly-varying sinusoidal k_y dependencies in $g_{1mm}^{\mathbf{kp}}$ because $k_y a_{\text{SC}} \ll 1$. We furthermore disregard k_y dependencies entering via the differences in Fermi–Dirac distributions (the tanh functions), since this mainly serves to suppress interactions away from the Fermi surface; and the inverse energy differences $(\Delta E_{00}^{\mathbf{kp}} - z)^{-1}$, which give rise to the anticrossings. Including all factors involving the cavity dimensions, the factor plotted was then proportional to

$$\begin{aligned}\frac{|g_{k_y}^{\eta}|^2}{\omega_{k_y}^2} \sum_{\mathbf{p}\approx\mathbf{p}_F}{}' \left(|g_{100}^{k_y\mathbf{p}}|^2 + |g_{111}^{k_y\mathbf{p}}|^2\right) &\propto \frac{|k_y \sin\theta_{k_y}|^2 |\cos\theta_{k_y}|^2}{\omega_{k_y}^4} \frac{L^2 N_{\text{FI}}}{V^2} \\ &\propto \frac{k_y^4}{\left[\left(\frac{\pi}{L_z}\right)^2 + k_y^2\right]^4 L_z^4}. \end{aligned} \tag{7.45}$$

Above, we assumed a square cavity $L_x = L_y = L$, and used that $V = L^2 L_z$, and $N_{\text{FI}} \propto L^2$ because the FI spans the cavity. We furthermore used that $\sum_{\mathbf{p}\approx\mathbf{p}_F}{}'$ is

symbolically proportional to L^2 because the SC spans the cavity (thus increasing the number of $\mathbf{p}$ summed over), and finally, that $\sin\theta_{k_y} = k_y/|\mathbf{Q}|$ and $\cos\theta_{k_y} = Q_z/|\mathbf{Q}|$. Treating k_y as a continuous variable, this indicates the strongest coupling occurs at around[9]

$$k_y = \frac{\pi}{L_z} \quad \Rightarrow \quad m_y = \frac{L_y}{2L_z}. \tag{7.46}$$

With the above cavity dimensions, this works out to $m_y \approx 83$, as seen in Fig. 7.7. Observe also that all factors L cancel; evidently, because the FI and SC dimensions scale to always span the cavity in this set-up, the coupling strength becomes approximately[10] independent of the transversal cavity dimensions. For small momenta $k_y \ll \frac{\pi}{L_z}$, also the dependency on the remaining cavity dimension L_z vanishes.

Gradients near the Fermi level

Recall that the interactions contributing to the self energy (7.42) are concentrated near the Fermi surface. Noting then that Figs. 7.4a and 7.4b only differ by the electron dispersion used, the results are seen to be sensitive to details in the SC quasiparticle spectra near the Fermi surface. In Fig. 7.4, simple expressions for the electron energies were used only to illustrate this dependency, because modelling the behavior of the material-specific electron bands near the material-specific Fermi surface is a project in its own right.

By inspection of Eq. (7.42), we readily identify gradients near the Fermi surface to be an important determining factor in the shape and magnitude of the self energy. These enter via the inverse energy differences $(\Delta E_{00}^{\mathbf{kp}} - z)^{-1}$. To see this, observe first that contributing interactions are concentrated at the SC Fermi surface, because this is where low-energy scattering events involving SC quasiparticles are concentrated (cf. Fig. 7.3). Here the momenta $\mathbf{p}$ are generally large. Secondly, interactions involving large photon energies $|\mathbf{k}| \gg Q_z$ are rapidly suppressed by the factor $\omega_{\mathbf{k}}^{-4} \propto |\mathbf{k}|^{-4}$, which is otherwise relatively constant ($\omega_{\mathbf{k}} \approx cQ_z$ for $|\mathbf{k}| \ll Q_z$) at lower momenta, due to the cavity set-up suppressing interactions via modes other than those with longitudinal momentum $Q_z = \pi/L_z$. We can therefore safely assume that $|\mathbf{k}| \ll |\mathbf{p}|$ for relevant interactions. By the definition (7.30) of $\Delta E_{00}^{\mathbf{kp}}$, then,

$$\begin{aligned}
\Delta E_{00}^{k_y\mathbf{p}} &= E_{\mathbf{p}0} - E_{\mathbf{p}-k_y\hat{e}_y,0} \\
&= \frac{E_{\mathbf{p}0} - E_{\mathbf{p}-k_y\hat{e}_y,0}}{k_y} k_y \\
&\approx -(\partial_{p_y} E_{\mathbf{p}0}) k_y .
\end{aligned} \tag{7.47}$$

[9] We stress "around", since there are other k_y dependencies that factor in. Importantly, this includes the anticrossing factors $(\Delta E_{00}^{\mathbf{kp}} - z)^{-1}$, whose distribution has proven to be an important factor for the magnitude of the self energy. This is discussed later in this section.

[10] "Approximately" stressed here because the symbolic scaling of $\sum'_{\mathbf{p}\approx\mathbf{p}_F}$ with L^2 is approximate.

We recognize this as, essentially, the projection of the gradient of $E_{\mathbf{p}0}$ at the near-Fermi momentum $\mathbf{p}$, in the p_y direction. More precisely, it is the linearization of the SC quasiparticle energy at this point and in this direction, with the gradient $-(\partial_{p_y} E_{\mathbf{p}0})$ the slope, and k_y the variable.

Anticrossings

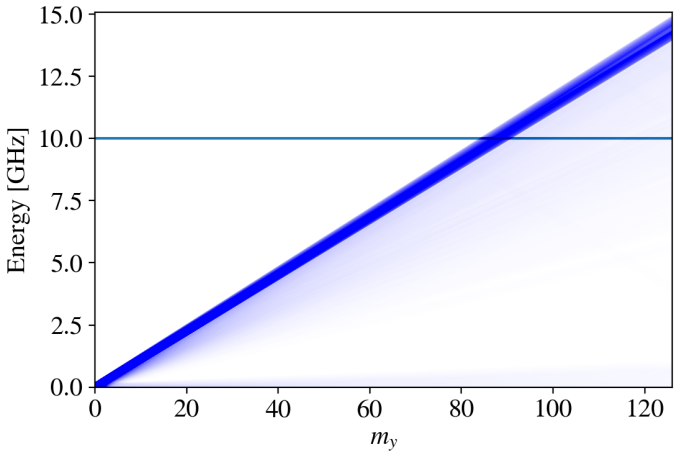

(a)

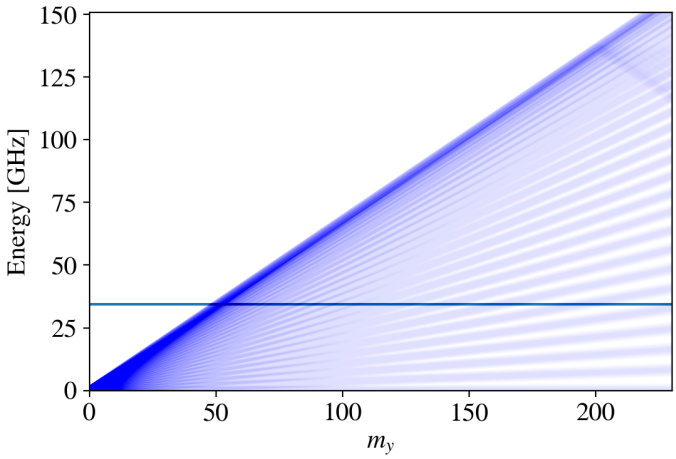

(b)

Figure 7.8: Plots showing intersections between the bare magnon energy $\hbar\lambda_{k_y} \approx g\mu_B B_{\text{ext}}$ (horizontal blue line), and SC quasiparticle energy differences $\Delta E_{00}^{k_y \mathbf{p}}$ for a wide sample of momenta $\mathbf{p}$ near the Fermi surface (faint dark blue). The parameter inputs are the same as in Fig. 7.4. (a) is plotted assuming a tight-binding electron dispersion, with $B_{\text{ext}} = 0.357\,\text{T}$; and (b) assuming a 2DEG dispersion, with $B_{\text{ext}} = 1.231\,\text{T}$. Their distribution is evidently very different. Note that the anomaly in the upper right corner of (b) is only an artefact of the plotting.

Observe now that the factors $(\Delta E_{00}^{\mathbf{kp}} - z)^{-1}$ clearly codes for localized divergent features in the self energy, namely *anticrossings*. The singularities are generally situated in the complex plane when taking into account losses ($\Im z \neq 0$), so the real part $\Re\Sigma_{\mathrm{SC}}^{\mathbf{k}}(\hbar\lambda_{\mathbf{k}})$ of the self energy only exhibits drawn-out peaks. The degree of drawing-out is determined by losses:

$$\frac{1}{\Delta E_{00}^{\mathbf{kp}} - z} = \frac{\Delta E_{00}^{\mathbf{kp}} - \Re z + \Im z}{\left(\Delta E_{00}^{\mathbf{kp}} - \Re z\right)^2 + (\Im z)^2}. \tag{7.48}$$

With the remaining factors in $\Sigma_{\mathrm{SC}}^{\mathbf{k}}(z)$ (Eq. (7.42)) real, taking its real part makes it a function of the factors $\frac{\Delta E_{00}^{\mathbf{kp}} - \Re z}{\left(\Delta E_{00}^{\mathbf{kp}} - \Re z\right)^2 + (\Im z)^2}$. As a function of $\Re z \approx \hbar\lambda_{\mathbf{k}}$ with constant losses, we see the divergence is suppressed by the factor $(\Im z)^2$ in the denominator.

The factors $(\Delta E_{00}^{\mathbf{kp}} - z)^{-1}$ appear in the summand of the sum over momenta $\mathbf{p}$ in Eq. (7.42). This indicates we are dealing with an enormous number of anticrossings: in principle, one for every $\mathbf{p}$ that gives rise to a positive $\Delta E_{00}^{\mathbf{kp}}$ (since $\Delta E_{00}^{\mathbf{kp}}$ crosses $\hbar\lambda_{\mathbf{k}}$ at positive energies). Numerically, we find that for the inputs that went into Fig. 7.4, the most pronounced individual anticrossings are no stronger than single-digit mHz. It is the constructive addition of their enormous number that results in a net self energy on the order of 0.05–5 MHz in Fig. 7.4. This collective appearance of many small anticrossings furthermore leaves only a resemblance of a typical single-anticrossing spectrum as seen in spectroscopy [13–17], and as sketched in Fig. 7.9.

In Fig. 7.8, we have plotted the intersections between $\Delta E_{00}^{k_y\mathbf{p}}$ and $\hbar\lambda_{k_y}$ for a broad sample of $\mathbf{p}$. Fig. 7.8a exhibits a higher density of intersections near a single point (near $m_y = 83$) than Fig. 7.8b (near $m_y = 50$). This is because the gradients in the p_y direction of the SC quasiparticle energy near the Fermi energy are more evenly distributed in the 2DEG case than in the tight-binding case.

Anticrossings flip sign upon passing the (complex-plane) singularity along the real axis, and the rate at which they do so depends on the magnitude of the losses. Whether anticrossings add constructively or destructively therefore depends on how closely situated they are, relative to losses. This is illustrated with a toy model in Fig. 7.9, where we add together two equal anticrossings $\Re[f(x,0) + f(x,\delta)]$, where $f(x,\delta) = -[(x-1+\delta)-0.1i]^{-1}$. $f(x,\delta)$ describes an anticrossing between a horizontal line at 0, and a diagonal line $x-1+\delta$, with losses of $|0.1i|$. δ serves to shift the crossing point away from 1. Observe that for $\delta = 0.0$, the sum is twice the summand, and retains an overall anticrossing-like appearance. This also holds for $\delta = 0.1$, with the peaks of the sum only slightly weakened. For $\delta = 0.2$, the sum develops a saddle point. For $\delta = 0.5$, two new peaks appears, and the overall response is more drawn out and weaker than for smaller values of δ. Evidently, these peculiarities become apparent only once the distance between the anticrossings approach or exceed twice the losses $2|0.1i|$.

Referring back to Figs. 7.4 and 7.8, then, we can understand that the many small anticrossings add more constructively in the tight-binding case over the

2DEG case, owing to the higher density of intersections in a narrow region along the magnon energy. The toy model furthermore indicates the origin of peculiarities in the self energies that deviate from a simple anticrossing. Compare the saddle point feature in Fig. 7.9c to Fig. 7.4a, and the appearance of new peaks in Fig. 7.9d to the coarseness seen in Fig. 7.4b. Compare also the localized, strong response for proximal anticrossings in Figs. 7.9a and 7.9d, and the relatively drawn-out and weaker response for distant anticrossings in Fig. 7.9d, to Figs. 7.4a and Fig. 7.4b, respectively.

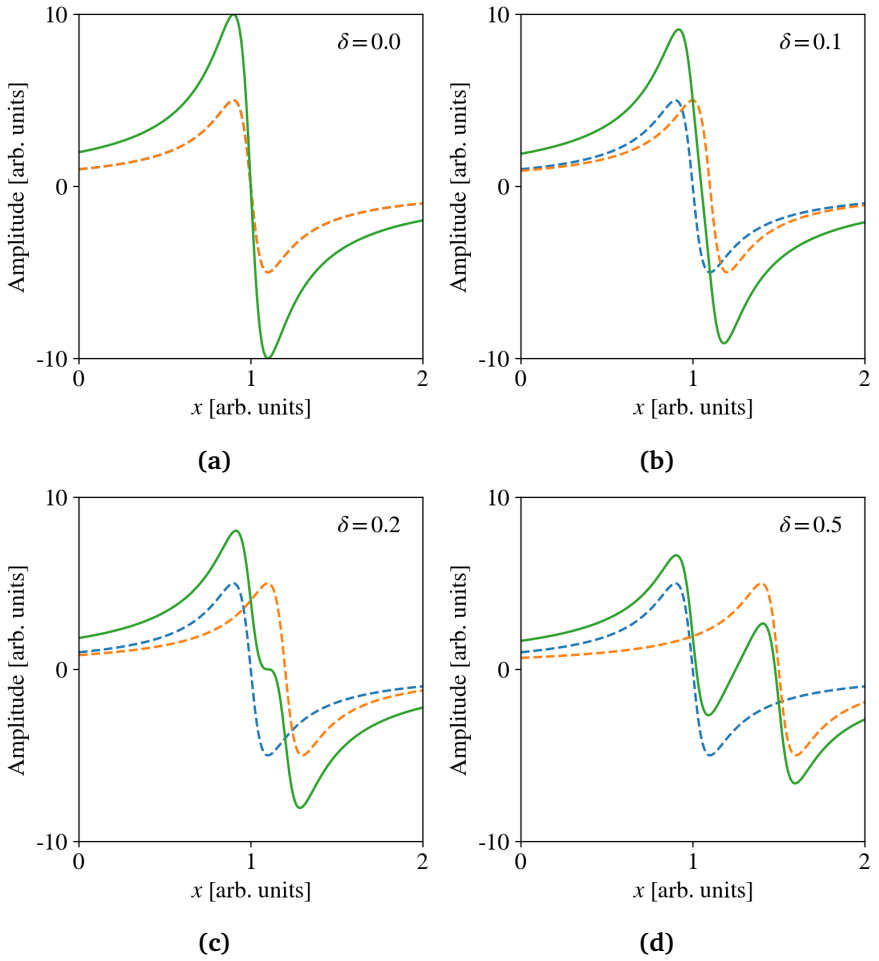

Figure 7.9: Toy model illustrating the effect of adding two anticrossings together. The functions are $\Re f(x,0)$ (dashed blue), $\Re f(x,\delta)$ (dashed orange) and $\Re[f(x,0)+f(x,\delta)]$ (solid green) where $f(x,\delta) = -[(x-1+\delta)-0.1i]^{-1}$, for a selection of values for displacements δ (inscribed). For displacements less than twice the losses $\delta < 2|0.1i|$ ((a) and (b)), the anticrossings add constructively across the range. However, at $\delta = 2|0.1i|$ (c), their sum develops a saddle point, and for $\delta > 2|0.1i|$ (d) they begin to add destructively across an intermediate region. For $\delta \geq 2|0.1i|$, the sum is visibly less pronounced and more drawn out, than when $\delta < 2|0.1i|$.

In Fig. 7.10, we take the toy model a step further, and explore how the toy self energy evolves with an increasing number of anticrossings, which are also increasingly spaced apart. The partial sums plotted are $\Re g(x,n) = \Re \sum_{m=0}^{n} (1 + \cos^{-1}[\pi m/25] - x + 0.1i)^{-1}$ for $n = 0, 1, \ldots, 12$. Here the distance between anticrossings increase as a $\cos^{-1}$ function. This is analogous to the distribution of intersections we found for the 2DEG case (Fig. 7.8b), which is seen as follows. Neglecting for simplicity the gap, the SC quasiparticle energies equate to the 2DEG dispersion $\xi(p) \propto p_x^2 + p_y^2$ up to an overall sign. The p_y-direction gradients at the Fermi surface are then $\hat{e}_y \cdot \nabla \xi(\mathbf{p}_F) \propto p_F \sin\theta_{\mathbf{p}}$, with $\mathbf{p}_F$ the Fermi momenta, and $\theta_{\mathbf{p}}$ the polar coordinate. The points of intersection between the magnon energy $\hbar\lambda_{k_y} \approx$ const. $\gg 0$, and the SC quasiparticle energy differences $\propto k_y \cdot p_F \sin\theta_{\mathbf{p}}$ for various near-Fermi momenta $\mathbf{p}$, therefore occur at $k_y \propto \sin^{-1}\theta_{\mathbf{p}}$ up to some multiplicative factor. Shifting $\theta_{\mathbf{p}}$ by $\pi/2$ to make the first intersection occur for the $\theta_{\mathbf{p}} = 0$ line, the intersections are distributed as $k_y \propto \cos^{-1}\theta_{\mathbf{p}}$, as assumed in the toy model.

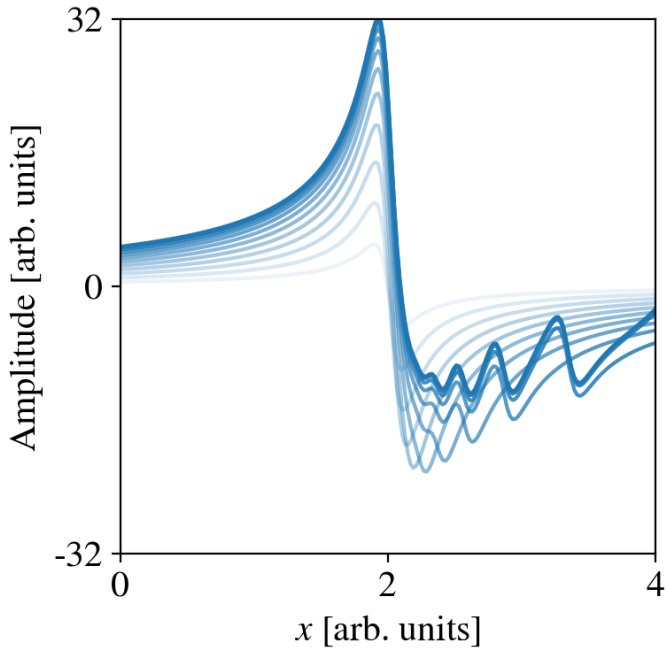

Figure 7.10: Toy model illustrating how the partial sums of anticrossings develops with an increasing number of terms, subject to a specific distribution. The partial sums are given by $\Re g(x,n) = \Re \sum_{m=0}^{n} (1+\cos^{-1}[\pi m/25] - x + 0.1i)^{-1}$ for $n = 0, 1, \ldots, 12$ (transparency decreasing with n). The spacing between anticrossings increase as a $\cos^{-1}$ function, in analogy to the 2DEG case plotted in Fig. 7.8b. Observe that with an increasing number of terms, the partial sums maintain a clean and (decreasingly) growing left peak, and develop an increasingly coarse right peak. The right peak initially grows in magnitude, but eventually decreases in magnitude and becomes drawn out.

Thus, observe that certain features seen here are analogous to peculiarities observed in the 2DEG self energy in Fig. 7.4b (also discernible in the tight-binding self energy at lower T, cf. Fig. 7.6): a strong and clean left peak, and a rugged, drawn-out right peak. In the toy model, the clean peak is a result of no anticrossing occuring for $x < 2$, and the rugged peak, of the anticrossing being increasingly spaced apart (compare this to the appearance of new peaks in Fig. 7.9d when spacing exceeds twice the losses). These observations are in rough agreement with the observed distributions of intersections (Fig. 7.8) compared to the shape of the self energies (Fig. 7.4).

One notable discrepancy from this behavior, is that in the 2DEG case (Fig. 7.4b), the self energy apparently maintains a clean left peak with its maximum at about $m_y = 75$, even though the first intersections (Fig. 7.8b) take place already at about $m_y = 50$, where they are also at their most dense. One important aspect we have not factored into the toy models, is the variation of the coupling strength associated with each anticrossing; instead the strength was assumed constant at 1, while the actual coupling strengths resolved across anticrossings in the self energy (7.42) varies with both $\mathbf{p}$ and $\mathbf{k}$; for the latter, see Fig. 7.7, which is seen to have a peak at a specific k_y (m_y), and taper towards zero on either side.

Behavior near T_c, and probing the gap

Lastly, concerning the technical aspects of the results, we comment on the temperature dependence observed in Fig. 7.6. It is seen that upon approaching the critical temperature T_c from above, the self energy maintains a relatively constant shape. As temperatures are lowered past T_c, the response self energy rapidly diminishes. This is readily understood from inspecting the self energy (7.42): The Fermi–Dirac functions $n_F(E_{\mathbf{p}0})$ (expressed in the self energy in terms of tanh functions) diminish rapidly at the onset of superconductivity. In physical terms, this is because the number of energetically available SC quasiparticle states diminishes rapidly with the onset of superconductivity, as the electron pairing energy (i.e. the gap) presents a barrier to low-energy scattering. In mathematical terms, it is because even near the Fermi surface, a finite gap renders the SC quasiparticle energy nonzero: $E_{\mathbf{p}0} \geq |\Delta_{\mathbf{p}}| > 0$ (cf. its definition (3.23); we neglect supercurrent ($\mathbf{P}$) in this discussion, as we did in the numerics). The minimum energy is $|\Delta_{\mathbf{p}}|$, and so the maximum $\tanh(|\Delta_{\mathbf{p}}|)$ of the Fermi–Dirac functions decreases exponentially with increasing $|\Delta_{\mathbf{p}}|$. Using the interpolation formula $|\Delta_{\mathbf{p}}| \propto \tanh\left(1.74\sqrt{\frac{T_c}{T}-1}\right)$ for an s-wave (isotropic) gap, we see that $|\Delta_{\mathbf{p}}|$ itself initially increases rapidly as T is lowered below T_c. Overall, the self energy therefore diminishes extremely fast at the onset of superconductivity.

Keeping this temperature dependence in mind, recall now that the magnon self energy is sensitive to the gradients of $E_{\mathbf{p}0}$ near the Fermi surface, with a selectively strong response to slopes in the p_y direction. Recall furthermore that this selective response stems from the coupling constant (7.24) asymmetrically scaling with k_y. This in-plane directional asymmetry is in turn a consequence of the external field

$\mathbf{B}_{\text{ext}}$ by design directing FI spins along $\hat{e}_y$, facilitating magnon excitations in $\hat{e}_x$.[11] Hence, by a specific choice of direction of the easily adjustable external field $\mathbf{B}_{\text{ext}}$, we made the FI selectively resolve gradients of $E_{\mathbf{p}0}$ in that direction, near its Fermi surface. Combined with the sensitivity to the onset of superconductivity, this is an intriguing observation in relation to the prospect of remotely resolving momentum information about generalized superconducting gaps in spintronic circuitry. We return to this point in Ch. 8, suggesting continuations of our research.

Key takeaways:

- The magnon spectrum is renormalized by bilinear terms precipitating from the effective theory derived in Ch. 6. The difference between the bare and renormalized spectrum is the real part of the magnon self energy $\Re\Sigma^{\mathbf{k}}$.
- Considering a set-up in which the external field $\mathbf{B}_{\text{ext}}$ across the FI is aligned with the y direction, and the FI and SC films span the cavity, only $+k$ and $-k$ magnon modes couple. Combining this with an assumption on weak coupling, we are able to extract analytical expressions for the self energy. The part involving the SC reads

$$\Sigma^{\mathbf{k}}_{\text{SC}}(\hbar\lambda_{\mathbf{k}}+\Im z) = \frac{2|g^{\eta}_{\mathbf{k}}|^2}{\hbar^2\omega^2_{\mathbf{k}}}\sum_{\mathbf{p}\approx\mathbf{p}_F}{}' \left(|g^{\mathbf{kp}}_{100}|^2+|g^{\mathbf{kp}}_{111}|^2\right)\frac{\tanh\left(\frac{\beta E_{\mathbf{p}-\mathbf{k},0}}{2\hbar}\right)-\tanh\left(\frac{\beta E_{\mathbf{p},0}}{2\hbar}\right)}{\Delta E^{\mathbf{kp}}_{00}-\hbar\lambda_{\mathbf{k}}+\Im z}.$$

- In a numerical example where we consider material parameters for Bi:YIG (FI) and Nb (SC) inside a $2\,\text{mm}\times 2\,\text{mm}\times 12\,\mu\text{m}$, we find a promising self energy on the order of expected losses when assuming a tight-binding electron dispersion. Assuming a 2DEG dispersion, the self energy is an order weaker, and therefore not within currently detectable range, in this arbitrary example.
- The amplitude and shape of the self energy depends on the distribution and density of gradients near the Fermi surface of the SC quasiparticle spectrum. The directional dependence on the gradients is partially biased in favor of the direction of $\mathbf{B}_{\text{ext}}$.
- The self energy diminishes rapidly as the temperature passes below T_c, i.e. at the onset of superconductivity.
- Combining the aforementioned dependencies suggests the prospective application of the renormalized magnon spectrum as a remote probe for momentum anisotropy in generalized superconducting gaps.

---

[11] Why does this coupling in $\hat{e}_x$ scale with the perpendicular component k_y? Because the spins $\mathbf{S}_i$ couple to $\mathbf{B}_{\text{cav}} \propto \nabla\times\mathbf{A}_{\text{cav}}$ (cf. sec. 5.1).

Chapter 8

Summary, discussion and outlook

8.1 Overall model

In this dissertation, we have provided a detailed derivation of a microscopic model for the cavity-mediated interactions between an FI and an SC, emphasizing the impact on the FI. This is the main result of our research; not only the final effective FI action (6.66), but also the intermediate result of an effective FI–SC action (presented in Paper II after integrating out the cavity). This microscopic model was motivated by a semiclassical proof of concept (Paper I) that demonstrated the use of cavity mediation to enable the magnetic moment of a ferromagnetic sphere, to remotely resolve the superconducting phase transition in a superconducting wire. We have furthermore provided an in-depth analysis of the first and second order effects of the SC on the FI, with respect to the paramagnetic coupling. These are, respectively, to reorient the spins of the FI (in other words, to induce an effective anisotropy field), and to renormalize the energy spectrum of the magnons. Our model is based on the Matsubara path integral formalism; in contrast to the perturbative Schrieffer–Wolff approach of related works [2, 10, 11], this allows for an exact integrating-out of the cavity, and the results are not limited to an off-resonant regime.

In deriving the effective FI action (6.66), we perturbed the system only with respect to the paramagnetic coupling, meaning there is freedom to let the FI and cavity hybridize without the model breaking down. This flexibility does not carry over to the results on the magnon self energy in Ch. 7 as weak coupling was eventually invoked, but it is applicable to the anisotropy results presented in Paper II.

Moreover, because the cavity facilitates interactions across distances above the length scales of proximity effects, the FI and SC are not subject to the same mutual disruption of their orders, such as the breaking of Cooper pairs near the SC boundary by the FI magnetization. The separation also enables the FI and SC

to be subjected to different temperatures[1] and different drives.

Owing to the placement of the FI and the SC inside the cavity, the cavity modes only interact with the spin degrees of freedom of the FI, and the momentum degrees of freedom of the SC. In effect, the cavity then takes on the role as an effective spin–orbit coupling between the FI and the SC. This interpretation becomes apparent during the intermediate calculations when the cavity is integrated out before the SC, as was done in Paper II.

The model derived in Ch. 6 allows for a broad range of FI, cavity and SC dimensions, as well as placements of the FI and SC inside the cavity. We only constrained the cavity dimensions, and the placement of the films. The cavity dimensions are such that $L_z \ll L_x, L_y$, which renders excitations of the cavity modes in the z direction energetically unfavorable. The FI and SC films are respectively placed at the top ($z = L_z$) and the middle ($z = L_z/2$) of the cavity, which limits coupling to $Q_z = \pi/L_z$ cavity modes, and consequently leaves the coupling purely magnetic (FI) and electric (SC). There are also implicit limitations to the model in the fact that we have used periodic boundary conditions in the transversal directions for the cavity modes. As they stand, our results only depend on the relative positions of the FI and SC. However, in a cavity with reflecting walls in all directions, the field strengths are modulated as sine and cosine functions in space, not as complex exponentials with modulus 1 (cf. the discussion on cavity boundary conditions in Ch. 4). For instance, a cavity wall extinguishes perpendicular components to the electric field in its vicinity, and the cavity–SC coupling is modified when such effects are considerable. The absolute positional dependency would be resolved by imposing reflecting boundary conditions on the cavity modes in all directions.

8.1.1 Coupling to gap fluctuations

In our model, we coupled to the quasiparticles of the SC. This has been demonstrated to enable extraction of momentum information about the superconducting gap via the FI in this dissertation and in the papers. In particular, the broken inversion symmetry due to an applied supercurrent gives rise to an effective anisotropy field; and the onset of superconductivity leads to rapidly suppressed corrections to the magnon energy, with a directional sensitivity to the gap (note that breaking inversion symmetry was not required for this result). An interesting avenue to pursue with the aim of extracting information about the superconducting gap, is to instead consider the cavity coupling to fluctuations in the gap. Such a coupling is considered in a number of papers [127–131]. Take Ref. [129] as an illustrative example. In order to derive a coupling to fluctuations, they bring the quartic electron interaction (3.13) directly into the Matsubara path integral, introduce the

[1]Note, however, that our model takes the system to be held at a single temperature. This is because the Matsubara formalism is based on the density matrix $\hat{\rho} \equiv e^{-\beta\mathcal{H}/\hbar}$ (cf. Ch. 6) for a canonical ensemble at thermal equilibrium. However, the space separating the FI and SI can be assumed thermally insulating, so the analysis is expected to hold also for an FI and SC at different temperatures.

gap and its conjugate as auxillary fields via a Hubbard–Stratonovich transformation[2], and perturb the exact integrals over the auxillary fields by considering them as mean-field values plus a perturbation (cf. Eq. (3.14)). Since our model is based on the same path integral formalism involving the same quartic electron term, our theory is readily extended to accommodate for a similar coupling to gap fluctuations.

8.1.2 Effective SC or cavity theory

Lastly on the topic of the model in general, we stress that although we ultimately extract an effective *magnon* theory, it is also possible to leave the SC action untouched and instead integrate out the FI along with the cavity. This would produce an effective *SC quasiparticle* theory, from which the influence of the FI and the cavity on the SC could be extracted. This can even be done without any perturbations or mean-field approximations, which by contrast was necessary to integrate out the SC in deriving the effective magnon theory, although for many purposes (like extracting pairing potentials) it is necessary after the action is derived. We can sketch the results of integrating out the cavity and FI instead, in that order:

- Starting with an electron theory with a quartic pairing term instead of the SC quasiparticle theory (which involved a mean-field approximation), the system Hamiltonian comprises terms of the forms $\eta^\dagger\eta$, $a^\dagger a$, $c^\dagger c$, $(\eta+\eta^\dagger)(a+a^\dagger)$, $(a+a^\dagger)c^\dagger c$ and $c^\dagger cc^\dagger c$.
- Integrating out the cavity, we get terms of the forms $\eta^\dagger\eta$, $c^\dagger c$, $(\eta+\eta^\dagger)(\eta+\eta^\dagger)$, $(\eta+\eta^\dagger)c^\dagger c$ and $c^\dagger cc^\dagger c$.
- Finally, integrating out the FI, we get terms of the forms $c^\dagger c$ and $c^\dagger cc^\dagger c$.

The influences of the FI and cavity on the SC have thus been collected into quartic electron interaction terms.

The Feynman diagrams for all the interactions that aggregate to $c^\dagger cc^\dagger c$ terms would follow quite a simple pattern (Fig. 8.1): besides the a priori electron pairing

[2]In broad terms, this transformation involves collecting the four electron operators into two composite operators $\rho_{\mathbf{p}}, \rho_{\mathbf{p}}^\dagger$ (e.g. $\rho_{\mathbf{p}} = c_{-\mathbf{p}\downarrow}c_{\mathbf{p}\uparrow}$, though precisely which two electrons in Eq. (3.13) are paired is generally arbitrary) in the path integral Z, and multiplying the path integral Z by 1 resolved into a Gaussian integral over an auxillary bosonic field $\phi_{\mathbf{p}}, \phi_{\mathbf{p}}^\dagger$. By then shifting the variables $\phi_{\mathbf{p}}, \phi_{\mathbf{p}}^\dagger$, the single integral over the quartic electron interaction (now appearing as $\rho_{\mathbf{p}}^\dagger\rho_{\mathbf{p}}$) is replaced by a double integral over bilinear electron terms coupled to the auxillary field ($\phi_{\mathbf{p}}\rho_{\mathbf{p}}^\dagger$ and $\rho_{\mathbf{p}}\phi_{\mathbf{p}}^\dagger$) [108].

Up to this point, everything is exact: the integrals over the composite and auxillary fields are equivalent to the original integrals over the electron variables. The power of this approach is made apparent upon applying physical considerations to simplify the integral over the auxillary field. By a suitable choice of paired electron operators, simplifying assumptions can be made to the auxillary field. The choices are referred to as channels; the example choice above is the pairing channel, made here because we recognize its connection to the BCS ordering parameter. From here it is clear that proceeding with an assumption of small fluctuations (cf. Eq. (3.14)), the integral over the auxillary field (identified as the BCS gap) can be simplified. Because this has been performed inside a path integral, the powerful tools of the path integral formalism can be used to analyze the system beyond leading, mean-field order.

term, there is a cavity-mediated electron pair interaction involving the exchange of a single photon (this is the term analyzed in Ref. [11] in an off-resonant regime), and an infinite series of terms in which the exchanged photon oscillates between a magnon and a photon state an arbitrary number of times. This series aggregates the influence of the FI on the SC, or more precisely on the electron pairing. From here, one could proceed by applying e.g. mean-field theory as was done in Ref. [11], in order to extract corrections to the electron pairing potential due to the FI. From this one would likely also find renormalizations in the electron spectra analogous to the ones observed in the magnon spectra in Ch. 7, since it is a mutual effect.

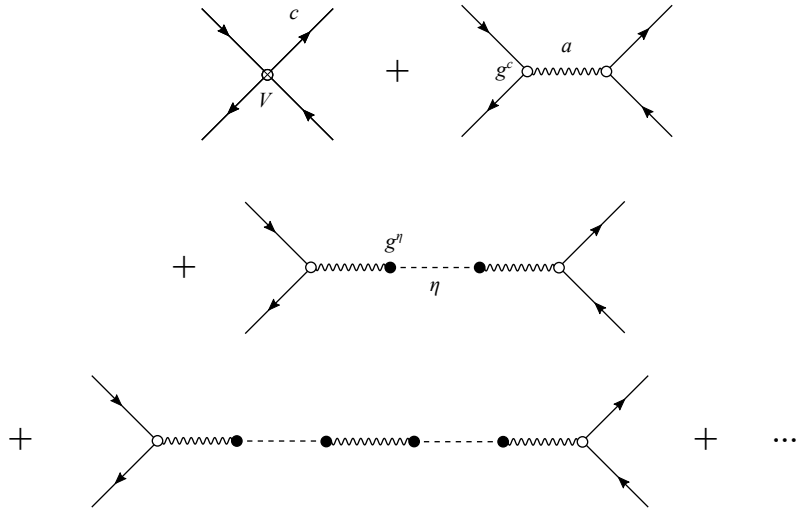

Figure 8.1: Feynman diagrams of the interactions collected into quartic electron terms in the effective electron theory. Here η are magnons, a photons, c electrons, V the a priori electron pairing potential, g^η the Zeeman coupling and g^c the paramagnetic coupling. The series is infinite, with the photons emitted or absorbed in the electron scattering events at the ends, oscillating between a magnon and a photon state an arbitrary number of times in-between (indicated by the ellipsis).

In the context of spectroscopic inquiry, it is of course also possible to instead integrate out the FI and the SC, leaving an effective cavity action. This avenue could be interesting to pursue for the purpose of experimental research. For instance, Ref. [13, 14] probed for the indirect coupling between a single magnon mode and a qubit mediated by a single cavity mode, by spectroscopically probing another cavity mode that coupled weakly to the qubit. This made the anticrossing in the qubit spectrum, caused by the mediated interaction with the magnon mode, to appear as an anticrossing also in the spectrum of the probed mode. This way, they did not significantly disturb the mediating mode during the spectroscopy.

8.2 Reorientation of FI spins

In Ch. 6, we showed that the leading effect of the SC on the FI, in orders of the paramagnetic coupling, is to reorient the spins of the latter, or in other words to give rise to an effective anisotropy field. In Paper II, we present the anisotropy field along with a numerical example. In this dissertation, we presented the reorientation of the spins, which additionally captures how the FI response is modified by FI–cavity–FI interactions, mixing magnons of positive and negative $\mathbf{k}$. It furthermore captures the suppression of the response by the magnitude of B_{ext} via $(\hbar\lambda_k)^{-1}$ (cf. Eq. (6.80)), which on the other hand needs to be sufficiently large to align spins and ensure the validity of the linearization[3] of the Holstein–Primakoff transformation. In order to achieve a finite realignment of spins, we showed it was necessary to break the inversion symmetry of the SC, which we did by applying a supercurrent. This supercurrent is notably implemented via the superconducting gap (see Eq. (3.17)), meaning this effect is a consequence of superconductivity. This suggests its application in spintronic circuitry to remotely resolve broken SC inversion symmetry.

Observe that this is not to say there is no magnetic effect of the SC on the FI as it exits the superconducting state due to temperatures rising above T_c, or the supercurrent exceeding the critical current. Such a normal-state effect is just not resolved in our system Hamiltonian. The Biot–Savart law $\nabla \times \mathbf{B} = \mu_0 \mathbf{J}$ dictates that a static current density $\mathbf{J}$ gives rise to a magnetostatic field $\mathbf{B}$. Since like $\mathbf{B}_{\text{ext}}$ it is magnetostatic, we can ignore the influence of the cavity. It is then clear that the FI will be subjected to an inhomogeneous magnetostatic field also in the normal-state case. However, this magnetostatic field is first of all expected to diminish upon entering the superconducting regime as the density of normal electrons diminishes (cf. Paper I), while the anisotropy field in our research is expected to stabilize at temperatures well below T_c as a measure of broken inversion symmetry (see discussion in Paper II). Secondly, the distribution of the normal-state magnetostatic field is determined by the SC geometry. This differs from the anisotropy field in our research, whose distribution is determined both by the SC with which the FI interacts, and by the cavity, through which the interaction is mediated. In particular, the spatial distribution of the range of mediating photon modes is determined by cavity geometry. This gives rise to an anisotropy field that is very different from the magnetostatic field in the normal case. One peculiarity we highlight in Paper II is that for a certain in-plane separation of the FI and SC, the effective anisotropy field can reverse its direction relative to the no-separation case. This effect is more obvious when considering mediation via a single mode as in Paper I, where the magnetic field can change direction depending on the position of the magnet inside the cavity.

[3] I.e., to limit unwanted magnon–magnon scattering, as expressed by higher order terms in the transformation.

8.2.1 Spatial decoherence of mediating modes

In the example presented in Paper II for the application of the model, the FI was assumed small relative to the cavity, substantially simplifying the calculations. This left the FI–SC interaction mediated by a wide range of cavity modes. For the aim of facilitating long-distance coupling, a significantly limiting factor was the relative differences in phases between the mediating waves: one range of cavity modes may contribute to the anisotropy field in one direction, while another may do so in the other direction, leading to a suppressed net anisotropy field. This results from the fact that cavity modes of increasing energy also oscillate increasingly fast (recall that $\omega_{\mathbf{q}} \propto |\mathbf{Q}|$), meaning they spatially decohere over distances; see Fig. 8.2. This dependency is expressed by the factors $e^{i\mathbf{q}\cdot\mathbf{r}_0^{\mathrm{FI}}}$ and $e^{i\mathbf{q}\cdot\mathbf{r}_0^{\mathrm{SC}}}$ that enter via the coupling constants (5.13) and (5.22). In the anisotropy field, their product enter as $e^{i\mathbf{q}\cdot(\mathbf{r}_0^{\mathrm{FI}}-\mathbf{r}_0^{\mathrm{SC}})}$, where $\mathbf{r}_0^{\mathrm{FI}}-\mathbf{r}_0^{\mathrm{SC}}$ is recognized as the in-plane separation between the center points of the FI and the SC. From this it is clear that when considering mediation by a range of photon modes ($\mathbf{q}$), increasing separation causes this factor to increasingly oscillate, ultimately leading to destructive addition when summing over $\mathbf{q}$.

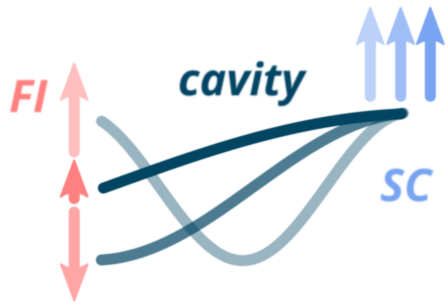

Figure 8.2: The cavity modes (dark blue) that mediate the interaction start out spatially coherent at the SC, and decohere over a distance until they reach the FI (unequal red arrows). The modes are distinguished by faintness. Thus the coherent signals from the SC (equal blue arrows), are received as decoherent signals by the FI (unequal red arrows), adding destructively to a weak net signal. Observe that in our model, these wave are complex exponentials with unit length, not real sinusoidals as might be understood from the illustration. Note also that this decoherence concerns spatial oscillations, not oscillations in time.

The destructive effect of this oscillation is limited by the suppression of contributions from high-energy photon modes, which is expressed by the factors $\frac{D_{0\mathbf{q}}^{\mathrm{FI}} D_{0,-\mathbf{q}}^{\mathrm{SC}}}{\omega_{\mathbf{q}}^2}$ entering the expression for the anisotropy field. This is discussed in more detail in Paper II. This decoherence effect of many modes stands in contrast to the case of single-mode mediation (cf. Paper I), where strong signals can travel across distances up to the order of the cavity dimensions. Despite this limitation, in Paper II,

we were able to extract a promising anisotropy field mediated across 130 μm in an arbitrary practical example, with material parameters for YIG and NB. With parameter optimization, we expect this can be made appreciable for a low-coercivity FI such as Bi:YIG, which is left for future work. The distance is two orders above the scale of anomalously long-ranged proximity effects reported in the literature [8, 9].

8.2.2 Easing constraints

Broken SC inversion symmetry is prerequisite to obtaining a finite anisotropy field, as elaborated near the end of sec. 6.1.4. In our model, this purpose was served by the supercurrent. However, the way in which this was implemented (giving the Cooper pairs an evenly distributed center-of-mass momentum $\mathbf{2P}$, cf. the Hamiltonian (3.17)) limits the SC dimension perpendicular to the direction of the DC to no more than the Pearl length λ^2/d. As an example, Ref. [125] measures penetration depths λ as low as around 240 nm for superconducting Nb films of depth d around 8 nm, equating to Pearl lengths of μm order for the thinnest films. It furthermore introduces the complication of needing to pass a DC through the cavity, without affecting the system. These limiting constrains could be mitigated by breaking inversion symmetry in other ways. One candidate is to take into account spin–orbit coupling on the SC and subjecting it to a magnetostatic field instead.

Another important constraint in our model that could be eased, is the requirement that the FI and SC do not overlap in-plane (cf. Fig. 1.3). This was assumed so that the perpendicular field $\mathbf{B}_{\text{ext}}$ could be passed through the FI, while also being shielded in order to keep it from interfering with the SC. This was done experimentally in Refs. [13, 14] for the same reason, with a superconducting qubit in place of an SC as such. However, as we also address in Paper II, certain material choices may render this constraint unnecessary. For instance, Bi:YIG (FI) exhibits very low out-of-plane coercivities of only about 0.3–6 mT in nm-thin Bi:YIG films, as reported in Refs. [117, 118]. Meanwhile, Ref. [119] reports an out-of-plane critical field of some 1–4 T for nm-thin Nb films. In this case the magnitude of $\mathbf{B}_{\text{ext}}$ would be sufficiently far below the critical field of Nb to have any meaningful impact, but would still align the FI spins. However, the SC would then also distort the spatial distribution of $\mathbf{B}_{\text{ext}}$ in its vicinity due to the Meissner effect, which would have to be taken into account.

Alternatively, it could be possible to do away with $\mathbf{B}_{\text{ext}}$ altogether by limiting the choice of the FI to materials with out-of-plane magnetic anisotropies (sufficiently thin Bi:YIG is such a material [117, 118]). The mathematical role of $\mathbf{B}_{\text{ext}}$ is then instead taken on by the internal magnetization field of the FI.

Easing the constraint on in-plane separation limits the material choices to low-coercivity ferromagnetic insulators, and high-critical field superconductors. To the extent that the purpose of the set-up is to resolve broken inversion symmetry of the SC in the FI, this is not a detrimental trade-off. On the contrary. As noted above, increasing in-plane separation leads to increasingly decoherent mediation

of interactions by the various cavity modes, leading to a diminished anisotropy field. In combination with imposing a minimum separation in order to keep the FI and SC from overlapping in-plane, this considerably limits the choices of FI and SC dimensions and placements given any particular cavity dimensions. Doing away with the requirement of a minimum separation would therefore allow for a considerably broader selection of system configurations.

8.3 Corrections to magnon spectrum

From the effective magnon theory, we derived the expression (7.42) for the corrections to the magnon spectrum due to mediated interactions with SC quasiparticles. We subsequently provided an in-depth numerical analysis of the self energy for the specific material choices of Bi:YIG (FI) and Nb (SC), inside a $2\,\mathrm{mm} \times 2\,\mathrm{mm} \times 12\,\mu\mathrm{m}$ cavity. The cavity dimensions accommodate for a vertical separation of the FI and SC of $6\,\mu\mathrm{m}$, an order above the scale of anomalous proximity effects. We demonstrated an anticrossing-like correction to the magnon spectrum, with a magnitude of 0.05–5 MHz (Fig. 7.4). This self energy is the net result of many small, individual anticrossings added together, with their many individual sharp peaks attenuated by losses. The magnitude was shown to increase with the number and density of individual anticrossings sufficiently near the same point along the magnon spectrum; their density and distribution in turn depends on the gradients near the Fermi level in the SC quasiparticle spectrum, with the strongest energy correction occurring for gradients in the direction determined by the easily adjustable external field $\mathbf{B}_{\mathrm{ext}}$. The greater the number of nearly equal gradients in this direction, the greater the magnon self energy.

With losses in the system expected to be on the order of 1–10 MHz based on experimental cavity set-ups [13–17], the numerical results are promising; the strongest results of around 5 MHz are on the same order as the anticrossing detected via spectroscopy of a cavity mode in Ref. [13]. On the other hand, the weaker results, for which the distribution of gradients at the Fermi level is more even, are not currently within a detectable range in our arbitrary example. More work is required to determine if the energy corrections can be made larger without relying on specific Fermi surfaces.

8.3.1 Other gap symmetries

In our model, we considered a simple *s*-wave superconductor. Here, we argue for the potential application of the FI, or more precisely the magnon spectrum, as a means for a spintronic component to remotely resolve the momentum anisotropy of other categories of superconducting gaps. The cavity-mediation facilitates interactions over distances exceeding those of proximity effects, which therefore do not involve the disruption of superconducting order present in proximity systems. Note that by contrast, the FI spin reorientation discussed in the last section cannot resolve gap anisotropies; the gap enters the anisotropy field (6.69) via the

cavity–SC coupling constant $g_{\varsigma mm}^{\mathbf{qpp}'}$ and the Fermi–Dirac distribution, but does so with diagonal indices in $\mathbf{p}' = \mathbf{p}$. This enables $\mathbf{q}$- and $\mathbf{p}$-dependent terms to be factorized. The photons ($\mathbf{q}$) are therefore unable to differentiate between SC quasiparticles ($\mathbf{p}$). The collection of SC modes thus homogeneously contribute to the FI spin reorientation.

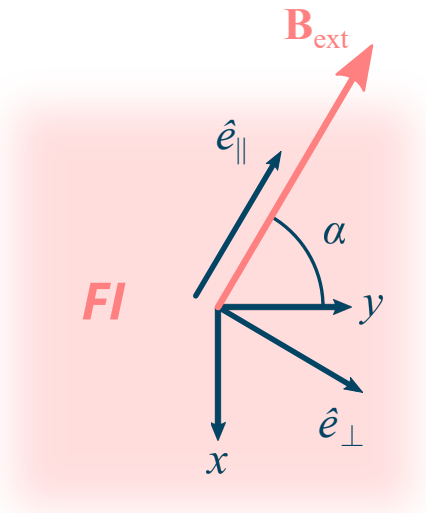

Figure 8.3: $\mathbf{B}_{\text{ext}}$ at an arbitrary in-plane angle α. The parallel and perpendicular directions are $\hat{e}_{\parallel}$ and $\hat{e}_{\perp}$, respectively.

In the calculations presented in Ch. 7, we took the external in-plane field $\mathbf{B}_{\text{ext}}$ to point in the y direction. This biased the contributing Zeeman coupling (7.24) towards the component q_y of the photon momenta. The model is readily generalized to allow for an arbitrary in-plane direction of $\mathbf{B}_{\text{ext}}$, and we show this here.

Let $\mathbf{B}_{\text{ext}}$ point in an arbitrary direction defined by its polar angle α (see Fig. 8.3). Then after the Holstein–Primakoff transformation (Sec. 2.2.1), the in-plane, perpendicular spin component $\mathbf{S}_{\perp}$ becomes

$$\mathbf{S}_{\perp} = \frac{\hbar\sqrt{2S}}{2}(-i\eta_i + (-i)^*\eta_i^{\dagger})\hat{e}_{\perp} \tag{8.1}$$

cf. Eq. (7.20). The only formal difference between this component and the component S_{ix} that contributed to the interactions in Ch. 7, is its direction $\hat{e}_{\perp}$. In terms of the xy directions, this unit vector reads

$$\hat{e}_{\perp} = -\hat{e}_y \cos\alpha + \hat{e}_x \sin\alpha. \tag{8.2}$$

Dotted with $\mathbf{B}_{\text{cav}} \propto q_y\hat{e}_x - q_x\hat{e}_y$ (Eq. (5.9a)), we find that the coupling constant (7.24) now does not scale only with q_y, but more generally with

$$\hat{e}_{\perp} \cdot (q_y\hat{e}_x - q_x\hat{e}_y) = q_x \cos\alpha + q_y \sin\alpha. \tag{8.3}$$

Its gradient,

$$\nabla_{\mathbf{q}}[q_x \cos\alpha + q_y \sin\alpha] = \hat{e}_x \cos\alpha + \hat{e}_y \sin\alpha = \hat{e}_{\|}, \tag{8.4}$$

shows that its greatest slope is now generally along $\hat{e}_{\|}$, i.e. $\mathbf{B}_{\text{ext}}$, with the same magnitude as before. Corrections to the magnon energy are now biased towards gradients in the SC quasiparticle energy pointing in *this* direction. Note that the bias does not favor complete alignment with $\mathbf{B}_{\text{ext}}$, as seen by considering the other $\mathbf{k}$-dependent factors entering the self energy (7.42). While the remaining factors in the Zeeman coupling (7.24) are isotropic in $\mathbf{q} = \mathbf{k}$, the paramagnetic coupling (7.15) instead introduces four-fold symmetry. It is seen to favor diagonals in $\mathbf{k}$ space over k_x or k_y by a multiplicative factor $\sqrt{2}$. This symmetry originates from the SC lattice geometry, taken to be square in our model for simplicity (the symmetry is also seen in Ref. [11]). If used as a probe for SC gap anisotropy, the magnon spectrum would have to be corrected for this lattice-geometry bias in order to isolate the effect of gap anisotropy.

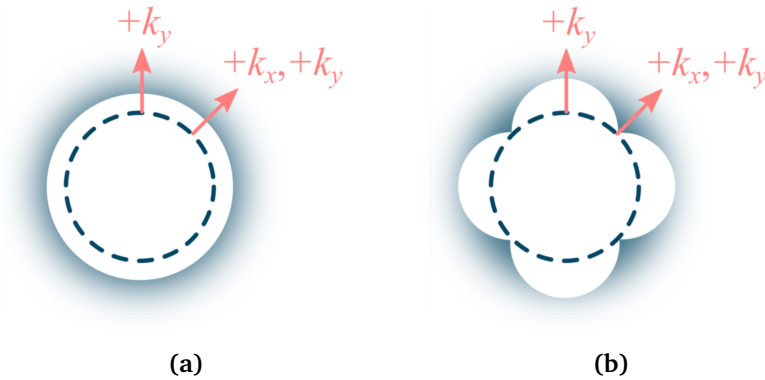

Figure 8.4: A circular Fermi level (dashed line) with (a) an s-wave gap, and (b) a d-wave gap, presenting an energy barrier up to the finite-temperature SC quasiparticles (cloud). Here we have for simplicity only taken into account the $m = 0$ type quasiparticles, which have energies above the Fermi level. Depending on what directional derivative (red arrows) of the quasiparticle energy is probed for by an appropriate adjustment of the angle of $\mathbf{B}_{\text{ext}}$ (hence $\mathbf{k}$ bias), the magnon energy correction will be more or less suppressed by anisotropy in the gap. Note that directional derivatives from all across $\mathbf{p}$ space enter the self energy, not just the singular points of the arrows at the Fermi level shown here.

The corrections to the magnon spectrum were shown to be rapidly suppressed by the onset of superconductivity, nearly halving in magnitude through 0.1 K below T_c (Fig. 7.6). However, a range of 0.1 K is well within experimental resolution. In effect, the magnon spectrum captures a "negative" of the gap, its absence. Combined with the readily adjustable directional sensitivity to Fermi level gradients, these energy corrections are promising candidates for detecting momentum anisotropy of the superconducting gap in remote spintronic circuitry, across distances exceeding the scales at which proximity effects effectuate disruption of the

magnetic and superconducting orders; see Fig. 8.4 for a conceptual drawing. Specifically, we anticipate the directional sensitivity selected by the readily adjustable field $\mathbf{B}_{\text{ext}}$, will lead to greater or lesser suppression of the magnon energy corrections by the gap at the onset of superconductivity. However, while the strongest numerical results are within a currently detectable range at T_c (i.e. in absence of a gap), the weaker results are not, and they are only distinguished by details of the Fermi surface. Before pursuing the question of probing general gaps, it is therefore first necessary to look for means to enhance the self energy above expected losses, without relying on favorable material-specific properties of the SC, including in particular the distribution of directional derivatives of the Fermi surface.

We stress that little work is required to accommodate for anisotropic gaps in our model. The isotoropy of the gap has only been invoked in the numerics (in Paper II and Secs. 7.4.1 and 7.4.2). The broader quality of even inversion symmetry in momentum space (along with spin antisymmetry) was assumed when introducing the pairing Hamiltonian (3.12). The analytics therefore already accomodate for inversion-symmetric singlet gaps, e.g. the d-wave gap illustrated in Fig. 8.4b. For inversion-antisymmetric (e.g. p-wave) gaps, it is necessary to follow through with symmetric (triplet) spin indices in the pairing Hamiltonian (3.12).[4]

8.3.2 Concluding remarks

In summary, our research has resulted in a versatile model for cavity-mediated interactions between an FI and an SC. We have demonstrated the theoretical strengths of the path integral formalism in this context, as compared to common approaches based on the Schrieffer–Wolff transformation, Jaynes–Cummings-like modelling, and classical modelling. Ultimately directing our focus towards the mediated effects of the SC on the FI, we have derived an expression for the reorientation of the FI spins in response to broken inversion symmetry in the SC, and also the correction to the magnon spectrum due to mediated resonances with the SC quasiparticles. We have moreover presented promising numerical results along with an in-depth analysis for the latter, within a detectable range weighed against expected losses. We have also provided a promising numerical example for the effective anisotropy field (i.e., spin reorientation) in Paper II, in which the FI and SC were separated by a distance 1–5 orders above the length scales of proximity effects. The long-distance mediation facilitates subjection of the FI and SC to separate drives and temperatures, as well as interactions without the mutual disruption of their orders associated with proximity effects, such as the breaking of Cooper pairs due to the FI magnetization.

The research leaves many interesting avenues to explore in continuations of the work. This includes refinements such as taking into account reflective boundary conditions in all directions in order to resolve absolute positional dependency

[4]Technically there exist exotic gaps that are p-wave singlet, and invert some other symmetry, such as time inversion [132]. However, these gaps are beyond our model, since we have disregarded the time (and orbital) index altogether.

inside the cavity; continuations such as analyzing the mediated effect of the FI on the SC, or both on the cavity; and extensions such as coupling to gap fluctuations, and considering other categories of the gap than the simple singlet *s*-wave (an isotropic gap). The latter is suggested in light of observations made in the analysis of the corrections to the magnon spectrum, viz., their sensitivity to directional derivates at the Fermi level of the SC, and their rapid suppression by the onset of superconductivity. We anticipate that combining these properties of the corrections would enable the magnon spectrum to resolve anisotropy in the SC gap. We stress that the analytics already accommodate for inversion-symmetric anisotropic gaps, and little work is required to implement inversion-antisymmetric gaps. As with many other dissertations, we conclude this one with an open ending.

Bibliography

1. H. D. Young, R. A. Freedman, A. L. Ford, *University Physics with Modern Physics* (Pearson, ed. 13, 2011), vol. 2.
2. Ø. Johansen, PhD thesis, Norwegian University of Science and Technology, 2019.
3. J. A. Ouassou, PhD thesis, Norwegian University of Science and Technology, 2019.
4. J. Linder, J. W. A. Robinson, *Nature Physics* **11**, 307 (2015).
5. T. Tokuyasu, J. A. Sauls, D. Rainer, *Phys. Rev. B* **38**, 8823 (1988).
6. E. A. Demler, G. B. Arnold, M. R. Beasley, *Phys. Rev. B* **55**, 15174 (1997).
7. M. Eschrig, *Rep. Prog. Phys.* **78**, 104501 (2015).
8. M. S. Anwar, F. Czeschka, M. Hesselberth, M. Porcu, J. Aarts, *Phys. Rev. B* **82**, 100501 (2010).
9. R. S. Keizer, S. T. B. Goennenwein, T. M. Klapwijk, G. Miao, X. G., A. Gupta, *Nature* **439**, 825 (2006).
10. Ø. Johansen, A. Brataas, *Phys. Rev. Lett.* **121**, 087204 (2018).
11. F. Schlawin, A. Cavalleri, D. Jaksch, *Phys. Rev. Lett.* **122**, 133602 (2019).
12. A. T. G. Janssønn, H. T. Simensen, A. Kamra, A. Brataas, S. H. Jacobsen, *Phys. Rev. B* **102**, 180506(R) (2020).
13. Y. Tabuchi, S. Ishino, A. Noguchi, T. Ishikawa, R. Yamazaki, K. Usami *et al.*, *Science* **349**, 405–408 (2015).
14. Y. Tabuchi, S. Ishino, A. Noguchi, T. Ishikawa, R. Yamazaki, K. Usami *et al.*, *Comptes Rendus Physique* **17**, 729 (2016).
15. H. Huebl, C. W. Zollitsch, J. Lotze, F. Hocke, M. Greifenstein, A. Marx *et al.*, *Phys. Rev. Lett.* **111**, 127003 (2013).
16. J. Bourhill, N. Kostylev, M. Goryachev, D. L. Creedon, M. E. Tobar, *Phys. Rev. B* **93**, 144420 (2016).
17. Y. Tabuchi, S. Ishino, T. Ishikawa, R. Yamazaki, K. Usami, Y. Nakamura, *Phys. Rev. Lett.* **113**, 083603 (2014).
18. F. Schlawin, D. M. Kennes, M. A. Sentef, *Appl. Phys. Rev.* **9**, 011312 (2022).

19. A. F. Kockum, A. Miranowicz, S. De Liberato, S. Savasta, F. Nori, *Nature* **1**, 19 (2019).
20. X. Liu, T. Galfsky, Z. Sun, F. Xia, E. Lin, S. Lee Y.-H. Kéna-Cohen *et al.*, *Nature Photonics* **9**, 30 (2015).
21. Q. Zhang, M. Lou, X. Li, J. L. Reno, W. Pan, J. D. Watson *et al.*, *Nature Physics* **12**, 1005 (2016).
22. A. Bayer, M. Pozimski, S. Schambeck, D. Schuh, R. Huber, D. Bougeard *et al.*, *Nano Letters* **17**, 6340 (2017).
23. J. Keller, G. Scalari, S. Cibella, C. Maissen, F. Appugliese, E. Giovine *et al.*, *Nano Letters* **17**, 7410 (2017).
24. D. Lachance-Quirion, Y. Tabuchi, A. Gloppe, K. Usami, Y. Nakamura, *Appl. Phys. Express* **12**, 070101 (2019).
25. Z. R. Rameshti, S. V. Kusminskiy, J. A. Haigh, K. Usami, D. Lachance-Quirion, Y. Nakamura *et al.*, *Phys. Rep.* **979**, 1 (2022).
26. Ö. O. Soykal, M. E. Flatté, *Phys. Rev. B* **82**, 104413 (2010).
27. Ö. O. Soykal, M. E. Flatté, *Phys. Rev. Lett.* **104**, 077202 (2010).
28. T. Liu, X. Zhang, H. X. Tang, M. E. Flatté, *Phys. Rev. B* **94**, 060405 (2016).
29. S. Viola Kusminskiy, H. X. Tang, F. Marquardt, *Phys. Rev. A* **94**, 033821 (2016).
30. M. Harder, C.-M. Hu, in *Solid State Physics*, ed. by R. E. Camley, R. L. Stamps (Academic Press, 2018), vol. 69, pp. 47–121.
31. H. Y. Yuan, Y. Cao, A. Kamra, R. A. Duine, P. Yan, *Phys. Rep.* **965**, 1 (2022).
32. L. Bai, M. Harder, Y. P. Chen, X. Fan, J. Q. Xiao, C.-M. Hu, *Phys. Rev. Lett.* **114**, 227201 (2015).
33. L. Liensberger, F. X. Haslbeck, A. Bauer, H. Berger, R. Gross, H. Huebl *et al.*, *Phys. Rev. B* **104**, L100415 (2021).
34. S. Khan, O. Lee, T. Dion, C. W. Zollitsch, S. Seki, Y. Tokura *et al.*, *Phys. Rev. B* **104**, L100402 (2021).
35. L. V. Abdurakhimov, S. Khan, N. A. Panjwani, J. D. Breeze, M. Mochizuki, S. Seki *et al.*, *Phys. Rev. B* **99**, 140401 (2019).
36. X. Zhang, C.-L. Zou, L. Jiang, H. X. Tang, *Phys. Rev. Lett.* **113**, 156401 (2014).
37. F. Schlawin, D. Jaksch, *Phys. Rev. Lett.* **123**, 133601 (2019).
38. M. A. Sentef, M. Ruggenthaler, A. Rubio, *Science Adv.* **4**, eaau6969 (2018).
39. F. P. Laussy, A. V. Kavokin, I. A. Shelykh, *Phys. Rev. Lett.* **104**, 106402 (2010).
40. G. Li, O. Bleu, M. M. Parish, J. Levinsen, *Phys. Rev. Lett.* **126**, 197401 (2021).

41. O. Cotleţ, S. Zeytinoğlu, M. Sigrist, E. Demler, A. Imamoğlu, *Phys. Rev. B* **93**, 054510 (2016).
42. A. Kavokin, P. Lagoudakis, *Nature Mater.* **16**, 599 (2016).
43. J. B. Curtis, Z. M. Raines, A. A. Allocca, M. Hafezi, V. M. Galitski, *Phys. Rev. Lett.* **122**, 167002 (2019).
44. J. Bloch, A. Cavalleri, V. Galitski, M. Hafezi, A. Rubio, *Nature* **606**, 41 (2022).
45. D. Lachance-Quirion, Y. Tabuchi, S. Ishino, A. Noguchi, T. Ishikawa, R. Yamazaki *et al.*, *Science Av.* **3**, e1603150 (2017).
46. A. Wallraff, D. I. Schuster, A. Blais, L. Frunzio, R.-S. Huang, J. Majer *et al.*, *Nature* **431**, 162 (2004).
47. M. A. Sillanpää, J. I. Park, R. W. Simmonds, *Nature* **449**, 438 (2007).
48. M. Hofheinz, E. M. Weig, M. Ansmann, R. C. Bialczak, E. Lucero, M. Neeley *et al.*, *Nature* **454**, 310 (2008).
49. J. M. Fink, M. Göppl, M. Baur, R. Bianchetti, P. J. Leek, A. Blais *et al.*, *Nature* **454**, 315 (2008).
50. A. Blais, R.-S. Huang, A. Wallraff, S. M. Girvin, R. J. Schoelkopf, *Phys. Rev. A* **69**, 062320 (2004).
51. B. Zare Rameshti, G. E. W. Bauer, *Phys. Rev. B* **97**, 014419 (2018).
52. N. J. Lambert, J. A. Haigh, S. Langenfeld, A. C. Doherty, A. J. Ferguson, *Phys. Rev. A* **93**, 021803 (2016).
53. A. Cottet, Z. Leghtas, T. Kontos, *Phys. Rev. B* **102**, 155105 (2020).
54. A. Chiocchetta, D. Kiese, C. P. Zelle, F. Piazza, S. Diehl, *Nature Commun.* **12**, 5901 (2021).
55. J. Román-Roche, D. Zueco, *SciPost Phys. Lect. Notes*, 50 (2022).
56. C. Kittel, *Introduction to solid state physics* (John Wiley & Sons, Inc., 2005).
57. *Electromagnetism – Historical survey*, Encyclopedia Britannica. `https://www.britannica.com/science/electromagnetism/Historical-survey`, accessed 2022-06-13.
58. D. Harper, *magnet (n.),* Online Etymological Dictionary. `https://www.etymonline.com/word/magnet`, accessed 2022-06-16.
59. L. Néel, *Ann. Phys. (Paris)* **11**, 232 (1936).
60. L. Néel, *Ann. Phys. (Paris)* **12**, 137 (1948).
61. L. Néel, *Proc. Phys. Soc., London, Sec. A* **65**, 869 (1952).
62. R. C. LeCraw, E. G. Spencer, C. S. Porter, *Phys. Rev.* **110**, 1311 (1958).
63. C. Vittoria, P. Lubitz, P. Hansen, W. Tolksdorf, *J. Appl. Phys.* **57**, 3699 (1985).

64. C. Hauser, T. Richter, N. Homonnay, C. Eisenschmidt, M. Qaid, H. Deniz *et al.*, *Sci. Rep.* **6**, 20827 (2016).
65. L. Sheng, J. Chen, H. Wang, H. Yu, *J. Phys. Soc. Japan* **90**, 081005 (2021).
66. P. C. Hemmer, *Kvantemekanikk* (Tapir Akademisk Forlag, 2005).
67. A. Hirohata, K. Yamada, Y. Nakatani, I.-L. Prejbeanu, B. Diény, P. Pirro *et al.*, *J. Mag. Mag. Mat.* **509**, 166711 (2020).
68. C. Kittel, *Quantum Theory of Solids* (John Wiley & Sons, Inc., 1963).
69. T. Holstein, H. Primakoff, *Physical Review* **58**, 1098 (1940).
70. E. Kreyszig, *Advanced Engineering Mathematics* (John Wiley & Sons, Inc., ed. 10, 2011).
71. M. Tinkham, *Introduction to Superconductivity* (McGraw-Hill, 1996).
72. H. Kammerling Onnes, *Leiden Comm.* **120b, 122b, 124c** (1911).
73. F. W. Meissner, R. Ochsenfeld, *Naturwissenschaften* **21**, 787 (1933).
74. *The Nobel Prize in Physics 1972*, Press release. NobelPrize.org. Nobel Prize Outreach AB 2022. `https://www.nobelprize.org/nobel_prizes/physics/laureates/1972/`, accessed 2022-06-09.
75. *The Nobel Prize in Physics 2003*, Press release. NobelPrize.org. Nobel Prize Outreach AB 2022. `https://www.nobelprize.org/nobel_prizes/physics/laureates/2003/`, accessed 2022-06-09.
76. *The Nobel Prize in Physics 1962*, Press release. NobelPrize.org. Nobel Prize Outreach AB 2022. `https://www.nobelprize.org/nobel_prizes/physics/laureates/1962/`, accessed 2022-06-09.
77. *The Nobel Prize in Physics 1913*, Press release. NobelPrize.org. Nobel Prize Outreach AB 2022. `https://www.nobelprize.org/nobel_prizes/physics/laureates/1913/`, accessed 2022-06-14.
78. F. London, H. London, *Proc. R. Soc., London* **A149**, 71 (1935).
79. D. C. Mattis, J. Bardeen, *Phys. Rev.* **111**, 412 (1958).
80. M. Dressel, *Adv. Cond. Matt. Phys.* **2013**, 104379 (2013).
81. F. London, *Phys. Rev.* **74**, 562 (1948).
82. A. B. Pippard, *Proc. Phys. Soc., London, Sec. A* **216**, 547 (1953).
83. R. G. Chambers, *Proc. Phys. Soc., London, Sec. A* **215**, 418 (1952).
84. J. Bardeen, L. N. Cooper, J. R. Schrieffer, *Phys. Rev.* **108**, 1175 (1957).
85. J. Bardeen, D. Pines, *Phys. Rev.* **99**, 1140 (1955).
86. M. Amundsen, PhD thesis, Norwegian University of Science and Technology, 2020.
87. J. P. Morten, A. Brataas, W. Belzig, *Phys. Rev. B* **70**, 212508 (2004).
88. L. P. Gor'kov, *Zh. Eksp. Teor. Fiz.* **34**, 505 (1958).

89. G. M. Eliashberg, *Zh. Eksp. Teor. Fiz.* **11**, 696 (1960).
90. G. Eilenberger, *Z. Phys. A* **2014**, 195 (1968).
91. U. Eckern, A. Schmid, *J. Low Temp. Phys.* **45**, 137 (1981).
92. J. Linder (private lecture notes). *Quasiclassical theory*, 2021.
93. K. D. Usadel, *Phys. Rev. Lett.* **25**, 507 (1970).
94. J. Linder, A. V. Balatsky, *Rev. Mod. Phys.* **91**, 045005 (2019).
95. E. Erlandsen, A. Brataas, A. Sudbø, *Phys. Rev. B* **101**, 094503 (2020).
96. K. Takasan, S. Sumita, Y. Yanase, *Phys. Rev. B* **106**, 014508 (2022).
97. J. Pearl, *Applied Physics Letters* **5**, 65 (1964).
98. *rav*, Store norske leksikon. `https://snl.no/rav`, accessed 2022-06-17.
99. D. J. Griffiths, *Introduction to Electrodynamics* (Pearson, ed. 4, 2014).
100. K. Kakazu, Y. S. Kim, *Phys. Rev. A* **50**, 1830 (1994).
101. R. A. Adams, C. Essex, *Calculus: A Complete Course* (Pearson, ed. 8, 2013).
102. C. P. Poole Jr., *Electron Spin Resonance* (John Wiley & Sons, Inc., 1983).
103. K. Rottmann, *Matematisk Formelsamling* (Spektrum forlag, ed. 13, 2013).
104. C. Tsallis, *J. Math. Phys.* **19**, 277 (1978).
105. J. L. van Hemmen, *Z. Phys. B* **38**, 271 (1980).
106. A. S. Cadellans, PhD thesis, Norwegian University of Science and Technology, 2020.
107. J. O. Andersen, *Introduction to statistical mechanics* (Akademisk forlag, 2012).
108. A. Altland, B. Simons, *Condensed Matter Field Theory* (Cambridge University Press, ed. 8, 2010).
109. A. Zee, *Quantum Field Theory in a Nutshell* (Princeton University Press, 2010).
110. M. Kachelrieß, *Quantum Fields: From the Hubble to the Planck Scale* (Oxford University Press, 2017).
111. J. Garcia, R. Rossignoli, *Phys. Rev. A* **96**, 062130 (2017).
112. R. Rossignoli, A. M. Kowalski, *Phys. Rev. A* **72**, 032101 (2005).
113. R. Rossignoli, A. M. Kowalski, *Phys. Rev. A* **79**, 062103 (2009).
114. J. W. Negele, H. Orland, *Quantum Many-Particle Systems* (Westview Press, 1998).
115. H. Bruus, K. Flensberg, *Many-body Quantum Theory in Condensed Matter Physics* (Oxford University Press, 2004).
116. K. Mæland, H. I. Røst, J. W. Wells, A. Sudbø, *Phys. Rev. B* **104**, 125125 (2021).

117. X. Liu, Q. Yang, D. Zhang, Y. Wu, H. Zhang, *AIP Adv.* **9**, 115001 (2019).

118. Y. Lin, L. Jin, H. Zhang, Z. Zhong, Q. Yang, Y. Rao *et al.*, *Journal of Magnetism and Magnetic Materials* **496**, 165886 (2020).

119. I. Zaytseva, A. Abaloszew, B. C. Camargo, Y. Syryanyy, M. Z. Cieplak, *Sci. Rep.* **10**, 19062 (2020).

120. P. R. Broussard, *J. Low. Temp. Phys.* **189**, 108 (2017).

121. M. A. Musa, R. S. Azis, N. H. Osman, J. Hassan, T. Zangina, *Results in Physics* **7**, 1135 (2017).

122. N. W. Ashcroft, N. D. Mermin, *Solid State Physics* (Saunders, 1976).

123. I. S. Tupitsyn, P. C. E. Stamp, A. L. Burin, *Phys. Rev. Lett.* **100**, 257202 (2008).

124. A. Kreisel, F. Sauli, L. Bartosch, P. Kopietz, *The Eur. Phys. J. B* **71**, 59 (2009).

125. A. I. Gubin, K. S. Il'in, S. A. Vitusevich, M. Siegel, N. Klein, *Phys. Rev. B* **72**, 064503 (2005).

126. C. M. Srivastava, R. Aiyar, *J. Phys. C* **20**, 1119 (1987).

127. Z. M. Raines, A. A. Allocca, M. Hafezi, V. M. Galitski, *Phys. Rev. Research* **2**, 013143 (2020).

128. M. Puviani, L. Schwarz, X.-X. Zhang, S. Kaiser, D. Manske, *Phys. Rev. B* **101**, 220507 (2020).

129. Y. Lu, R. Ojajärvi, P. Virtanen, M. Silaev, T. T. Heikkilä, arXiv:2108.06202 (accepted in Phys. Rev. B).

130. A. Moor, A. F. Volkov, K. B. Efetov, *Phys. Rev. Lett.* **118**, 047001 (2017).

131. S. Nakamura, Y. Iida, Y. Murotani, R. Matsunaga, H. Terai, R. Shimano, *Phys. Rev. Lett.* **122**, 257001 (2019).

132. J. Linder, A. V. Balatsky, *Rev. Mod. Phys.* **91**, 045005 (2019).

133. J. Als-Nielsen, R. J. Birgeneau, *Am. J. Phys.* **45**, 554 (1977).

Paper I

Rapid Communications

Macroscale nonlocal transfer of superconducting signatures to a ferromagnet in a cavity

Andreas T. G. Janssønn, Haakon T. Simensen, Akashdeep Kamra, Arne Brataas, and Sol H. Jacobsen*
Center for Quantum Spintronics, Department of Physics, Norwegian University of Science and Technology (NTNU), NO-7491 Trondheim, Norway

(Received 22 June 2020; revised 17 September 2020; accepted 14 October 2020; published 23 November 2020)

Cavity spintronics recently heralded nonlocal magnonic signal transfer between magnetic samples. Here we show that by including superconductors in the cavity, we can make use of these principles to bring composite superconductor-ferromagnet systems to the macroscale. We analyze how a superconductor's ac conductivity influences the spin dynamics of a spatially separated magnet, and we discuss the potential impact on spintronic applications.

DOI: 10.1103/PhysRevB.102.180506

The field of superconducting spintronics has been gathering pace in the last decade as the promise of achieving low dissipation spin and charge transport has been increasingly refined and realized [1–3]. It relies on the proximity effect, whereby properties of one material can persist in an adjacent thin film. This places a tight nanometer constraint on the operational range in most cases. The most anomalously long-ranged persistence of superconductive signatures is reportedly up to the micrometer range [4,5]. However, in this Rapid Communication we highlight the untapped potential of composite superconductor-ferromagnet systems to make use of advances in cavitronics, and that photon-mediated processes can enable the detection of centimeter-ranged superconductive signatures. We provide a readily accessible example to establish the proof of concept, and discuss multiple directions for exploration to highlight the potential for innovation in superconducting spintronic applications.

Cavity spintronics, or cavitronics, is an emerging interdisciplinary field in which microwave or optical cavity photon modes can couple to magnons (also called spin waves). Experiments have shown strong coupling of cavity modes to both ferri- and ferromagnets [6,7]. This is observed as a hybridization of the photon and magnon modes, indicated by avoided crossings/Rabi splitting in the normal mode frequency spectrum. It was recently shown that magnonic interactions between two nonlocal magnetic samples can be mediated by the cavity modes [8–10]. This means information encoded in the magnitude and phase of the spin waves (i.e., spintronic information) can be transmitted nonlocally over macroscopic length scales. We explore the question of magnons coupling nonlocally to excitations in a superconductor.

Light with frequencies above the superconducting gap breaks Cooper pairs and thus weakens the superconductivity. However, light can also enhance or induce superconductivity [11–13]. In-cavity manipulation of a superconductive component might appear restrictive, demanding effective screening of the contact wires while maintaining the quality factor of the cavity, but also this has been achieved experimentally recently [14]. In that case, researchers succeeded in driving a black box transmon qubit inside a cavity, coupling the oscillations between the two levels of the qubit to the microwave cavity modes. The transmon qubit is engineered by using the nonlinearity of a superconducting Josephson junction to create an effective two-level system, as in circuit quantum electrodynamics (QED) [15]. Consequently, this qubit-cavity coupling generated excitement about the potential prospect of unifying quantum optics and solid state quantum computing [16,17].

Qubit-cavity coupling demonstrated the feasibility of screening wiring to a superconducting system inside microwave cavities. However, superconductivity in that case is used as a means to generate a two-level system, i.e., realize a qubit, and not as a means to probe and use the superconductive signatures themselves. By combining standard approaches for the electrodynamics of superconductivity, cavity coupling, and magnetism dynamics, we will here provide a proof of principle that there is considerable potential to do just that.

We begin by considering the setup illustrated in Fig. 1. It depicts a microwave cavity containing an electrically screened thin wire, which has a small exposed superconducting segment (SC) held at temperature T, connected to an alternating current (ac) source, as well as a small ferromagnetic sphere (FM). The internal current density $\boldsymbol{J}$ and electric field $\boldsymbol{E}_{\mathrm{SC}}$ of the SC are treated as uniform; i.e., internal spatial variations are neglected. The SC and the FM are placed in regions of maximum electric and magnetic field $\boldsymbol{E}_{\mathrm{cav}}$ and $\boldsymbol{B}_{\mathrm{cav}}$ of a selected cavity mode, respectively. The dimensions of the SC and the FM are assumed sufficiently small for the local fields across their respective regions to be approximately uniform, and their spatial extension is effectively taken to be linelike and pointlike at positions $\boldsymbol{r}_{\mathrm{SC}}$ and $\boldsymbol{r}_{\mathrm{FM}}$, respectively.

The SC is directed along the y direction, and has a critical temperature T_c. The ac source produces signal frequency ω, which is resonant with the cavity frequency and the frequency of the precessing FM magnetization. By lowering T, we pass through the superconducting transition and induce

*Corresponding author: sol.jacobsen@ntnu.no

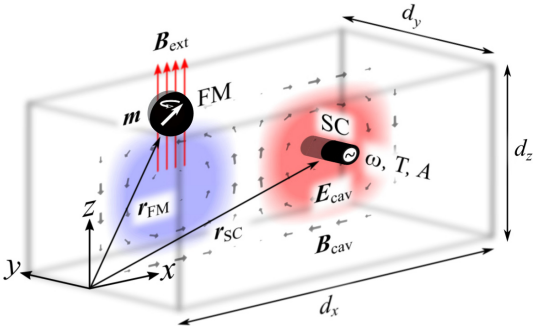

FIG. 1. The proposed model for inducing macroscale photon-mediated superconducting signatures in a magnet (not to scale). The photonic microwave resonator of dimensions $\{d_x, d_y, d_z\}$ contains a short, thin superconducting wire segment (SC) along the y direction and with a cross-sectional area A, connected to an alternating current source via screened wiring through the cavity walls, as well as a small ferromagnetic sphere (FM) with a uniform magnetization $\boldsymbol{m}$. The FM and SC are positioned at $\boldsymbol{r}_{\rm FM}$ and $\boldsymbol{r}_{\rm SC}$, respectively, corresponding to extrema of the magnetic and electric components of the cavity modes $\boldsymbol{B}_{\rm cav}$ and $\boldsymbol{E}_{\rm cav}$. Across the SC, $\boldsymbol{E}_{\rm cav}$ is directed along the y axis, and across the FM, $\boldsymbol{B}_{\rm cav}$ is directed along the x axis. The FM is additionally subjected to a strong external magnetostatic field $\boldsymbol{B}_{\rm ext}$ such that $|\boldsymbol{B}_{\rm ext}| \gg |\boldsymbol{B}_{\rm cav}|$, which fixes the precessional axis of $\boldsymbol{m}$ along the z direction. We use the TE_{201} cavity mode as an example. The SC current, cavity mode, and FM mode couple resonantly at the input ac frequency ω. The relative amounts of supercurrent and resistive currents passed through the SC is modulated by the temperature T.

a change in the superconductors conductivity. This in turn alters the excitation of the cavity, and the resultant effect on the spin dynamics in the magnet can be harnessed as a nonlocal detector. That is, by exploiting the mutually resonant coupling to the cavity, it is possible to probe the superconducting transition via a change in the magnonic precession response. We consider the weak-coupling approximation, in which the back-action does not alter the physical response of either system (the back-action cannot alter the established electromagnetic response of the superconducting transition).

As a concrete example, we consider the TE_{201} cavity mode, where $\boldsymbol{E}_{\rm cav}$ is directed along the y axis over the SC, and $\boldsymbol{B}_{\rm cav}$ along the x axis over the FM. $\boldsymbol{B}_{\rm cav}$ then couples predominantly to the Kittel mode of the FM, i.e., the uniform mode of the spherical spin field, quantified by the unit magnetization vector $\boldsymbol{m}$. The FM is additionally exposed to a relatively strong external magnetic field $\boldsymbol{B}_{\rm ext}$ such that $|\boldsymbol{B}_{\rm ext}| \gg |\boldsymbol{B}_{\rm cav}|$, which fixes the precessional axis of $\boldsymbol{m}$ along the z direction. $|\boldsymbol{B}_{\rm ext}|$ also regulates the resonance frequency of the spin field mode, and reduces the impact of $\boldsymbol{B}_{\rm cav}$ to small perturbations on the motion of $\boldsymbol{m}$. The resonance frequency of the TE_{201} mode is determined by $\{d_x, d_z\}$, which one may thus match to the resonance frequency of the Kittel mode and the frequency of the input ac by adjusting $|\boldsymbol{B}_{\rm ext}|$ and ω.

The current response of a superconductor to an applied electric field, taking into account both frequency and temperature, may be derived from microscopic theories of superconductivity, such as BCS or Eliashberg theory. Mattis-Bardeen theory is derived from the former [19,20], and provides accurate descriptions of the optical conductivity of BCS superconductors. However, these theories are generally cumbersome to deal with analytically, and will be reserved for numerical calculations. To analytically model the transition from resistive to superconducting current in the SC, we employ the well established framework of the two-fluid model [21].

The SC is treated as two parallel channels carrying normal (n) and superconducting (s) electrons, respectively. The superconducting channel is characterized by an asymptotically infinite relaxation time $\tau_s \longrightarrow \infty$, and the normal channel assumes a low input frequency $\omega\tau_n \ll 1$ relative to the relaxation time of n electrons. In this case,

$$\frac{d\boldsymbol{J}_s(\omega, T, t)}{dt} = \frac{N_s(T)e^2}{m_e}\boldsymbol{E}_{\rm SC}(\omega, T, t), \tag{1}$$

$$\frac{\boldsymbol{J}_n(\omega, T, t)}{\tau_n} = \frac{N_n(T)e^2}{m_e}\boldsymbol{E}_{\rm SC}(\omega, T, t), \tag{2}$$

where m_e is the electron mass, and $\boldsymbol{J}_i$ and N_i are the current and electron densities of the respective channels. For sinusoidal time dependencies there is therefore a relative phase difference of $\pm\pi/2$ between the contributions of $\boldsymbol{J}_s$ and $\boldsymbol{J}_n$ to $\boldsymbol{E}_{\rm SC}$ in a current-driven system. $\boldsymbol{E}_{\rm SC}$ thus acquires a phase relative to the net current density $\boldsymbol{J} = \boldsymbol{J}_n + \boldsymbol{J}_s$ between 0 and $\pm\pi/2$. We argue that this phase shift can be used to bridge superconducting and spintronic circuits via nonlocal coupling to magnons. In this case it can monitor the superconducting transition, and be implemented as a superconducting switch. More broadly, it opens the door for wider investigations of macroscale effects in superconducting circuits.

Upon connecting the SC to an ac source, the net current density magnitude $J(\omega, t) = I\exp(i\omega t)/A$, where I is the current amplitude, A the SC cross-sectional area, and ω the input frequency. Inserting into Eqs. (1) and (2), we have

$$E_{\rm SC}(\omega, T, t) = \frac{I}{A\sigma(\omega, T)}\exp(i\omega t), \tag{3}$$

where

$$\sigma(\omega, T) = \frac{e^2}{m_e}\left(N_n(T)\tau_n - i\frac{N_s(T)}{\omega}\right) \equiv \sigma_1(T) - i\sigma_2(\omega, T). \tag{4}$$

The phenomenological temperature dependency of N_i, and by extension σ_1 and σ_2, is

$$N_s(T) = N[1 - (T/T_c)^4], \quad N_n(T) = N(T/T_c)^4, \tag{5}$$

where N is the total electron density, and $T \leqslant T_c$ [21]. For the purpose of analytic insight we retain this simple form, although we include the standard temperature modification of the gap in the numerics [21]. Above T_c, σ reduces to the normal metal direct current conductivity $\sigma_0 \equiv Ne^2\tau_n/m_e$. Note that according to the Mattis-Bardeen theory, σ_1 is frequency dependent; near T_c, it has a pronounced coherence peak at lower frequencies, and a kink at higher frequencies due to optical excitations across the superconducting gap (see Fig. 2) [19,20]. Neither feature is captured by the two-fluid model. Nevertheless, in terms of the relative magnitudes of σ_1 and σ_2, and their point of intersection marking the boundary

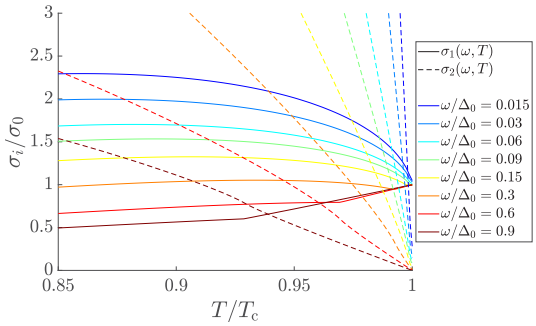

FIG. 2. Intersections of the real (σ_1) and negative imaginary (σ_2) part of the SC conductivity $\sigma = \sigma_1 - i\sigma_2$, as a function of T, for frequency inputs ω. Material parameters for Nb are used ($T_c = 9.26$ K) [18]; σ_0 is the normal state direct current conductivity. These plots are generated numerically using the Mattis-Bardeen theory [19].

between the superconducting and resistive regimes, the two-fluid model and Mattis-Bardeen theory coincide very well at the experimentally relevant lower frequencies. Figure 2 thus shows the predicted temperatures for the transition between normal and superconducting current [22].

$\boldsymbol{E}_{\rm SC}$ and $\boldsymbol{E}_{\rm cav}$ are assumed to be purely tangential to the SC-cavity interface in our setup (see Fig. 1). Thus, by the continuity of the tangential electric field across any interface, $\boldsymbol{E}_{\rm SC}(\boldsymbol{r}_{\rm SC},\omega,T,t) = \boldsymbol{E}_{\rm cav}(\boldsymbol{r}_{\rm SC},\omega,T,t)$ at the surface of the SC. Upon computing the cavity modes by imposing rectangular boundary conditions on the fields, one finds that across the FM and specifically for the $\rm TE_{201}$ mode, $\boldsymbol{B}_{\rm cav}$ at the FM is [23,24]

$$\begin{aligned}\boldsymbol{B}_{\rm cav}(\boldsymbol{r}_{\rm FM},\omega,T,t) &= B_{\rm cav}(\boldsymbol{r}_{\rm FM},\omega,T,t)\hat{x}\\ &= -\frac{\pi E_{\rm cav}(\boldsymbol{r}_{\rm SC},\omega,T,t)}{i\omega d_z}\hat{x}.\end{aligned} \tag{6}$$

Furthermore, the resonance frequency of the $\rm TE_{201}$ mode is

$$\omega = c\sqrt{\left(\frac{2\pi}{d_x}\right)^2 + \left(\frac{\pi}{d_z}\right)^2}, \tag{7}$$

where c is the speed of light in vacuum. With d_x and d_z given, this equality for resonant coupling is ensured by tuning ω.

The precessional motion of the FM magnetization vector m is adequately described by the Landau-Lifshitz-Gilbert (LLG) equation:

$$\begin{aligned}\frac{\partial \boldsymbol{m}(\omega,T,t)}{\partial t} &= -\gamma \boldsymbol{m}(\omega,T,t)\times \boldsymbol{B}(\omega,T,t)\\ &\quad + \alpha \boldsymbol{m}(\omega,T,t)\times\frac{\partial \boldsymbol{m}(\omega,T,t)}{\partial t}.\end{aligned} \tag{8}$$

Here, γ and α are the gyromagnetic ratio and the phenomenological damping parameter of the LLG equation, respectively. $\boldsymbol{B}$ is the effective magnetic field inside the FM, including the external, the demagnetization, and the magnetocrystalline anisotropy field [25,26]. The latter two are generally influenced by the geometry and crystal structure of the FM, and may influence ω and the orbit of $\boldsymbol{m}$. We assume an easy axis such as ⟨111⟩ for YIG [27], coinciding with the z direction; and negligible demagnetization and anisotropy fields relative to $\boldsymbol{B}_{\rm ext}$. The latter is reasonably expected to hold down to an input frequency of 5 GHz [27–30]. The effective magnetic field across the FM is then

$$\begin{aligned}\boldsymbol{B}(\omega,T,t) &= \boldsymbol{B}_{\rm cav}(\boldsymbol{r}_{\rm FM},\omega,T,t) + B_{\rm ext}\hat{z}\\ &= -\frac{\pi E_{\rm SC}(\boldsymbol{r}_{\rm SC},\omega,T,t)}{i\omega d_z}\hat{x} + B_{\rm ext}\hat{z}.\end{aligned} \tag{9}$$

When $|B_{\rm ext}| \gg |\boldsymbol{B}_{\rm cav}|$, $m_z \approx 1 \gg |m_x|, |m_y|$, to first order. In Eq. (8), terms of higher order than linear in $B_{\rm cav}$, m_x, and m_y, may then be neglected. In addition, the coupling between the cavity mode and the FM is resonant by design. Solving the LLG equation with complex time dependencies $\exp(i\omega t)$ in $\boldsymbol{B}$ and $\boldsymbol{m}$, one finally extracts the real parts as physical solutions [33]. Note that $\boldsymbol{B}_{\rm cav}$ oscillates exclusively along the x axis, which breaks the symmetry of the linearized LLG equation. The resulting orbits are consequently elliptical. The expression for $\boldsymbol{m}$ therefore has the form $\boldsymbol{m}(\omega,T,t) \approx \hat{z} + \boldsymbol{m}_p(\omega,T,t)$, with precessing component

$$\boldsymbol{m}_p(\omega,T,t) = [m_x(\omega,T)\hat{x} + m_y(\omega,T)\hat{y}]\exp(i\omega t). \tag{10}$$

Solving Eq. (8) for m_x and m_y and assuming weak damping $\alpha \ll 1$, one finds the phases relative to the input ac [34]:

$$\varphi_{m_x}(\omega,T) \equiv \arg[m_x(\omega,T)] \approx \arctan\frac{\sigma_2(\omega,T)}{\sigma_1(T)} + \frac{\alpha}{2}, \tag{11}$$

$$\varphi_{m_y}(\omega,T) \equiv \arg[m_y(\omega,T)] \approx \arctan\frac{\sigma_2(\omega,T)}{\sigma_1(T)} - \frac{\alpha}{2} - \frac{\pi}{2}. \tag{12}$$

Reinserting the solutions for m_x and m_y into Eq. (8), then taking the absolute value of both sides, yields $\omega = |\gamma B_{\rm ext}|$. For a given ω, this equality for resonant coupling is ensured by tuning $B_{\rm ext}$.

The phase and magnitude of the magnon precession allows us to extract measurable spintronic responses to changes in the superconductor. The magnitude of the precessing component $|\mathrm{Re}(\boldsymbol{m}_p)|$ relates to the cone angle of the precession, and is given by [35].

$$\begin{aligned}&|\mathrm{Re}[\boldsymbol{m}_p(\omega,T,t)]|\\ &\approx |m_y(\omega,T)|\sqrt{2\alpha\cos^2\left(\omega t + \varphi_{m_y} + \alpha + \frac{\pi}{2} - \theta\right) - \alpha + 1},\end{aligned} \tag{13}$$

where

$$|m_y(\omega,T)| \approx \frac{|\gamma|\pi I}{2A|\sigma(\omega,T)|\omega^2 d_z \alpha}, \tag{14}$$

$$\theta \approx \frac{3\pi + \alpha}{4}. \tag{15}$$

Within experimental limits such as the critical current of the SC, $|\mathrm{Re}(\boldsymbol{m}_p)| \lesssim 0.1$ may easily be achieved by regulating the input current amplitude I. Above this value, second- and higher-order corrections of the orbit become significant, and the full LLG must be employed. Note that for a negligible α, $|\mathrm{Re}(\boldsymbol{m}_p)|$ becomes independent of time; the orbit is then circular with $\varphi_{m_y} \longrightarrow \varphi_{m_x} - \pi/2$.

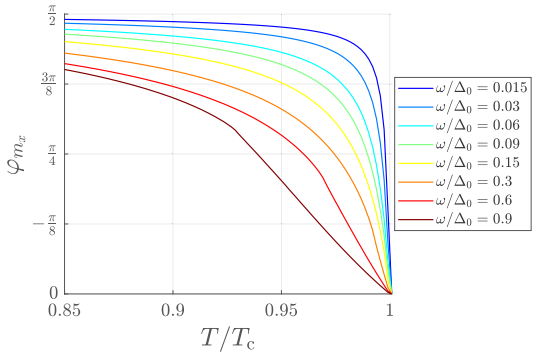

FIG. 3. Phase of the magnon precession φ_{m_x}, as a function of T, for frequency inputs ω, using the Mattis-Bardeen theory to compute the SC conductivity. Material parameters for Nb and YIG are used, with $T_c = 9.26$ K and $\alpha = 10^{-5}$ [18,26,31,32]. This phase may be measured relative to the input signal passed through the SC, and its value indicates the relative presence of supercurrent and resistive current in the SC. For this α, $\varphi_{m_y} \approx \varphi_{m_x} - \pi/2$.

Plots of φ_{m_x} and $|\mathrm{Re}(\boldsymbol{m}_p)|$ with realistic parameters using the Mattis-Bardeen theory are presented in Figs. 3 and 4. Equations (11) and (12) show as expected that in passing from a superconducting regime, i.e., $\sigma_2 \gg \sigma_1$, to a resistive regime, i.e., $\sigma_2 \ll \sigma_1$, the phase of $\mathrm{Re}(\boldsymbol{m}_p)$ will shift by $-\pi/2$, exactly corresponding to the simultaneous shift in $\boldsymbol{E}_{\mathrm{SC}}$. Moreover, it becomes clear from Eqs. (11)–(13) that as the FM damping α increases, the orbit becomes tilted in the xy plane with respect to its principal axes, and becomes progressively more eccentric [34]. The tilting angle between the x axis and the

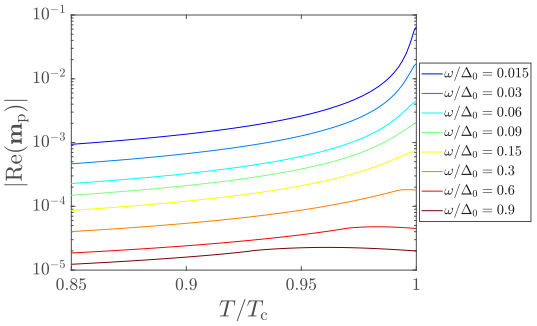

FIG. 4. The magnitude of the precessing component of the magnetization vector $|\mathrm{Re}(\boldsymbol{m}_p)|$, as a function of T, for frequency inputs ω, using the Mattis-Bardeen theory to compute the SC conductivity. Material parameters for Nb, a microwave cavity, and YIG are used, with $T_c = 9.26$ K, $\alpha = 10^{-5}$, $\gamma = 176$ GHz/T, $I = 0.6$ A, $A = 10^{-11}$ cm^2, and $d_z = 5$ cm [18,26,31,32]. Within experimental limits such as the critical current of the SC, the decrease in magnitude for increasing frequencies may be counteracted by increasing the input current.

major axis of the elliptic orbit is θ as given by Eq. (15). This phenomenon may be of particular interest in future works if one couples the FM and the SC by circularly instead of linearly polarized light, and if one operates with triplet instead of singlet superconductivity.

The above coupling mechanism shows clearly that a transition from the resistive to the superconducting state translates directly to a measurable nonlocal phase shift in the magnon precession frequency, with an experimentally resolvable perturbation of $\boldsymbol{m}$ of a few percent expected to be possible for various choices of magnetic and superconducting materials. The magnon excitations can be incorporated into extended spintronic circuitry outside the cavity, with no proximity coupling to the SC required. The shift in φ_{m_x} and φ_{m_y} may be measured, e.g., via Faraday rotation [36,37], or via ac spin pumping [25,38–41]. The method of Faraday rotation has sufficient resolution to detect single oscillations in the resonance frequency regimes of interest. The phase can then be measured relative to the ac input signal, as a function of the input frequency ω. Alternatively, ac spin pumping would be more easily achieved by changing the geometry of the ferromagnetic sphere to a film with deposited platinum layer. The analytics would then require the inclusion of the demagnetization field and associated shift in resonance, but it would not otherwise alter the physics.

This work shows that photon-mediated superconducting signatures are a feasible way to provide a bridging circuit for spintronic applications. In device design this can feature as a superconductive switch, but also to monitor the superconducting transition and critical temperature of the superconductor directly.

However, the importance of the result also goes beyond these applications as it opens up a plethora of interesting investigative avenues. For example, by switching from a conventional singlet superconductor to a triplet source (either intrinsically p wave or odd-frequency s wave), then there are no longer two simple coupling relationships to the cavity as in the case of the ac-driven oscillators in Eqs. (1) and (2). The nature of this coupling remains to be explored, but it seems plausible in that case that one may employ the cavity setup to probe and differentiate between the different current components. This may make cavity spintronics with superconductors—or super cavitronics—an interesting new tool for probing unconventional superconductors.

For the physical picture presented above, it is sufficient to consider a classical description of the coupling. However, it would be interesting to explore a microscopic picture along the line of cavity QED as outlined in Ref. [42]. In that case we can of course not neglect the details of the mesoscopic circuit by tracing over the mesoscopic degrees of freedom, meaning the mathematical approach becomes rather involved. Nevertheless, it is expected to yield valuable insight into the case of fermionic reservoirs in a cavity.

We thank H. Huebl for useful discussions. We acknowledge funding via the "Outstanding Academic Fellows" programme at NTNU, the Research Council of Norway Grant No. 302315, as well as through its Centres of Excellence funding scheme, Project No. 262633, QuSpin.

[1] J. Linder and J. W. A. Robinson, Nat. Phys. **11**, 307 (2015).
[2] M. Eschrig, Phys. Today **64** (1), 43 (2011).
[3] M. Eschrig, Rep. Prog. Phys. **78**, 104501 (2015).
[4] R. S. Keizer, S. T. B. Goennenwein, T. M. Klapwijk, G. Miao, G. Xiao, and A. Gupta, Nature (London) **439**, 825 (2006).
[5] M. S. Anwar, F. Czeschka, M. Hesselberth, M. Porcu, and J. Aarts, Phys. Rev. B **82**, 100501(R) (2010).
[6] H. Huebl, C. W. Zollitsch, J. Lotze, F. Hocke, M. Greifenstein, A. Marx, R. Gross, and S. T. B. Goennenwein, Phys. Rev. Lett. **111**, 127003 (2013).
[7] J. Bourhill, N. Kostylev, M. Goryachev, D. L. Creedon, and M. E. Tobar, Phys. Rev. B **93**, 144420 (2016).
[8] N. J. Lambert, J. A. Haigh, S. Langenfeld, A. C. Doherty, and A. J. Ferguson, Phys. Rev. A **93**, 021803(R) (2016).
[9] B. Zare Rameshti and G. E. W. Bauer, Phys. Rev. B **97**, 014419 (2018).
[10] Ø. Johansen and A. Brataas, Phys. Rev. Lett. **121**, 087204 (2018).
[11] D. Fausti, R. I. Tobey, N. Dean, S. Kaiser, A. Dienst, M. C. Hoffmann, S. Pyon, T. Takayama, H. Takagi, and A. Cavalleri, Science **331**, 189 (2011).
[12] M. Mitrano, A. Cantaluppi, D. Nicoletti, S. Kaiser, A. Perucchi, S. Lupi, P. D. Pietro, D. Pontiroli, M. Ricc, S. R. Clark, D. Jaksch, and A. Cavalleri, Nature (London) **530**, 461 (2016).
[13] A. Cavalleri, Contemp. Phys. **59**, 31 (2018).
[14] Y. Tabuchi, S. Ishino1, A. Noguchi, T. Ishikawa, R. Yamazaki, K. Usami, and Y. Nakamura, Science **349**, 405 (2015).
[15] A. Wallraff, D. I. Schuster, A. Blais, L. Frunzio, R.-S. Huang, J. Majer, S. Kumar, S. M. Girvin, and R. J. Schoelkopf, Nature (London) **431**, 162 (2004).
[16] A. Osada, R. Hisatomi, A. Noguchi, Y. Tabuchi, R. Yamazaki, K. Usami, M. Sadgrove, R. Yalla, M. Nomura, and Y. Nakamura, Phys. Rev. Lett. **116**, 223601 (2016).
[17] D. Lachance-Quirion, Y. Tabuchi, S. Ishino, A. Noguchi, T. Ishikawa, R. Yamazaki, and Y. Nakamura, Sci. Adv. **3**, e1603150 (2017).
[18] B. T. Matthias, T. H. Geballe, and V. B. Compton, Rev. Mod. Phys. **35**, 1 (1963).
[19] D. C. Mattis and J. Bardeen, Phys. Rev. **111**, 412 (1958).
[20] M. Dressel, Adv. Condens. Matter Phys. **2013**, 104379 (2013).
[21] M. Tinkham, *Introduction to Superconductivity* (McGraw-Hill, New York, 1996).
[22] The high-frequency cases are illustrative for materials with lower critical temperature at the relevant lower frequencies.
[23] C. P. Poole, Jr., *Electron Spin Resonance* (Wiley, New York, 1983).
[24] The minus sign in the last line of Eq. (6) is due to the relative positions of the SC and the FM in Fig. 1.
[25] Y. Tserkovnyak, A. Brataas, and G. E. W. Bauer, Phys. Rev. Lett. **88**, 117601 (2002).
[26] V. Risinggård, E. G. Tveten, A. Brataas, and J. Linder, Phys. Rev. B **96**, 174441 (2017).
[27] M. Wu, *Nonlinear Spin Waves in Magnetic Film Feedback Rings* (Elsevier, New York, 2010).
[28] V. Kalappattil, R. Das, M.-H. Phan, and H. Srikanth, Nat. Sci. Rep. **7**, 13316 (2017).
[29] S. Lee, S. Grudichak, J. Sklenar, C. C. Tsai, M. Jang, Q. Yang, H. Zhang, and J. B. Ketterson, J. Appl. Phys. **120**, 033905 (2016).
[30] M. Schreier, T. Chiba, A. Niedermayr, J. Lotze, H. Huebl, S. Geprags, S. Takahashi, G. E. W. Bauer, R. Gross, and S. T. B. Goennenwein, Phys. Rev. B **92**, 144411 (2015).
[31] A. M. Ferona and R. E. Camley, Phys. Rev. B **95**, 104421 (2017).
[32] B. Flebus, K. Shen, T. Kikkawa, K. I. Uchida, Z. Qiu, E. Saitoh, R. A. Duine, and G. E. W. Bauer, Phys. Rev. B **95**, 144420 (2017).
[33] In contrast, the general LLG equation mixes real and imaginary parts, so they are generally not solutions to the LLG equation by themselves.
[34] See Supplemental Material at http://link.aps.org/supplemental/10.1103/PhysRevB.102.180506 for explicit solutions for m_x and m_y, and an illustration of the elliptic orbit of $|\mathrm{Re}(m_p)|$.
[35] $|\mathrm{Re}(m_p)| \lesssim 0.1$ ensures consistency with the approximations of linear response and elliptical orbits. The real part of m_p is used here as it is a physical solution of the linearized LLG equation. The complex vector m_p is not a physical solution.
[36] K. Xia, N. Zhao, and J. Twamley, Phys. Rev. A **92**, 043409 (2015).
[37] T. Kampfrath, A. Sell, G. Klatt, A. Pashkin, S. Mhrlein, T. Dekorsy, M. Wolf, M. Fiebig, A. Leitenstorfer, and R. Huber, Nat. Photonics **5**, 31 (2011).
[38] H. J. Jiao and G. E. W. Bauer, Phys. Rev. Lett. **110**, 217602 (2013).
[39] M. Weiler, J. M. Shaw, H. T. Nembach, and T. J. Silva, Phys. Rev. Lett. **113**, 157204 (2014).
[40] C. Hahn, G. de Loubens, M. Viret, O. Klein, V. V. Naletov, and J. Ben Youssef, Phys. Rev. Lett. **111**, 217204 (2013).
[41] D. Wei, M. Obstbaum, M. Ribow, C. H. Back, and G. Woltersdorf, Nat. Commun. **5**, 3768 (2014).
[42] A. Cottet, Z. Leghtas, and T. Kontos, Phys. Rev. B **102**, 155105 (2020).

Paper II

Photon-mediated superconductor–ferromagnetic insulator coupling

Andreas T. G. Janssønn, Henning G. Hugdal, Arne Brataas, and Sol H. Jacobsen
Center for Quantum Spintronics, Department of Physics,
NTNU Norwegian University of Science and Technology, NO-7491 Trondheim, Norway

A recent proof of concept showed that cavity photons can mediate superconducting (SC) signatures to a ferromagnetic insulator (FI) over a macroscopic distance [Phys. Rev. B, **102,** 180506(R) (2020)]. In contrast with conventional proximity systems, this facilitates long-distance FI–SC coupling, local subjection to different drives and temperatures, and studies of their mutual interactions without proximal disruption of their orders. Here we derive a microscopic theory for these interactions, with an emphasis on the leading effect on the FI, namely, an induced anisotropy field. An arbitrary practical example shows an anisotropy field on the order of microtesla, such that parameter optimization is expected to give detectable results for low-coercivity FIs such as Bi-YIG. We discuss the implications and potential applications of such a system in the context of superconducting spintronics.

I. INTRODUCTION

Enabling low-dissipation charge and spin transport, superconducting spintronics presents a pathway to reducing energy costs of data processing, and provides fertile ground for exploring new fundamental physics [1–3]. Conventionally, superconducting and spintronic systems are coupled by the proximity effect, with properties of adjacent materials transported across an interface. The superconducting coherence length thus limits the extent to which superconducting properties can be harnessed in proximity systems, to a range of nm–μm near interfaces [4–8].

By contrast, cavity-coupled systems offer mediation across macroscopic distances [9–13]. They also offer interaction strengths that relate inversely to the cavity volume [14, 15], which is routinely utilized experimentally to achieve strong coupling in e.g. GHz–THz cavity set-ups [16–19]. Furthermore, research on the coupling of magnets and cavity photons shows that the effective interaction strengths scale with the number of spins involved [9, 20–22], which has been utilized experimentally to achieve effective coupling strengths far exceeding losses [11, 13, 23, 24].

Theoretically, a number of methods have been employed to extract mediated effects in cavity-coupled systems. This includes classical modelling for coupling two ferromagnets [25], and a ferromagnet to a superconductor [10]; application of Jaynes–Cummings-like models for coupling a ferromagnet and a qubit [12], and two ferromagnets [26]; perturbative diagonalization by the Schrieffer–Wolff transformation for coupling a ferro- and antiferromagnet [9, 20], and a normal metal to itself [14]; and perturbative evolution of the density matrix, as well as perturbative diagonalization by the non-equilibrium Keldysh path integral formalism, for coupling a mesoscopic circuit to a cavity [27].

In this paper, we will employ the Matsubara path integral formalism [28–31] to derive a microscopic theory for the cavity-mediated coupling of a ferromagnetic insulator (FI) with a singlet s-wave superconductor (SC). In particular, we consider the Zeeman coupling to the FI, and the paramagnetic coupling to the SC. We show that with this approach, we may exactly integrate out the net mediated effect by the cavity photons. This is in contrast to the Schrieffer–Wolff approach, which would limit the integrating-out of the cavity to off-resonant regimes [20]. For instance, a pairing term analogous to the one found via the Schrieffer–Wolff transformation in Ref. [14] also appears in our calculations, without the limitation to an off-resonant regime. Furthermore, unlike many preceding works which single out the coupling to the uniform mode of the magnet [9, 10, 13, 21, 23, 24], we retain the influence of a range of modes in our model. Their non-negligible influence when the magnet exceeds a certain size relative to the cavity, has been emphasized by both experimentalists [24] and theorists [21].

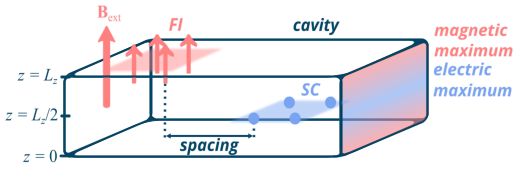

FIG. 1. Illustration of the set-up. A thin ferromagnetic insulator and thin superconductor are placed spaced apart inside a rectangular, electromagnetic cavity. The FI is subjected to an aligning external magnetic field $\mathbf{B}_{\text{ext}}$. The cavity is short along the z direction, and long along the perpendicular xy directions, causing cavity modes to separate into a band-like structure. The FI and the SC are respectively placed in regions of maximum magnetic ($z = L_z$) and electric ($z = L_z/2$) cavity field of the $\ell_z = 1$ modes, as defined in Sec. II B 1 and illustrated above by the colored field cross-section on the right wall.

By a careful choice of cavity dimensions and the placement of subsystems, we couple the insulator to the momentum degrees of freedom of the superconductor. In this case, the cavity acts as an effective spin–orbit coupling. Here, we emphasize the leading effect of the superconductor on the insulator, namely, the induction of an anisotropy field. In an arbitrary, practical example, we achieve a field on the order of μT; parameter optimization is expected to yield results within a detectable range for an insulator of sufficiently low coercivity such as Bi-YIG, and is left for future work. Since the cavity facilitates coupling across unconventionally long distances, it enables the FI and SC to be held at different temperatures, be subjected separately to external drives, and have them inter-

act without the same mutual disruption of their orders associated with the proximity effect [2, 10], such as the breaking of Cooper pairs by magnetic fields from the FI. In practical applications, our system may be used to bridge superconducting and other spintronic circuitry.

The article is organised as follows. In Section II A we present the set-up: A cavity with an FI and SC film placed at magnetic and electric antinodes as shown in Fig. 1, with no overlap in the xy plane. In Section II B we cover theoretical preliminaries: The quantized gauge field, the magnon-basis Hamiltonian for the insulator, and the Bogoliubov quasiparticle-basis Hamiltonian for the superconductor. The system Hamiltonian is subsequently constructed. In Sec. II C–II E, we construct an effective magnon theory using the path integral formalism. Here we exactly integrate out the cavity, and perturbatively the superconductor. In Section III, we extract from the effective theory the leading effect of the superconductor on the insulator, namely, the induced anisotropy field. In a practical example, we calculate this field numerically, and find here an induced field on the order of μT in magnitude. Finally, in Section IV, we give concluding remarks, discussing the results and their significance, and an outlook. In the appendices, we affirm the mathematical consistency of the effective theory with an alternative derivation, explore a variation of the set-up with the SC placed at the opposite magnetic antinode, and elaborate on the interpretation of certain quantities in the effective action as an effective anisotropy field.

II. THEORY

A. Set-up

Our set-up is illustrated in Fig. 1. We place two thin layers, one of a ferromagnetic insulator (FI) and one of a superconductor (SC), spaced apart inside a rectangular electromagnetic cavity. The dimensions of the cavity are $L_x, L_y \gg L_z$, with L_z on the μm–mm scale, and L_x, L_y on the cm scale. The aspect ratios render photons more easily excited in the xy directions. The FI is placed at the upper magnetic antinode of the $\ell_z = 1$ modes (cf. Sec. II B 1), and the SC at the corresponding electric antinode, as illustrated in Fig. 1. Because the layers are thin in comparison to L_z, the local spatial variation of the modes in the z direction is negligible, i.e., the modes are treated as uniform in the z direction [32].

The FI is locally subjected to an aligning and perpendicular uniform, external magnetostatic field, which vanishes across the SC. This was achieved experimentally with external coils and magnetic shielding in Tabuchi *et al.* [13]. Furthermore, the SC is subjected to a supercurrent. This may be realized by passing a direct current (DC) through small electric wires, entering the cavity via small holes in the walls and connecting along the sides of the SC, similarly to Ref. [33]. Provided the wires and holes are sufficiently small, their influence on the cavity modes are negligible. Provided the sample width does not exceed the Pearl length λ^2/d [33–35], the leading effect of the DC is to induce an equilibrium supercurrent with a Cooper pair center-of-mass momentum $2\mathbf{P}$, with the magnitude of $\mathbf{P}$ determined by the current. Here λ is the effective magnetic penetration depth, and d is the sample depth. For Nb thin films, we expect the Pearl length criterion to be met at widths of up to $0.1\,\mathrm{mm}$ for a d down to $1\,\mathrm{nm}$ [36].

B. Hamiltonian

In the following, we deduce a Hamiltonian

$$\mathcal{H} \equiv \mathcal{H}_{\mathrm{FI}} + \mathcal{H}_0^{\mathrm{cav}} + \mathcal{H}_{\mathrm{SC}}. \tag{1}$$

for the system illustrated in Fig. 1. We begin by quantizing the cavity gauge field, and introducing the cavity Hamiltonian $\mathcal{H}_0^{\mathrm{cav}}$. Following this, we deduce a Hamiltonian $\mathcal{H}_{\mathrm{FI}}$ for the FI in the magnon basis, including the Zeeman coupling to the cavity. Finally, we deduce a Hamiltonian $\mathcal{H}_{\mathrm{SC}}$ for the SC in the quasiparticle basis, including the paramagnetic coupling to the cavity.

1. *Cavity gauge field*

We begin by presenting the expression for the quantized cavity gauge field $\mathbf{A}_{\mathrm{cav}}$ [15]. Starting from the Fourier decomposition of the classical vector potential, we impose the transverse gauge and quantize the field. We employ reflecting boundary conditions at the cavity walls in the z direction, and periodic boundary conditions at the comparatively distant walls in the xy directions. The gauge field is thus

$$\mathbf{A}_{\mathrm{cav}} \equiv \sum_{\mathbf{Q}\varsigma} \sqrt{\frac{\hbar}{2\epsilon\omega_{\mathbf{Q}}}} (a_{\mathbf{Q}\varsigma}\bar{\mathbf{u}}_{\mathbf{Q}\varsigma} + a^\dagger_{\mathbf{Q}\varsigma}\bar{\mathbf{u}}^*_{\mathbf{Q}\varsigma}). \tag{2}$$

Above,

$$\mathbf{Q} \equiv (Q_x, Q_y, Q_z) \equiv (2\pi\ell_x/L_x, 2\pi\ell_y/L_y, \pi\ell_z/L_z) \tag{3}$$

are the momenta of each photonic mode, with $\ell_x, \ell_y = 0, \pm1, \pm2, \ldots$ and $\ell_z = 0, 1, 2, \ldots$. The discretization of Q_z differs from that of Q_x and Q_y due to the different boundary conditions in the transverse and longitudinal directions. Furthermore, $\varsigma = 1, 2$ labels polarization directions, ϵ is the permittivity of the material filling the cavity, and

$$\omega_{\mathbf{Q}} = c|\mathbf{Q}| \tag{4}$$

is the cavity dispersion relation, with c the speed of light. $a^\dagger_{\mathbf{Q}\varsigma}$ and $a_{\mathbf{Q}\varsigma}$ are photon creation and annihilation operators, satisfying

$$[a_{\mathbf{Q}\varsigma}, a^\dagger_{\mathbf{Q}'\varsigma'}] = \delta_{\mathbf{Q}\mathbf{Q}'}\delta_{\varsigma\varsigma'}, \tag{5}$$

where the factors on the right-hand side are Kronecker delta functions.

Lastly, the mode functions

$$\bar{\mathbf{u}}_{\mathbf{Q}\varsigma} \equiv \sum_D \hat{e}_D O^{\mathbf{Q}}_{\varsigma D} u_{\mathbf{Q}D} \tag{6}$$

encapsulate the spatial modulation of the modes. Here, $\hat{e}_D$ is the unit vector in the $D = x, y, z$ direction. $O^{\mathbf{Q}}_{\varsigma D}$ are elements of a matrix that rotates the original xyz basis of unit vectors to a new basis labeled 123, with the 3 direction aligned with $\mathbf{Q}$ (see Fig. 2):

$$\begin{pmatrix} \hat{e}_1^{\mathbf{Q}} \\ \hat{e}_2^{\mathbf{Q}} \\ \hat{e}_3^{\mathbf{Q}} \end{pmatrix} = O^{\mathbf{Q}} \begin{pmatrix} \hat{e}_x \\ \hat{e}_y \\ \hat{e}_z \end{pmatrix}, \tag{7}$$

$$O^{\mathbf{Q}} \equiv \begin{pmatrix} \cos\theta\cos\varphi & \cos\theta\sin\varphi & -\sin\theta \\ -\sin\varphi & \cos\varphi & 0 \\ \sin\theta\cos\varphi & \sin\theta\sin\varphi & \cos\theta \end{pmatrix}. \tag{8}$$

Here $\theta = \theta_{\mathbf{Q}}$ and $\varphi = \varphi_{\mathbf{Q}}$ are the polar and azimuthal angles illustrated in Fig. 2. $O^{\mathbf{Q}}$ originates from the implementation of the transverse gauge, which amounts to neglecting the longitudinal 3 component of the gauge field. Finally, $u_{\mathbf{Q}D}$ are the mode functions in the xyz basis, given by

$$u_{\mathbf{Q}x} = u_{\mathbf{Q}y} = \sqrt{\frac{2}{V}} e^{iQ_x x + iQ_y y} i \sin Q_z z, \tag{9}$$

$$u_{\mathbf{Q}z} = \sqrt{\frac{2}{V}} e^{iQ_x x + iQ_y y} \cos Q_z z, \tag{10}$$

where V is the volume of the cavity [37].

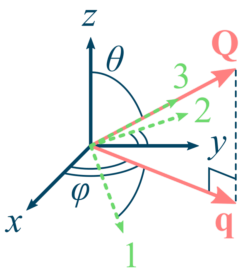

FIG. 2. Illustration of the 123 coordinate system. $\mathbf{Q}$ is the photon momentum vector, and $\mathbf{q}$ is its component in the xy plane. θ (single line) is the polar, and φ (double line) the azimuthal angle associated with $\mathbf{Q}$ in relation to the xyz basis. The 123 axes results from a rotation of the xyz axes by an angle θ about the y axis, followed by a rotation by an angle φ about the original z axis. In the illustration, the 1 axis points somewhat outwards and downwards, the 2 axis points somewhat inwards and is confined to the original xy plane, and the 3 axis aligns with $\mathbf{Q}$.

Our set-up facilitates coupling to the $\ell_z = 1$ band of cavity modes, as the FI and SC are placed in field maxima as illustrated in Fig. 1. We will only consider variations of the in-plane part $\mathbf{q}$ of the general momenta $\mathbf{Q}$, defined via

$$\mathbf{Q} \equiv \mathbf{q} + \pi \hat{e}_z / L_z. \tag{11}$$

For this reason we will use the subscript $\mathbf{q}$ for functions of $\mathbf{Q}$ where the z component is locked to the $\ell_z = 1$ mode, e.g.

$$\omega_{\mathbf{q}} \equiv \omega_{\mathbf{Q}}\big|_{\mathbf{Q}=\mathbf{q}+\pi\hat{e}_z/L_z} = c\sqrt{\left(\frac{\pi}{L_z}\right)^2 + \mathbf{q}^2}. \tag{12}$$

The cavity itself contributes to the system Hamiltonian with the term

$$\mathcal{H}_0^{\text{cav}} \equiv \sum_{\mathbf{q}\varsigma} \hbar\omega_{\mathbf{q}} a^\dagger_{\mathbf{q}\varsigma} a_{\mathbf{q}\varsigma}, \tag{13}$$

where we have disregarded the zero-point energy, since it does not influence our results.

2. *Ferromagnetic insulator*

The Hamiltonian of the FI in the cavity is

$$\mathcal{H}_{\text{FI}} \equiv \mathcal{H}_{\text{ex}} + \mathcal{H}_{\text{ext}} + \mathcal{H}_{\text{FI-cav}}, \tag{14}$$

with

$$\mathcal{H}_{\text{ex}} \equiv -J \sum_{\langle i,j \rangle} \mathbf{S}_i \cdot \mathbf{S}_j, \tag{15a}$$

$$\mathcal{H}_{\text{ext}} \equiv -\frac{g\mu_B}{\hbar} B_{\text{ext}} \sum_i S_{iz}, \tag{15b}$$

$$\mathcal{H}_{\text{FI-cav}} \equiv -\frac{g\mu_B}{\hbar} \sum_i \mathbf{S}_i \cdot \mathbf{B}_{\text{cav}}(\mathbf{r}_i). \tag{15c}$$

The first term is the exchange interaction: $J > 0$ is the exchange interaction strength for a ferromagnetic insulator, $\mathbf{S}_i$ is the spin at lattice site i, and only nearest neighbor interactions are taken into account, as indicated by the angle brackets. The next two terms are Zeeman couplings: g is the gyromagnetic ratio, μ_B is the Bohr magneton, B_{ext} is a strong (i.e. $|B_{\text{ext}}| \gg |\mathbf{B}_{\text{cav}}|$) and uniform external magnetostatic field aligning the spins in the z direction, and $\mathbf{B}_{\text{cav}}(\mathbf{r}_i)$ is the magnetic component of the cavity field at lattice site i. The corresponding position vector is $\mathbf{r}_i$.

It is convenient to transition from the spin basis $\{S_{ix}, S_{iy}, S_{iz}\}$ to a bosonic magnon basis $\{\eta_i, \eta_i^\dagger\}$. This is achieved with the Holstein–Primakoff transformation [38], which is covered in detail in Refs. [20, 39].

Each FI lattice site carries spin S. The aligning field B_{ext} regulates the excitation energy of magnons (cf. Eq. (21)), hence a sufficiently strong field implies few magnons per lattice site, i.e.

$$\langle \eta_i^\dagger \eta_i \rangle \ll 2S. \tag{16}$$

We can therefore Taylor-expand the Holstein–Primakoff transformation, leading to the relations

$$S_{iz} = \hbar(S - \eta_i^\dagger \eta_i), \tag{17}$$

$$S_{id} \approx \frac{\hbar\sqrt{2S}}{2}(\nu_d \eta_i + \nu_d^* \eta_i^\dagger), \tag{18}$$

where $d = x, y$ and $\{\nu_x, \nu_y\} = \{1, -i\}$.

Now, upon Fourier-decomposing the magnon operators

$$\eta_{\mathbf{r}_i} \equiv \frac{1}{\sqrt{N_{\text{FI}}}} \sum_{\mathbf{k}} \eta_{\mathbf{k}} e^{i\mathbf{k}\cdot\mathbf{r}_i}, \tag{19}$$

we obtain the conventional expression for $\mathcal{H}_{\rm ex}+\mathcal{H}_{\rm ext}$ in the magnon basis [39]:

$$\mathcal{H}_{\rm ex}+\mathcal{H}_{\rm ext}\approx\mathcal{H}_0^{\rm FI}\equiv\sum_{\mathbf{k}}\hbar\lambda_{\mathbf{k}}\eta_{\mathbf{k}}^\dagger\eta_{\mathbf{k}}, \tag{20}$$

where we have introduced the magnon dispersion relation

$$\lambda_{\mathbf{k}}\equiv 2\hbar JN_\delta S\left(1-\frac{1}{N_\delta}\sum_{\boldsymbol{\delta}}e^{i\mathbf{k}\cdot\boldsymbol{\delta}}\right)+\frac{g\mu_B}{\hbar}B_{\rm ext}. \tag{21}$$

Above, $N_{\rm FI}$ is the total number of FI lattice points, $N_\delta=4$ is the number of nearest-neighbor lattice sites on a 2D square monolayer (neglecting edges and corners), and $\boldsymbol{\delta}=\pm a_{\rm FI}\hat{e}_x,\pm a_{\rm FI}\hat{e}_y$ are nearest-neighbor lattice vectors. The magnon momenta are

$$\mathbf{k}\equiv(2\pi m_x^{\rm FI}/l_x^{\rm FI},2\pi m_y^{\rm FI}/l_y^{\rm FI},0)\equiv(k_x,k_y,0), \tag{22}$$

where $m_d^{\rm FI}=-\left\lfloor\frac{N_d^{\rm FI}-1}{2}\right\rfloor,\ldots,N_d^{\rm FI}-1-\left\lfloor\frac{N_d^{\rm FI}-1}{2}\right\rfloor$ covers the first Brillouin zone (1BZ), with $N_d^{\rm FI}$ the number of FI lattice points in direction d, and $\lfloor\cdot\rfloor$ the floor function. Note that the set of magnon momenta generally does not overlap with that of photon momenta in Eq. (3). Observe furthermore that the magnon energies (21) can easily be regulated experimentally by adjusting $B_{\rm ext}$.

Proceeding to the interaction term, we deduce the magnetic cavity field $\mathbf{B}_{\rm cav}(\mathbf{r}_i)$ across the FI, which is the curl of the gauge field at $z=L_z$:

$$\begin{aligned}&\mathbf{B}_{\rm cav}(\mathbf{r}_i)\big|_{\rm FI}=\nabla\times\mathbf{A}_{\rm cav}(\mathbf{r}_i)\big|_{\rm FI}\\&=\sum_{\mathbf{q}d}i\nu_d^2q_{\bar{d}}\hat{e}_d\sin\theta_{\mathbf{q}}\sqrt{\frac{\hbar}{\epsilon\omega_{\mathbf{q}}V}}e^{i\mathbf{q}\cdot\mathbf{r}_i}(a_{\mathbf{q}1}+a_{-\mathbf{q}1}^\dagger).\end{aligned} \tag{23}$$

Above, $\bar{d}$ "inverts" d such that $\bar{x}=y$ and $\bar{y}=x$. Note that the photon momentum component $q_{\bar{d}}$ enters the sum with an inverted lower index. Observe that only the 1 direction enters the expression, because $\mathbf{A}_{\rm cav}$ at $z=L_z$ points purely along the z direction. The 2 direction is by definition locked to the xy plane, and does therefore not contribute at $z=L_z$.

Inserting Eqs. (17)–(19) and (23) into Eq. (15c), we find

$$\mathcal{H}_{\rm FI-cav}\approx\sum_{\mathbf{k}d}\sum_{\mathbf{q}\varsigma}g_d^{\mathbf{kq}}(\nu_d\eta_{-\mathbf{k}}+\nu_d^*\eta_{\mathbf{k}}^\dagger)(a_{\mathbf{q}1}+a_{-\mathbf{q}1}^\dagger), \tag{24}$$

and hence a complete FI Hamiltonian $\mathcal{H}_{\rm FI}\approx H_0^{\rm FI}+\mathcal{H}_{\rm FI-cav}$. Above, we defined the coupling strength

$$g_d^{\mathbf{kq}}\equiv-g\mu_Bq_{\bar{d}}i\nu_d^2\sin\theta_{\mathbf{q}}\sqrt{\frac{S\hbar N_{\rm FI}}{2\epsilon\omega_{\mathbf{q}}V}}D_{\mathbf{kq}}^{\rm FI}e^{i\mathbf{q}\cdot\mathbf{r}_0^{\rm FI}}. \tag{25}$$

$D_{\mathbf{kq}}^{\rm FI}$ quantifies the degree of overlap between magnonic and photonic modes, and is defined via

$$\begin{aligned}&N_MD_{\mathbf{l}_M\mathbf{q}}^M\equiv e^{i(\mathbf{l}_M-\mathbf{q})\cdot\mathbf{r}_0^M}\sum_{i\in M}e^{-i(\mathbf{l}_M-\mathbf{q})\cdot\mathbf{r}_i}\\&\approx N_M\prod_d\mathrm{sinc}\left[\pi N_d^M\left(\frac{m_d^M}{N_d^M}-\frac{\ell_da_M}{L_d}\right)\right].\end{aligned} \tag{26}$$

Here $M=\{\rm FI,SC\}$ is a material index, $\mathbf{l}_M$ represents either a magnon or a Bogoliubov quasiparticle momentum, $\mathbf{r}_0^M$ is the center position of lattice M relative to the origin, and the photon momentum numbers $\ell_d=\ell_x,\ell_y$ were defined under Eq. (3). The latter, along with other SC quantities, are defined in Sec. II B 3. The sum over i is taken over either FI or SC lattice points, as indicated by M, and the last equality holds for $N_d^M\gg1$.

$D_{\mathbf{kq}}^{\rm FI}$ reduces to a Kronecker delta $\delta_{\mathbf{kq}}$ only when $L_d=l_d=a_{\rm FI}N_d^{\rm FI}$, i.e. when the FI and the cavity share dimensions [40]. At the other end of the scale, when the FI becomes infinitely small, $D_{\mathbf{kq}}^{\rm FI}$ reduces to $\delta_{\mathbf{k0}}$, implying all cavity modes couple exclusively to the uniform magnon mode, which is often assumed in cavity implementations [9, 10, 13, 23].

3. *Superconductor*

The SC Hamiltonian is

$$\mathcal{H}_{\rm SC}=\mathcal{H}_{\rm sing}+\mathcal{H}_{\rm BCS}+\mathcal{H}_{\rm para}, \tag{27}$$

with

$$\mathcal{H}_{\rm sing}\equiv\sum_{\mathbf{p}}\xi_{\mathbf{p}}c_{\mathbf{p}\sigma}^\dagger c_{\mathbf{p}\sigma'}, \tag{28a}$$

$$\mathcal{H}_{\rm BCS}\equiv-\sum_{\mathbf{p}}\left(\Delta_{\mathbf{p}}c_{\mathbf{p}+\mathbf{P},\uparrow}^\dagger c_{-\mathbf{p}+\mathbf{P},\downarrow}^\dagger+\Delta_{\mathbf{p}}^*c_{-\mathbf{p}+\mathbf{P},\downarrow}c_{\mathbf{p}+\mathbf{P},\uparrow}\right), \tag{28b}$$

$$\mathcal{H}_{\rm para}\equiv\sum_d\sum_jj_d(\mathbf{r}_j)A_d\left(\frac{\mathbf{r}_{j+I_d}+\mathbf{r}_j}{2}\right), \tag{28c}$$

$\mathcal{H}_{\rm sing}$ is the single-particle energy, where $\xi_{\mathbf{p}}$ is the lattice-dependent electron dispersion, and $c_{\mathbf{p}\sigma}$ and $c_{\mathbf{p}\sigma}^\dagger$ are fermionic operators for an electron of lattice momentum $\mathbf{p}$ and spin σ. The momenta are discretized as

$$\mathbf{p}\equiv(2\pi m_x^{\rm SC}/l_x^{\rm SC},2\pi m_y^{\rm SC}/l_y^{\rm SC},0)\equiv(p_x,p_y,0), \tag{29}$$

where $m_d^{\rm SC}$ is defined analogously to $m_d^{\rm FI}$ (see below Eq. (22)), covering the 1BZ of the SC with $N_d^{\rm SC}$ the number of SC lattice points in direction d.

$\mathcal{H}_{\rm BCS}$ is the BCS pairing term, with $\Delta_{\mathbf{p}}$ the pairing potential. The leading order effect of applying a DC across the SC is to shift the center of the SC pairing potential from $\mathbf{p}=\mathbf{0}$ to $\mathbf{p}=\mathbf{P}$, where $2\mathbf{P}$ is the generally finite center-of-mass momentum of the Cooper pairs [33, 41, 42]. The maximum value of $\mathbf{P}$ is limited by the critical current of the superconductor.

$\mathcal{H}_{\rm para}$ is the paramagnetic coupling. $j_d(\mathbf{r}_j)$ is the d component of the discretized electric current operator at lattice site j with the position vector $\mathbf{r}_j$, and is defined as [14]

$$j_d(\mathbf{r}_j)\equiv\frac{ia_{\rm SC}et}{\hbar}\sum_\sigma(c_{j+I_d,\sigma}^\dagger c_{j\sigma}-c_{j\sigma}^\dagger c_{j+I_d,\sigma}), \tag{30}$$

where $a_{\rm SC}$ is the lattice constant, e is the electric charge, t is the lattice hopping parameter, and $c_{j\sigma}$ and $c_{j\sigma}^\dagger$ are real-space

fermionic operators for electrons with spin σ at lattice site j. They relate to $c_{\mathbf{p}\sigma}$ and $c^\dagger_{\mathbf{p}\sigma}$ via

$$c_{j\sigma} = \frac{1}{\sqrt{N_{\rm SC}}} \sum_{\mathbf{p}} c_{\mathbf{p}\sigma} e^{i\mathbf{p}\cdot\mathbf{r}_j}, \tag{31}$$

with $N_{\rm SC}$ the total number of SC lattice points. Furthermore, I_d represents a unit step in the d direction with respect to lattice labels. For instance, if $j = (1,1)$, then $j + I_x = (1+1,1) = (2,1)$.

Inserting Eqs. (2), (30) and (31) into Eq. (28c) yields

$$\mathcal{H}_{\rm para} = \sum_{\mathbf{p}\mathbf{p}'\sigma} \sum_{\mathbf{q}\varsigma} g_\varsigma^{\mathbf{q}\mathbf{p}\mathbf{p}'} (a_{\mathbf{q}\varsigma} + a^\dagger_{-\mathbf{q}\varsigma}) c^\dagger_{\mathbf{p}\sigma} c_{\mathbf{p}'\sigma}. \tag{32}$$

Here, we have introduced the coupling constant

$$g_\varsigma^{\mathbf{q}\mathbf{p}\mathbf{p}'} \equiv -\frac{a_{\rm SC} e t}{\hbar} \sqrt{\frac{\hbar}{\epsilon \omega_{\mathbf{q}} V}} D^{\rm SC}_{\mathbf{p}-\mathbf{p}',\mathbf{q}} e^{i\mathbf{q}\cdot\mathbf{r}_0^{\rm SC}} \cdot \sum_d \left(e^{-i(\mathbf{p}-\mathbf{q}/2)\cdot\boldsymbol{\delta}_d} - e^{i(\mathbf{p}'+\mathbf{q}/2)\cdot\boldsymbol{\delta}_d} \right) O^{\mathbf{q}}_{\varsigma d}, \tag{33}$$

where $\boldsymbol{\delta}_d \equiv a_{\rm SC}\hat{e}_d$ are primitive lattice vectors. $D^{\rm SC}_{\mathbf{p}-\mathbf{p}',\mathbf{q}}$ is defined in Eq. (26), quantifying the degree of overlap between two electron modes and a photon mode. It reduces to $\delta_{\mathbf{p}-\mathbf{p}',\mathbf{q}}$ only when the cavity and the SC share dimensions, as is the case in Ref. [14].

As we move onto the imaginary time (Matsubara) path integral formalism in the next sections, it becomes convenient to eliminate creation–creation and annihilation–annihilation fermionic operator products. To this end, we absorb the BCS term (28b) into the diagonal term (28a) by a straight-forward diagonalization:

$$\begin{aligned} &\mathcal{H}_{\rm sing} + \mathcal{H}_{\rm BCS} \\ &= \sum_{\mathbf{p}} \begin{pmatrix} c_{\mathbf{p}+\mathbf{P},\uparrow} \\ c^\dagger_{-\mathbf{p}+\mathbf{P},\downarrow} \end{pmatrix}^\dagger \begin{pmatrix} \xi_{\mathbf{p}+\mathbf{P}} & -\Delta_{\mathbf{p}} \\ -\Delta^*_{\mathbf{p}} & -\xi_{-\mathbf{p}+\mathbf{P}} \end{pmatrix} \begin{pmatrix} c_{\mathbf{p}+\mathbf{P},\uparrow} \\ c^\dagger_{-\mathbf{p}+\mathbf{P},\downarrow} \end{pmatrix} \\ &= \sum_{\mathbf{p}} \begin{pmatrix} \gamma_{\mathbf{p}0} \\ \gamma_{\mathbf{p}1} \end{pmatrix}^\dagger \begin{pmatrix} E_{\mathbf{p}0} & 0 \\ 0 & E_{\mathbf{p}1} \end{pmatrix} \begin{pmatrix} \gamma_{\mathbf{p}0} \\ \gamma_{\mathbf{p}1} \end{pmatrix}. \end{aligned} \tag{34}$$

Here we introduced the Bogoliubov quasiparticle basis $\{\gamma_{\mathbf{p}m}, \gamma^\dagger_{\mathbf{p}m}\}$, with $m = 0, 1$ and dispersion relations

$$\begin{aligned} E_{\mathbf{p}m} = &\frac{1}{2}\Big[\xi_{\mathbf{p}+\mathbf{P}} - \xi_{-\mathbf{p}+\mathbf{P}} \\ &+ (-1)^m \sqrt{(\xi_{\mathbf{p}+\mathbf{P}} + \xi_{-\mathbf{p}+\mathbf{P}})^2 + 4|\Delta_{\mathbf{p}}|^2}\Big]. \end{aligned} \tag{35}$$

The elements $u_{\mathbf{p}}$ and $v_{\mathbf{p}}$ of the basis transformation matrix are defined through [35]

$$c_{\mathbf{p}+\mathbf{P},\uparrow} \equiv u^*_{\mathbf{p}} \gamma_{\mathbf{p}0} + v_{\mathbf{p}} \gamma_{\mathbf{p}1}, \quad c^\dagger_{-\mathbf{p}+\mathbf{P},\downarrow} \equiv -v^*_{\mathbf{p}} \gamma_{\mathbf{p}0} + u_{\mathbf{p}} \gamma_{\mathbf{p}1}. \tag{36}$$

Inserting the above into Eq. (34), one finds the relations

$$\frac{\Delta^*_{\mathbf{p}} v_{\mathbf{p}}}{u_{\mathbf{p}}} = \frac{1}{2}\left[(E_{\mathbf{p}0} - E_{\mathbf{p}1}) - (\xi_{\mathbf{p}+\mathbf{P}} + \xi_{-\mathbf{p}+\mathbf{P}})\right], \tag{37a}$$

$$|v_{\mathbf{p}}|^2 = 1 - |u_{\mathbf{p}}|^2 = \frac{1}{2}\left(1 - \frac{\xi_{\mathbf{p}+\mathbf{P}} + \xi_{-\mathbf{p}+\mathbf{P}}}{E_{\mathbf{p}0} - E_{\mathbf{p}1}}\right), \tag{37b}$$

which determine $u_{\mathbf{p}}$ and $v_{\mathbf{p}}$. Recasting $\mathcal{H}_{\rm para}$ in terms of this basis yields

$$\mathcal{H}_{\rm para} = \sum_{\mathbf{p}\mathbf{p}'} \sum_{\mathbf{q}\varsigma} \sum_{mm'} g_{\varsigma mm'}^{\mathbf{q}\mathbf{p}\mathbf{p}'} (a_{\mathbf{q}\varsigma} + a^\dagger_{-\mathbf{q}\varsigma}) \gamma^\dagger_{\mathbf{p}m} \gamma_{\mathbf{p}'m'}, \tag{38}$$

where the coupling constant is now

$$g_{\varsigma mm'}^{\mathbf{q}\mathbf{p}\mathbf{p}'} \equiv \begin{pmatrix} g_\varsigma^{\mathbf{q},\mathbf{p}+\mathbf{P},\mathbf{p}'+\mathbf{P}} u_{\mathbf{p}} u^*_{\mathbf{p}'} + g_\varsigma^{\mathbf{q},\mathbf{p}-\mathbf{P},\mathbf{p}'-\mathbf{P}} v_{\mathbf{p}} v^*_{\mathbf{p}'} & g_\varsigma^{\mathbf{q},\mathbf{p}+\mathbf{P},\mathbf{p}'+\mathbf{P}} u_{\mathbf{p}} v_{\mathbf{p}'} - g_\varsigma^{\mathbf{q},\mathbf{p}-\mathbf{P},\mathbf{p}'-\mathbf{P}} v_{\mathbf{p}} u_{\mathbf{p}'} \\ -g_\varsigma^{\mathbf{q},\mathbf{p}-\mathbf{P},\mathbf{p}'-\mathbf{P}} u^*_{\mathbf{p}} v^*_{\mathbf{p}'} + g_\varsigma^{\mathbf{q},\mathbf{p}+\mathbf{P},\mathbf{p}'+\mathbf{P}} v^*_{\mathbf{p}} u^*_{\mathbf{p}'} & g_\varsigma^{\mathbf{q},\mathbf{p}-\mathbf{P},\mathbf{p}'-\mathbf{P}} u^*_{\mathbf{p}} u_{\mathbf{p}'} + g_\varsigma^{\mathbf{q},\mathbf{p}+\mathbf{P},\mathbf{p}'+\mathbf{P}} v^*_{\mathbf{p}} v_{\mathbf{p}'} \end{pmatrix}_{mm'}. \tag{39}$$

This concludes the derivation of the terms entering the system Hamiltonian in terms of the various (quasi)particle bases. We now turn our focus to the construction of an effective FI theory.

C. Imaginary time path integral formalism

We now seek to extract the influence of the SC on the FI, in particular the anisotropy field induced across the FI. Diagonalizing the Hamiltonian directly, as was done in Eq. (34), would in this case be very challenging, as it couples many more modes, and furthermore contains trilinear operator products. Since the external drives ($\mathbf{B}_{\rm ext}$ and the DC) only give rise to equilibrium phenomena in our system, the Matsubara path integral formalism of evaluating thermal correlation functions is valid [28]. This translates the evaluation into a path integral problem, which is very convenient for our purposes. The path integral approach facilitates aggregation of the influences of specific subsystems into effective actions, without explicit diagonalization. On this note, for comparison, Cottet *et al.* [27] analyze a scenario in which the non-equilibrium Keldysh path integral formalism is used to analyze the net influence of a QED circuit on a cavity.

The starting point is the imaginary time action

$$\begin{aligned} S &\equiv S_0^{\mathrm{FI}} + S_0^{\mathrm{cav}} + S_0^{\mathrm{SC}} + S_{\mathrm{int}}^{\mathrm{FI-cav}} + S_{\mathrm{int}}^{\mathrm{cav-SC}} \\ &= \int \mathrm{d}\tau \Big[\sum_{\mathbf{k}} \eta_{\mathbf{k}}^\dagger \hbar \partial_\tau \eta_{\mathbf{k}} + \sum_{\mathbf{q}\varsigma} a_{\mathbf{q}\varsigma}^\dagger \hbar \partial_\tau a_{\mathbf{q}\varsigma} \\ &\quad + \sum_{\mathbf{p}m} \gamma_{\mathbf{p}m}^\dagger \hbar \partial_\tau \gamma_{\mathbf{p}m} + \mathcal{H} \Big]. \end{aligned} \tag{40}$$

τ is a temperature parameter treated as imaginary time, which relates to the thermal equilibrium density matrix $\exp(-\beta\mathcal{H}/\hbar)$, with $\beta \equiv \hbar/k_{\mathrm{B}}T$ the inverse temperature T in units of time, and $\mathcal{H}$ the system Hamiltonian. The dependence of the field operators on temperature (τ) is implied. In formulating the path integral, the magnon, photon and Bogoliubov quasiparticle operators have been replaced by eigenvalues of the respective coherent states [28]; i.e. the bosonic operators have been replaced by complex numbers, and the fermionic operators by Graßmann numbers. The magnons, photons and Bogoliubov quasiparticles are furthermore taken to be functions of τ [28]. The integral over τ is taken over the interval $(0, \beta]$. Note that we assume the gap to be fixed to the bulk mean field value, and therefore do not include a gap action or integration in the partition function.

We now replace the integral over τ by an infinite sum over discrete frequencies by a Fourier transform of the magnon, photon and Bogoliubov quasiparticle operators with respect to τ. The conjugate Fourier parameters are Matsubara frequencies:

$$\Omega_n = \frac{2n\pi}{\beta} \tag{41}$$

for bosons, and

$$\omega_n = \frac{(2n+1)\pi}{\beta} \tag{42}$$

for fermions, with $n \in \mathbb{Z}$. The transforms read

$$\eta_{\mathbf{k}} = \frac{1}{\sqrt{\beta}} \sum_{\Omega_m} \eta_{-\Omega_m,\mathbf{k}} e^{-i\Omega_m \tau}, \tag{43a}$$

$$a_{\mathbf{q}\varsigma} = \frac{1}{\sqrt{\beta}} \sum_{\Omega_n} a_{-\Omega_n,\mathbf{q}\varsigma} e^{-i\Omega_n \tau}, \tag{43b}$$

$$\gamma_{\mathbf{p}m} = \frac{1}{\sqrt{\beta}} \sum_{\omega_n} \gamma_{-\omega_n,\mathbf{p}m} e^{-i\omega_n \tau}. \tag{43c}$$

To avoid clutter, we introduce the 3-vectors

$$k \equiv (-\Omega_m, \mathbf{k}), \tag{44a}$$

$$q \equiv (-\Omega_n, \mathbf{q}), \tag{44b}$$

$$p \equiv (-\omega_n, \mathbf{p}), \tag{44c}$$

and the generally complex energies

$$\hbar\lambda_k \equiv -i\hbar\Omega_m + \hbar\lambda_{\mathbf{k}}, \tag{45a}$$

$$\hbar\omega_q \equiv -i\hbar\Omega_n + \hbar\omega_{\mathbf{q}}, \tag{45b}$$

$$E_{pm} \equiv -i\hbar\omega_n + E_{\mathbf{p}m}. \tag{45c}$$

The actions in (40) then become

$$S_0^{\mathrm{FI}} = \sum_k \hbar\lambda_k \eta_k^\dagger \eta_k, \tag{46a}$$

$$S_0^{\mathrm{cav}} = \sum_{q\varsigma} \hbar\omega_q a_{q\varsigma}^\dagger a_{q\varsigma}, \tag{46b}$$

$$S_0^{\mathrm{SC}} = \sum_{pm} E_{pm} \gamma_{pm}^\dagger \gamma_{pm}, \tag{46c}$$

$$S_{\mathrm{int}}^{\mathrm{FI-cav}} = \sum_{kd} \sum_{q\varsigma} g_{d\varsigma}^{kq} (\nu_d \eta_{-k} + \nu_d^* \eta_k^\dagger)(a_{q\varsigma} + a_{-q\varsigma}^\dagger), \tag{46d}$$

$$S_{\mathrm{int}}^{\mathrm{cav-SC}} = \frac{1}{\sqrt{\beta}} \sum_{q\varsigma} \sum_{pm} \sum_{p'm'} g_{\varsigma mm'}^{qpp'} (a_{q\varsigma} + a_{-q\varsigma}^\dagger) \gamma_{pm}^\dagger \gamma_{p'm'}, \tag{46e}$$

where we introduced the coupling functions

$$g_{d\varsigma}^{kq} \equiv g_d^{\mathbf{kq}} \delta_{\varsigma 1} \delta_{\Omega_m,\Omega_n}, \tag{47}$$

$$g_{\varsigma mm'}^{qpp'} \equiv g_{\varsigma mm'}^{\mathbf{qpp'}} \delta_{\omega_{n'},\omega_n - \Omega_n}. \tag{48}$$

We additionally introduced a redundant Kronecker delta function $\delta_{\varsigma 1}$ to the coupling (47), which will facilitate the gathering of interaction terms in Eq. (51). We will use the notation g^η and g^γ for the magnitudes of the FI–cavity and cavity–SC coupling, respectively.

We are now equipped to construct effective actions by integrating out the photonic and fermionic degrees of freedom, to which end we will consider the imaginary-time partition function [28, 30]

$$\begin{aligned} Z &\equiv \langle \mathrm{vac}, t = \infty | \mathrm{vac}, t = -\infty \rangle \\ &= \int \mathcal{D}[\eta, \eta^\dagger] \int \mathcal{D}[a, a^\dagger] \int \mathcal{D}[\gamma, \gamma^\dagger] e^{-S/\hbar}, \end{aligned} \tag{49}$$

where e.g.

$$\int \mathcal{D}[\gamma, \gamma^\dagger] \equiv \prod_{pm} \int \mathcal{D}[\gamma_{pm}, \gamma_{pm}^\dagger] \tag{50}$$

is to be understood as the path integrals over every Bogoliubov quasiparticle mode.

D. Integrating out the cavity photons

The order in which we integrate out the cavity and the SC is inconsequential. We will begin with the cavity, which can be integrated out exactly. We show that interchanging the order of integrations leads to identical results in Appendix A.

We gather the interactions between the cavity and FI and SC,

$$S_{\mathrm{int}}^{\mathrm{cav}} = \sum_{q,\varsigma} [J_{q\varsigma} a_{q\varsigma} + J_{-q\varsigma} a_{-q\varsigma}^\dagger], \tag{51}$$

where we have defined

$$J_{q\varsigma} = \sum_{ks} g^{kq}_{d\varsigma}(\nu_d \eta_{-k} + \nu^*_d \eta^\dagger_k) + \frac{1}{\sqrt{\beta}} \sum_{pp'} \sum_{mm'} g^{qpp'}_{\varsigma mm'} \gamma^\dagger_{pm} \gamma_{p'm'}. \quad (52)$$

These interaction terms are illustrated by the diagrams in the top panel of Fig. 3. Integrating out the cavity modes [28], we therefore get the effective action

$$S_{\text{eff}} = -\sum_{q\varsigma} \frac{J_{q\varsigma} J_{-q\varsigma}}{\hbar \omega_q}. \quad (53)$$

Inserting the expression for $J_{q\varsigma}$ we get three different terms, $S_{\text{eff}} = S_1^{\text{FI}} + S_1^{\text{SC}} + S_{\text{int}}$, shown diagrammatically in the bottom panel of Fig. 3. The first term,

$$S_1^{\text{FI}} = -\sum_{qkk'} \sum_{\varsigma dd'} \frac{g^{kq}_{d\varsigma} g^{k'-q}_{d'\varsigma}}{\hbar \omega_q} \times (\nu_d \eta_{-k} + \nu^*_d \eta^\dagger_k)(\nu_{d'} \eta_{-k'} + \nu^*_{d'} \eta^\dagger_{k'}), \quad (54)$$

is a renormalization of the magnon theory due to interactions with the cavity, resulting in a non-diagonal theory. The second term,

$$S_1^{\text{SC}} = -\frac{1}{\beta} \sum_{\substack{qpp' \\ oo'}} \sum_{\substack{\varsigma mm' \\ nn'}} \frac{g^{qpp'}_{\varsigma mm'} g^{-qoo'}_{\varsigma nn'}}{\hbar \omega_q} \gamma^\dagger_{pm} \gamma_{p'm'} \gamma^\dagger_{on} \gamma_{o'n'}, \quad (55)$$

is an interaction term coupling four quasiparticles, similar to the term found in Ref. [14] for a normal metal coupled to a cavity, leading to superconducting correlations. Note that unlike the pairing term found in Ref. [14] via the Schrieffer–Wolff transformation, the term above is not limited to an off-resonant regime. In principle it could also lead to renormalization of the quasiparticle spectrum and lifetime. Since we are here concerned with the effects of the cavity and SC on the FI, we will neglect this term as it only leads to higher order corrections.

Finally, we have the cavity-mediated magnon-quasiparticle coupling,

$$S_{\text{int}} = -\frac{1}{\sqrt{\beta}} \sum_{kpp'} \sum_{dmm'} V^{kpp'}_{dmm'} (\nu_d \eta_{-k} + \nu^*_d \eta^\dagger_k) \gamma^\dagger_{pm} \gamma_{p'm'}, \quad (56)$$

where we have defined the effective FI-SC interaction

$$V^{kpp'}_{dmm'} = \sum_{q\varsigma} g^{kq}_{d\varsigma} g^{-qpp'}_{\varsigma mm'} \left[\frac{1}{\hbar \omega_q} + \frac{1}{\hbar \omega_{-q}} \right]. \quad (57)$$

This term is generally nonzero, and we therefore see that the cavity photons lead to a coupling between the FI and SC, potentially over macroscopic distances. This means that the FI and SC will have a mutual influence on each other, possibly leading to experimentally observable changes in the two materials. We therefore integrate out the Bogoliubov quasiparticles and calculate the effective FI theory below. We reiterate that the interaction is exact at this point, not a result of a perturbative expansion.

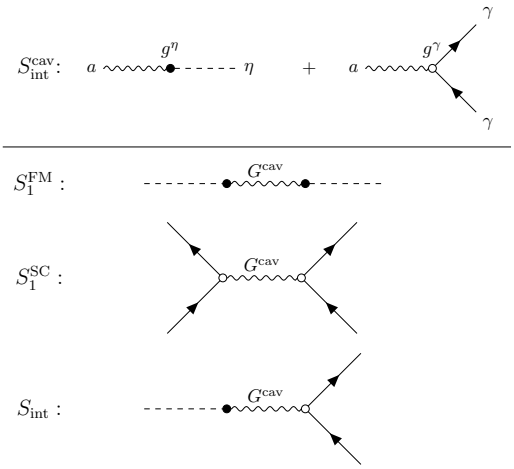

FIG. 3. Feynman diagrams [43] of the bare cavity coupling to the FI and SC, and the resulting terms in the FI and SC effective actions after integrating out the cavity photons, where G^{cav} is the photon propagator.

E. Integrating out the SC quasiparticles — effective FI theory

The full effective SC action comprises the sum $S_0^{\text{SC}} + S_1^{\text{SC}} + S_{\text{int}}$. The second term is second order in g^γ, but does not contain FI operators, and will therefore only have an indirect effect on the effective FI action. In a perturbation expansion of the effective FI action, the term S_1^{SC} will therefore contribute higher order correction terms compared to S_{int}. We therefore neglect this term in the following, leading to the SC action

$$S^{\text{SC}} \approx -\sum_{pp'} \sum_{mm'} \gamma^\dagger_{pm} (G^{-1})^{pp'}_{mm'} \gamma_{p'm'}, \quad (58)$$

where we have defined $G^{-1} = G_0^{-1} + \Sigma$, with

$$(G_0^{-1})^{pp'}_{mm'} = -E_{pm} \delta_{pp'} \delta_{mm'}, \quad (59)$$

$$\Sigma^{pp'}_{mm'} = \frac{1}{\sqrt{\beta}} \sum_{kd} V^{kpp'}_{dmm'} (\nu_d \eta_{-k} + \nu^*_d \eta^\dagger_k). \quad (60)$$

Integrating out the SC quasiparticles results in the effective FI action [28]

$$S^{\text{FI}} = S_0^{\text{FI}} + S_1^{\text{FI}} - \hbar \operatorname{Tr} \ln(-\beta G^{-1}/\hbar). \quad (61)$$

The Green's function matrix G^{-1} contains magnon fields, and will be treated perturbatively in order to draw out the lowest

order terms in the effective FI theory. We expand the logarithm to second order in the FI–SC interaction,

$$\ln\left(-\frac{\beta G^{-1}}{\hbar}\right) \approx \ln\left(-\frac{\beta G_0^{-1}}{\hbar}\right) + G_0\Sigma - \frac{1}{2}G_0\Sigma G_0\Sigma, \tag{62}$$

where G_0 is the inverse of G_0^{-1}. This expansion is valid when $|G_0\Sigma| \ll 1$, meaning $|g^\eta g^\gamma/\hbar\omega_q E_{pm}| \ll 1$, where we use shorthand notation for the couplings g^η and g^γ between cavity photons and η and γ fields respectively. The first term in Eq. (62) does not contain magnonic fields, and therefore does not contribute to the FI effective action [44]. The third term contains bilinear terms in magnonic fields, and gives a correction to the magnon dispersion of order $|[g^\eta g^\gamma/\hbar\omega_q]^2/E_{pm}|$, a factor of $|(g^\gamma)^2/\hbar\omega_q E_{pm}|$ smaller than the corrections contained in S_1^{FI}, and will therefore also be neglected. Keeping only the second term, and using the fact that G_0 is diagonal in both quasiparticle type m and momentum p, we therefore get the effective FI action to leading order,

$$\begin{aligned} S^{\mathrm{FI}} = &\sum_k \hbar\lambda_k \eta_k^\dagger \eta_k - g\mu_B \sum_{kd} h_d^k \cdot \sqrt{\frac{S}{2}}(\nu_d \eta_{-k} + \nu_d^* \eta_k^\dagger) \\ &+ \sum_{kk'dd'} Q_{dd'}^{kk'}(\nu_d \eta_{-k} + \nu_d^* \eta_k^\dagger)(\nu_{d'}\eta_{-k'} + \nu_{d'}^* \eta_{k'}^\dagger), \end{aligned} \tag{63}$$

where we have defined the anisotropy field due to the coupling to the superconductor,

$$h_d^k = -\frac{\hbar}{g\mu_B}\sqrt{\frac{2}{S\beta}}\sum_{pm}\frac{V_{dmm}^{kpp}}{E_{pm}}, \tag{64}$$

and a function

$$Q_{dd'}^{kk'} \equiv -\sum_{q\varsigma}\frac{g_{d\varsigma}^{kq} g_{d'\varsigma}^{k'-q}}{\hbar\omega_q}. \tag{65}$$

describing the cavity-mediated self-interaction in the ferromagnetic insulator.

III. RESULTS

The main result of our work is the effective magnon action (63). The interaction with the cavity and the SC gives rise to linear and bilinear correction terms to the diagonal magnon theory, corresponding to an induced anisotropy field and corrections to the magnon spectra.

To extract a specific quantity, we consider the leading order effect of coupling the FI to the SC via the cavity, namely the linear magnon term. Physically this can be understood as a contribution from an additional magnetic field trying to reorient the FI in a direction other than along the z axis. We can see this explicitly if we Fourier transform the linear magnon term back to real space and imaginary time,

$$S_{\mathrm{lin}}^{\mathrm{FI}} = -\frac{g\mu_B}{\hbar}\int d\tau \sum_{\mathbf{r}_i}\sum_d h_d(\mathbf{r}_i,\tau) S_{id}(\tau), \tag{66}$$

where we have used the definition of the in-plane spin components in Eq. (18), and defined the real space anisotropy field components due to the interaction with the superconductor

$$h_d(\mathbf{r}_i,\tau) = \frac{1}{\sqrt{N_{\mathrm{FI}}\beta}}\sum_k h_d^k e^{ik\cdot r_i}. \tag{67}$$

Above, we introduced the 3-vector

$$r_i \equiv (\tau, \mathbf{r}_i). \tag{68}$$

In order for the anisotropy field components to be real, we require $h_d^k = (h_d^{-k})^*$. Inserting the expressions for E_{pm} and V_{dmm}^{kpp} from Eqs. (45c) and (57) into Eq. (64), and performing the sum over the Matsubara frequencies [28], we get the following expression for the Fourier transposed anisotropy field components,

$$\begin{aligned} h_d^k = &-\sqrt{N_{\mathrm{FI}}\beta}\delta_{\Omega_m 0}\sum_{\mathbf{q},d'}\frac{4\pi a_{\mathrm{SC}} e t}{\hbar\epsilon\omega_{\mathbf{q}}^2 V L_z}\frac{q_{\bar{d}} q_{d'}}{|\mathbf{Q}|^2}\nu_d^2 e^{i\mathbf{q}\cdot(\mathbf{r}_0^{\mathrm{FI}} - \mathbf{r}_0^{\mathrm{SC}})} \\ &\times D_{\mathbf{k},\mathbf{q}}^{\mathrm{FI}} D_{\mathbf{0},-\mathbf{q}}^{\mathrm{SC}} e^{-iq_{d'}a_{\mathrm{SC}}/2}\Pi_{\mathbf{P}d'}, \end{aligned} \tag{69}$$

where the dependence on the supercurrent comes in through the factor

$$\begin{aligned} \Pi_{\mathbf{P}d} = \sum_{\mathbf{p}} \big\{ &\sin[(p_d + P_d)a_{\mathrm{SC}}]|u_{\mathbf{p}}|^2 \\ &+ \sin[(p_d - P_d)a_{\mathrm{SC}}]|v_{\mathbf{p}}|^2\big\}\tanh\frac{\beta E_{\mathbf{p}0}}{2\hbar}. \end{aligned} \tag{70}$$

Notice that the field is finite only for zero Matsubara frequency, meaning that it is time-independent (magnetostatic). It is possible to show that $h_d^k = (h_d^{-k})^*$ by letting $\mathbf{q} \to -\mathbf{q}$ in the sum in Eq. (69), and using $D_{\mathbf{k},\mathbf{q}}^{\mathrm{FI}} = (D_{-\mathbf{k},-\mathbf{q}}^{\mathrm{FI}})^*$, $D_{0,-\mathbf{q}}^{\mathrm{SC}} = (D_{0,\mathbf{q}}^{\mathrm{SC}})^*$ from the definition in Eq. (26). Observe that in the case of no DC (i.e. $\mathbf{P} = \mathbf{0}$), the summand in Eq. (70) is odd in $\mathbf{p}$, and the sum therefore zero, i.e., $\Pi_{\mathbf{P}d} = 0$ if $P_d = 0$. Hence there is no anisotropy field induced across the FI in the absence of a supercurrent. This stresses the necessity of breaking the inversion symmetry of the SC in order to induce an influence on the FI.

A. Special case: small FM

The anisotropy field (67) generally gives rise to complicated, local reorientation of the FI spins. However, there are special cases in which it takes on a simple form. In particular, assume the FI to be very small relative to the cavity, i.e. $\ell_x l_x^{\mathrm{FI}}, \ell_y l_y^{\mathrm{FI}} \ll L_x, L_y$. In this case, the FI sum (26) becomes highly localized around $\mathbf{k} = \mathbf{0}$ for the relevant ranges of ℓ_x and ℓ_y, which are limited by the other factors $D_{\mathbf{0q}}^{\mathrm{SC}}$ and $(\omega_{\mathbf{q}}|\mathbf{Q}|)^{-2}$ found in Eq. (69). We may therefore set $\mathbf{k} = \mathbf{0}$. For a specified set of material parameters and dimensions, the validity is confirmed numerically. In this case, Eq. (67) thus reduces to

$$h_d = \frac{h_d^0}{\sqrt{N_{\mathrm{FI}}\beta}}, \tag{71}$$

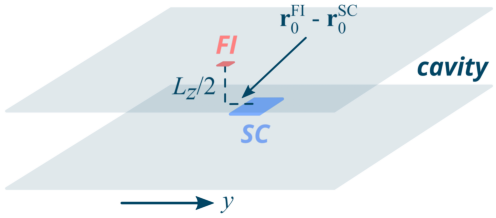

FIG. 4. Illustration of the set-up used in the example given in Sec. III A. A small, square FI and SC are placed spaced apart in the y and z directions inside a comparatively large cavity. Only a small portion of the cavity length in y is utilized as the contributions by the various mediating cavity modes add constructively only over short distances. The FI and SC are nevertheless separated by hundreds of μm, 2–5 orders larger than typical effectual lengths in proximity systems.

representing a uniform anisotropy field across the FI. In this limit we can simplify the expression for the anisotropy field components,

$$h_d = -\sum_{\mathbf{q},d'} \frac{2\pi a_{\mathrm{SC}} e t}{\hbar\epsilon\omega_{\mathbf{q}}^2 V L_z} \nu_d^2 D^{\mathrm{FI}}_{\mathbf{0},\mathbf{q}} D^{\mathrm{SC}}_{\mathbf{0},-\mathbf{q}} \Pi_{\mathbf{P}d'} \frac{q_{\bar{d}} q_{d'}}{|\mathbf{Q}|^2} \times \left[\cos q_x L_x^{\mathrm{sep}} \cos q_y L_y^{\mathrm{sep}} - \sin q_x L_x^{\mathrm{sep}} \sin q_y L_y^{\mathrm{sep}}\right], \tag{72}$$

where we have assumed $e^{-iq_{d'}a_{\mathrm{SC}}/2} \approx 1$, which is a good approximation as long as the cavity dimensions far exceed the lattice constant and only low $|\mathbf{q}|$ contribute to the sum, and used the fact that $D^M_{\mathbf{0},\mathbf{q}}$ [Eq. (26)] is an even function in $\mathbf{q}$. We have also defined the separation length $L_d^{\mathrm{sep}} = (\mathbf{r}_0^{\mathrm{FI}} - \mathbf{r}_0^{\mathrm{SC}})\cdot\hat{e}_d$. Assuming a finite separation between the FI and SC only in one direction, the last term in the above equation vanishes, making every remaining factor even in q_d, except the product $q_{\bar{d}}q_{d'}$ for $\bar{d} \neq d'$. The sum over $\mathbf{q}$ therefore picks out terms such that $\bar{d} = d'$. In order to get a finite h_d we must, therefore, have $\Pi_{\mathbf{P}\bar{d}} \neq 0$, i.e., the supercurrent momentum must be finite in the direction $\bar{d}$. Hence, in the case that the separation between the FI and SC is finite in only one direction, applying a supercurrent in the x direction can only induce an anisotropy field in the y direction, and vice versa.

We consider the specific case of a small, square FI and SC displaced along y and z (Fig. 4). In Fig. 5 we show numerically how the effective anisotropy field varies with the supercurrent momentum in this special case, using Nb and YIG as material choices for the FI and SC films, respectively; see Table I. We furthermore use the interpolation formula [45]

$$\Delta = 1.76 k_B T_{c0} \tanh(1.74\sqrt{T_{c0}/T - 1}) \tag{73}$$

for the superconducting gap, and a simple cubic tight-binding electron dispersion. With the FI and SC center points separated by 140 μm in the y direction (meaning they are separated edge-to-edge by 115 μm in-plane), we find an anisotropy field with a magnitude of $\lesssim 1\,\mu\mathrm{T}$ (Fig. 5a). If the constraint on separating the FI and SC in-plane is eased, the magnitude is increased by a factor of 1.5 in our specific example (Fig. 5b). We discuss the latter case in the concluding remarks.

Two factors determine the inhomogeneous distribution of the responses seen in Fig. 5. First, the anisotropy field is nearly linear in the components P_d of the supercurrent momentum, which is seen by expanding the anisotropy field (see Eq. (70)) around $P_d a_{\mathrm{SC}} = 0$ (note that $P_c a_{\mathrm{SC}} \approx 0.001$). This generally makes the response stronger for larger $|\mathbf{P}|$, which is as expected, since it relies on breaking the $\mathbf{p}$-inversion symmetry. This dependency is evident in Fig. 5.

Second, the factor $e^{i\mathbf{q}\cdot(\mathbf{r}_0^{\mathrm{FI}} - \mathbf{r}_0^{\mathrm{SC}})}$ renders the anisotropy field very sensitive to the separation of the FI and SC center points in the in-plane directions. This factor expresses that cavity modes associated with a range of different in-plane momenta $\mathbf{q}$ (i.e., spatial oscillations) with a coherent amplitude at no in-plane separation ($\mathbf{r}_0^{\mathrm{FI}} - \mathbf{r}_0^{\mathrm{SC}} = 0$), become increasingly decoherent with increasing separation. Eventually, this decoherence causes states in the SC to contribute oppositely, hence destructively, to the effective anisotropy field. The destructive addition at finite separation is limited by the range of low-$\mathbf{q}$ cavity modes that contribute to the mediated interaction until the coupling is suppressed by the factor $D^{\mathrm{FI}}_{\mathbf{0q}} D^{\mathrm{SC}*}_{\mathbf{0q}} / \omega_{\mathbf{q}}^2 \mathbf{Q}^2$, which in turn is determined by the dimensions of the three subsystems. For sufficiently small separations (determined by the contributing range of $\mathbf{q}$), this oscillation is mild, and can be used to change the polarity of the anisotropy field without extinguishing the response. This is why the polarity of the response component h_x changes between Figs. 5a and 5b.

It is furthermore clear by inspection of Eq. (70) that the main contributions to the anistotropy field come from states near the Fermi surface. Series-expanding the expression in $\mathbf{P}$, most terms are seen to cancel due the odd symmetry in $\mathbf{p}$ that was remarked below Eq. (70). The strongest asymmetry caused by $\mathbf{P}$ is seen to originate from the factor $\sin[(p_{d'} + P_{d'})a_{\mathrm{SC}}]\,|u_{\mathbf{p}}|^2 + \sin[(p_{d'} - P_{d'})a_{\mathrm{SC}}]\,|v_{\mathbf{p}}|^2$ in the summand, due to the step-like nature of $|u_{\mathbf{p}}|^2$ and $|v_{\mathbf{p}}|^2$ near the Fermi surface. This is as expected, since we consider interactions involving the scattering of SC quasiparticles, hence the low-energy events are concentrated near the Fermi surface.

TABLE I. Table of numerical parameter values.

YIG (FI)		Nb (SC)	
a_{FI}	1.240 nm [46]	a_{SC}	0.330 nm [47]
		T_{c0}	6 K [36]
		t	0.35 eV[a]
		P_c	$3.1 \times 10^7\ \mathrm{m}^{-1}$[b]
		E_F	5.32 eV[c] [47]

[a] Based on the tight-binding expression $t = \hbar^2/2ma_{\mathrm{SC}}^2$ [14], with m the effective electron mass.
[b] Based on $P_c = j_c m/\hbar e n_s$ [33], with an estimated critical current $j_c = 4\,\mathrm{MA/cm^2}$ [48], and a superfluid density $n_s = m/\mu_0 e^2 \lambda^2$ [35] with a penetration depth $\lambda = 200$ nm [36].
[c] Fermi energy for Nb. Does not appear explicitly in Eq. (72), but is used in the electron dispersion.

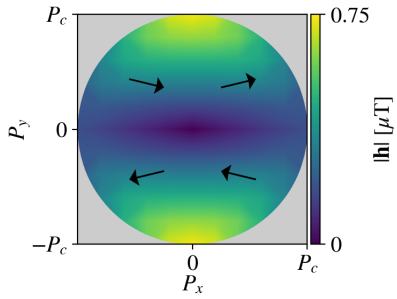

(a)

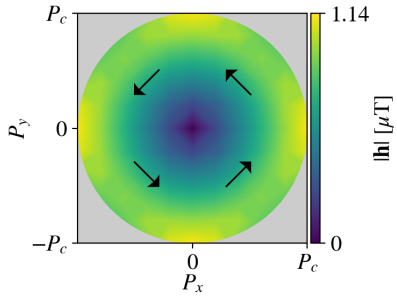

(b)

FIG. 5. The magnitude and direction (arrows) of the effective anisotropy field [Eq. (72)] at $T = 1\,\mathrm{K}$ as a function of the supercurrent momentum $\mathbf{P}$, for the simple case of a small FI ($l_x^{\mathrm{FI}} = l_y^{\mathrm{FI}} = 10\,\mu\mathrm{m}$) relative to the cavity ($L_x = L_y = 10\,\mathrm{cm}$, $L_z = 0.1\,\mathrm{mm}$). The SC dimensions are $l_x^{\mathrm{SC}} = l_y^{\mathrm{SC}} = 50\,\mu\mathrm{m}$. The FI and SC center points are separated by (a) $L_y^{\mathrm{sep}} = 140\,\mu\mathrm{m}$ and (b) nothing (placed directly over each other). Observe the change in both the strength and direction of the anisotropy field.

IV. CONCLUDING REMARKS

In this paper, we have calculated the cavity-mediated coupling between an FI and an SC by exactly integrating out the cavity photons. The main result is the effective FI action (63), in which linear and bilinear magnon terms appear in addition to the diagonal terms. These respectively correspond to an induced anisotropy field, and corrections to the magnon spectra. In contrast to conventional proximity systems, the cavity-mediation allows for relatively long-distance interactions between the FI and the SC, without destructive effects on order parameters associated with proximity systems, such as pair-breaking magnetic fields. The separation furthermore facilitates subjection of the FI and the SC to separate drives and temperatures. In contrast to common perturbative approaches to cavity-mediated interactions involving the Schrieffer–Wolff transformation [9, 14, 20] or Jaynes–Cummings-like models [12, 13, 26], the path-integral approach allows for an exact integrating-out of the cavity, without limitations to off-resonant regimes. This carries the additional advantage of allowing for magnon–photon hybridization; that is, we are not theoretically limited to regimes of weak FI–cavity Zeeman coupling. We furthermore take into account that the finite and different FI, cavity and SC dimensions enable interactions between large ranges of particle modes, which is neglected in various preceding works [9, 10, 13, 14, 21, 23, 24], although its importance has been emphasized by both experimentalists [24] and theorists [21].

In an arbitrary practical example, we estimate numerically the effective anisotropy field induced by leading-order interactions across a YIG film (FI) due to mediated interactions with an Nb film (SC). We find it is $\lesssim 1\,\mu\mathrm{T}$, mediated across $130\,\mu\mathrm{m}$ edge-to-edge accounting for both in-plane and out-of-plane separation, inside a $10\,\mathrm{cm} \times 10\,\mathrm{cm} \times 0.1\,\mathrm{mm}$ cavity (Fig. 5a). With out-of-plane coercivities in nm-thin Bi-doped YIG films reportedly as low as $300\,\mu\mathrm{T}$ [49], we anticipate the response can be made more appreciable relative to $\mathbf{B}_{\mathrm{ext}}$ with parameter optimization, which is left for future work. The separation is 2–5 orders of magnitude greater than the typical length scales of influence in proximity systems, and facilitates local subjection to different drives and temperatures. The main contributions from the SC originate from a narrow vicinity of the Fermi surface determined by the Cooper pair center-of-mass momentum $2\mathbf{P}$. The response is very sensitive to the in-plane separation of the FI and SC center points due to the spatial decoherence of the mediating cavity modes over distances, which in turn depends on the dimensions of the FI, cavity and SC. For this reason, the in-plane separation of FI and SC was much smaller than the cavity width.

In Appendix B we have included the calculation of the anisotropy field when placing the SC at the magnetic antinode at $z = 0$. Since the vector potential is purely out of plane in this case, the paramagnetic coupling is zero, and we therefore couple the cavity to the SC via the Zeeman coupling. As shown in the appendix, this results in a much weaker coupling and therefore much smaller anisotropy field. This can be understood by comparing the effective fields the SC couples to in the two cases. The strength of the Zeeman coupling is proportional to $\mathbf{q} \times \mathbf{A}$, which for the lowest cavity modes gives a field strength proportional to $|\mathbf{A}|/L$. However, for the paramagnetic coupling, the effective field is proportional to $\mathbf{p} \cdot \mathbf{A}$. In both cases, the main contribution to the anisotropy field originates from a narrow vicinity of the Fermi level, the extent of which is determined by the magnitude of the symmetry-breaking supercurrent (electric antinode) or applied field (magnetic antinode). Thus, we have a paramagnetic coupling proportional to $p_{\mathrm{F}}|\mathbf{A}|$, where p_{F} is the Fermi momentum. A Fermi energy of $5.32\,\mathrm{eV}$ gives $p_F \sim 10^{10}\,\mathrm{m}^{-1} \gg 1/L$ for cavities with lengths in the mm to cm range. Together with the fact that the contributing components of $\mathbf{A}$ are larger for low $|\mathbf{q}|$ at the electric antinode compared with the magnetic antinode, the difference in length scales leads to a much larger paramagnetic coupling between cavity and SC compared to the Zeeman coupling, resulting in a much larger effective FI–SC coupling and anisotropy field.

One important constraint in our model that can potentially

be eased, is that the FI and the SC cannot overlap in-plane. In this case, we found a stronger response (cf. Fig. 5b). This was assumed in order to enable the FI to be subjected to the aligning magnetostatic field $\mathbf{B}_{\text{ext}}$ without affecting the SC, analogously to the experimental set-up in Refs. [12, 13]. Combined with the eventually destructive contributions of various cavity modes over finite in-plane distances that limited us to using only a fraction of the cavity width in our example, this leads to significant constraints on the dimensions and relative placements of the FI and SC. However, Ref. [50] reports out-of-plane critical fields of nm-thin Nb films of roughly 1–4 T, while Ref. [49] reports out-of-plane coercivities in nm-thin Bi-doped YIG films of roughly $3 \times 10^{-4}\,\mathrm{T}$. An aligning field can therefore be many orders of magnitude smaller than the SC critical field with appropriate material choices. One would then expect the effect of $\mathbf{B}_{\text{ext}}$ on the SC to be negligible. However, we have not considered here the subsequent effect of the SC on the spatial distribution of $\mathbf{B}_{\text{ext}}$, which was taken to be uniform across the FI.

Moreover, the Pearl length criterion, which greatly limits SC dimensions, can potentially be disregarded if the odd $\mathbf{p}$ symmetry of the anisotropy field (64) is broken by other means than a supercurrent. A candidate for this is taking into account spin–orbit coupling on the SC and subjecting it to a weak (non-pair breaking) magnetostatic field.

Furthermore, in our set-up, we have considered coupling to the quasiparticle excitations of the SC. This has partly been motivated by the prospect of using the FI to probe detailed spin and momentum information about the SC gap, which would require an extension of our present model. Another interesting avenue to explore is coupling directly to the gap by considering fluctuations from its mean-field value. This has been explored for an FI–SC bilayer, where the Higgs mode of the SC couples linearly to a spin exchange field [51]. This has a significant impact on the SC spin susceptibility in a bilayer set-up.

Despite coupling to the quasiparticles, we find that the anisotropy field magnitude nearly constant at low temperatures, and rapidly decreases to zero near the critical temperature. This can be understood from the fact that the symmetry-breaking supercurrent momentum enters the system Hamiltonian via the gap (cf. Eq. (28b)). Hence, when the gap vanishes, so does the quantity that breaks the symmetry. On the other hand, for temperatures substantially below T_{c0}, the gap varies little with temperature; the anisotropy field becomes close to constant, with a magnitude depending on the momentum associated with the inversion symmetry-breaking current $\mathbf{P}$.

In the normal state, the DC through the SC induces a surrounding magnetostatic field, by the Biot–Savart law. This differs from the response in the superconducting state by instead being appreciable above T_{c0}, and by its spatial distribution; for instance, the magnetostatic field cannot reverse the field direction as observed between Fig. 5a and 5b.

Lastly, it is seen from Eq. (64) that the SC quasiparticle modes uniformly affect the anisotropy field in our current set-up, as the sum over fermion momenta $\mathbf{p}$ can be factored out from the sum over photon momenta $\mathbf{q}$. This limits the resolution of SC features in the anisotropy field, and by extension the FI. However, to higher order in the calculations, the quantity $G^{qq'}_{\varsigma\varsigma'}$ defined in Eq. (A6) enters, with sums over fermion momenta $\mathbf{p}$ and $\mathbf{p}'$ that are inseparable from the cavity momenta $\mathbf{q}$ and $\mathbf{q}'$. This quantity is a candidate for extracting more features of the SC via the FI.

ACKNOWLEDGMENTS

We acknowledge funding via the "Outstanding Academic Fellows" programme at NTNU, the Research Council of Norway Grant number 302315, as well as through its Centres of Excellence funding scheme, project number 262633, "QuSpin".

Appendix A: Integrating out the SC first

The order in which we integrate out the cavity and the SC is inconsequential. We show this here by integrating out the SC first, starting from the partition function (49).

We introduce the interaction matrix G with elements

$$G^{pp'}_{mm'} \equiv \frac{1}{\sqrt{\beta}} \sum_{q\varsigma} g^{qpp'}_{\varsigma mm'} (a_{q\varsigma} + a^{\dagger}_{-q\varsigma}), \tag{A1}$$

and furthermore the diagonal matrix E with elements

$$E^{pp'}_{mm'} \equiv E_{pm} \delta_{pp'} \delta_{mm'}. \tag{A2}$$

Hence the action involving the SC can be written as

$$S_0^{\text{SC}} + S_{\text{int}}^{\text{cav}-SC} = \sum_{pm} \sum_{p'm'} (E+G)^{pp'}_{mm'} \gamma^{\dagger}_{pm} \gamma_{p'm'}. \tag{A3}$$

The part of the partition function (49) which depends on the SC is a Gaussian integral, and can now be written as [28]

$$\begin{aligned} Z^{\text{SC}} &\equiv \int \mathcal{D}[\gamma, \gamma^{\dagger}] \exp\left[-\frac{1}{\hbar} \sum_{pm} \sum_{p'm'} (E+G)^{pp'}_{mm'} \gamma^{\dagger}_{pm} \gamma_{p'm'} \right] \\ &\approx \exp\left[\mathrm{Tr}\left[E^{-1}G - E^{-1}GE^{-1}G/2 \right] \right]. \end{aligned} \tag{A4}$$

In the last line, we neglected a factor $\exp \mathrm{Tr} \ln(\beta E/\hbar)$ that is constant with respect to the integration variables, and expanded another logarithm to second order in $|E^{-1}G|$. Hence, integrating out the SC to second order in the cav–SC coupling yields an effective action

$$\begin{aligned} S_1^{\text{cav}} &\equiv -\hbar \mathrm{Tr}\left[E^{-1}G - E^{-1}GE^{-1}G/2 \right] \\ &= -\frac{\hbar}{\sqrt{\beta}} \sum_{q\varsigma} \sum_{pm} \frac{g^{qpp}_{\varsigma mm}}{E_{pm}} (a_{q\varsigma} + a^{\dagger}_{-q\varsigma}) \\ &\quad + \sum_{q\varsigma} \sum_{q'\varsigma'} G^{qq'}_{\varsigma\varsigma'} (a_{q\varsigma} + a^{\dagger}_{-q\varsigma})(a_{q'\varsigma'} + a^{\dagger}_{-q'\varsigma'}), \end{aligned} \tag{A5}$$

where we introduced the coefficient

$$G^{qq'}_{\varsigma\varsigma'} \equiv \frac{\hbar}{2\beta}\sum_{pm}\sum_{p'm'}\frac{g^{qpp'}_{\varsigma mm'}g^{q'p'p}_{\varsigma' m'm}}{E_{pm}E_{p'm'}}. \tag{A6}$$

We now proceed to isolate the photonic terms and integrate out the cavity, i.e., we will perform the integral

$$Z^{\rm cav} \equiv \int \mathcal{D}[a,a^\dagger]e^{-S^{\rm cav}/\hbar}, \tag{A7}$$

where the effective cavity action is

$$S^{\rm cav} \equiv S^{\rm cav}_0 + S^{\rm cav}_1 + S^{\rm FI-cav}_{\rm int}. \tag{A8}$$

To this end, we introduce the current operator

$$J_{q\varsigma} \equiv -\sum_{kd} G^{kq}_{d\varsigma}(\nu_d\eta_{-k} + \nu^*_d\eta^\dagger_k) + s_{q\varsigma}, \tag{A9}$$

and perform a shift of integration variables

$$a_{q\varsigma} \to a_{q\varsigma} + J_{-q\varsigma}/\hbar\omega_q, \tag{A10a}$$
$$a^\dagger_{q\varsigma} \to a^\dagger_{q\varsigma} + J_{q\varsigma}/\hbar\omega_q. \tag{A10b}$$

The quantities $G^{kq}_{d\varsigma}$ (to be distinguished from $G^{qq'}_{\varsigma\varsigma'}$) and $s_{q\varsigma}$ are coefficients of linear photon terms to be determined.

We now require that the shifts (A10a)–(A10b) absorb the explicit linear photon terms in the action (A8), leaving only bilinear and constant terms in the shifted variables. This leads to self-consistency equations for $G^{kq}_{d\varsigma}$ and $s_{q\varsigma}$. However, to second order in $|E^{-1}G|$, it can be shown that only the lowest-order expressions for $G^{kq}_{d\varsigma}$ and $s_{q\varsigma}$ affect the anisotropy field to be extracted at the end, cf. Sec. III. These are

$$G^{kq}_{d\varsigma} = g^{kq}_{d\varsigma}, \tag{A11}$$
$$s_{q\varsigma} = \frac{\hbar}{\sqrt{\beta}}\sum_{pm}\frac{g^{qpp}_{\varsigma mm}}{E_{pm}}. \tag{A12}$$

Hence, the action (A8) can be written as

$$S^{\rm cav} = S^{\rm cav}_{\rm bil} + S^{\rm cav}_{\rm con} \tag{A13}$$

where

$$S^{\rm cav}_{\rm bil} \equiv \sum_{q\varsigma}\hbar\omega_q a^\dagger_{q\varsigma}a_{q\varsigma} + \sum_{q\varsigma}\sum_{q'\varsigma'}G^{qq'}_{\varsigma\varsigma'}(a_{q\varsigma} + a^\dagger_{-q\varsigma})(a_{q'\varsigma'} + a^\dagger_{-q'\varsigma'}), \tag{A14}$$

$$S^{\rm cav}_{\rm con} \equiv \sum_{q\varsigma}\frac{J_{q\varsigma}J_{-q\varsigma}}{\hbar\omega_q} + \sum_{q\varsigma}\sum_{q'\varsigma'}G^{qq'}_{\varsigma\varsigma'}J_{-q\varsigma}J_{-q'\varsigma'}\left[\frac{1}{\hbar\omega_q}+\frac{1}{\hbar\omega_{-q}}\right]\left[\frac{1}{\hbar\omega_{q'}}+\frac{1}{\hbar\omega_{-q'}}\right]. \tag{A15}$$

$S^{\rm cav}_{\rm bil}$ contains all bilinear terms with respect to the shifted variables, and $S^{\rm cav}_{\rm con}$ all constant terms.

Returning to the integral (A7), by Eq. (A13), we now have

$$Z^{\rm cav} = \int \mathcal{D}[a,a^\dagger]e^{-S^{\rm cav}/\hbar} = e^{-S^{\rm cav}_{\rm con}/\hbar}\int \mathcal{D}[a,a^\dagger]e^{-S^{\rm cav}_{\rm bil}/\hbar}. \tag{A16}$$

The integrand is now independent of magnons, and therefore inconsequential to the physics of the ferromagnetic insulator. We can therefore neglect the integral, leaving only the exponential prefactor. We are thus left with an effective FI partition function

$$Z^{\rm FI} \equiv \int \mathcal{D}[\eta,\eta^\dagger]e^{-S^{\rm FI}/\hbar}, \tag{A17}$$

where the effective FI action is

$$S^{\rm FI} \equiv S^{\rm FI}_0 + S^{\rm cav}_{\rm con}. \tag{A18}$$

Neglecting magnon-independent terms, $S^{\rm FI}$ reads, after some rewriting,

$$S^{\rm FI} = \sum_k \hbar\lambda_k\eta^\dagger_k\eta_k + \sum_{kd}\sum_{k'd'}Q^{kk'}_{dd'}(\nu_d\eta_{-k} + \nu^*_d\eta^\dagger_k)(\nu_{d'}\eta_{-k'} + \nu^*_{d'}\eta^\dagger_{k'}) - g\mu_B\sum_{kd}h^k_d\cdot\sqrt{\frac{S}{2}}(\nu_d\eta_{-k} + \nu^*_d\eta^\dagger_k). \tag{A19}$$

Above, we introduced

$$Q^{kk'}_{dd'} \equiv -\sum_{q\varsigma}\left[\frac{g^{kq}_{d\varsigma}g^{k'-q}_{d'\varsigma}}{\hbar\omega_q} + \sum_{q'\varsigma'}G^{qq'}_{\varsigma\varsigma'}\left[\frac{1}{\hbar\omega_q}+\frac{1}{\hbar\omega_{-q}}\right]\left[\frac{1}{\hbar\omega_{q'}}+\frac{1}{\hbar\omega_{-q'}}\right]g^{kq}_{d\varsigma}g^{k'q'}_{d'\varsigma'}\right], \tag{A20}$$

$$h_d^k = -\frac{\hbar}{g\mu_B}\sqrt{\frac{2}{S\beta}}\sum_{pm}\frac{V_{dmm}^{kpp}}{E_{pm}}, \tag{A21}$$

which to leading order in the paramagnetic coupling are indeed the same as Eqs. (64) and (65).

Appendix B: SC at magnetic antinode

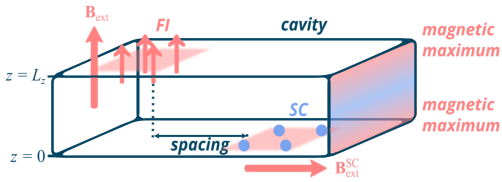

FIG. 6. Illustration of the set-up with the SC placed at the magnetic antinode. The SC is subjected to an aligning external in-plane magnetic field $\mathbf{B}_{\rm ext}^{\rm SC}$. This set-up is otherwise identical to the one illustrated in Fig. 1.

To compare our results for the FI-SC coupling with the SC placed at the electric antinode, we examine what happens when we place the superconductor at a magnetic maximum at $z \approx 0$, cf. Fig. 6. In this case the vector potential $\mathbf{A}$ points purely in the z direction, and therefore does not couple to the SC via the paramagnetic coupling term used above. We therefore couple the SC to the cavity via the Zeeman coupling, and calculate the resulting anisotropy field across the FI. For the setup considered in the main text, it was necessary to break the inversion symmetry to get a finite anisotropy field, achieved, for instance, by applying a DC current. For the present setup, it is necessary to break the in-plane spin rotation symmetry, which can be achieved by applying an in-plane magnetic field to the SC. This becomes evident when considering the coupling between the cavity and SC. Placing the SC at $z \approx 0$, the cavity magnetic field is purely in-plane, pointing in the opposite direction to the field Eq. (23) at $z = L_z$, resulting in a coupling term,

$$S_{\rm Zeeman} = \sum_{qpp'}\sum_{\sigma\sigma'} g_{\sigma\sigma'}^{qpp'}(a_{q1} + a_{-q1}^\dagger)c_{p\sigma}^\dagger c_{p'\sigma'}, \tag{B1}$$

with interaction matrix

$$g_{\sigma\sigma'}^{qpp'} = \delta_{\Omega_n,\omega_n-\omega_n'} \times \sqrt{\frac{\hbar\mu_B^2}{\epsilon\omega_{\mathbf{q}}V}} D_{\mathbf{p}-\mathbf{p}',\mathbf{q}}^{\rm SC} e^{i\mathbf{q}\cdot\mathbf{r}_0^{\rm SC}} i\sin\theta_{\mathbf{q}}(\boldsymbol{\sigma}\times\mathbf{q})_{\sigma\sigma'}\cdot\hat{e}_z. \tag{B2}$$

This interaction alone would lead to a SC-cavity coupling that is off-diagonal in quasiparticle basis. The anisotropy field, corresponding to the diagram for $S_{\rm int}$ in Fig. 3 with connected quasiparticle lines will therefore be exactly zero unless one breaks the spin-rotation symmetry by an in-plane magnetostatic field $\mathbf{B}_{\rm ext}^{\rm SC}$. The latter can for example be experimentally realized using external coils, as suggested for $\mathbf{B}_{\rm ext}$. In that case the quasiparticle bands are spin-split, resulting in the SC term

$$S_0^{\rm SC} = \sum_{pn}(-i\hbar\omega_n + E_{\mathbf{p}n})\gamma_{pn}^\dagger\gamma_{pn}, \tag{B3}$$

with the four quasiparticle bands

$$E_{\mathbf{p}n} = (-1)^{\lfloor n/2\rfloor}E_{\mathbf{p}} + (-1)^n H, \tag{B4}$$

with $E_{\mathbf{p}} = \sqrt{\xi_{\mathbf{p}}^2 + |\Delta_{\mathbf{p}}|^2}$, $n \in [0,1,2,3]$ and $H = |\mu_B\mathbf{B}_{\rm ext}^{\rm SC}|$. The bands are independent of in-plane direction of the field $\mathbf{B}_{\rm ext}^{\rm SC}$, with the directional dependence entering through the coupling between the quasiparticles and the cavity photons,

$$S_{\rm int}^{\rm SC-cav} = \frac{1}{2\sqrt{\beta}}\sum_{qpp'}\sum_{nn'} g_{nn'}^{qpp'}(a_{q1} + a_{-q1}^\dagger)\gamma_{pn}^\dagger\gamma_{p'n'}, \tag{B5}$$

where we have defined the interaction matrix in the Bogoliubov quasiparticle basis

$$g_{nn'}^{qpp'} = -\frac{1}{2}g_{\uparrow\downarrow}^{qpp'}e^{i\phi}\begin{pmatrix}[u_p^\dagger u_{p'} + v_p v_{p'}^\dagger][\sigma_z + i\sigma_y] & [u_p^\dagger v_{p'} - v_p u_{p'}^\dagger][\sigma_0 - \sigma_x]\\ [v_p^\dagger u_{p'} - u_p v_{p'}^\dagger][\sigma_0 + \sigma_x] & [v_p^\dagger v_{p'} + u_p u_{p'}^\dagger][\sigma_z - i\sigma_y]\end{pmatrix}_{nn'} - \frac{1}{2}g_{\downarrow\uparrow}^{qpp'}e^{-i\phi}\begin{pmatrix}[u_p^\dagger u_{p'} + v_p v_{p'}^\dagger][\sigma_z - i\sigma_y] & [u_p^\dagger v_{p'} - v_p u_{p'}^\dagger][\sigma_0 + \sigma_x]\\ [v_p^\dagger u_{p'} - u_p v_{p'}^\dagger][\sigma_0 - \sigma_x] & [v_p^\dagger v_{p'} + u_p u_{p'}^\dagger][\sigma_z + i\sigma_y]\end{pmatrix}_{nn'}, \tag{B6}$$

where σ_0 is the 2×2 identity matrix, and ϕ is the angle of the in-plane field relative to the x axis. We have also defined the functions

$$u_{\mathbf{p}} = e^{i\theta_{\mathbf{p}}}\sqrt{\frac{1}{2}\left(1 + \frac{\xi_{\mathbf{p}}}{E_{\mathbf{p}}}\right)}, \tag{B7a}$$

$$v_{\mathbf{p}} = e^{i\theta_{\mathbf{p}}}\sqrt{\frac{1}{2}\left(1-\frac{\xi_{\mathbf{p}}}{E_{\mathbf{p}}}\right)}, \tag{B7b}$$

which satisfy $|u_{\mathbf{p}}|^2 + |v_{\mathbf{p}}^2| = 1$. Here $2\theta_{\mathbf{p}}$ is the phase of the order parameter.

Following the same procedure of integrating out the cavity photons and quasiparticles in the SC, we get an expression identical to Eq. (63), with the only change coming in the anisotropy field, which is now defined as

$$h_d^k \equiv -\frac{\hbar}{\sqrt{2S\beta}g\mu_B}\sum_{pn}\frac{V_{dnn}^{kpp}}{E_{pn}}, \tag{B8}$$

with

$$V_{dnn'}^{kpp'} = \sum_q g_{d1}^{kq} g_{nn'}^{-qpp'}\left[\frac{1}{\hbar\omega_q}+\frac{1}{\hbar\omega_{-q}}\right]. \tag{B9}$$

The additional factor of $1/2$ in the definition of h_d^k is due to the field integral resulting in the Pfaffian of the antisymmetrized Green's function in this case, which is the square root of the determinant [52]. The reason for this is the necessity of an expanded Nambu spinor, which contains both creation and annihilation operators of both types of quasiparticles when including an in-plane field [53].

Inserting Eqs. (B6) and (B9) into Eq. (B8) and performing the sum over fermionic Matsubara frequencies [28], we get

$$h_d^k = \frac{\sqrt{\beta}\delta_{\Omega_m 0}}{\sqrt{2S}g\mu_B}\sum_{\mathbf{qp}}\frac{g_d^{\mathbf{kq}}}{\hbar\omega_{\mathbf{q}}}[g_{\uparrow\downarrow}^{-\mathbf{qpp}}e^{i\phi}+g_{\downarrow\uparrow}^{-\mathbf{qpp}}e^{-i\phi}] \times\left[\tanh\frac{\beta(E_{\mathbf{p}}+H)}{2\hbar}-\tanh\frac{\beta(E_{\mathbf{p}}-H)}{2\hbar}\right], \tag{B10}$$

where we have used the fact that $\omega_{\mathbf{q}}$ is even in $\mathbf{q}$. Here it is clear that the anisotropy field is exactly zero when the in-plane field is zero, since the last two terms exactly cancel in that case. Moreover, since the anisotropy field is independent of the frequency Ω_m, we define the time-independent anisotropy field $h_d^{\mathbf{k}} = \sum_{\Omega_m} h_d^k e^{-i\Omega_m\tau}/\sqrt{\beta}$. Inserting the expressions for $g_d^{\mathbf{kq}}$ and $g_{\sigma\sigma'}^{-\mathbf{qpp}}$ from Eqs. (25) and (B2) we get

$$h_d^{\mathbf{k}} = -\frac{\mu_B\sqrt{N_{\mathrm{FI}}}}{\epsilon V}\sum_{\mathbf{q}}e^{i\mathbf{q}\cdot(\mathbf{r}_0^{\mathrm{FI}}-\mathbf{r}_0^{\mathrm{SC}})}\frac{D_{\mathbf{kq}}^{\mathrm{FI}}D_{\mathbf{0q}}^{\mathrm{SC}*}\sin^2\theta_{\mathbf{q}}}{\omega_{\mathbf{q}}^2}q_{\bar{d}}\nu_d^2[q_y\cos\phi-q_x\sin\phi]\sum_{\mathbf{p}}\left[\tanh\frac{\beta(E_{\mathbf{p}}+H)}{2\hbar}-\tanh\frac{\beta(E_{\mathbf{p}}-H)}{2\hbar}\right]. \tag{B11}$$

We focus on the anisotropy field averaged across the FI, $\langle h_d\rangle = \sum_i h_d(\mathbf{r}_i,\tau)/N_{\mathrm{FI}} = \sum_i\sum_{\mathbf{k}} h_d^{\mathbf{k}}e^{i\mathbf{k}\cdot\mathbf{r}_i}/N_{\mathrm{FI}}^{3/2} = h_d^{\mathbf{0}}/\sqrt{N_{\mathrm{FI}}}$ (cf. Eq. (67)), rewrite the first sum such that it becomes dimensionless, and transform the second sum into an integral using a free electron gas dispersion $\xi_{\mathbf{k}} = \hbar^2\mathbf{p}^2/2m-\mu$. Assuming cavity dimensions $L_x = L_y = L$ and an s-wave gap, we get

$$\langle h_d\rangle = -\frac{\mu_B m A_{\mathrm{SC}}\Delta_0}{2\pi\hbar^2\epsilon c^2 V}\sum_{\mathbf{q}}e^{i\mathbf{q}\cdot(\mathbf{r}_0^{\mathrm{FI}}-\mathbf{r}_0^{\mathrm{SC}})}D_{0\mathbf{q}}^{\mathrm{FI}}D_{0\mathbf{q}}^{\mathrm{SC}*}\frac{\ell_{\bar{d}}\nu_d^2[\ell_y\cos\phi-\ell_x\sin\phi][\ell_x^2+\ell_y^2]}{\left[\ell_x^2+\ell_y^2+\left(\frac{L}{2L_z}\right)^2\right]^2} \times\int_{-\mu/\Delta_0}^{\xi_{\max}/\Delta_0}dx\left[\tanh\frac{1.764T_c\left(\sqrt{x^2+|\Delta/\Delta_0|^2}+H/\Delta_0\right)}{2T}-\tanh\frac{1.764T_c\left(\sqrt{x^2+|\Delta/\Delta_0|^2}-H/\Delta_0\right)}{2T}\right]. \tag{B12}$$

Here A_{SC} and Δ_0 are the area and zero temperature gap of the superconductor, respectively, and m the electron mass. ℓ_x and ℓ_y are integer indexes corresponding to cavity momentum $\mathbf{q}$. From the above expression we expect terms even in ℓ_d to dominate, resulting in the anisotropy field and expectation values of the in-plane spin components to have a ϕ dependence given by $h_x^{\mathbf{k}} \sim \langle S_{ix}\rangle \propto -\cos\phi$ and $h_y^{\mathbf{k}} \sim \langle S_{iy}\rangle \propto -\sin\phi$. This is in good agreement with numerical solutions of Eq. (B12), as shown in Fig. 7. Notice, however, that the magnitude of the anisotropy field is very small, on the order of 10^{-11} T. This is several orders of magnitude smaller than the previously considered setup, and we do not expect this to be a measurable effect. Here we have neglected the effect of a in-plane finite separation between the SC and FI by placing them directly above each other. A finite separation would further reduce the anisotropy field.

At zero temperature the two hyperbolic tangent functions in Eq. (B12) are always equal to one, as long as $H < \Delta_0$. Since the field must be below the critical field $H_{c0} = \Delta_0/\sqrt{2}$ in the superconducting state, the two terms in the integral always cancel exactly at zero temperature. On the other hand, in the case of temperatures just above the critical temperature, $T \gtrsim T_c$, and $\mu, \xi_{\max} > H$, we get the analytical result $4H/\Delta_0$ from the integral. Hence we expect the anisotropy field to increase from zero to the normal state value as temperature increases towards T_c, and that $\langle h_d\rangle$ increases linearly with applied field in the normal state. This is found to be in good agreement with numerical results, see the inset in Fig. 7 for $|\mathbf{H}| > H_c$. In the numerical calculations we have assumed $\mu, \xi_{\max} \gg \Delta_0$, and that the gap's dependence on

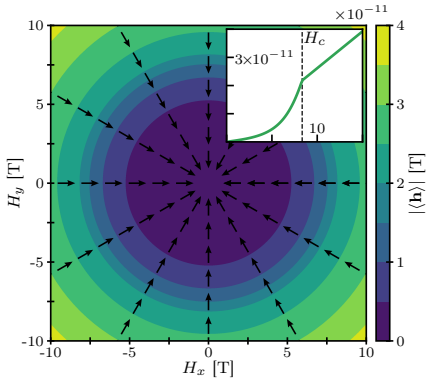

FIG. 7. Absolute value (contour plot) and direction (arrows) of the averaged anisotropy field as a function of applied field strength and direction. The anisotropy field points opposite the applied field over the SC, following a $\cos\phi$ and $\sin\phi$ dependence for the x and y component respectively. The inset shows the absolute value of the in-plane projection as a function of the field strength. The temperature is set to $T = 0.5T_{c0}$. The cavity dimensions are $L_x = L_y = L = 10\,\mathrm{cm}$ and $L_z = 1\,\mathrm{mm}$, and the FI and SC have sides of length $0.001L$ and are placed at the center of the cavity.

temperature and applied field is described by Eq. (73) multiplied with $\sqrt{1-(H/H_c)^2}$ [45, 54], and the critical field depends on temperature as $H_c = H_{c0}[1-(T/T_{c0})^2]$ [35], where T_{c0} is the critical temperature for zero field. Below the critical temperature and field, the field-dependence of the anisotropy field is more complicated due to the additional effect of reducing the superconducting gap, see inset in Fig. 7. The difference in temperature and applied field-dependence of the anisotropy field between the normal and superconducting state could therefore in principle be a way of detecting the onset of superconductivity without directly probing the superconductor, though the anisotropy field calculated here is too small to be detectable.

Appendix C: Linear terms as an anisotropy field

In this appendix, we take a closer look at the interpretation of the linear magnon terms as interactions with an effective anisotropy field. Consider an FI in an inhomogeneous applied field,

$$\mathcal{H} = -J\sum_{\langle i,j\rangle}\mathbf{S}_i\cdot\mathbf{S}_j - \sum_i \mathbf{H}_i\cdot\mathbf{S}_i. \tag{C1}$$

Above, $\mathbf{H}_i = (H_i^x, H_i^y, H^z)$ is the inhomogeneous external field, with H^z assumed homogeneous and much larger than H_i^x, H_i^y. We therefore assume ordering in the z direction when performing the Holstein–Primakoff transformation, resulting in the Fourier-transformed Hamiltonian

$$\mathcal{H} = E_0 + \sum_{\mathbf{k}}\left[\hbar\lambda_{\mathbf{k}}\eta_{\mathbf{k}}^\dagger\eta_{\mathbf{k}} - h_{\mathbf{k}}\eta_{\mathbf{k}}^\dagger - h_{\mathbf{k}}^*\eta_{\mathbf{k}}\right]. \tag{C2}$$

Here $\hbar\lambda_{\mathbf{k}}$ is the dispersion defined in Eq. (21), the classical ground state energy is

$$E_0 = -\hbar S N_{\mathrm{FI}}\left[J\hbar S N_\delta + H_z\right], \tag{C3}$$

and the momentum-dependent in-plane magnetic energy

$$h_{\mathbf{k}} = \sqrt{\frac{S}{2N_{\mathrm{FI}}}}\hbar\sum_i (H_i^x + iH_i^y)e^{-i\mathbf{k}\cdot\mathbf{r}_i}. \tag{C4}$$

Since the applied field has in-plane components, the z direction is not the exact ordering direction in the ground state, leading to a non-diagonal Hamiltonian with linear terms. To get rid of these terms, we translate the fields according to

$$\begin{aligned}\eta_{\mathbf{k}} &\to \eta_{\mathbf{k}} + t_{\mathbf{k}},\\ \eta_{\mathbf{k}}^\dagger &\to \eta_{\mathbf{k}}^\dagger + t_{\mathbf{k}}^*,\end{aligned} \tag{C5}$$

and require that linear terms cancel. Translating the fields leads to the Hamiltonian

$$\begin{aligned}\mathcal{H} \to E_0 + \sum_{\mathbf{k}}\Big\{&\hbar\lambda_{\mathbf{k}}\eta_{\mathbf{k}}^\dagger\eta_{\mathbf{k}} + [\hbar\lambda_{\mathbf{k}}t_{\mathbf{k}} - h_{\mathbf{k}}]\eta_{\mathbf{k}}^\dagger\\ &+ [\hbar\lambda_{\mathbf{k}}t_{\mathbf{k}}^* - h_{\mathbf{k}}^*]\eta_{\mathbf{k}} + \hbar\lambda_{\mathbf{k}}t_{\mathbf{k}}^*t_{\mathbf{k}} - h_{\mathbf{k}}t_{\mathbf{k}}^* - h_{\mathbf{k}}^*t_{\mathbf{k}}\Big\},\end{aligned} \tag{C6}$$

and we therefore require

$$t_{\mathbf{k}} = \frac{h_{\mathbf{k}}}{\hbar\lambda_{\mathbf{k}}}. \tag{C7}$$

The resulting diagonal Hamiltonian is

$$\mathcal{H} = E_0 + \sum_{\mathbf{k}}[\hbar\lambda_{\mathbf{k}}\eta_{\mathbf{k}}^\dagger\eta_{\mathbf{k}} - \hbar\lambda_{\mathbf{k}}t_{\mathbf{k}}^*t_{\mathbf{k}}]. \tag{C8}$$

The last term in the above equation results in a renormalization of the classical ground state,

$$\begin{aligned}E_0 &\to E_0 - \sum_{\mathbf{k}}\hbar\lambda_{\mathbf{k}}t_{\mathbf{k}}^*t_{\mathbf{k}}\\ &= E_0 - \sum_{i,j,\mathbf{k}}\frac{S\hbar^2(H_i^x + iH_i^y)(H_j^x - iH_j^y)^2e^{i\mathbf{k}\cdot(\mathbf{r}_j-\mathbf{r}_i)}}{2N_{\mathrm{FI}}\hbar\lambda_{\mathbf{k}}}.\end{aligned} \tag{C9}$$

In the case of constant in-plane components, this simplifies to

$$\begin{aligned}E_0 =& -\hbar S N_{\mathrm{FI}}\left\{J\hbar S N_\delta + \left[H^z + \frac{(H^x)^2 + (H^y)^2}{2H^z}\right]\right\}\\ \approx& -\hbar S N_{\mathrm{FI}}\left[J\hbar S N_\delta + |\mathbf{H}|\right],\end{aligned} \tag{C10}$$

where the approximation in the last line is valid in the limit $|H^x|, |H^y| \ll |H^z|$. This is as expected, since the classical ground state is generally oriented along $\mathbf{H}$, not H^z. The translation of magnon operators in Eq. (C5) can therefore be understood as a local rotation of the spin ordering ansatz due to small inhomogeneous in-plane fields, valid in the limit $|H_i^{x,y}| \ll |H^z|$.

[1] M. Eschrig, Physics Today **64**, 43 (2011).

[2] J. Linder and J. W. A. Robinson, Nature Physics **11**, 307 (2015), 1510.00713.

[3] V. K. Joshi, Engineering Science and Technology, an International Journal **19**, 1503 (2016).

[4] T. Tokuyasu, J. A. Sauls, and D. Rainer, Phys. Rev. B **38**, 8823 (1988).

[5] E. A. Demler, G. B. Arnold, and M. R. Beasley, Phys. Rev. B **55**, 15174 (1997).

[6] R. S. Keizer, S. T. B. Goennenwein, T. M. Klapwijk, G. Miao, X. G., and A. Gupta, Nature **439**, 825 (2006).

[7] M. S. Anwar, F. Czeschka, M. Hesselberth, M. Porcu, and J. Aarts, Phys. Rev. B **82**, 100501 (2010).

[8] M. Eschrig, Rep. Prog. Phys. **78**, 104501 (2015).

[9] Ø. Johansen and A. Brataas, Phys. Rev. Lett. **121**, 087204 (2018).

[10] A. T. G. Janssønn, H. T. Simensen, A. Kamra, A. Brataas, and S. H. Jacobsen, Phys. Rev. B **102**, 180506(R) (2020).

[11] Y. Tabuchi, S. Ishino, T. Ishikawa, R. Yamazaki, K. Usami, and Y. Nakamura, Phys. Rev. Lett. **113**, 083603 (2014).

[12] Y. Tabuchi, S. Ishino, A. Noguchi, T. Ishikawa, R. Yamazaki, K. Usami, and Y. Nakamura, Science **349**, 405 (2015), https://www.science.org/doi/pdf/10.1126/science.aaa3693.

[13] Y. Tabuchi, S. Ishino, A. Noguchi, T. Ishikawa, R. Yamazaki, K. Usami, and Y. Nakamura, Comptes Rendus Physique **17**, 729 (2016), quantum microwaves / Micro-ondes quantiques.

[14] F. Schlawin, A. Cavalleri, and D. Jaksch, Phys. Rev. Lett. **122**, 133602 (2019).

[15] K. Kakazu and Y. S. Kim, Phys. Rev. A **50**, 1830 (1994).

[16] X. Liu, T. Galfsky, Z. Sun, F. Xia, E. Lin, S. Lee, Y.-H. Kéna-Cohen, and V. M. Menon, Nature Photonics **9**, 30 (2015).

[17] Q. Zhang, M. Lou, X. Li, J. L. Reno, W. Pan, J. D. Watson, M. J. Manfra, and J. Kono, Nature Physics **12**, 1005 (2016).

[18] A. Bayer, M. Pozimski, S. Schambeck, D. Schuh, R. Huber, D. Bougeard, and C. Lange, Nano Letters **17**, 6340 (2017), pMID: 28937772, https://doi.org/10.1021/acs.nanolett.7b03103.

[19] J. Keller, G. Scalari, S. Cibella, C. Maissen, F. Appugliese, E. Giovine, R. Leoni, M. Beck, and J. Faist, Nano Letters **17**, 7410 (2017), pMID: 29172537, https://doi.org/10.1021/acs.nanolett.7b03228.

[20] Ø. Johansen, *Antiferromagnetic Insulator Spintronics*, Ph.D. thesis, Norwegian University of Science and Technology (2019).

[21] Ö. O. Soykal and M. E. Flatté, Phys. Rev. B **82**, 104413 (2010).

[22] Ö. O. Soykal and M. E. Flatté, Phys. Rev. Lett. **104**, 077202 (2010).

[23] H. Huebl, C. W. Zollitsch, J. Lotze, F. Hocke, M. Greifenstein, A. Marx, R. Gross, and S. T. B. Goennenwein, Phys. Rev. Lett. **111**, 127003 (2013).

[24] J. Bourhill, N. Kostylev, M. Goryachev, D. L. Creedon, and M. E. Tobar, Phys. Rev. B **93**, 144420 (2016).

[25] B. Zare Rameshti and G. E. W. Bauer, Phys. Rev. B **97**, 014419 (2018).

[26] N. J. Lambert, J. A. Haigh, S. Langenfeld, A. C. Doherty, and A. J. Ferguson, Phys. Rev. A **93**, 021803 (2016).

[27] A. Cottet, Z. Leghtas, and T. Kontos, Phys. Rev. B **102**, 155105 (2020).

[28] A. Altland and B. Simons, *Condensed Matter Field Theory*, 8th ed. (Cambridge University Press, 2010).

[29] N. B. Kopnin, *Theory of Nonequilibrium Superconductivity* (Oxford University Press, 2009).

[30] M. Kachelrieß, *Quantum Fields: From the Hubble to the Planck Scale* (Oxford University Press, 2017).

[31] J. W. Negele and H. Orland, *Quantum Many-Particle Systems* (Westview Press, 1998).

[32] Formulated as a criterion, consider an FI film with a finite depth d. Along the z axis, the magnetic component of the cavity modes are modulated as $\cos\frac{\pi z}{L_z} \approx -1 + \frac{\pi^2(z-L_z)^2}{2!L_z^2}$ near $z = L_z$. A negligible modulation from the top of the FI $z = L_z$, to the bottom $z = L_z - d$, then translates to $\frac{\pi^2 d^2}{2!L_z^2} \ll 1$. The argument is analogous for the SC. For simplicity, we therefore model the FI and SC as 2D square-lattice monolayers. Their lattice constants are respectively a_{FI} and a_{SC}, and dimensions l_x^{FI}, l_y^{FI}, l_x^{SC} and l_y^{SC}.

[33] K. Takasan, S. Sumita, and Y. Yanase, arXiv:2110.06959 (2021).

[34] J. Pearl, Applied Physics Letters **5**, 65 (1964).

[35] M. Tinkham, *Introduction to Superconductivity* (McGraw-Hill, 1996).

[36] A. I. Gubin, K. S. Il'in, S. A. Vitusevich, M. Siegel, and N. Klein, Phys. Rev. B **72**, 064503 (2005).

[37] We have neglected a prefactor $\sqrt{w_{\ell_z} w_z}$ of $u_{\mathbf{Q}z}$ which is inconsequential to us. The function w is $1/2$ when its argument is 0, and 1 otherwise. This prefactor is due to the reflecting boundary conditions.

[38] T. Holstein and H. Primakoff, Physical Review **58**, 1098 (1940).

[39] C. Kittel, *Quantum Theory of Solids* (John Wiley & Sons, Inc., 1963).

[40] More precisely, $D^{\mathrm{FI}}_{\mathbf{kq}}$ equals an infinite sum of Kronecker delta functions when the FI and the cavity share dimensions: one for each $\mathbf{q}$ that is equivalent to $\mathbf{k}$ up to an FI Brillouin zone. We are anyhow only concerned with the first Brillouin zone, since the interaction strengths decrease rapidly with increasing $|\mathbf{q}|$ due to factors $\omega_{\mathbf{q}}^{-1}$ entering the coupling constants.

[41] R. Takashima, S. Fujimoto, and T. Yokoyama, Physical Review B **96**, 121203(R) (2017).

[42] L. G. Johnsen, H. T. Simensen, A. Brataas, and J. Linder, Phys. Rev. Lett. **127**, 207001 (2021).

[43] J. P. Ellis, Computer Physics Communications **210**, 103 (2017).

[44] For the same reason the term S_1^{SC} in the SC action would only contribute when paired with Σ, leading to terms two orders higher in g^γ compared to the terms containing Σ only.

[45] F. Gross, B. S. Chandrasekhar, D. Einzel, K. Andres, P. J. Hirschfeld, H. R. Ott, J. Beuers, Z. Fisk, and J. L. Smith, Zeitschrift für Physik B Condensed Matter **64**, 175 (1986).

[46] M. A. Musa, R. S. Azis, N. H. Osman, J. Hassan, and T. Zangina, Results in Physics **7**, 1135 (2017).

[47] N. W. Ashcroft and N. D. Mermin, *Solid State Physics* (Saunders, 1976).

[48] K. Il'in, D. Rall, M. Siegel, A. Engel, A. Schilling, A. Semenov, and H.-W. Huebers, Physica C: Superconductivity **470**, 953 (2010), vortex Matter in Nanostructured Superconductors.

[49] Y. Lin, L. Jin, H. Zhang, Z. Zhong, Q. Yang, Y. Rao, and M. Li, Journal of Magnetism and Magnetic Materials **496**, 165886 (2020).

[50] I. Zaytseva, A. Abaloszew, B. C. Camargo, Y. Syryanyy, and M. Z. Cieplak, Sci. Rep. **10**, 19062 (2020).

[51] Y. Lu, R. Ojajärvi, P. Virtanen, M. Silaev, and T. T. Heikkilä, arXiv:2108.06202 (2022).

[52] F. Wegner, *Supermathematics and its Applications in Statistical*

Physics, Lecture Notes in Physics, Vol. 920 (Springer-Verlag Berlin Heidelberg, 2016).
[53] F. N. Krohg and A. Sudbø, Physical Review B **98**, 014510 (2018).
[54] D. H. Douglass, Physical Review Letters **6**, 346 (1961).

Appendix A

Mean field theory

Appendix summary: Using mean field theory, the spin reorientation (6.80) can be reproduced to first order in the paramagnetic coupling. We demonstrate this here, and compare it to the path integral result.

After introducing all the quasiparticle bases, the full system Hamiltonian reads

$$\begin{aligned}\mathcal{H} = &\sum_{\mathbf{k}} \hbar\lambda_{\mathbf{k}} \eta^\dagger_{\mathbf{k}} \eta_{\mathbf{k}} + \sum_{\mathbf{p}m} E_{\mathbf{p}m} \gamma^\dagger_{\mathbf{p}m} \gamma_{\mathbf{p}m} + \sum_{\mathbf{q}\varsigma} \hbar\omega_{\mathbf{q}} a^\dagger_{\mathbf{q}\varsigma} a_{\mathbf{q}\varsigma} \\ &+ \sum_{\mathbf{k}d} \sum_{\mathbf{q}} g_d^{\mathbf{kq}} (\nu_d \eta_{-\mathbf{k}} + \nu_d^* \eta^\dagger_{\mathbf{k}})(a_{\mathbf{q}1} + a^\dagger_{-\mathbf{q}1}) \\ &+ \sum_{\mathbf{q}\varsigma} \sum_{\mathbf{p}m} \sum_{\mathbf{p}'m'} g_{\varsigma m m'}^{\mathbf{qpp}'} (a_{\mathbf{q}\varsigma} + a^\dagger_{-\mathbf{q}\varsigma}) \gamma^\dagger_{\mathbf{p}m} \gamma_{\mathbf{p}'m'}. \end{aligned} \tag{A.1}$$

We now separate $\gamma^\dagger_{\mathbf{p}m}\gamma_{\mathbf{p}'m'}$ into an expectation value and a fluctuation (cf. Eq. (3.14)):

$$\gamma^\dagger_{\mathbf{p}m}\gamma_{\mathbf{p}'m'} = \langle \gamma^\dagger_{\mathbf{p}m}\gamma_{\mathbf{p}'m'}\rangle + \left(\gamma^\dagger_{\mathbf{p}m}\gamma_{\mathbf{p}'m'} - \langle \gamma^\dagger_{\mathbf{p}m}\gamma_{\mathbf{p}'m'}\rangle\right) \equiv \langle \gamma^\dagger_{\mathbf{p}m}\gamma_{\mathbf{p}'m'}\rangle + \delta(\gamma^\dagger_{\mathbf{p}m}\gamma_{\mathbf{p}'m'}). \tag{A.2}$$

This relation is exact. The mean-field approach amounts to assuming that the fluctuation is small, usually expressed as "$\delta(\gamma^\dagger_{\mathbf{p}m}\gamma_{\mathbf{p}'m'}) \ll \langle \gamma^\dagger_{\mathbf{p}m}\gamma_{\mathbf{p}'m'}\rangle$".[1] In our case, this assumption is justified by considering a weak cavity–SC coupling. Then

[1] More rigorously, in order to quantify $\delta(\gamma^\dagger_{\mathbf{p}m}\gamma_{\mathbf{p}'m'})$ (whose expectation value is zero: $\langle\delta(\gamma^\dagger_{\mathbf{p}m}\gamma_{\mathbf{p}'m'})\rangle = \langle \gamma^\dagger_{\mathbf{p}m}\gamma_{\mathbf{p}'m'}\rangle - \langle \gamma^\dagger_{\mathbf{p}m}\gamma_{\mathbf{p}'m'}\rangle = 0$), one can instead consider its root mean square (rms):

$$\begin{aligned}\mathrm{rms}(\delta(\gamma^\dagger_{\mathbf{p}m}\gamma_{\mathbf{p}'m'})) &\equiv \sqrt{\langle (\delta\gamma^\dagger_{\mathbf{p}m}\gamma_{\mathbf{p}'m'})^\dagger \delta\gamma^\dagger_{\mathbf{p}m}\gamma_{\mathbf{p}'m'}\rangle} \\ &= \sqrt{\langle \gamma^\dagger_{\mathbf{p}'m'}\gamma_{\mathbf{p}m}\gamma^\dagger_{\mathbf{p}m}\gamma_{\mathbf{p}'m'}\rangle - |\langle \gamma^\dagger_{\mathbf{p}m}\gamma_{\mathbf{p}'m'}\rangle|^2}. \end{aligned} \tag{A.3}$$

We can then formulate the mean-field criterion rigorously as an rms version of the Ginzburg criterion [133], namely

$$\mathrm{rms}(\delta(\gamma^\dagger_{\mathbf{p}m}\gamma_{\mathbf{p}'m'})) \ll \langle \gamma^\dagger_{\mathbf{p}m}\gamma_{\mathbf{p}'m'}\rangle. \tag{A.4}$$

the corrections to the diagonal SC theory will be small compared to the leading-order (non-interacting) mean field value,

$$\langle \gamma^\dagger_{\mathbf{p}m}\gamma_{\mathbf{p}'m'}\rangle = n_F(E_{\mathbf{p}m})\delta_{\mathbf{p}\mathbf{p}'}\delta_{mm'}. \tag{A.5}$$

We can therefore disregard the fluctuations $\delta(\gamma^\dagger_{\mathbf{p}m}\gamma_{\mathbf{p}'m'})$, which in effect decouples the SC from the rest of the system in the Hamiltonian (A.1). We therefore discard the diagonal SC terms. Since we are ultimately interested in the effect on the magnons, and the magnons only couple to the $\varsigma = 1$ photons, we also discard $\varsigma = 2$ photons. Thus, the Hamiltonian reads

$$\begin{aligned}\mathcal{H} = &\sum_{\mathbf{k}}\hbar\lambda_{\mathbf{k}}\eta^\dagger_{\mathbf{k}}\eta_{\mathbf{k}} + \sum_{\mathbf{q}}\hbar\omega_{\mathbf{q}}a^\dagger_{\mathbf{q}1}a_{\mathbf{q}1} \\ &+ \sum_{\mathbf{k}d}\sum_{\mathbf{q}} g_d^{\mathbf{k}\mathbf{q}}(v_d\eta_{-\mathbf{k}} + v_d^*\eta^\dagger_{\mathbf{k}})(a_{\mathbf{q}1} + a^\dagger_{-\mathbf{q}1}) + \sum_{\mathbf{q}}\Gamma_{\mathbf{q}}(a_{\mathbf{q}1} + a^\dagger_{-\mathbf{q}1}),\end{aligned} \tag{A.6}$$

where we introduced

$$\Gamma_{\mathbf{q}} \equiv \sum_{\mathbf{p}m} g^{\mathbf{q}\mathbf{p}\mathbf{p}}_{\varsigma mm} n_F(E_{\mathbf{p}m}). \tag{A.7}$$

The Hamiltonian has thus acquired linear photon terms. If absorbed into the bilinear magnon and photon terms, it does not only lead to a shift in the photon operators: Because of the Zeeman coupling, a shift in the photon theory $a_{\mathbf{q}1} \to a_{\mathbf{q}1} + s_{\mathbf{q}}$ will also lead to linear terms in the magnon theory, proportional to $s_{\mathbf{q}}$ and $s^*_{-\mathbf{q}}$. In order to completely absorb the new linear photon term, it is therefore necessary to also shift the magnon theory $\eta_{\mathbf{k}} \to \eta_{\mathbf{k}} + t_{\mathbf{k}}$. We identify $t_{\mathbf{k}}$ as analogous to the quantity (6.80) we found for the reorientation of the FI spins.

Neglecting a contribution to the zero-point energy, the bilinear magnon and photon theory therefore reads

$$\begin{aligned}\mathcal{H} = &\sum_{\mathbf{k}}\hbar\lambda_{\mathbf{k}}(\eta_{\mathbf{k}} + t_{\mathbf{k}})^\dagger(\eta_{\mathbf{k}} + t_{\mathbf{k}}) + \sum_{\mathbf{q}}\hbar\omega_{\mathbf{q}}(a_{\mathbf{q}1} + s_{\mathbf{q}})^\dagger(a_{\mathbf{q}1} + s_{\mathbf{q}}) \\ &+ \sum_{\mathbf{k}d}\sum_{\mathbf{q}} g_d^{\mathbf{k}\mathbf{q}}(v_d(\eta_{-\mathbf{k}} + t_{-\mathbf{k}}) + v_d^*(\eta_{\mathbf{k}} + t_{\mathbf{k}})^\dagger)((a_{\mathbf{q}1} + s_{\mathbf{q}}) + (a_{-\mathbf{q}1} + s_{-\mathbf{q}})^\dagger).\end{aligned} \tag{A.8}$$

Isolating all the linear operator terms, and requiring that they absorb the linear terms in Eq. (A.6), yields

$$\sum_{\mathbf{q}}\hbar\omega_{\mathbf{q}}(a^\dagger_{\mathbf{q}1}s_{\mathbf{q}} + a_{\mathbf{q}1}s^*_{\mathbf{q}}) + \sum_{\mathbf{k}d}\sum_{\mathbf{q}} g_d^{\mathbf{k}\mathbf{q}}(a_{\mathbf{q}1} + a^\dagger_{-\mathbf{q}1})(v_d t_{-\mathbf{k}} + v_d^* t^*_{\mathbf{k}}) = \sum_{\mathbf{q}}\Gamma_{\mathbf{q}}(a_{\mathbf{q}1} + a^\dagger_{-\mathbf{q}1}), \tag{A.9}$$

$$\sum_{\mathbf{k}}\hbar\lambda_{\mathbf{k}}(\eta^\dagger_{\mathbf{k}}t_{\mathbf{k}} + \eta_{\mathbf{k}}t^*_{\mathbf{k}}) + \sum_{\mathbf{k}d}\sum_{\mathbf{q}} g_d^{\mathbf{k}\mathbf{q}}(s_{\mathbf{q}} + s^*_{-\mathbf{q}})(v_d\eta_{-\mathbf{k}} + v_d^*\eta^\dagger_{\mathbf{k}}) = 0. \tag{A.10}$$

Since all operators $a_{\mathbf{q}1}$, $a^\dagger_{\mathbf{q}1}$, $\eta_{\mathbf{k}}$ and $\eta^\dagger_{\mathbf{k}}$ are linearly independent, we can gather their coefficients and equate them to zero separately. From the first line, we find

$$s_{\mathbf{q}} = \frac{1}{\hbar\omega_{\mathbf{q}}}\left(\Gamma_{\mathbf{q}} - \sum_{\mathbf{k}d}\sum_{\mathbf{q}} g_d^{\mathbf{k}\mathbf{q}}(v_d t_{-\mathbf{k}} + v_d^* t^*_{\mathbf{k}})\right). \tag{A.11}$$

Inserting the expression for $\Gamma_{\mathbf{q}}$, the second line then yields the following self-consistency equation for $t_{\mathbf{k}}$:

$$t_{\mathbf{k}} = -\frac{1}{\hbar\lambda_{\mathbf{k}}}\sum_{d\mathbf{q}}\frac{2g_d^{\mathbf{kq}}\nu_d^*}{\hbar\omega_{\mathbf{q}}}\left(-\sum_{\mathbf{k}'d'}g_{d'}^{\mathbf{k}',-\mathbf{q}}(\nu_{d'}t_{-\mathbf{k}'}+\nu_{d'}^*t_{\mathbf{k}}'^*)+\sum_{\mathbf{p}m}g_{1mm}^{-\mathbf{qpp}}n_F(E_{\mathbf{p}m})\right). \tag{A.12}$$

This is seen to be equivalent to Eq. (6.80). Recall that t_k was the shift in the Matubara basis η_k, so $t_{\mathbf{k}}$ and t_k relate by

$$t_{\mathbf{k}} = \frac{1}{\sqrt{\beta}}\sum_{\Omega_m}t_k e^{-i\Omega_m\tau}. \tag{A.13}$$

To all orders in the coupling constants, t_k carries a factor $\delta_{\Omega_m 0}$ originating from P_d^k (Eq. (6.69)), so we find that

$$t_{\mathbf{k}} = \frac{t_{(0,\mathbf{k})}}{\sqrt{\beta}}. \tag{A.14}$$

This is a straight-forward validation of the anisotropy result. However, this does not imply that the mean field theory captures the broad results of the path integral approach. Observe that from this mean field theory, we are only able to extract the anisotropy field to leading order in the cavity–SC coupling. Meanwhile, the path integral approach has enabled us to readily extend the theory to second order. We demonstrated the use of going to this order when deriving corrections to the magnon spectrum in Ch. 7, where it is necessary to go to this order to capture the contributions from the SC. Moreover, with the path integral approach, we are readily able to integrate out the effect of the mediator (the cavity), leaving an exact effective FI–SC theory (see Paper II). This is a very interesting result in its own right, and provides a route to accurately extract influences on the SC (such as the pairing potential induced by interactions with the cavity [11]). While mean field theory offers a fast way to the leading-order result, it is not a replacement for the path integral approach.

Appendix B

Schrieffer–Wolff transformation

Appendix summary: Preceding the Matsubara path integral approach presented in the main thesis, we eliminated the cavity from the calculations by way of a perturbative Schrieffer–Wolff approach. Aiming to extract effects of the SC on the FI, this approach did not come to fruition for the reasons discussed at the end of this appendix. As it is a common approach in similar works, we provide an instructional comparison between these calculations, and those resulting from mean field theory and the path integral approach.

Not all research ends in positive results. In this section, instead of exactly integrating out the cavity by means of the Matsubara path integral formalism, we will do so approximately by means of the Schrieffer–Wolff transformation. While leaving some open questions, and not turning out particularly fruitful for the purpose of extracting renormalized magnon energies or the induced anisotropy field across the FI, it can still be valuable for a reader to see the approach and its results for our system. This transformation was used in Ref. [10] to extract renormalized magnon energies as a function of an applied magnetostatic field, for a ferro- and antiferromagnetic magnon mode coupled via a cavity. It was also used it Ref. [11] to extract an effective electron–electron pairing potential in a normal metal induced by interactions with a cavity, giving rise to Amperean superconductivity.

A Schrieffer–Wolff transformation likewise involves rotating a Hamiltonian using a unitary matrix S, such that

$$\mathcal{H}' \equiv e^{S}\mathcal{H}e^{-S} = e^{S}(\mathcal{H}_0 + \mathcal{H}_{\text{int}})e^{-S}. \tag{B.1}$$

Here $\mathcal{H}_0 \equiv \mathcal{H}_0^{\text{FI}} + \mathcal{H}_0^{\text{cav}} + \mathcal{H}_0^{\text{SC}}$ comprises the free terms, and $\mathcal{H}_{\text{int}} \equiv \mathcal{H}_{\text{FI-cav}} + \mathcal{H}_{\text{cav-SC}}$ comprises the interaction terms. The unitarity of S ensures that the eigenvalues of the $\mathcal{H}$ remain the same after the transformation [2]. By the Hadamard lemma, this expression may be series expanded in powers of S, yielding

$$e^{S}(\mathcal{H}_0 + \mathcal{H}_{\text{int}})e^{-S} = \mathcal{H}_0 + \mathcal{H}_{\text{int}} + [S, \mathcal{H}_0 + \mathcal{H}_{\text{int}}] + \frac{1}{2!}[S,[S, \mathcal{H}_0 + \mathcal{H}_{\text{int}}]] + \dots \tag{B.2}$$

The series is now truncated at second order; as will be shown, the expansion in S is equivalent to an expansion in resonance parameters of the form g/δ, where g is the FI–cavity or cavity–SC coupling strength, and δ the difference between magnon or SC quasiparticle energies, and photon energies, respectively. Truncation is therefore justified by limiting energies to off-resonant regimes.

The trick is now to eliminate $\mathcal{H}_{\text{int}}$ by choosing S such that

$$[\mathcal{H}_0, S] = \mathcal{H}_{\text{int}} = -[S, \mathcal{H}_0]. \tag{B.3}$$

Inserting this into Eq. (B.2), one may readily verify that

$$\mathcal{H}' \approx \mathcal{H}_0 + \frac{1}{2}[S, \mathcal{H}_{\text{int}}]. \tag{B.4}$$

$\mathcal{H}_{\text{int}}$ is then eliminated in favor of $\frac{1}{2}[S, \mathcal{H}_{\text{int}}]$, which contains the effective FI–SC interaction.

Following Refs. [2, 11, 106], we postulate a general form for S

$$\begin{aligned} S \equiv & \sum_{\mathbf{k}\mathbf{q}d} g_d^{\mathbf{k}\mathbf{q}} \big[a_{\mathbf{q}1} (A_1^{\mathbf{k}\mathbf{q}} \nu_d \eta_{-\mathbf{k}} + A_2^{\mathbf{k}\mathbf{q}} \nu_d^* \eta_{\mathbf{k}}^\dagger) + a_{-\mathbf{q}1}^\dagger (A_3^{\mathbf{k}\mathbf{q}} \nu_d \eta_{-\mathbf{k}} + A_4^{\mathbf{k}\mathbf{q}} \nu_d^* \eta_{\mathbf{k}}^\dagger) \big] \\ & + \sum_{\mathbf{p}\mathbf{p}'} \sum_{\mathbf{q}\varsigma} \sum_{mm'} g_{\varsigma mm'}^{\mathbf{q}\mathbf{p}\mathbf{p}'} (B_{\varsigma mm',1}^{\mathbf{p}\mathbf{p}'\mathbf{q}} a_{\mathbf{q}\varsigma} + B_{\varsigma mm',2}^{\mathbf{p}\mathbf{p}'\mathbf{q}} a_{-\mathbf{q}\varsigma}^\dagger) \gamma_{\mathbf{p}m}^\dagger \gamma_{\mathbf{p}'m'} \end{aligned} \tag{B.5}$$

where $A_i^{\mathbf{k}\mathbf{q}}$ and $B_{\varsigma mm',i}^{\mathbf{p}\mathbf{p}'\mathbf{q}}$ are coefficients. In the following, we will deal with a number of commutators. We will make use of the following commutator identities, with A, B, C, D operators:

$$[A, BC] = [A, B]C + B[A, C], \tag{B.6}$$

$$[AB, C] = A[B, C] + [A, C]B, \tag{B.7}$$

$$[AB, CD] = A[B, C]D + [A, C]BD + CA[B, D] + C[A, D]B, \tag{B.8}$$

$$[A, B + C] = [A, B] + [A, C], \tag{B.9}$$

$$[A, B] = 2AB - \{A, B\}. \tag{B.10}$$

The last identity is particularly useful for commutators of fermionic operators, the braces denoting the anticommutator. Inserting now the system Hamiltonian (6.1) and the postulated form (B.5) for S into Eq. (B.3), one finds the coefficients

$$A_1^{\mathbf{k}\mathbf{q}} = -A_4^{\mathbf{k}\mathbf{q}} = \frac{1}{\hbar(-\omega_{\mathbf{k}}^\eta - \omega_{\mathbf{q}})}, \quad A_3^{\mathbf{k}\mathbf{q}} = -A_2^{\mathbf{k}\mathbf{q}} = \frac{1}{\hbar(-\omega_{\mathbf{k}}^\eta + \omega_{\mathbf{q}})}, \tag{B.11}$$

$$B_{\varsigma mm',1}^{\mathbf{p}\mathbf{p}'\mathbf{q}} = \frac{1}{(-1)^m E_{\mathbf{p}} - (-1)^{m'} E_{\mathbf{p}'} - \hbar\omega_{\mathbf{q}}}, \quad B_{\varsigma mm',2}^{\mathbf{p}\mathbf{p}'\mathbf{q}} = \frac{1}{(-1)^m E_{\mathbf{p}} - (-1)^{m'} E_{\mathbf{p}'} + \hbar\omega_{\mathbf{q}}}. \tag{B.12}$$

By inspection of S in Eq. (B.5), it becomes clear that the truncation of the series in Eq. (B.2) is justified if the denominators of the coefficients (B.11) and (B.12) are much larger than the coupling constants.

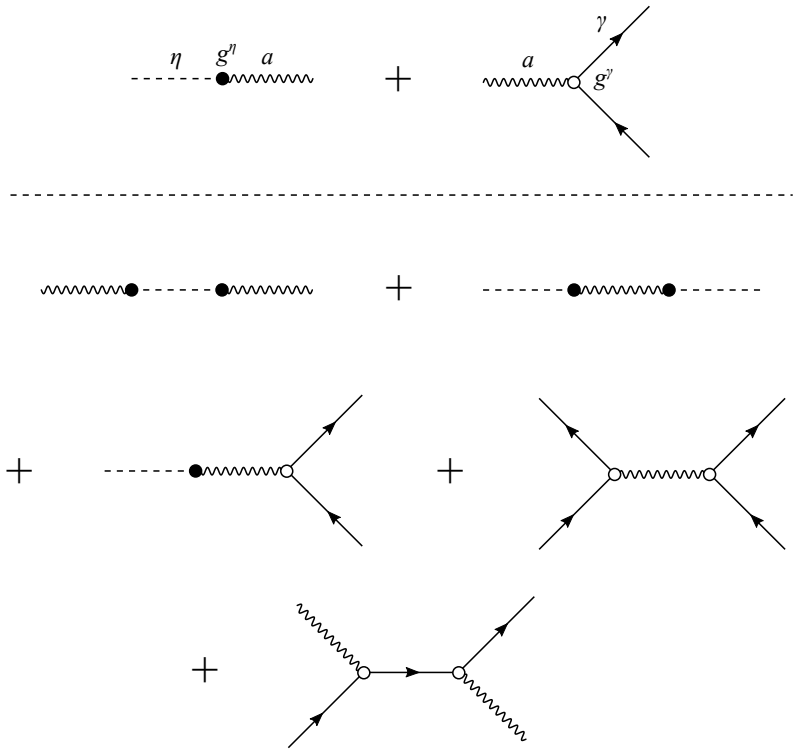

Figure B.1: Leading order effective interactions resulting from the Scrieffer–Wolff transformation, cf. Eq. (B.17). Magnons (η) and photons (a) interact via the Zeeman coupling (g^η), and photons and SC quasiparticles (γ) via the paramagnetic coupling (g^γ). Diagrammatically, the effective interactions can be obtained by joining the ends of the building blocks in the first line. Note that the first and the last term do not appear in the Matsubara path integral after integrating out the cavity (see Ch. Chapter 6 and in particular Paper II, where the cavity is integrated out first); this because these terms are there handled by a substitution of photon variables that decouples the cavity, which is subsequently neglected, leaving only the diagrams with internal photon lines. Inspired by the corresponding figure in Paper II, courtesy of H. G. Hugdal.

$[S, \mathcal{H}_{\text{int}}]$ remains to be computed. This involves the following commutators:

$$\begin{aligned}
&[a_{\mathbf{q}1}(A_1^{\mathbf{kq}}\nu_d\eta_{-\mathbf{k}} + A_2^{\mathbf{kq}}\nu_d^*\eta_{\mathbf{k}}^\dagger) + a_{-\mathbf{q}1}^\dagger(A_3^{\mathbf{kq}}\nu_d\eta_{-\mathbf{k}} + A_4^{\mathbf{kq}}\nu_d^*\eta_{\mathbf{k}}^\dagger, (\nu_{d'}\eta_{-\mathbf{k}'} + \nu_{d'}^*\eta_{\mathbf{k}'}^\dagger)(a_{\mathbf{q}'1} + a_{-\mathbf{q}'1}^\dagger)] \\
&= \delta_{-\mathbf{k}\mathbf{k}'}\Big[a_{\mathbf{q}1}(\nu_d\nu_{d'}^* A_1^{\mathbf{kq}} - \nu_d^*\nu_{d'}A_2^{\mathbf{kq}}) + a_{-\mathbf{q}1}^\dagger(\nu_d\nu_{d'}^* A_3^{\mathbf{kq}} - \nu_d^*\nu_{d'}A_4^{\mathbf{kq}})\Big](a_{\mathbf{q}'1} + a_{-\mathbf{q}'1}^\dagger) \\
&\quad + \delta_{\mathbf{q},-\mathbf{q}'}(\nu_{d'}\eta_{-\mathbf{k}'} + \nu_{d'}^*\eta_{\mathbf{k}'}^\dagger)\Big[(A_1^{\mathbf{kq}} - A_3^{\mathbf{kq}})\nu_d\eta_{-\mathbf{k}} + (A_2^{\mathbf{kq}} - A_4^{\mathbf{kq}})\nu_d^*\eta_{\mathbf{k}}^\dagger\Big],
\end{aligned} \tag{B.13}$$

$$\begin{aligned}
&[a_{\mathbf{q}1}(A_1^{\mathbf{kq}}\nu_d\eta_{-\mathbf{k}} + A_2^{\mathbf{kq}}\nu_d^*\eta_{\mathbf{k}}^\dagger) + a_{-\mathbf{q}1}^\dagger(A_3^{\mathbf{kq}}\nu_d\eta_{-\mathbf{k}} + A_4^{\mathbf{kq}}\nu_d^*\eta_{\mathbf{k}}^\dagger, (a_{\mathbf{q}'\varsigma'} + a_{-\mathbf{q}'\varsigma'}^\dagger)\gamma_{\mathbf{p}m}^\dagger\gamma_{\mathbf{p}'m'}] \\
&= \delta_{\mathbf{q},-\mathbf{q}'}\delta_{1,\varsigma'}\Big[(A_1^{\mathbf{kq}} - A_3^{\mathbf{kq}})\nu_d\eta_{-\mathbf{k}} + (A_2^{\mathbf{kq}} - A_4^{\mathbf{kq}})\nu_d^*\eta_{\mathbf{k}}^\dagger\Big]\gamma_{\mathbf{p}m}^\dagger\gamma_{\mathbf{p}'m'},
\end{aligned} \tag{B.14}$$

$$
\begin{aligned}
&[(B^{\mathbf{pp'q}}_{\varsigma mm',1}a_{\mathbf{q}\varsigma}+B^{\mathbf{pp'q}}_{\varsigma mm',2}a^\dagger_{-\mathbf{q}\varsigma})\gamma^\dagger_{\mathbf{p}m}\gamma_{\mathbf{p'}m'},(\nu_{d'}\eta_{-\mathbf{k'}}+\nu^*_{d'}\eta^\dagger_{\mathbf{k'}})(a_{\mathbf{q'}1}+a^\dagger_{-\mathbf{q'}1})]\\
&\quad=\delta_{\mathbf{q},-\mathbf{q'}}\delta_{\varsigma,1}(B^{\mathbf{pp'q}}_{\varsigma mm',1}-B^{\mathbf{pp'q}}_{\varsigma mm',2})(\nu_{d'}\eta_{-\mathbf{k'}}+\nu^*_{d'}\eta^\dagger_{\mathbf{k'}})\gamma^\dagger_{\mathbf{p}m}\gamma_{\mathbf{p'}m'},
\end{aligned}
\tag{B.15}
$$

$$
\begin{aligned}
&[(B^{\mathbf{pp'q}}_{\varsigma mm',1}a_{\mathbf{q}\varsigma}+B^{\mathbf{pp'q}}_{\varsigma mm',2}a^\dagger_{-\mathbf{q}\varsigma})\gamma^\dagger_{\mathbf{p}m}\gamma_{\mathbf{p'}m'},(a_{\mathbf{q'}\varsigma'}+a^\dagger_{-\mathbf{q'}\varsigma'})\gamma^\dagger_{\tilde{\mathbf{p}}\tilde{m}}\gamma_{\tilde{\mathbf{p}}'\tilde{m}'}]\\
&=\delta_{\mathbf{q},-\mathbf{q'}}\delta_{\varsigma\varsigma'}(B^{\mathbf{pp'q}}_{\varsigma mm',1}-B^{\mathbf{pp'q}}_{\varsigma mm',2})\gamma^\dagger_{\mathbf{p}m}\gamma_{\mathbf{p'}m'}\gamma^\dagger_{\tilde{\mathbf{p}}\tilde{m}}\gamma_{\tilde{\mathbf{p}}'\tilde{m}'}\\
&\quad+(a_{\mathbf{q'}\varsigma'}+a^\dagger_{-\mathbf{q'}\varsigma'})(B^{\mathbf{pp'q}}_{\varsigma mm',1}a_{\mathbf{q}\varsigma}+B^{\mathbf{pp'q}}_{\varsigma mm',2}a^\dagger_{-\mathbf{q}\varsigma})(\gamma^\dagger_{\mathbf{p}m}\gamma_{\tilde{\mathbf{p}}'\tilde{m}'}\delta_{\mathbf{p'}\tilde{\mathbf{p}}}\delta_{m'\tilde{m}}-\gamma^\dagger_{\tilde{\mathbf{p}}\tilde{m}}\gamma_{\mathbf{p'}m'}\delta_{\mathbf{p}\tilde{\mathbf{p}}'}\delta_{m\tilde{m}'}).
\end{aligned}
\tag{B.16}
$$

Gathering terms, we then find that the perturbed Hamiltonian (B.4) becomes

$$
\begin{aligned}
\mathcal{H}'\approx&\mathcal{H}_0+\frac{1}{2}[S,\mathcal{H}_{\text{int}}]\\
=&\sum_{\mathbf{k}}\hbar\lambda_{\mathbf{k}}\eta^\dagger_{\mathbf{k}}\eta_{\mathbf{k}}+\sum_{\mathbf{p}m}E_{\mathbf{p}m}\gamma^\dagger_{\mathbf{p}m}\gamma_{\mathbf{p}m}+\sum_{\mathbf{q}\varsigma}\hbar\omega_{\mathbf{q}}a^\dagger_{\mathbf{q}\varsigma}a_{\mathbf{q}\varsigma}\\
&+\frac{1}{2}\sum_{\mathbf{kq}d}g^{\mathbf{kq}}_d\Big[\sum_{\mathbf{q'}d'}g^{-\mathbf{kq'}}_{d'}\Big[a_{\mathbf{q}1}(\nu_d\nu^*_{d'}A^{\mathbf{kq}}_1-\nu^*_d\nu_{d'}A^{\mathbf{kq}}_2)+a^\dagger_{-\mathbf{q}1}(\nu_d\nu^*_{d'}A^{\mathbf{kq}}_3-\nu^*_d\nu_{d'}A^{\mathbf{kq}}_4)\Big](a_{\mathbf{q'}1}+a^\dagger_{-\mathbf{q'}1})\\
&\quad+\sum_{\mathbf{k'}d'}g^{\mathbf{k'},-\mathbf{q}}_{d'}(\nu_{d'}\eta_{-\mathbf{k'}}+\nu^*_{d'}\eta^\dagger_{\mathbf{k'}})\Big[(A^{\mathbf{kq}}_1-A^{\mathbf{kq}}_3)\nu_d\eta_{-\mathbf{k}}+(A^{\mathbf{kq}}_2-A^{\mathbf{kq}}_4)\nu^*_d\eta^\dagger_{\mathbf{k}}\Big]\\
&\quad+\sum_{\mathbf{pp'}}\sum_{mm'}g^{-\mathbf{qpp'}}_{1mm'}\Big[(A^{\mathbf{kq}}_1-A^{\mathbf{kq}}_3+(B^{\mathbf{pp'},-\mathbf{q}}_{\varsigma mm',1}-B^{\mathbf{pp'},-\mathbf{q}}_{\varsigma mm',2}))\nu_d\eta_{-\mathbf{k}}\\
&\qquad+(A^{\mathbf{kq}}_2-A^{\mathbf{kq}}_4+(B^{\mathbf{pp'},-\mathbf{q}}_{\varsigma mm',1}-B^{\mathbf{pp'},-\mathbf{q}}_{\varsigma mm',2}))\nu^*_d\eta^\dagger_{\mathbf{k}}\Big]\gamma^\dagger_{\mathbf{p}m}\gamma_{\mathbf{p'}m'}\Big]\\
&+\frac{1}{2}\sum_{\mathbf{pp'}}\sum_{\mathbf{q}\varsigma}\sum_{mm'}g^{\mathbf{qpp'}}_{\varsigma mm'}\Big[\sum_{\tilde{\mathbf{p}}\tilde{\mathbf{p}}'}\sum_{\tilde{m}\tilde{m}'}g^{-\mathbf{q}\tilde{\mathbf{p}}\tilde{\mathbf{p}}'}_{\varsigma\tilde{m}\tilde{m}'}(B^{\mathbf{pp'},-\mathbf{q}}_{\varsigma mm',1}-B^{\mathbf{pp'},-\mathbf{q}}_{\varsigma mm',2})\gamma^\dagger_{\mathbf{p}m}\gamma_{\mathbf{p'}m'}\gamma^\dagger_{\tilde{\mathbf{p}}\tilde{m}}\gamma_{\tilde{\mathbf{p}}'\tilde{m}'}\\
&\quad+\sum_{\mathbf{q'}\varsigma'}(a_{\mathbf{q'}\varsigma'}+a^\dagger_{-\mathbf{q'}\varsigma'})(B^{\mathbf{pp'},-\mathbf{q}}_{\varsigma mm',1}a_{\mathbf{q}\varsigma}+B^{\mathbf{pp'},-\mathbf{q}}_{\varsigma mm',2}a^\dagger_{-\mathbf{q}\varsigma})\sum_{\tilde{\mathbf{p}}\tilde{m}}(g^{\mathbf{qp'}\tilde{\mathbf{p}}}_{\varsigma' m'\tilde{m}}\gamma^\dagger_{\mathbf{p}m}\gamma_{\tilde{\mathbf{p}}\tilde{m}}-g^{\mathbf{q}\tilde{\mathbf{p}}\mathbf{p}}_{\varsigma'\tilde{m}m}\gamma^\dagger_{\tilde{\mathbf{p}}\tilde{m}}\gamma_{\mathbf{p'}m'})\Big].
\end{aligned}
\tag{B.17}
$$

In the second equality above, the terms in the first line are the unperturbed particle energies; in the second line, photon self-interactions via magnons; in the third line, magnon self-interactions via photons; in the fourth and fifth line, magnon–SC quasiparticle interactions via photons; in the sixth line, a quasiparticle (electron) pairing term analogous to the main result in Ref. [11]; and finally, in the seventh line, various photon–quasiparticle interactions mediated by a virtual quasiparticle (photon–quasiparticle scattering, and quasiparticle pair annihilation/creation). Diagrams of these effective interactions are found in Fig. B.1.

B.1 Extracting results

We now ask how we can proceed from Eq. (B.17), in order to extract the influence of the SC on the FI. Note first that the Schrieffer–Wolff transformation did not

decouple the cavity from the remaining system, leaving a term of the form $(a + a^\dagger)(a + a^\dagger)(\gamma^\dagger\gamma - \gamma^\dagger\gamma)$. However, these terms, as well as the $\gamma^\dagger\gamma\gamma^\dagger\gamma$ pairing terms, will only couple to magnons to higher orders in the expansion parameters. We can therefore neglect these, leaving the cavity uncoupled, and the SC and FI coupling only via the $(\eta + \eta^\dagger)\gamma^\dagger\gamma$ terms:

$$\begin{aligned}\mathcal{H}' \approx &\sum_{\mathbf{k}} \hbar\lambda_{\mathbf{k}}\eta^\dagger_{\mathbf{k}}\eta_{\mathbf{k}} + \sum_{\mathbf{p}m} E_{\mathbf{p}m}\gamma^\dagger_{\mathbf{p}m}\gamma_{\mathbf{p}m} \\ &+ \frac{1}{2}\sum_{\mathbf{kq}d} g_d^{\mathbf{kq}}\Big[\sum_{\mathbf{k}'d'} g_{d'}^{\mathbf{k}',-\mathbf{q}}(\nu_{d'}\eta_{-\mathbf{k}'} + \nu^*_{d'}\eta^\dagger_{\mathbf{k}'})\Big[(A_1^{\mathbf{kq}} - A_3^{\mathbf{kq}})\nu_d\eta_{-\mathbf{k}} + (A_2^{\mathbf{kq}} - A_4^{\mathbf{kq}})\nu^*_d\eta^\dagger_{\mathbf{k}}\Big] \\ &\quad + \sum_{\mathbf{pp}'}\sum_{mm'} g_{1mm'}^{-\mathbf{qpp}'}\Big[(A_1^{\mathbf{kq}} - A_3^{\mathbf{kq}} + (B^{\mathbf{pp}',-\mathbf{q}}_{\varsigma mm',1} - B^{\mathbf{pp}',-\mathbf{q}}_{\varsigma mm',2}))\nu_d\eta_{-\mathbf{k}} \\ &\quad + (A_2^{\mathbf{kq}} - A_4^{\mathbf{kq}} + (B^{\mathbf{pp}',-\mathbf{q}}_{\varsigma mm',1} - B^{\mathbf{pp}',-\mathbf{q}}_{\varsigma mm',2}))\nu^*_d\eta^\dagger_{\mathbf{k}}\Big]\gamma^\dagger_{\mathbf{p}m}\gamma_{\mathbf{p}'m'}\Big].\end{aligned} \tag{B.18}$$

B.1.1 Second Schrieffer–Wolff transformation

Performing a second Schrieffer–Wolff transformation with a rotation matrix of the form $S' \sim (\eta + \eta^\dagger)\gamma^\dagger\gamma$ in a similar attempt to decouple the FI and SC is tempting, but would not be fruitful. Including the off-diagonal magnon terms in the interaction Hamiltonian, it would be of the form $\mathcal{H}'_{\text{int}} \sim (\eta + \eta^\dagger)(\eta + \eta^\dagger) + (\eta + \eta^\dagger)\gamma^\dagger\gamma$. Then the commutator $[S', \mathcal{H}'_{\text{int}}] \sim (\eta + \eta^\dagger)\gamma^\dagger\gamma + (\eta + \eta^\dagger)(\eta + \eta^\dagger)\gamma^\dagger\gamma + \gamma^\dagger\gamma\gamma^\dagger\gamma$. Clearly this transformation would fail to decouple the FI and SC.

In relation to the SC, this additional Schrieffer–Wolff transformation could be useful for eventually extracting corrections to the electron pairing potential due mediated interactions with the magnons. These corrections would enter via the $\gamma^\dagger\gamma\gamma^\dagger\gamma$ terms. However, these corrections would be limited to off-resonant regimes; we have already outlined how an exact effective SC theory can be constructed using the path integral approach in the main thesis (see Sec. 8.1.2), without limitations to off-resonant regimes.

B.1.2 Mean field theory

Another way forward is mean field theory (cf. Appendix A). Assuming weak interactions, $\gamma^\dagger_{\mathbf{p}m}\gamma_{\mathbf{p}'m'}$ can be replaced by its leading-order expectation value $\langle\gamma^\dagger_{\mathbf{p}m}\gamma_{\mathbf{p}'m'}\rangle = n_F(E_{\mathbf{p}m})\delta_{\mathbf{pp}'}\delta_{mm'}$. In effect, this decoupled the FI and the SC, leaving behind linear magnon terms. We can thus extract the leading-order anisotropy field across the FI due to the SC, by absorbing the linear magnon terms into the bilinear terms, as was done in Sec. 6.1.4.

However, we demonstrated in Appendix A that one can apply mean field theory already to the initial system Hamiltonian to extract precisely this quantity. To this end, the Schrieffer–Wolff transformation is therefore redundant.

We conclude this appendix here, as we transitioned to the path integral approach of the main thesis around this point in the research. Unlike the Schrieffer–Wolff approach, the path integral formalism makes short work of the cavity: since the system action (see Ch. 6) is no more than bilinear in the photon variables, the corresponding path integral is Gaussian, allowing us to exactly integrate out the cavity without reference to the Schrieffer–Wolff constraint on off-resonance (cf. Paper II). The path integral formalism furthermore enabled us to readily go an order beyond mean field theory with respect to the cavity–SC coupling.

Appendix C

Draft on corrections to the magnon spectrum

In light of the results and analysis presented in Ch. 7 on corrections to the magnon spectrum, it is instructional to contrast this with a previous attempt by us at deriving renormalized magnon energies analytically, which led to overestimated energy corrections. A draft for a manuscript written in parallel with these calculations is attached below in this appendix. There we proceeded with the approach outlined in Sec. 7.1.2, amounting to solving the equation $m_\rho(z) = 0$ (Eq. (7.12)) for the eigenvalues of the effective action matrix, in order to determine the renormalized energies.

In order to extract analytical solutions to $m_\rho(z) = 0$, it was necessary to reduce its order in z. The step that ultimately yielded a different answer from what was presented above, is seen to be the replacement of $\Delta E_{00}^{\mathbf{kp}}$ with a weighted average $\langle \Delta E_{00}^{\mathbf{kp}} \rangle$. This enabled extraction of the factor $(\langle \Delta E_{00}^{\mathbf{kp}} \rangle - z)^{-1}$ from the sum over $\mathbf{p}$, and rendered analytical solutions to z attainable. Proceeding with these solutions numerically, we were able to produce promising energy corrections of almost 30 MHz for a set of parameter inputs specified in the draft. However, in light of the discussion on the importance of the distribution of intersections between the magnon energy and the SC quasiparticle energy differences, it is clear that replacing $\Delta E_{00}^{\mathbf{kp}}$ with $\langle \Delta E_{00}^{\mathbf{kp}} \rangle$ equates to collecting all the different intersections into one for all. This leads to a maximal constructive addition of individual anticrossings, and leads to a large overestimation of the actual self energy.

For comparison, the self energy approach presented in this thesis involves the same issues, but solves them differently. First, the issue of extracting eigenmode propagators from the non-diagonal effective action (7.28) is achieved by assuming weak coupling $|Q^k| \ll |\hbar\lambda_k|$, which immediately brings the action to a diagonal form. The propagators can then be read off directly. Second, the analogous issue

of Eq. (7.6) being of enormous order[1] in z is solved again by invoking the weak coupling assumption, enabling us to replace z by the magnon energy in the expression for the self energy (Eq. (7.44)). The solutions following either approach is seen to converge if weak coupling is invoked in place of replacing $\Delta E_{00}^{\mathbf{kp}}$ with $\langle \Delta E_{00}^{\mathbf{kp}} \rangle$. Ultimately, the analytical expression obtained for the self energy in this thesis evidently provides more accurate information about the shape and magnitude of the correction, than when the correction is approximated by collecting all anticrossings into one.

[1]The order reflects the number of mutually interacting particles. This number was elaborated on in Sec. 7.2. The brunt of this order stems from the magnon modes coupling to the entire range of SC quasiparticle modes via scattering on photons.

Photon-mediated superconductor–ferromagnetic insulator anticrossing

Andreas T. G. Janssønn, Henning G. Hugdal, Arne Brataas, and Sol H. Jacobsen
Center for Quantum Spintronics, Department of Physics,
NTNU Norwegian University of Science and Technology, NO-7491 Trondheim, Norway

...

NB: under construction.

I. INTRODUCTION

Superconducting and spintronic technology are two promising low-loss alternatives to electronics (insert refs), while cavities allow for careful engineering of electromagnetic interactions via volume-dependent interaction strengths [1] (insert refs), isolated regions of either magnetic and electric fields (insert refs), long-distance mediated interactions [2, 3], and more.

When two coupled systems approach resonant frequencies, the eigenmode energies exhibit deflection where the dispersion relations of the uncoupled systems would otherwise cross. These are *anticrossings*, or *avoided crossings*: regimes in which the particles of the respective subsystems hybridize. The magnitude of the anticrossing is determined by the interaction strength. The literature is rich in experimental and theoretical research involving anticrossings, including the hybridization of directly coupled magnons and cavity photons [3–9], and cavity-mediated coupling of magnons and qubits [3], and ferro- and antiferromagnetic magnons [10, 11].

In this paper, we derive, theoretically and numerically, anticrossings in the magnon dispersion relation of a ferromagnetic insulator, due to cavity-mediated interactions with a superconductor. We find an experimentally tangible anticrossing for a micrometer cavity. For practical applications, this can serve as a preliminary for designing a bridge for superconducting–spintronic circuitry, with the insulator able to resolve momentum information from the superconductor quasiparticle energies.

II. THEORY

Including the well-known photon term $\mathcal{H}_0^{\text{cav}} \equiv \sum_{\mathbf{q}} \hbar\omega_{\mathbf{q}} a_{\mathbf{q}}^\dagger a_{\mathbf{q}}$, the Hamiltonian for the system of a ferromagnetic insulator (FI), cavity (cav) and superconductor (SC) illustrated in Fig. 1 reads

$$\mathcal{H} \equiv \mathcal{H}_0^{\text{FI}} + \mathcal{H}_{\text{FI-cav}} + \mathcal{H}_0^{\text{cav}} + \mathcal{H}_{\text{cav-SC}} + \mathcal{H}_0^{\text{SC}}, \quad (1)$$

where the labels indicate free terms and interactions. In this section, we first expand upon the set-up, and proceed to specify the remaining terms of $\mathcal{H}$. Then, we use the Matsubara path integral formalism to construct an effective magnon theory. Thence we extract dispersion relations for the quasiparticles of the diagonal theory by equating the determinant of the effective theory to zero, corresponding to divergences in the propagators of the diagonal theory. We limit these solutions to energies near the magnon energy. Finally, from these we extract the magnitude of the anticrossing between the magnons and the SC quasiparticles, to be plotted numerically and compared with expected losses in the next section.

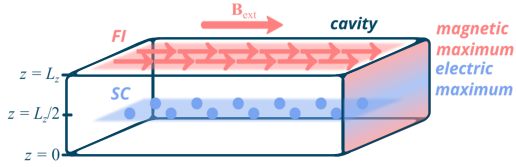

FIG. 1. Illustration of the set-up. A thin ferromagnetic insulator is placed at the top ($z = L_z$), and a thin superconductor in the middle ($z = L_z/2$), inside a rectangular, electromagnetic cavity. The FI and SC span the cavity. The FI is subjected to an external magnetostatic field $\mathbf{B}_{\text{ext}}$ in the y direction. The cavity is short along the z direction (L_z), and long along the perpendicular xy directions, causing cavity modes to separate into a band-like structure. Combined with the placement of the FI and SC, this facilitates coupling to only a subset of cavity modes, modulated in the z direction as illustrated on the right wall.

A. Set-up

Consider a rectangular, electromagnetic cavity, inside of which is placed a thin ferromagnetic insulator (FI) at the top ($z = L_z$), and a thin superconductor (SC) in the middle ($z = L_z/2$). For simplicity, we treat both as square lattice monolayers, with respective lattice constants a_{FI} and a_{SC}. The FI and the SC span the cavity, which has dimensions $L_z \ll L_x, L_y$. The small L_z increases interaction strengths proportional to $1/\sqrt{V}$, with $V = L_x L_y L_z$ the cavity volume; along with the placement of the FI and SC, it furthermore facilitates coupling to the subset of cavity modes modulated in the z direction as illustrated in Fig. 1, as exciting modes in this direction becomes energetically unfavorable. We are only interested in the positional dependency of the FI and SC in the z direction, so we employ reflective boundary conditions for the upper and lower wall of the cavity, and mathematically simpler periodic boundary conditions for the orthogonal directions.

We subject the FI to an external magnetostatic field $\mathbf{B}_{\text{ext}} = B_{\text{ext}}\hat{e}_y$, We can potentially drop this field for YIG which can be achieved using external coils [3, 6–8]. We furthermore subject the SC to a supercurrent, which can be achieved by passing DC through thin wires entering the cavity through

small holes in the walls, too small to affect the cavity modes. The leading effect of the DC is to induce an equilibrium supercurrent with a Cooper pair center-of-mass momentum $2\mathbf{P}$, provided the sample width does not exceed the Pearl length λ^2/d, with λ the effective magnetic penetration depth, and d the sample depth. Specify if this criterion is met in our set-up

With this set-up in mind, we proceed to construct a system Hamiltonian.

B. Hamiltonian: FI

We here present the expressions for the terms of the FI Hamiltonian in the magnon basis, coupling to the cavity by the Zeeman coupling.

Each FI lattice site i is spin-S, with spin vector $\mathbf{S}_i$. The external field $\mathbf{B}_{\text{ext}}$ leads us to consider a magnon basis $\{\eta_i, \eta_i^\dagger\}$ defined with respect to the y axis. By the Holstein–Primakoff transformation, when assuming a low number $\langle \eta_i^\dagger \eta_i \rangle \ll 2S$ of magnons per lattice site, the Cartesian components of the spin read $S_{iy} = \hbar(S - \eta_i^\dagger \eta_i)$, $S_{id} \approx \frac{\hbar\sqrt{2S}}{2}(\nu_d \eta_i + \nu_d^* \eta_i^\dagger)$ in the magnon basis [11–13]. Here $d = z, x$ and $\{\nu_z, \nu_x\} = \{1, -i\}$.

Resolved in its Fourier components, the magnon operator is $\eta_{\mathbf{r}_i} \equiv \sum_{\mathbf{k}} \eta_{\mathbf{k}} e^{i\mathbf{k}\cdot\mathbf{r}_i}/\sqrt{N_{\text{FI}}}$ with N_{FI} the number of FI lattice sites, $\mathbf{k} = (k_x, k_y, 0)$ the magnon momenta, and $\sum_{\mathbf{k}}$ running over the first Brillouin zone (1BZ) of the FI. Include comment on neglecting positional prefactor $\exp(ikr_0)$? The exchange interaction and the Zeeman coupling to $\mathbf{B}_{\text{ext}}$ can then be written on the diagonal form [11–13]

$$\mathcal{H}_0^{\text{FI}} \equiv \sum_{\mathbf{k}} \hbar\lambda_{\mathbf{k}} \eta_{\mathbf{k}}^\dagger \eta_{\mathbf{k}}, \tag{2}$$

where we have introduced the magnon dispersion relation

$$\lambda_{\mathbf{k}} \equiv 2\hbar J N_\delta S \left(1 - \frac{1}{N_\delta}\sum_{\boldsymbol{\delta}} \cos \mathbf{k}\cdot\boldsymbol{\delta}\right) + \frac{g\mu_B}{\hbar} B_{\text{ext}}. \tag{3}$$

Here, $J > 0$ is the ferromagnetic exchange interaction strength, $N_\delta = 4$ the number of nearest neighbors on a square lattice, g the gyromagnetic ratio and μ_B the Bohr magneton. Lastly, $\boldsymbol{\delta} = \{\pm a_{\text{FI}}\hat{e}_x, \pm a_{\text{FI}}\hat{e}_y\}$ are nearest-neighbor lattice vectors.

We move onto the FI–cavity Zeeman interaction. In spin basis, the term reads $\mathcal{H}_{\text{FI-cav}} \equiv -g\mu_B \sum_i \mathbf{S}_i \cdot \mathbf{B}_{\text{cav}}(\mathbf{r}_i)/\hbar$. Here, the cavity magnetic field is $\mathbf{B}_{\text{cav}}(\mathbf{r}_i)$, with $\mathbf{r}_i$ the position of FI lattice site i. In the transversal gauge, $\mathbf{B}_{\text{cav}}$ across the FI ($z = L_z$) reads [1, 14]

$$\begin{aligned}&\mathbf{B}_{\text{cav}}(\mathbf{r}_i)\big|_{\text{FI}} \\ &= \sum_{\mathbf{q}} i(q_y\hat{e}_x - q_x\hat{e}_y)\sin\theta_{\mathbf{q}} \sqrt{\frac{\hbar}{\epsilon\omega_{\mathbf{q}} V}} e^{i\mathbf{q}\cdot\mathbf{r}_i}(a_{\mathbf{q}} + a_{-\mathbf{q}}^\dagger),\end{aligned} \tag{4}$$

where $\mathbf{q} = (q_x, q_y, 0)$ is the in-plane photon momentum, ϵ is the permeability of the cavity, and $\omega_{\mathbf{q}} = c\sqrt{(\pi/L_z)^2 + \mathbf{q}^2}$ is the photon dispersion. Note that $\mathbf{q}$ is only a component of the photon momentum $\mathbf{Q} \equiv \pi\hat{e}_z/L_z + \mathbf{q}$. The factor $\sin\theta_{\mathbf{q}}$ originates from the implementation of the transversal gauge, with $\theta_{\mathbf{q}}$ the polar angle of $\mathbf{Q}$ [14]. Lastly, $\{a_{\mathbf{q}}, a_{\mathbf{q}}^\dagger\}$ is the photon basis; note that we do not resolve this into two linear polarization directions orthogonal to $\mathbf{Q}$ [14], because only one couples to the FI in our set-up.

Inserting the above along with the magnon-basis Cartesian spin components into $\mathcal{H}_{\text{FI-cav}}$, we find [15, 16]

$$\mathcal{H}_{\text{FI-cav}} \approx \sum_{\mathbf{k}} g_{\mathbf{k}}^\eta (\eta_{-\mathbf{k}} - \eta_{\mathbf{k}}^\dagger)(a_{\mathbf{k}} + a_{-\mathbf{k}}^\dagger), \tag{5}$$

where we introduced the FI–cavity coupling constant

$$g_{\mathbf{k}}^\eta \equiv -g\mu_B k_y \sin\theta_{\mathbf{k}} \sqrt{\frac{\hbar S N_{\text{FI}}}{2\epsilon\omega_{\mathbf{k}} V}}. \tag{6}$$

In deriving Eq. (5), we used the Fourier kernel $\sum_i e^{-i(\mathbf{k}-\mathbf{q})\cdot\mathbf{r}_i} = N^{\text{FI}} \sum_{\mathbf{k}} \delta_{\mathbf{qk}}$, with $\delta_{\mathbf{qk}}$ the Kroenecker delta function. We also neglected a scattering term $\sim \eta_{\mathbf{k}}^\dagger \eta_{\mathbf{k}-\mathbf{k}'}(a_{\mathbf{k}'} + a_{-\mathbf{k}'}^\dagger)$, which only results in vanishing contributions to the effective magnon theory due to the low number of magnons.

C. Hamiltonian: SC

Moving onto the SC, we here similarly present the terms of the SC Hamiltonian in the Bogoliubov quasiparticle basis, coupling to the cavity by the paramagnetic coupling.

We consider an s wave superconductor with an equilibrium supercurrent. In the electron basis $\{c_{\mathbf{p}\sigma}, c_{\mathbf{p}\sigma}^\dagger\}$, the non-interacting SC Hamiltonian reads $\mathcal{H}_0^{\text{SC}} \equiv \sum_{\mathbf{p}} \xi_{\mathbf{p}} c_{\mathbf{p}\sigma}^\dagger c_{\mathbf{p}\sigma'} - \sum_{\mathbf{p}} \left(\Delta_{\mathbf{p}} c_{\mathbf{p}+\mathbf{P},\uparrow}^\dagger c_{-\mathbf{p}+\mathbf{P},\downarrow}^\dagger + \Delta_{\mathbf{p}}^* c_{-\mathbf{p}+\mathbf{P},\downarrow} c_{\mathbf{p}+\mathbf{P},\uparrow}\right)$, with $\mathbf{p} = (p_x, p_y, 0)$ the electron momenta, $\sigma = \uparrow, \downarrow$ the spin index, $\xi_{\mathbf{p}}$ the single-electron energy, and $\Delta_{\mathbf{p}}$ the superconducting gap. This is readily diagonalized by a Bogoliubov quasiparticle basis $\{\gamma_{\mathbf{p}m}, \gamma_{\mathbf{p}m}^\dagger\}$, yielding

$$\mathcal{H}_0^{\text{SC}} = \sum_{\mathbf{p}m} E_{\mathbf{p}m} \gamma_{\mathbf{p}m}^\dagger \gamma_{\mathbf{p}m}, \tag{7}$$

where $m = 0, 1$ indexes the quasiparticle type, and the energies are

$$\begin{aligned}E_{\mathbf{p}m} = &\frac{1}{2}\Big[\xi_{\mathbf{p}+\mathbf{P}} - \xi_{-\mathbf{p}+\mathbf{P}} \\ &+ (-1)^m \sqrt{(\xi_{\mathbf{p}+\mathbf{P}} + \xi_{-\mathbf{p}+\mathbf{P}})^2 + 4|\Delta_{\mathbf{p}}|^2}\Big].\end{aligned} \tag{8}$$

The electron and Bogoliubov quasiparticle bases relate via [17]

$$c_{\mathbf{p}+\mathbf{P},\uparrow} \equiv u_{\mathbf{p}}^* \gamma_{\mathbf{p}0} + v_{\mathbf{p}} \gamma_{\mathbf{p}1}, \quad c_{-\mathbf{p}+\mathbf{P},\downarrow}^\dagger \equiv -v_{\mathbf{p}}^* \gamma_{\mathbf{p}0} + u_{\mathbf{p}} \gamma_{\mathbf{p}1}, \tag{9}$$

and the absolute values of the transformation coefficients $u_{\mathbf{p}}$ and $v_{\mathbf{p}}$ satisfy

$$|v_{\mathbf{p}}|^2 = 1 - |u_{\mathbf{p}}|^2 = \frac{1}{2}\left(1 - \frac{\xi_{\mathbf{p}+\mathbf{P}} + \xi_{-\mathbf{p}+\mathbf{P}}}{E_{\mathbf{p}0} - E_{\mathbf{p}1}}\right). \tag{10}$$

Moving onto the interaction term, we use the same discretized coupling as was used in Ref. [1]. We only need to include photons polarized in the same direction as the ones coupling to the FI, cf. Eq. (5). In electron basis, the coupling reads

$$\mathcal{H}_{\mathrm{cav-SC}} = \sum_{\mathbf{p}\sigma}\sum_{\mathbf{q}} g^{\mathbf{qp}}(a_{\mathbf{q}} + a^\dagger_{-\mathbf{q}})c^\dagger_{\mathbf{p}\sigma}c_{\mathbf{p}-\mathbf{q},\sigma}, \tag{11}$$

with the coupling constant

$$\begin{aligned} g^{\mathbf{qp}} \equiv & 2i\frac{a_{\mathrm{SC}}et}{\hbar}\sqrt{\frac{\hbar}{\epsilon\omega_{\mathbf{q}}V}} \\ & \cdot\sum_b \sin\left[(p_b - q_b/2)a_{\mathrm{SC}}\right] O_b^{\mathbf{q}}. \end{aligned} \tag{12}$$

Above, e is the elementary charge, t is the tight-binding hopping parameter, $b = x, y$, and $O_b^{\mathbf{q}} = (\cos\theta_{\mathbf{q}}\cos\varphi_{\mathbf{q}}, \cos\theta_{\mathbf{q}}\sin\varphi_{\mathbf{q}})_b$ is a part of a larger rotation matrix that aligns the original z direction with $\mathbf{Q}$ [1, 14]. Here $\varphi_{\mathbf{q}}$ is the azimuthal angle of $\mathbf{Q}$.

Recasting $\mathcal{H}_{\mathrm{para}}$ in terms of the $\{\gamma_{\mathbf{p}m}, \gamma^\dagger_{\mathbf{p}m}\}$ basis is now a straight-forward exercise. Note first that the physics is anticipated to be concentrated at the Fermi surface, hence for relevant momenta, $|\mathbf{P}|, |\mathbf{q}| \ll |\mathbf{p}| \approx |\mathbf{p}_F|$, the Fermi momenta. Then coupling between different quasiparticle types m nearly vanishes, so it is neglected. We are then left with

$$\mathcal{H}_{\mathrm{cav-SC}} = \sum_{\mathbf{p}m}\sum_{\mathbf{q}} g_m^{\mathbf{qp}}(a_{\mathbf{q}} + a^\dagger_{-\mathbf{q}})\gamma^\dagger_{\mathbf{p}m}\gamma_{\mathbf{p}-\mathbf{q},m}, \tag{13}$$

where the coupling constant is now $g_m^{\mathbf{qp}} \equiv (g^{\mathbf{q},\mathbf{p}+\mathbf{P}}u_{\mathbf{p}}u^*_{\mathbf{p}-\mathbf{q}} + g^{\mathbf{q},\mathbf{p}-\mathbf{P}}v_{\mathbf{p}}v^*_{\mathbf{p}-\mathbf{q}}, g^{\mathbf{q},\mathbf{p}-\mathbf{P}}u^*_{\mathbf{p}}u_{\mathbf{p}-\mathbf{q}} + g^{\mathbf{q},\mathbf{p}+\mathbf{P}}v^*_{\mathbf{p}}v_{\mathbf{p}-\mathbf{q}})_m$.

D. Matsubara path integral formalism

Having specified all terms in $\mathcal{H}$, we now aim to construct an effective magnon theory from which to extract anticrossings in the renormalized magnon dispersion relation. To this end, we employ the Matsubara path integral formalism to integrate out the photonic and fermionic degrees of freedom. The Matsubara action reads [18–20]

$$\begin{aligned} S \equiv \int_0^\beta \mathrm{d}\tau\Bigg[& \sum_{\mathbf{k}} \eta^\dagger_{\mathbf{k}}\hbar\partial_\tau\eta_{\mathbf{k}} + \sum_{\mathbf{q}} a^\dagger_{\mathbf{q}}\hbar\partial_\tau a_{\mathbf{q}} \\ & + \sum_{\mathbf{p}m}\gamma^\dagger_{\mathbf{p}m}\hbar\partial_\tau\gamma_{\mathbf{p}m} + \mathcal{H}\Bigg], \end{aligned} \tag{14}$$

where τ is an imaginary-time parameter, and $\beta = \hbar/k_BT$ is the inverse temperature T in units of time. The particle operators have now been replaced by complex (bosons) and Graßmann (fermions) numbers. The integral is now converted into a sum over Matsubara frequencies by decomposing the particles into thermal Fourier modes, i.e. $\eta_{\mathbf{k}}(\tau) = \sum_{\Omega_m}\eta_k e^{-i\Omega_m\tau}/\sqrt{\beta}$ and similarly for the other particles. Here $\Omega_n = 2n\pi/\beta$, $n \in \mathbb{Z}$, are the bosonic Matsubara frequencies; for the fermions, they are $\omega_n = (2n-1)\pi/\beta$. We furthermore introduced the 4-vector $k = (-\Omega_m, \mathbf{k})$, and do the same for the other momenta: $q = (-\Omega_n, \mathbf{q})$ and $p = (-\omega_n, \mathbf{p})$. The partial derivatives $\hbar\partial_\tau$ in Eq. (14) are thus integrated into the diagonal particle terms as e.g.

$$\int_0^\beta \mathrm{d}\tau\sum_{\mathbf{k}}\eta^\dagger_{\mathbf{k}}\hbar(\partial_\tau + \lambda_{\mathbf{k}})\eta_{\mathbf{k}} = \sum_k \eta^\dagger_k\hbar\lambda_k\eta_k, \tag{15}$$

where we used the Fourier kernel $\int_0^\beta \mathrm{d}\tau\exp(-i\Omega\tau) = \beta\delta(\tau)$, with $\delta(\tau)$ the Dirac delta function. We also defined

$$\lambda_k \equiv -i\Omega_m + \lambda_{\mathbf{k}}, \tag{16}$$

and likewise define $\omega_q \equiv -i\Omega_n + \omega_{\mathbf{q}}$ and $E_{pm} \equiv -i\hbar\omega_n + E_{\mathbf{p}m}$.

Moving on, the imaginary-time partition function reads

$$Z \equiv \int\mathcal{D}[\eta,\eta^\dagger]\int\mathcal{D}[a,a^\dagger]\int\mathcal{D}[\gamma,\gamma^\dagger]e^{-S/\hbar}, \tag{17}$$

where $\int\mathcal{D}[\dots]$ is shorthand for the path integrals over every particle mode. In constructing an effective magnon theory, we need to account for the influences of $\int\mathcal{D}[a,a^\dagger]$ and $\int\mathcal{D}[\gamma,\gamma^\dagger]$ on $\int\mathcal{D}[\eta,\eta^\dagger]$. The former is readily accounted for by a shift of integration variables $a_q \to a_q + J_{-q}/\hbar\omega_{\mathbf{q}}$ and $a^\dagger_q \to a^\dagger_q + J_q/\hbar\omega_{\mathbf{q}}$, with J_q a current operator that aggregates the interactions with the cavity. This decouples the cavity from the remaining system, leaving behind an exact effective addition $-\sum_q J_qJ_{-q}/\hbar\omega_q$ to the action, containing effective FI–FI, SC–SC and FI–SC interaction terms.

The fermionic integral is then performed perturbatively, to order $\mathcal{O}\left[(g^\eta g^\gamma/\hbar\omega_q E_{pm})^2\right]$. To this order, the effective SC–SC term (analogous to the pairing term found for a normal metal in Ref. [1]) does not influence the magnon theory, so it is neglected. The remaining SC terms are bilinear in the $\{\gamma_{\mathbf{p}m}, \gamma^\dagger_{\mathbf{p}m}\}$ basis, hence the $\int\mathcal{D}[\gamma,\gamma^\dagger]$ path integral is Gaussian. This evaluates to a determinant, which by $\det(1+X) = \exp\mathrm{Tr}\ln(1+X) = \exp\mathrm{Tr}(X - X^2/2 + \mathcal{O}\left[(g^\eta g^\gamma/\hbar\omega_q E_{pm})^3\right])$ is reinserted into the magnon theory as more effective additions to the action.

Now, effective magnon terms with products of more than two η's and $\eta^\dagger$'s, i.e. trilinear and higher order terms, can be neglected on account of the low number of magnons. Furthermore, linear terms can be removed from the theory by a shift of variables without affecting the quantity of interest, the particle dispersions. We are thus left with a bilinear magnon theory with an effective action

$$S^{\mathrm{FI}} = \sum_k \hbar\lambda_k\eta^\dagger_k\eta_k + \sum_k Q^k(\eta_{-k} - \eta^\dagger_k)(\eta_k - \eta^\dagger_{-k}), \tag{18}$$

with

$$\begin{aligned} Q^k \equiv & |g^\eta_{\mathbf{k}}|^2\Bigg(\frac{1}{\hbar\omega_k} + \frac{2\hbar^2\omega^2_{\mathbf{k}}}{(\hbar^2\omega^2_{\mathbf{k}} + \hbar^2\Omega^2_m)^2} \\ & \cdot\sum_{\mathbf{p}m}|g^{\mathbf{kp}}_m|^2\frac{n_F(E_{\mathbf{p}m}) - n_F(E_{\mathbf{p}-\mathbf{k},m})}{\Delta E^{\mathbf{kp}}_m - i\hbar\Omega_m}\Bigg). \end{aligned} \tag{19}$$

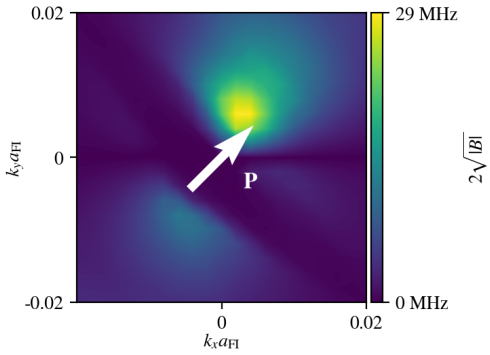

FIG. 2. $2\sqrt{|B|}$ as a function of $\mathbf{k}$, in units of Hz. We have assumed cavity dimensions $L_x = L_y = 10\,\mu\text{m}$, $L_z = 1\,\mu\text{m}$ and temperature $T = 1\,\text{K}$. The remaining parameters are material; these are summarized in Tab. I for YIG (FI) and MgB_2 (SC). The losses are expected to be $\leq 10\,\text{MHz}$, which the maxima of $2\sqrt{|B|}$ exceed. For maximum anticrossing, $\hbar\lambda_{\mathbf{k}}$ and $\langle \Delta E_0^{\mathbf{kp}} \rangle_{\mathbf{p}}$ need to be tuned to cross at the $\mathbf{k}$ of maximum $2\sqrt{|B|}$. This can be achieved by tuning the external field $\mathbf{B}_{\text{ext}}$; we find that this must be (insert values). Note that the coupling is asymmetric (hence (a) and (c) are not the same up to a rotation, and (b) is visibly offset from the direction of $\mathbf{P}$) because the Zeeman coupling (6) is asymmetric. The Zeeman coupling is furthermore linear in $q_y = k_y$, hence the horizontal line for $k_y = 0$ where the coupling is extinguished.

Above, we introduced the energy difference

$$\Delta E_m^{\mathbf{kp}} \equiv E_{\mathbf{p}m} - E_{\mathbf{p}-\mathbf{k},m}. \tag{20}$$

We lastly note that this action can be recast on vector–matrix–vector form as [21–25]

$$S^{\text{FI}} = \sum_k \eta_k^\dagger \mathcal{M}_k \eta_k. \tag{21}$$

with $\eta_k \equiv (\eta_k, \eta_{-k}, \eta_k^\dagger, \eta_{-k}^\dagger)^T$ the vector of coupled magnon modes, and $\mathcal{M}_k$ the matrix collecting coefficients.

We can thus move onto the objective, namely, to extract the anticrossings incurred to the magnon dispersion in the effective theory.

E. Anticrossings

The summand under $\sum_{\Omega_m}$ in the effective action (18) is now analytically continued to complex values of $z \equiv i\hbar\Omega_m$. If we had diagonalized the effective theory, the energies of the eigenmodes would be the solutions for z for which the propagators diverges [20]. These relate inversely to the matrix $\mathcal{G}^{-1}$ of the diagonal theory, hence proportionally to $1/\det \mathcal{G}^{-1}$. Divergent regimes thus corresponds to $\det \mathcal{G}^{-1}(z) = 0$. Since $\mathcal{G}^{-1}$ relates to $\mathcal{M}$ by an invertible transformation, we can equivalently solve for $\det \mathcal{M}(z) = 0$. Finally, we can reduce the order of this equation in z by using $\det \mathcal{M} = \prod_\rho m_\rho$, with m_ρ the eigenvalues of $\mathcal{M}$. Here ρ is the eigenmode index. These can be shown to come in duplicate pairs [21–25], hence we only label $\rho = \pm$. Thus, we need to solve $m_\pm(z) = 0$.

As the equation stands, the solutions are numerically, but not analytically tangible. We therefore look for simplifications. First, we note that there is a solution for every particle coupling directly (photons) or indirectly (fermions) to a given magnon mode. We can therefore reduce the number of solutions by assuming $z \approx \hbar\lambda_{\mathbf{k}} \ll \hbar\omega_{\mathbf{q}}$, hence $\hbar\omega_{\mathbf{q}} \pm z \approx \hbar\omega_{\mathbf{q}}$. Hence, after performing the sum over m,

$$Q^k \approx |g_{\mathbf{k}}^\eta|^2 \left(\frac{1}{\hbar\omega_{\mathbf{k}}} + \frac{2}{\hbar^2\omega_{\mathbf{k}}^2} \cdot \sum_{\mathbf{p}} |g_0^{\mathbf{kp}}|^2 \frac{\tanh\left(\frac{\beta E_{\mathbf{p}-\mathbf{k},0}}{2\hbar}\right) - \tanh\left(\frac{\beta E_{\mathbf{p},0}}{2\hbar}\right)}{\Delta E_0^{\mathbf{kp}} - i\hbar\Omega_m} \right). \tag{22}$$

Furthermore, the energies $\Delta E_0^{\mathbf{kp}}$ give rise to a large number of anticrossings with $\hbar\lambda_{\mathbf{k}}$, with maximal anticrossings at certain values of $\mathbf{p}$, with a decreasing and ultimately negligible anticrossing at nearby values. We therefore instead extract the net anticrossing due to all these anticrossings, by replacing all $\Delta E_0^{\mathbf{kp}}$ with a single weighted average only depending on $\mathbf{k}$, meaning we are left with only a single anticrossing, and hence only two solutions to $m_\pm(z) = 0$ near the anticrossing.

Finally, because a sufficiently strong field $\mathbf{B}_{\text{ext}}$ renders $\hbar\lambda_{\mathbf{k}}$ positive for all $\mathbf{k}$ (cf. Eq. (3)), the anticrossing of interest will occur at positive energies, so we can limit $\sum_{\mathbf{p}}$ in Eq. (22) to $\mathbf{p}$ for which $\Delta E_0^{\mathbf{kp}}$ is positive. Then we do not have to take into account that the difference in $\tanh$ functions goes from being negative to positive as $\Delta E_0^{\mathbf{kp}}$ goes from being positive to negative. Thus, we substitute $\Delta E_0^{\mathbf{kp}}$ for the weighted average

$$\langle \Delta E_0^{\mathbf{kp}} \rangle_{\mathbf{p}} \equiv \frac{\sum_{\mathbf{p}} |g_0^{\mathbf{kp}}|^2 \left(\tanh\left(\frac{\beta E_{\mathbf{p}-\mathbf{k},0}}{2\hbar}\right) - \tanh\left(\frac{\beta E_{\mathbf{p},0}}{2\hbar}\right)\right) \Delta E_0^{\mathbf{kp}}}{\sum_{\mathbf{p}} |g_0^{\mathbf{kp}}|^2 \left(\tanh\left(\frac{\beta E_{\mathbf{p}-\mathbf{k},0}}{2\hbar}\right) - \tanh\left(\frac{\beta E_{\mathbf{p},0}}{2\hbar}\right)\right)}. \tag{23}$$

The eigenvalues $m_\pm$ of $\mathcal{M}_k$ in Eq. (21) are readily found. With the shorthand notation $\lambda \equiv \hbar\lambda_{\mathbf{k}}$, $E \equiv \langle \Delta E_0^{\mathbf{kp}} \rangle_{\mathbf{p}}$, $A \equiv 2\frac{|g_{\mathbf{k}}^\eta|^2}{\hbar\omega_k}$ and

$$B \equiv \frac{4}{\hbar^2\omega_{\mathbf{k}}^2} \sum_{\mathbf{p}}{}' |g_0^{\mathbf{kp}}|^2 \left(\tanh\left(\frac{\beta E_{\mathbf{p}-\mathbf{k},0}}{2\hbar}\right) - \tanh\left(\frac{\beta E_{\mathbf{p},0}}{2\hbar}\right)\right), \tag{24}$$

The positive solutions to $m_\pm(z) = 0$ read

$$z_\pm \equiv \left(\frac{1}{2}\left(\lambda^2 - 2\lambda A + E^2 + 2B\right) \pm \frac{1}{2}\sqrt{\left(\lambda^2 - 2\lambda A - E^2 + 2B\right)^2 + 8B\lambda(E+\lambda)} \right)^{\frac{1}{2}}. \tag{25}$$

At the center of the anticrossing, using $E^2 = \lambda^2 - 2\lambda A \approx \lambda^2$ and $|B| \ll \lambda$, these eigenmode bands reduce to

$$z_\pm \approx \lambda \pm \sqrt{|B|}, \tag{26}$$

hence the magnitude of the anticrossing is quantified by $2\sqrt{B}$.

III. RESULTS AND DISCUSSION

For $2\sqrt{|B|}$ to be measurable, it needs to exceed losses in the system. Losses are usually cited in units of Hz, meaning energies are divided by $2\pi\hbar = h$. For reference, Refs. [3, 6, 7] report losses of 1–12 MHz for low modes of Cu or superconducting Nb cavities, the uniform mode of various YIG samples, and a superconducting qubit. Ref. [6] reports losses of 50 MHz in a Ga-doped YIG crystal, but stresses that losses in pure YIG are significantly smaller. Hence, $2\sqrt{|B|}/2\pi\hbar \gtrsim 10\,\mathrm{MHz}$ is expected to be measurable for similar material choices. In Fig. 2, we compute $2\sqrt{|B|}$ numerically for a micrometer cavity and for a specific supercurrent momentum $\mathbf{P}$, yielding upwards of $2\sqrt{|B|} = 29\,\mathrm{MHz}$. Include also numerics.

TABLE I. Table of numerical parameter values.

Numerical parameters	
YIG (FI)	MgB_2 (SC)

(include words on how the results extend to other gaps (p, d wave etc.). include corresponding numerics.)

ACKNOWLEDGMENTS

We acknowledge funding via the "Outstanding Academic Fellows" programme at NTNU, the Research Council of Norway Grant number 302315, as well as through its Centres of Excellence funding scheme, project number 262633, "QuSpin".

[1] F. Schlawin, A. Cavalleri, and D. Jaksch, Phys. Rev. Lett. **122**, 133602 (2019).
[2] A. T. G. Janssønn, H. T. Simensen, A. Kamra, A. Brataas, and S. H. Jacobsen, Phys. Rev. B **102**, 180506(R) (2020).
[3] Y. Tabuchi, S. Ishino, A. Noguchi, T. Ishikawa, R. Yamazaki, K. Usami, and Y. Nakamura, Comptes Rendus Physique **17**, 729 (2016), quantum microwaves / Micro-ondes quantiques.
[4] Ö. O. Soykal and M. E. Flatté, Phys. Rev. B **82**, 104413 (2010).
[5] Ö. O. Soykal and M. E. Flatté, Phys. Rev. Lett. **104**, 077202 (2010).
[6] H. Huebl, C. W. Zollitsch, J. Lotze, F. Hocke, M. Greifenstein, A. Marx, R. Gross, and S. T. B. Goennenwein, Phys. Rev. Lett. **111**, 127003 (2013).
[7] J. Bourhill, N. Kostylev, M. Goryachev, D. L. Creedon, and M. E. Tobar, Phys. Rev. B **93**, 144420 (2016).
[8] Y. Tabuchi, S. Ishino, T. Ishikawa, R. Yamazaki, K. Usami, and Y. Nakamura, Phys. Rev. Lett. **113**, 083603 (2014).
[9] Y. Tabuchi, S. Ishino, A. Noguchi, T. Ishikawa, R. Yamazaki, K. Usami, and Y. Nakamura, Science **349**, 405 (2015), https://www.science.org/doi/pdf/10.1126/science.aaa3693.
[10] Ø. Johansen and A. Brataas, Phys. Rev. Lett. **121**, 087204 (2018).
[11] Ø. Johansen, *Antiferromagnetic Insulator Spintronics*, Ph.D. thesis, Norwegian University of Science and Technology (2019).
[12] C. Kittel, *Quantum Theory of Solids* (John Wiley & Sons, Inc., 1963).
[13] T. Holstein and H. Primakoff, Physical Review **58**, 1098 (1940).
[14] K. Kakazu and Y. S. Kim, Phys. Rev. A **50**, 1830 (1994).
[15] S. M. Rezende, *Fundamentals of Magnonics* (Springer, 2020).
[16] S. Chaudhuri and F. Keeper, Journal of Physics and Chemistry of Solids **45**, 47 (1984).
[17] M. Tinkham, *Introduction to Superconductivity* (McGraw-Hill, 1996).
[18] A. Altland and B. Simons, *Condensed Matter Field Theory*, 8th ed. (Cambridge University Press, 2010).
[19] M. Kachelrieß, *Quantum Fields: From the Hubble to the Planck Scale* (Oxford University Press, 2017).
[20] J. W. Negele and H. Orland, *Quantum Many-Particle Systems* (Westview Press, 1998).
[21] C. Tsallis, Journal of Mathematical Physics **19**, 277 (1978), https://doi.org/10.1063/1.523549.
[22] J. L. van Hemmen, Z. Phys. B **38**, 271 (1980).
[23] R. Rossignoli and A. M. Kowalski, Phys. Rev. A **72**, 032101 (2005).
[24] R. Rossignoli and A. M. Kowalski, Phys. Rev. A **79**, 062103 (2009).
[25] J. Garcia and R. Rossignoli, Phys. Rev. A **96**, 062130 (2017).

Appendix D

Proof that $\langle \eta'_k \rangle = 0$

We want to show $\langle \eta'_k \rangle = 0$ (cf. Sec. 6.1.4). To see this, note first that $\langle \eta'_k \rangle = \frac{1}{\sqrt{\beta}} \int_0^\beta \mathrm{d}\tau \langle \eta'_{\mathbf{k}} \rangle e^{i\Omega_m \tau}$ by the inverse of Eq. (6.12). It therefore suffices to show $\langle \eta'_{\mathbf{k}} \rangle = 0$. Now, the corresponding action $S^{\mathrm{FI}'}$ for the magnon theory in the $\{\eta'_k, \eta'^\dagger_k\}$ basis is the same as S^{FI} (Eq. (6.66)) less the linear magnon terms. Adding a source term $\int_0^\beta \mathrm{d}\tau \sum_{\mathbf{k}} (J^*_{\mathbf{k}} \eta'_{\mathbf{k}} + J_{\mathbf{k}} \eta'^\dagger_{\mathbf{k}}) = \sum_k (J^*_k \eta'_k + J_k \eta'^\dagger_k)$ to the action, the quantity $\langle \eta'_{\mathbf{k}} \rangle$ can thus be evaluated using the path integral result [110]

$$\langle \eta'_{\mathbf{k}} \rangle = \frac{1}{Z^{\mathrm{FI}}} \frac{\delta Z^{\mathrm{FI}}}{\delta J^*_{\mathbf{k}}} \bigg|_{J=J^*=0}, \tag{D.1}$$

with δ indicating the functional derivative, and $J = J^* = 0$ shorthand for setting all sources to zero. Absorbing these source terms into the remaining action produces a partition function of the form

$$Z^{\mathrm{FI}} = \exp\left(\sum_{kk'} F^*(J_k, J^*_k) \mathcal{M}_{kk'} F(J_{k'}, J^*_{k'}) \right) \int \mathcal{D}[\eta', \eta'^\dagger] e^{-S^{\mathrm{FI}'}/\hbar}, \tag{D.2}$$

where F is some function of J_k and J^*_k, $\mathcal{M}$ is some matrix, and the path integral is independent of the sources. It now suffices to note that $F(J_k, J^*_k)|_{J=J^*=0} = F(0,0) = 0$ since there would be no source terms to absorb in this case. Thus

$$\begin{aligned} \langle \eta'_{\mathbf{k}} \rangle \propto & \frac{\delta Z^{\mathrm{FI}}}{\delta J^*_{\mathbf{k}}} \bigg|_{J=J^*=0} \\ = & \sum_{k'k''} \Bigg(\frac{\delta F^*(J_{k'}, J^*_{k'})}{\delta J^*_{\mathbf{k}}} \mathcal{M}_{k'k''} F(J_{k''}, J^*_{k''}) \\ & + F^*(J_{k'}, J^*_{k'}) \mathcal{M}_{k'k''} \frac{\delta F(J_{k''}, J^*_{k''})}{\delta J^*_{\mathbf{k}}} \Bigg) Z^{\mathrm{FI}} \bigg|_{J=J^*=0} \\ = & 0, \end{aligned} \tag{D.3}$$

since all terms in the second line contain either $F(0,0)$ or $F^*(0,0)$. Hence $\langle \eta'_k \rangle = \langle \eta_k \rangle - t_k = 0$.

ISBN 978-82-326-6434-4 (printed ver.)
ISBN 978-82-326-6369-9 (electronic ver.)
ISSN 1503-8181 (printed ver.)
ISSN 2703-8084 (online ver.)

NTNU

Norwegian University of
Science and Technology